

DISSERTATION ZUR ERLANGUNG DES DOKTORGRADES
DER FAKULTÄT FÜR PHYSIK
DER LUDWIG-MAXIMILLIANS-UNIVERSITÄT

MICROFABRICATION OF CELL-LIKE 3D GEOMETRY
FOR *IN VITRO* RECONSTITUTION OF DYNAMIC
PROTEIN SYSTEMS

HIROMUNE ETO

aus Tokio, Japan

2021

Dissertation eingereicht am 10.05.2021

1. Gutachterin: Prof. Dr. Petra Schwille

2. Gutachter: Prof. Dr. Chase Broedersz

Mündliche Prüfung am 25.06.2021

親愛なる家族のみんなへ

ZUSAMMENFASSUNG

Die Erzeugung von *in vitro* Umgebungen, die zelluläre Bedingungen imitieren, ist ein wichtiger Bestandteil der synthetischen Bottom-up-Biologie. Solche Umgebungen müssen relevante biochemische und biophysikalische Funktionalitäten sowie die richtige Form enthalten - da die Geometrie bei vielen biologischen Prozessen eine entscheidende Rolle spielt. In dieser Hinsicht ist die Mikrofabrikation ein effektiver Weg, um Strukturen auf Längenskalen zu bilden, die die Proteinfunktion beeinflussen können. Mit den neu aufkommenden Verfahren in der Biochemie und den Fabrikationstechnologien stehen wir vor der ständigen Herausforderung, uns an neue Methoden anzupassen und dann innovative Designideen zu entwickeln, die uns ein besseres Verständnis des jeweiligen biologischen Systems ermöglichen.

In dieser Arbeit habe ich mich auf die Entwicklung von Werkzeugen konzentriert, mit denen wir die Geometrie von *in vitro* Umgebungen kontrollieren können, die insbesondere Lipidmembranen involvieren. Die Lipidgrenzfläche ist eine entscheidender Teil der zellulären Umgebung, an der viele Proteinfunktionen stattfinden. Ihre Morphologie zuverlässig zu kontrollieren ist jedoch ein Problem, das noch nicht zufriedenstellend gelöst ist.

In einer Reihe von Projekten habe ich Möglichkeiten entwickelt, gestützte Lipidmembranen auf starren Trägern zu strukturieren, und zwar in Dimensionen, die von planaren 2D-Substraten über geprägte 2,5D-Kompartimente bis hin zu vollständigen 3D-Strukturen reichen. Diese wurden wiederum genutzt, um die Geometriesensitivität des *E. coli* MinDE-Systems zu erforschen. Dieses Proteinsystem bildet ein Reaktions-Diffusions-Netzwerk, das sich selbst zu dynamischen Mustern organisiert, die auf einem komplizierten Wechselspiel zwischen ihrer Diffusion zwischen dem gelösten Zustand und der Membran sowie ihrer zugehörigen Reaktionskinetik basieren. Daher spielt die Membrangeometrie eine entscheidende Rolle bei dessen Musterbildung und wurde daher zum Ziel einer tieferen Untersuchung.

Mit dem Ziel nach freistehenden Membrangeometrien zu erzeugen, welche zelluläre Formen nachahmen, demonstrierte ich die Herstellung von dynamischen, formverändernden 4D-Strukturen aus proteinbasierten Hydrogelen, die Lipidvesikel verformen. Außerdem untersuchte ich die Herstellung von stabileren freistehenden Membransystemen aus synthetisierten Dendrimer-Molekülen, die extremere Formtransformationen erlauben. Indem wir MinDE-Muster auf diesen synthetischen Membranen rekapitulierten, zeigten wir ihre funktionelle Analogie zur Lipiddoppelschicht und schlugen damit ein alternatives Modellmembransystem für die synthetische Biologie vor. Schließlich wendete ich den 3D-Druck an, um die Mikroskopie von Bakterien in aufrechter Position zu ermöglichen, was die Darstellung des Divisoms durch supraauflösende Techniken erleichtert.

Während sich diese Untersuchungen in erster Linie um das Studium des Min-Systems drehen, haben die in dieser Arbeit entwickelten Methoden breitere Anwendungen in der synthetischen Biologie im Allgemeinen, vor Allem für membraninteragierende oder membranassoziierte Proteine mit geometriesensitiven Eigenschaften.

Der 3D-Druck von dynamischen, formverändernden Strukturen hat auch Auswirkungen über Membransysteme hinaus, wo wir weitere Entwicklungen erwarten können, die auf dieser Technologie aufbauen, um komplexere, biomimetische Verhaltensweisen zu rekapitulieren. Somit präsentiert diese Arbeit spannende methodische Fortschritte für die synthetische Bottom-up-Biologie.

ABSTRACT

The creation of *in vitro* environments that mimic cellular conditions is a key part of bottom-up synthetic biology. Such environments must contain relevant biochemical and biophysical functionalities, as well as the right kind of shape - as geometry plays a crucial role in many biological processes. In this regard, microfabrication is an effective way to pattern structures on length scales that can influence protein function. With emerging technologies in biochemical and fabrication tools, we face a continuous challenge to adapt to new methods, and then to innovate on design ideas that would give us a better understanding of the biological system in question.

In this thesis, I focused on developing tools with which we can modulate the geometry of *in vitro* environments that involve, in particular, lipid membranes. The lipid interface is a crucial component of the cellular environment, where many protein functions take place. However, reliably controlling their morphology is an issue that has not yet been conclusively solved.

In a series of projects, I developed ways to pattern supported lipid membranes on rigid supports, in dimensions ranging from planar 2D substrates, embossed 2.5D compartments, and fully 3D structures. These were in turn used to interrogate the geometry sensitivity of the *E. coli* MinDE system. This protein system forms a reaction-diffusion network, which self-organise into dynamic patterns based on an intricate interplay between their diffusion between the bulk and the membrane, as well as their associated reaction kinetics. Therefore, the membrane geometry plays a crucial role in their pattern formation, and thus became a target of deeper investigation.

In a quest to then create free-standing membrane geometries that mimic cellular shapes, I demonstrated the fabrication of dynamic, shape-shifting 4D structures made of protein-based hydrogels that deform lipid vesicles. I also investigated the reengineering of more stable free-standing membrane systems from synthesized dendrimer molecules that permit more extreme shape transformations. By recapitulating MinDE patterns on these synthetic membranes, we demonstrated their functional analogy to the lipid bilayer, thus proposing an alternative model membrane system for synthetic biology. Finally, I applied 3D printing to enable the upright imaging of bacteria, facilitating the imaging of the divisome by super-resolution techniques.

While these investigations primarily revolve around the study of the Min system, the methods developed in this thesis have wider applications in synthetic biology in general, where membrane interacting or associated proteins with geometry sensitive properties are concerned. The 3D printing of dynamic, shape-transforming structures also have implications beyond membranous systems, where we can anticipate further developments that build on this technology to recapitulate more complex, biomimetic behaviours. Thus, this thesis presents exciting methodological advancements for bottom-up synthetic biology.

PUBLICATIONS AND MANUSCRIPTS

PUBLICATIONS AND MANUSCRIPTS INCLUDED IN THIS THESIS

Eto H, Franquelim HG, Heymann M, Schwille P (2021) Membrane-coated 3D architectures for bottom-up synthetic biology. *Soft Matter* DOI: 10.1039/D1SM00112D (see section 6.3)

Ramm B, Goychuk A, Khmelinskaia A, Blumhardt P, Ganzinger K, **Eto H**, Frey E, Schwille P (2021) ATP driven diffusiophoresis: active cargo transport without motor proteins. *Nat. Phys.* DOI: 10.1038/s41567-021-01213-3 (see section 6.1.4)

Jia H, Litschel T, Heymann M, **Eto H**, Franquelim HG, Schwille P (2019) Shaping Giant Membrane Vesicles in 3D-Printed Protein Hydrogel Cages. *Small* 16, 27, 1906259 (see section 7.1)

Eto H, Soga N, Franquelim HG, Glock P, Khmelinskaia A, Kai L, Heymann M, Noji H, Schwille P (2019) Design of Sealable Custom-Shaped Cell Mimicries Based on Self-Assembled Monolayers on CYTOP Polymer. *ACS Appl. Mater. Interfaces* 11, 24, 21372-21380 (see section 6.2)

ADDITIONAL PUBLICATIONS AND MANUSCRIPTS

Jia H, Flommersfeld J, Heymann M, Vogel SK, Franquelim HG, Brückner DB, **Eto H**, Broedersz CP, Schwille P. Exoskeleton powered by molecular motors: Actuating miniature soft robots the biological way. *In review*.

Contents

ZUSAMMENFASSUNG	iii
ABSTRACT	v
PUBLICATIONS	vi
CONTENTS	vii
I Scientific Context	1
1 MICROFABRICATION IN <i>IN VITRO</i> BIOLOGY	3
1.1 Photolithography	5
1.2 Soft Lithography	6
1.3 3D Printing and two-photon direct laser writing	7
2 BIOLOGICAL FUNCTIONALISATION USING MEMBRANES	11
2.1 Solid supported membranes	11
2.2 Droplets and Vesicles	13
3 BIOPRINTING	15
3.1 3D printing of protein-based hydrogels	15
4 <i>IN VITRO</i> RECONSTITUTION OF DYNAMIC PROTEIN SYSTEMS	19
4.1 <i>E. coli</i> Min system	19
4.1.1 Min oscillation mechanism	21
4.1.2 Geometry sensing and Microfabrication	22
5 OBJECTIVE OF THIS THESIS	25

II	Results and Discussion	27
6	FROM 2D TO 3D: PATTERNING MEMBRANES TO STUDY MINDE DYNAMICS	29
6.1	Directing diffusiophoretic transport of DNA nanostructures by the MinDE system through the use of 2D patterned lipid membranes . . .	30
6.1.1	Introduction	30
6.1.2	Methods	31
6.1.3	Results	33
6.1.4	PUBLICATION P1: A diffusiophoretic mechanism for ATP-driven transport without motor proteins	35
6.2	PUBLICATION P2: Design of Sealable Custom-Shaped Cell Mimicried Based on Self-Assembled Monolayers on CYTOP Polymer	65
6.3	PUBLICATION P3: Membrane-coated 3D architectures for bottom-up synthetic biology	84
6.4	Dendrimersome synthetic cells harbor the cell division machinery of bacteria	104
6.4.1	Introduction	104
6.4.2	Methods	106
6.4.3	Results	108
7	DEVELOPMENT OF PROTEIN-BASED HYDROGELS FOR 4D BIOPRINTING	113
7.1	PUBLICATION P4: Shaping Giant Membrane Vesicles in 3D-Printed Protein Hydrogel Cages	113
8	OTHER APPLICATIONS OF MICROFABRICATION	141
8.1	Microwells for upright imaging of bacteria	141
8.1.1	Introduction	141
8.1.2	Methods	142
8.1.3	Results	143
9	DISCUSSION AND FUTURE PERSPECTIVES	145
III	Appendix	151
A.1	Appendix to Section 6.1.4	153
A.2	Appendix to Section 6.4	215
A.3	Appendix to Chapter 9	216
A.4	General contribution to the public	217
	LIST OF FIGURES	223
	LIST OF ABBREVIATIONS	225
	BIBLIOGRAPHY	227
	ACKNOWLEDGEMENTS	241

Part I

Scientific Context

1

Microfabrication in *in vitro* biology

One of the greatest challenges in biological research is to precisely manipulate relevant molecules in space and time, so that we can systematically investigate their impacts on the biological system in question. Over the past few decades, microfabrication has emerged as an effective method to recreate *in vitro* environments in which we can controllably pattern and modulate such biomolecules [1–3]. Technological advancements have provided us with a variety of tools to construct devices at micrometer or even smaller resolutions [4–6]. Since many biological processes and features, including cellular reactions, protein structures, cells as well as higher level multicellular structures, exist and interplay on such length scales, this has become a powerful tool [7, 8]. With the ability to dynamically regulate these microenvironments, these devices can then exert a high degree of spatiotemporal control over the system under investigation, and therefore, has made a significant impact on biological research in general [9–11].

In the most widely used form of microfabrication, a microstructure is typically fabricated through local modification of the chemical or physical properties of a flat substrate, resulting in 2D patterns or extruded structures that are imprinted on a flat surface [12]. Common techniques include photolithography and e-beam lithography, which allows sub-micron features to be fabricated with high reproducibility (Fig 1.1). This first became prominent in the semiconductor industry, which requires high-precision, two-dimensional patterning methods to fabricate integrated circuits [12]. Since these patterns could be used as masks for downstream patterning of other materials by chemical etching, metal deposition or even biological molecules, this also became widespread in biology [7, 13, 14], and also forms the basis for a number of techniques explored in this thesis.

Such a photo-patterned structure can also be used as a template, whose designs can be directly transferred to another substrate through direct physical contact. This is called soft lithography, and elastic, mouldable and inexpensive materials such as polydimethylsiloxane (PDMS) allows one master chip to be reused as a template hundreds of times [5]. These structural copies then be applied in a variety of downstream techniques, including negative molding, microcontact printing as well as chip fabrication for microfluidics, and is therefore an extremely important technology that allows us to create dynamic physical and chemical environments on micron length scales in a facile, cost-effective way [5]. Through the evolution of these methods, we are also able to create more complex structures, for example, microfluidic valves

using multi-layered soft lithography [10]. However, since these structures are made from imprints of a 2D template, some 3D structures, such as a sphere, a monkey bar or a windmill that requires detachable parts, are impossible to fabricate, and is also limited in their ability to faithfully reconstruct complex biological shapes that are abundant in nature.

In more recent developments, 3D printing has emerged as a powerful tool to fabricate biologically relevant microenvironments (Fig 1.1). In contrast to constructing limited 3D shapes that are extrusions from 2D designs (termed 2.5D), 3D printers can place, position or pattern relevant materials with three-dimensional degree of freedom, and can therefore create complex 3D features that were difficult or impossible to achieve with previous methods. In particular, two-photon direct laser writing (2PP-DLW) is a prominent focus of this thesis, which requires two photon absorption to crosslink UV sensitive photoresists, thus allows us to fabricate features with micron scale resolution.

In the following sections, I introduce fabrication techniques that are more prominently featured in this thesis in more detail, and highlight their applications in *in vitro* biology.

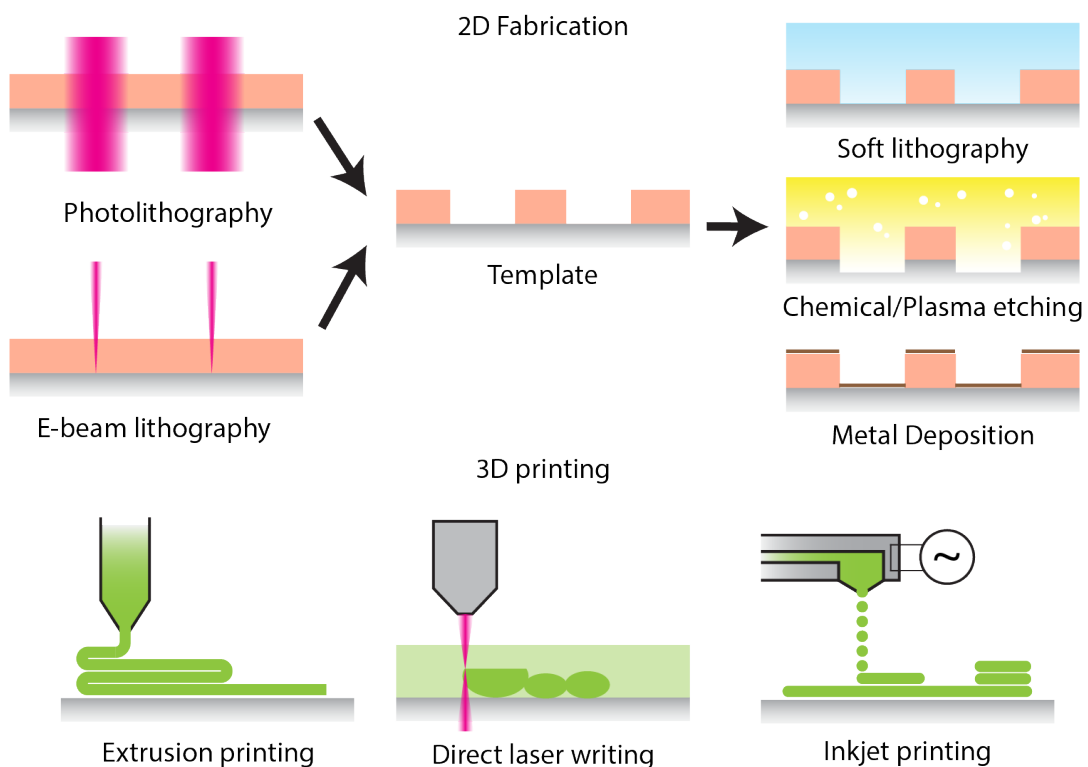


Figure 1.1. Commonly used microfabrication techniques. 2D fabrication methods, such as photolithography and e-beam lithography, are commonly used to pattern chemically responsive polymers, called "resists", into a template. This is then used for downstream patterning methods, such as soft lithography, etching and metal deposition. 3D printing methods include extrusion printing, which extrudes materials through a mechanically controlled nozzle; direct laser writing, which uses a focused beam of light to crosslink photoresins; and inkjet printing, which eject bioinks through an actuator as controlled droplets.

1.1 Photolithography

In general terms, lithography is a technique that transfers copies of a master pattern onto the surface of a solid material, such as a silicon wafer. Typically, this process starts by depositing a thin layer of organic materials, called “resist”, onto the substrate surface through spin coating. In photolithography, the resist is then patterned through exposure to UV light, whereby the UV illumination makes a local area on the resist either soluble or insoluble in a solvent. These areas can subsequently be dissolved away, leaving a device that has nano- or microscale features, which may be directly used or can be subject to further processing such as etching, surface modification, and other patterning steps.

The popularity of photolithography stems from its ability to transfer digitally designed, complex 2D patterns to a master template with high fidelity and high spatial resolution with facile and well-documented preparation steps [15]. This allows us to design custom-shapes and tailor geometries that are relevant for the specific biological system in question. Photoresists are commercially readily available, whose the main classes of resists are positive tone resists, which become more soluble upon UV exposure, and negative tone resists, which become less soluble due to light-initiated polymer cross-linking. (Fig 1.2) They vary in physical and chemical properties that are suitable for different applications. Resists with certain viscosities can be chosen to set the overall thickness upon spin coating and therefore the vertical dimensions of the micropatterns, which can range from 100 nm to 150 μm [12, 15]. Photosensitivity and photochemistry are also optimised according to the desired minimum feature size, which can be down to around 1 μm or the diffraction limit of light [12]. Substrate adhesion as well as chemical resistance are also important parameters for subsequent downstream processing and surface modifications.

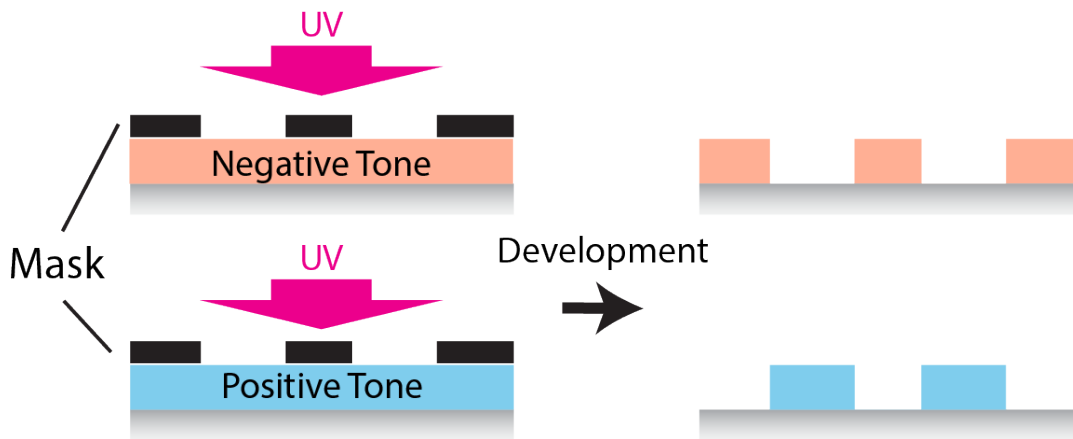


Figure 1.2. Positive and negative tone photoresists. Positive tone resists become more soluble upon UV exposure, whereas negative tone resists become less soluble due to light-initiated polymer cross-linking.

The patterns prepared in this way can then be subsequently used as "masks" to pattern different materials. Metal deposition, although more commonly employed in semiconductor manufacturing, has for example been used to pattern supported lipid membranes for *in vitro* reconstitution assays [16–18]. Chemical etching has been

used to fabricate microfluidic lanes in glass, providing the platform for recapitulating coupled oscillators in synthetic systems [19]. Reactive ion etching, which uses high energy plasma to etch away materials, was employed to fabricate microwells in CYTOP to reconstitute membrane proteins *in vitro* [20]. Biomolecules can also be effectively deposited on photolithography patterned substrates, for example, cell adhesion molecules that regulate intracellular cytoskeletal networks [13], and nucleator molecules to control growth of actin filaments [14].

When smaller feature sizes are required, electron-beam lithography can be employed, which makes use of a tightly focused beam of electrons, rather than photons, to draw patterns into a chemically modifiable resist. With this technique, features can be resolved below the diffraction limit, and can be as low as a few nanometers [12]. Applications in *in vitro* biology include sub-micron dots to study cell adhesion [21], creating nanotopography inside microfluidic channels for cell culture [22], and creating confined environments for bacteria with high curvature structures [23].

A major drawback of photolithography, however, is the intrinsic cost associated with specialised equipment and materials that are required for fabrication. A purpose-built cleanroom is generally necessary, which is inaccessible for many labs without specific microfabrication expertise. The downstream patterning steps also become progressively more tricky - for example, the photopatterning of CYTOP by reactive ion etching requires the fabrication of a photomask, then a mask aligner to expose the photoresist, and then a reactive ion etcher with oxygen supply, which all independently incur high costs and expertise to operate [20].

1.2 Soft Lithography

The structures created by the above methods can be used as templates for molding, which forms the basis for soft lithography. Soft, often elastomeric materials such as PDMS can be poured onto the stamp, hardened, and subsequently detached, such that the patterns are copied repeatedly from the master template to produce hundreds of devices. This technique still relies on the use of methods such as photolithography to fabricate the master, but once that is available, most of the fabrication tasks can be continued outside a clean room. This is a significant advantage for those who do not have routine access to expensive clean room facilities or for applications where a high number of replicates are necessary, where the cost per device can be a serious concern.

The molded PDMS structures can then be used in many biological applications. For example, microcontact printing a technique where the surface of a stamp can be coated with a material, e.g., proteins, which can be transferred onto another surface by stamping onto it (Fig 1.3). This has been widely used as a method of two-dimensional bioprinting, and cells are known to respond to patterns created by this method [1, 24].

Another application of soft lithography is microfluidics, which has revolutionised the field of biotechnology since its invention [25]. Through manipulation of small reaction volumes and micron-scale compartments, it can create physical and chemical environments, such as a constant pressure or constant nutrient replenishment, on a length scale that is relevant for biological systems [23]. In *in vitro* synthetic biology, it has been widely used to create mimics of cellular environments, such as microfluidic generation of droplets, vesicles as well as membranous compartments. They can also

be used as traps to keep vesicles for microscopy observation [26–28], or to mechanically deform them into aspherical shapes, mimicking the shape of bacteria [29, 30]. Multi-layered devices and incorporation of valves have also allowed the implementation of large-scale, complex manipulation of reaction volumes for applications in organ-on-chip devices as well as high-throughput screening systems [10].

In many ways, PDMS is an ideal material to fabricate micron-scale structures. PDMS has soft, elastomeric properties with a shear modulus of 0.25 MPa and a Young’s modulus of roughly 0.5 MPa, which allows it to conform to a surface and achieve atomic-level contact [5]. This enables template patterns to be replicated with high fidelity, and they can be peeled off the substrate very easily after molding and curing. It is non-toxic and optically transparent down to about 300 nm [5]. It is intrinsically hydrophobic, but its surface can be modified by a variety of surface chemistry methods. In particular, oxygen plasma treatment can render the surface hydrophilic, and it can adhere and seal irreversibly to many types of substrates – a feature that is particularly extensively used in microfluidic systems.

On the other hand, PDMS has a refractive index of 1.43, which is significantly different to water ($n=1.33$). This creates distortions during optical imaging, for example, fluorescence microscopy, thus severely degrading image quality. They are also permeable to most gases including water vapour, and therefore, it is challenging to retain aqueous volumes within PDMS-sealed devices for a long time. In this regard, materials with superior physicochemical properties are sometimes preferred over PDMS.

Soft lithography also offers access to a much broader range of materials through another molding technique called replica molding. Once an elastomeric copy of the template is made, e.g., with PDMS, it is stamped and imprinted onto a different, uncured material. Once the material cross-links, the stamp is peeled off to leave the imprint on the desired material. This allows a choice with much greater freedom of materials with physical and chemical properties matched to the application. As an example, cyclic olefin copolymer (COC), which is a commonly used thermoplastic that offers increased solvent as well as heat resistance, higher rigidity and water vapour impermeability, was replica molded to withstand the temperature cycling required for crystallography experiments [31]. In this thesis, I explored this method to pattern CYTOP as a refractive-index matched polymer that is ideal for imaging, and dramatically increasing the accessibility and cost-effectiveness compared to the previously employed method by reactive ion etching.

1.3 3D Printing and two-photon direct laser writing

3D printing has more recently emerged as an alternative tool to fabricate microstructures relevant for biological research [6]. In contrast to previous fabrication methods, which can only transfer patterns to two-dimensional surfaces and thus the structures created are 2D embossed or extruded structures, 3D printers can place, position or pattern relevant materials with three-dimensional degrees of freedom, which can create complex 3D features that were difficult or impossible to achieve with previous two-dimensional fabrication methods.

Several methods of 3D printing play a key role in biofabrication, including extrusion-based, inkjet, and stereolithography-based printing [32–35]. They vary

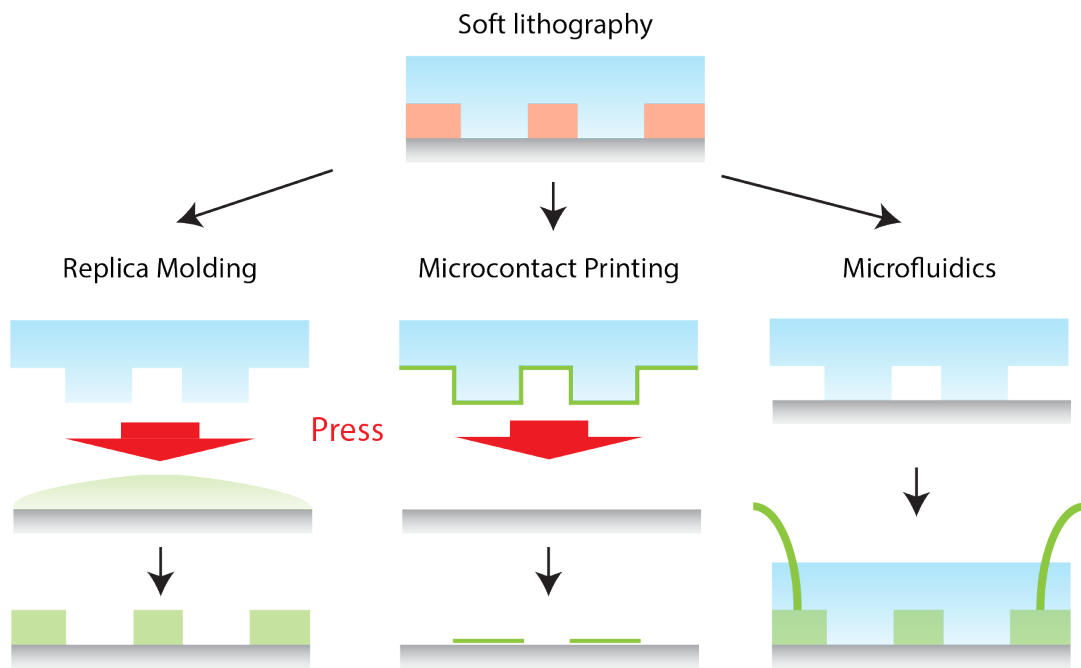


Figure 1.3. Applications of soft lithography. PDMS stamps made from a master template can be used for various applications. Replica molding: the stamp can in turn be used as a template to transfer patterns onto a different material. Microcontact printing: the surface of a stamp can be coated with a material, e.g. proteins, which can be transferred onto another surface, e.g. glass, by stamping onto it. Microfluidics: a plasma-activated PDMS is commonly bonded to a glass surface, thereby creating channels and microenvironments, in which small volumes of solutions are manipulated.

in printing resolution, speed and cost of fabrication, and available materials, which govern printing fidelity and stability, as well as physical properties such as mechanical strength and elasticity, and chemical properties such as biocompatibility. In this thesis, I focus on stereolithography, and in particular, two-photon direct laser writing, as it manages to print structures with micron or even sub-micron resolutions which is necessary to study protein function [6, 35].

3D printing by laser stereolithography relies on light-initiated polymerization of photoactive resins to fabricate 3D structures. Much like 2D photolithography, high-energy light irradiation turns uncrosslinked resins into cross-linked, solid/gel-like polymeric networks, and the incident light is focused into a more defined 3D focal volume. This focal volume traces lines in the resin volume and sequentially builds up a three-dimensional design by polymerizing materials layer-by-layer.

In a single-photon set up, one photon, usually in the UV range, is absorbed by a photosensitive molecule. The energy from this single photon is enough to promote the molecule to a higher energy state, thus triggering bond formation. In a multiphoton set up, two (or more) low energy photons are absorbed quasi-simultaneously (<1 fs of each other) by a single molecule, and only then does it have enough energy to be promoted to a higher energy state [35]. The importance of this distinction is because the likelihood of a 2-photon excitation falls off dramatically away from the centre of the focal volume, which means that 2-photon absorption and crosslinking is only likely to occur at this very point, where the laser is very tightly focused and thus laser intensity is at its maximum (Fig 1.4). With this tight spatial control of the crosslinking point, 2-photon lithography is able to print structures with high resolutions, becoming extremely relevant for *in vitro* biological studies where processes and features occur at these micron length scales.

Additionally, 2PP-DLW uses lower energy photons, often in the near IR-range, to excite the photoresist. By using IR radiation as opposed to UV, this can limit interaction with the resin through which the laser passes to reach the focal volume. This can be crucial for preventing damage to, for example, proteins or DNA, which can readily absorb UV irradiation.

The main issue facing 2PP-DLW for biological applications is the availability of suitable biocompatible and biorelevant photopolymerisable materials. Materials such as SU8, Ormocomp, pentaerythritol triacrylate (PETA) and trimethylolpropane ethoxylate triacrylate (TPETA) are well established polymer systems in bio-applications because they have low cytotoxicity, are easy to handle, and show minimal autofluorescence with good transmittance of light for imaging [35, 36]. Other materials are being rapidly being developed, including non-toxic organic polymers, ceramics, hydrogels [6], as well as post-functionalisation methods to alter their surface properties [37]. Direct protein printing is also possible, where a concentrated solution of proteins such as bovine serum albumin (BSA), avidin and collagen are prepared with photoinitiators, so that the protein molecules themselves crosslink to each other to form a polymer network. I introduce this in more detail in Chapter 3.

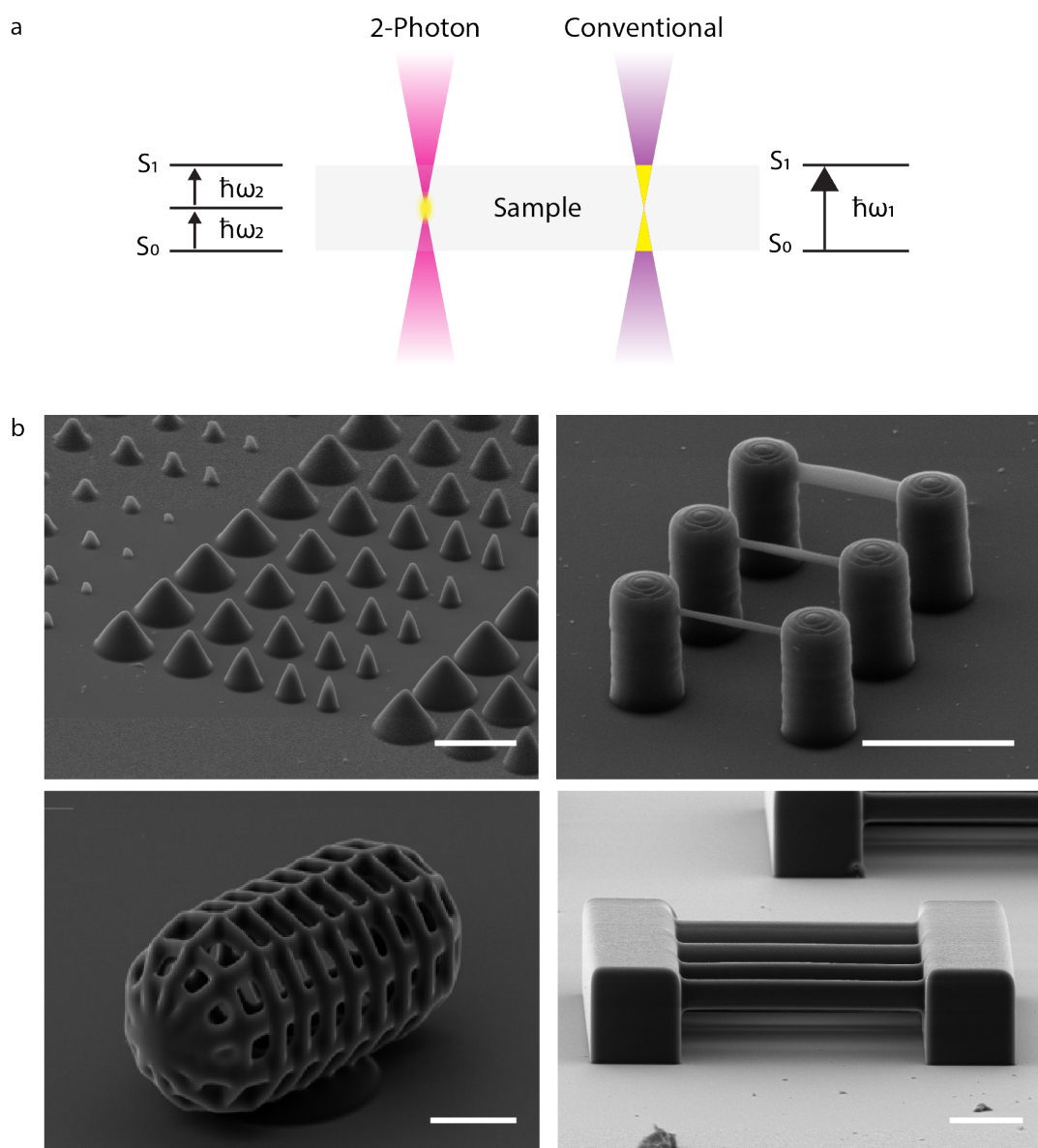


Figure 1.4. Working principles of two-photon direct laser writing. (top) In 2-photon direct laser lithography, two low energy photons are absorbed quasi-simultaneously (<1 fs of each other) by a single molecule, and only then does it have enough energy to be promoted to a higher energy state. The likelihood of such an event is high only at very high laser intensities, which occurs at the very centre of the focal volume. (bottom) Examples of structures printed by 2PP-DLW. Scale bar $10\ \mu\text{m}$.

2

Biological Functionalisation using membranes

The efficacy of using microfabricated environments to study biology hinges greatly on how closely we can mimick the biological functionality that is relevant to the system in question. Recreating such microenvironments entails passivating or functionalising the microfabricated devices with relevant biological molecules. This ensures that they have the desired interactions with their target molecules but do not interfere with others. In this thesis, I focused on recreating membranous environments to study lipid-interacting protein systems through *in vitro* reconstitution experiments.

The cellular membrane is an extremely dynamic and complex system that contains a diversity of closely regulated lipid types. Membrane structures like phase separated rafts, as well as a myriad of membrane proteins that weakly or strongly associate with the membrane also alter membrane properties [38]. Model membrane systems, on the other hand, are simplified mimics of the cellular membrane that still manage to recapitulate key functionalities, and have tremendously accelerated our understanding of lipid-protein interactions [39–41]. Many different model membrane systems have been established for *in vitro* reconstitution experiments (Fig 2.1). These include supported lipid monolayers and bilayers, free-standing membranes such as pore spanning bilayers and black lipid membranes as well as compartmentalised systems such as water-in-oil droplets and unilamellar vesicles [39, 41]. In the following sections, I detail solid supported membranes and compartmentalised systems (droplets and vesicles) in particular, which became the focus of my thesis.

2.1 Solid supported membranes

The solid supported membrane is a model membrane system where a mono- or bilayer of lipids coats the surface of a solid substrate. A large number of systems has been described, including solid-supported lipid monolayers, supported lipid bilayers, polymer-cushioned lipid bilayers, tethered lipid bilayers, and supported vesicular layers [42]. Mechanical stability is an attractive property of this model membrane system, and they can also be formed on patterned supports to vary their geometry, which makes them an ideal target for *in vitro* reconstitution studies.

Solid supported membranes are typically formed by a process called vesicle deposition, where vesicles adsorb onto the substrate, deform and then rupture and

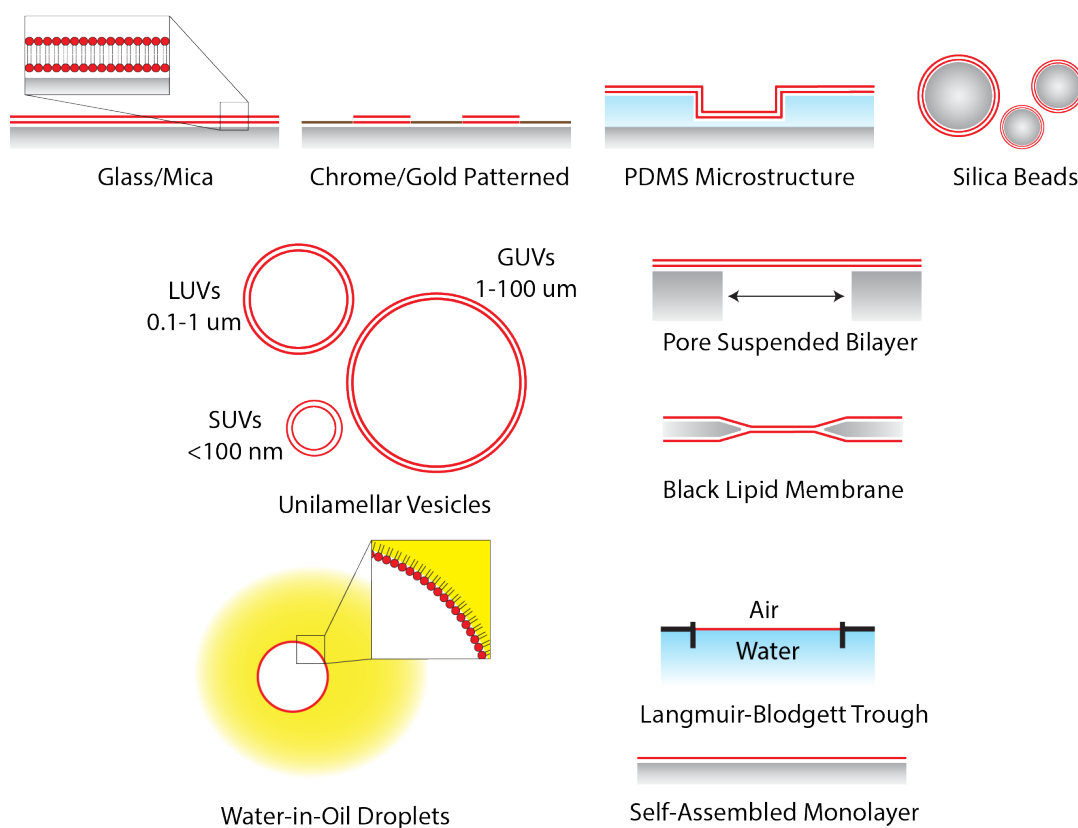


Figure 2.1. Commonly used model membrane systems. Solid supported membranes are formed on substrates such as glass/mica, which can also be patterned by gold/chromium. PDMS and silica beads can also be used. Free-standing bilayer systems include vesicles of various sizes: small, large and giant unilamellar vesicles, as well as pore suspended bilayers and black lipid membranes. Monolayer systems consist of water-in-oil droplets, Langmuir-Blodgett troughs and self-assembled monolayers on ultra-hydrophobic surfaces.

spread into planar membranes. This process is a complex interplay of lipid-substrate and lipid-lipid interactions. In particular, the substrate-membrane interaction is a crucial parameter governing the initial rupture process of the vesicles. Physically, the balance between the gain in adhesion energy as the lipids come into contact with the surface, and the cost in the vesicles' curvature energy determines vesicle rupture [43]. In the case of bilayer formation, attractive electrostatic interactions between hydrophilic substrates and charged lipids is considered essential. This can be further tuned by buffer conditions such as pH and ionic strength that can screen long-range charge interactions. Divalent cations such as calcium or magnesium do not only participate in the screening of charges, but they also directly interact as a "bridge" between surfaces and lipids promoting the adsorption and rupture of vesicles and supported lipid bilayer (SLB) formation [44]. Hydrophobic surfaces generally do not trigger membrane formation, but ultra-hydrophobic surfaces can cause a rearrangement of the membrane structure such that the lipid tails come into contact with the substrate, forming a monolayer membrane [45]. Other parameters such as surface roughness and lipid composition (physical size, charge strength, tail length, saturation) also determine the fluidity of the membrane, which can play an important role in protein-lipid interactions. It is therefore paramount that these considerations are taken into account when recreating a lipidated environment.

By patterning the substrate, we can also modulate the geometry of solid supported membranes. For example, in a study by Groves et al. patterned strips of metal were deposited on a glass substrate by thin film evaporation [16]. Different metals exhibited different interactions with vesicles: aluminium oxide completely prevented vesicle rupture on its surface, whereas immobile membranes formed on chrome, indium tin oxide (ITO) and gold [17]. These areas served as diffusion barriers that prevent different regions of membranes from interconnecting, thereby introducing boundary conditions for surface-interacting proteins [18, 46].

Another effective way to modify the geometry of solid supported membranes is to directly form them on substrates with a particular geometry, e.g. silica beads or rods, or on microfabricated structures [47, 48]. This is particularly useful to elucidate biological functions dependent on certain spatial features. For example, the curvature sensitivity of septin was demonstrated by a binding assay on beads with defined sizes that were covered with membranes. In other studies, supported membranes were formed on PDMS microwells, whose membrane coated walls were used to imitate rod-like geometry of *E. coli*. The robust patterning methods available for solid supported membranes makes it attractive for investigating the effect of geometry on membrane-associated protein function.

2.2 Droplets and Vesicles

In contrast to solid supported membranes, droplets and vesicles offer a compartmentalised model system with free-standing mono or bilayer membranes. Due to their typical sizes (1-100 μm) and geometry resembling those of cells, they have been widely used to mimic the cytosolic conditions of cells in *in vitro* reconstitution assays [49–51].

Water-in-oil droplets are aqueous volumes in the femto- to nanolitre range dispersed in an oil phase, whose interface is often stabilised by surfactants. Droplets can be easily made by using a stirrer, homogeniser or simply by shaking to mix the two

phases together to form emulsions, but more controlled methods such as microfluidics has also been employed to improve the monodispersity of generated droplets [52]. Many combinations of surfactants and oils have been explored to improve the stability and biological compatibility of these systems [53], and the use of lipids as surfactants has been particularly effective for *in vitro* reconstitution experiments. Dynamic activity of actomyosin cortices [54] and cellular division machinery such as FtsZ and Min proteins have been reconstituted inside droplets as minimal models of cell mimicks, as well as more complex bottom-up assembly of biochemical modules that recapitulated functions of organelles [55].

Synthetic vesicles, or liposomes, are aqueous volumes that are encapsulated by a lipid bilayer, and are arguably truer mimicks of the cellular membrane. Smaller-sized liposomes, such as small unilamellar vesicles (SUVs) (<100 nm) and large unilamellar vesicles (LUVs) (100 - 1000 nm) have been used to study protein-membrane interactions or curvature recognition, but are too small for visualization of dynamic processes by optical microscopy [39, 56]. giant unilamellar vesicles (GUVs), in turn, with their size between 1 - 100 μm are both on the scale of living cells and amenable to optical microscopy [39–41]. In recent years, a variety of methods have been developed to encapsulate reaction volumes inside GUVs, mimicking the construction of minimal protocells [57, 58].

Water-in-oil droplets and vesicles are ideal systems to encapsulate reaction volumes, where lipid interacting proteins are reconstituted in a cell-like environment. For both water-in-droplets and vesicles, however, deformation away from their equilibrium, spherical shape is mechanically challenging. Droplets have a high interfacial tension that prevents strong deformation, whereas vesicles become highly unstable beyond their optimum spherical geometry. Although microfluidic tools have been shown to deform vesicles using pre-shaped traps and a careful osmotic control [29, 30], the range of different shapes that it can create is rather limited and difficult to deform reliably.

3

Bioprinting

Bioprinting involves the controlled deposition of biomolecules, often proteins, in 2D or 3D, and is an effective way to mimic the complexity of biological entities like cells and organelles. There are several established and developing methods that can form features on a wide variety of substrates: microcontact printing (section 1.2), dip-pen nanolithography [59] and light-induced molecular patterning [60, 61]. Of particular interest are 3D printing techniques that can pattern relevant biomolecules in micron-sized 3D structures, and I describe such a method in this section in more detail.

3.1 3D printing of protein-based hydrogels

two-photon direct laser writing (2PP-DLW) has emerged as an alternative method to pattern proteinaceous environments in 3D [62]. A protein-based photoresin consists of a highly concentrated protein solution mixed with a two-photon excited photoinitiator (schematic in Fig 3.1a), and laser irradiation causes a radical chain reaction that crosslinks adjacent protein molecules into a polymer, hydrogel-like network. Thus, protein solutions can be directly structured into soft, actuatable 3D printed shapes. Owing to the high spatial resolution of 2PP-DLW, structures can be printed at sub-micron length scales with high reproducibility (section 1.3), and thus has attracted interest in synthetic biology and bioengineering.

For crosslinking using such high laser intensities, the integrity of protein functionality after polymerisation naturally comes under question. The cross-linking mechanisms associated with these techniques are not yet fully understood, although several mechanisms have been proposed [62]. A study by Spikes et al. [63] suggested that certain amino acid residues, such as tyrosine, is involved in the generation of radicals, which then trigger bond formation in other amino acid residues such as tryptophan, tyrosine, cysteine, histidine and methionine in adjacent protein molecules [62]. Such additional bond formations could disrupt the protein's tertiary structure, and thus cause loss of protein functionality. So far, it has been shown that certain biochemical functions do remain intact, for example, biotin-avidin affinity [64], as well as the function of fibrinogen as biomarkers for cell adhesion [65].

The choice of photoinitiators is also a point of consideration. Commonly-used photoactivators include Rose Bengal (RB), Flavin Mononucleotide (FMN) and Flavin Adenine Dinucleotide (FAD) for their good absorption properties and their ability

to generate radicals (Fig 3.1b,c). Type-2 initiators are often preferred, which initiate crosslinking by radical generation but are not incorporated into the polymer network themselves [66]. This prevents the printed structures themselves being photosensitive, which can lead to further generation of radicals that interfere with protein function, or the structures can deform and swell during imaging. Rose Bengal is particularly widely used because of its photoefficiency, but its binding affinity with commonly used protein such as BSA results in highly autofluorescent and photosensitised structures [67, 68]. There is a continuous effort to improve the photoinitiator properties for protein printing, including a benzophenone derivative (BPD), which is a type-II initiator with lower protein binding affinity that has been used to cross-link small amounts of various types of collagen [66, 69].

Several different proteins have been successfully printed, including BSA, avidin, collagen, fibrinogen and lysozyme [62]. These proteinaceous structures were successful in capturing and guiding cells in multicomponent scaffolds [70] as well as in more complex, tissue-like geometry [71]. Proteinaceous scaffolds were also used as microactuators, since they can reversibly swell or shrink due to external stimuli like pH or salt concentration [72–74], or sensitised to light [75].

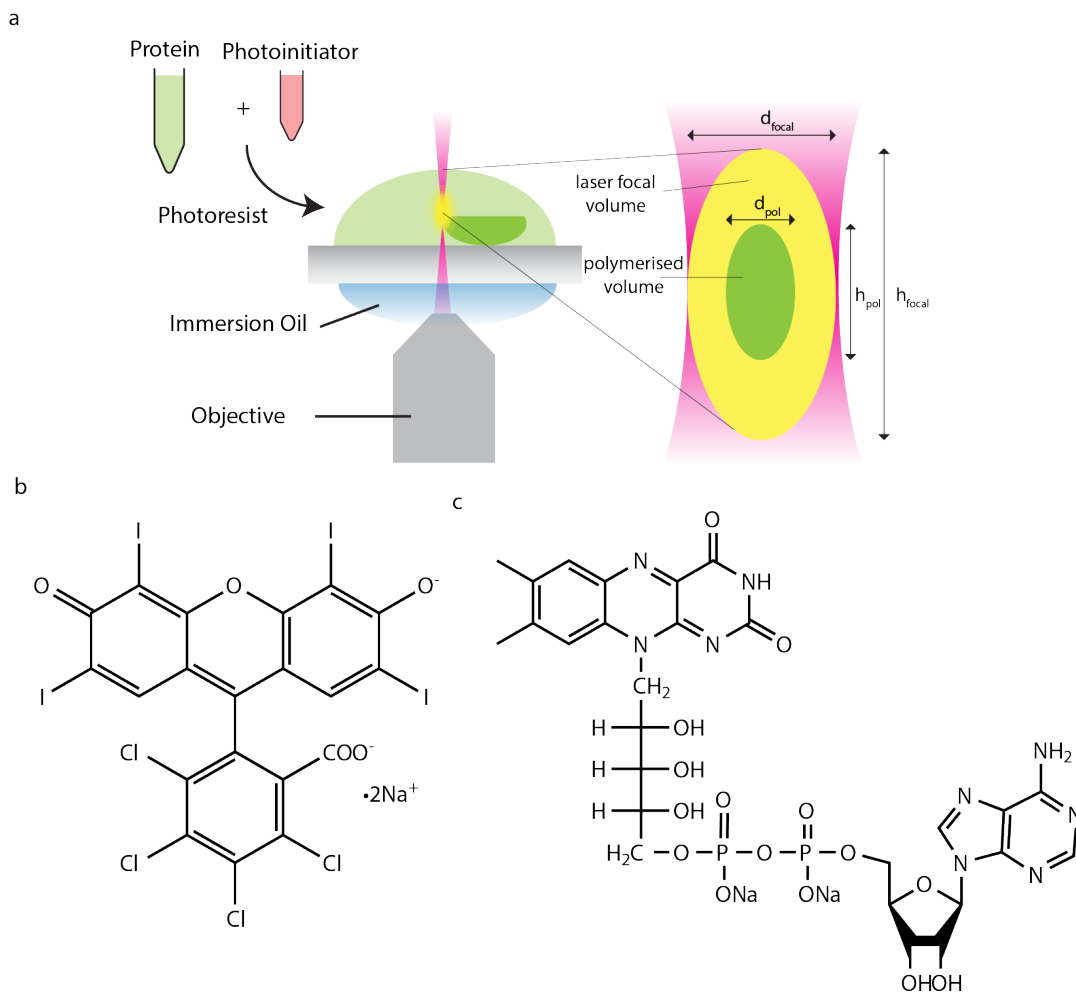


Figure 3.1. 3D printing of protein-based hydrogels. a) Schematic illustrating 2PP-DLW of protein based hydrogels. A protein-based photoresin consists of a highly concentrated protein solution mixed with a two-photon excited photoinitiator. The photoresin is then crosslinked in a 2PP-DLW setup. The polymerised voxel (width d_{pol} , height h_{pol}) is ellipsoidal in shape, and lies at the centre of the actual laser focal volume (width d_{focal} , height h_{focal}), which gives tight spatial control over the crosslinked region. Chemical structures of common photoinitiators (b) Rose Bengal and (c) FMN.

4

in vitro reconstitution of dynamic protein systems

in vitro reconstitution aims at recapturing functional modules of some of life's most fundamental processes, such as replication, division, energy harvest, growth, signalling and motility, in an artificial environment. The ultimate goal of reconstitution efforts is to construct an artificial cell from the bottom-up – to a point where each of the components are understood and can be manipulated freely, so that a minimal living entity can be created from scratch. In this process, these components are studied in isolation, in environments where parameters can be varied systematically, and this approach has delivered crucial insights into biological systems. Notable examples of these include the F1-ATPase, which was immobilised on a glass surface, and by attaching an actin fragment to its g-subunit, its rotation was directly visualised, revealing the detailed kinetics of one of the most fundamental enzymes in biology [76]. The development of cell-free protein expression (CFPE) systems [77, 78] have also allowed synthetic gene circuits [79], generate integral and peripheral membrane proteins [80], and even the production of large viral assemblies capable of infection [79]. These efforts have not only given answers to some of the most fundamental questions about what and how basic modules of life function, but also generated new avenues for biotechnological applications [81].

One area where *in vitro* reconstitution has had a considerable impact in is the study of bacterial cell division machinery [81, 82]. In particular, our understanding of the *E. coli* Min system has been accelerated by the use of microfabricated, artificial microenvironments, and is also one of the main systems explored in this thesis. In the following sections, I introduce this protein system in more detail.

4.1 *E. coli* Min system

The Min system of *Escherichia coli* (*E. coli*) is a crucial component of cell division. It was first identified by mutations of its corresponding genetic locus *minB* that led to the formation of miniature cells, called "minicells", and these did not contain any DNA [83]. Three proteins encoded by *minB*: MinC, MinD and MinE [84], were then found to play a crucial part in ensuring symmetrical division of *E. coli* cells [84]. MinD and MinE are membrane binding proteins that self-organise according to a reaction-diffusion mechanism. They oscillate rapidly from pole to pole, and their

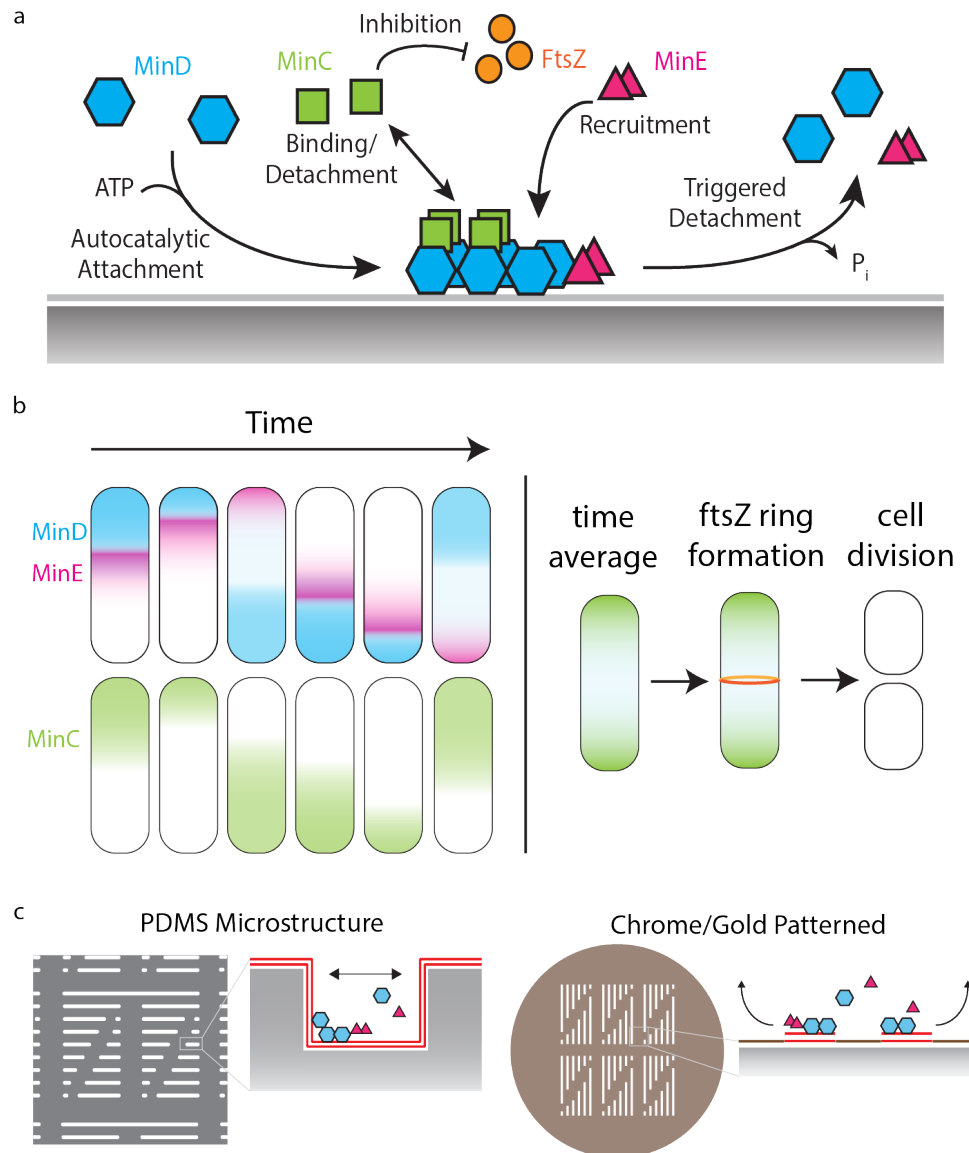


Figure 4.1. Overview of the *E. coli* MinDE system. Schematics depicting a) the molecular mechanism behind Min self-organisation; b) Min oscillations *in vivo* that position the division ring in the cell middle; c) previously employed microfabrication techniques to study Min pattern formation: PDMS "bathtub" structures to create confinement, and chrome/gold patterned SLBs to define membrane boundaries in 2D.

time averaged concentration gradient is depleted in the middle of the cell. MinC is the “effector” protein, which binds to MinD inhibits the polymerisation of FtsZ (filamentous temperature sensitive Z), thus preventing formation of the Z-ring at anywhere other than the midcell.

Since the cell division of *E. coli* is initiated by the formation of this Z-ring, positioning of this machinery in the cell middle by the Min system is key to obtaining two viable daughter cells of the same size. In a more detailed mechanism, FtsZ is anchored to the membrane by FtsA and ZipA, which then recruits further components of the divisome, such as FtsN, FtsW, FtsBLQ and many more, which include intracellular stabilizers, proteins that cross the plasma membrane, and cell wall synthases that build and remodel septal peptidoglycan [85–87].

Since its initial discovery, *in vivo* assays to study the Min system had been hindered by a number of factors, such as the small size of bacteria, which makes imaging by optical microscopy difficult below the diffraction limit, and the severe defects upon MinCDE mutation that made it difficult to pinpoint the particular change to a phenotype. A major breakthrough in the understanding of the Min self-organisation mechanism arrived in 2008, where purified MinDE proteins were reconstituted *in vitro* on planar lipid bilayers [88]. In the absence of additional cellular components, Min proteins self-organised into striking travelling wave and spiral patterns, which demonstrated that MinD, MinE, ATP and a lipid membrane are necessary and sufficient for pattern formation.

A notable difference between *in vitro* and *in vivo*, however, is that the wavelength of reconstituted Min waves are typically 30–100 μm , about 10 times larger than the length of bacteria. Shorter wavelengths can be recapitulated by adding macromolecular crowding agents in solution that slows down protein diffusion, which might better mimic the dense intracellular organisation of the bacterial cytosol [46, 89, 90].

4.1.1 Min oscillation mechanism

MinD is an ATPase that dimerize upon ATP and binds to the membrane through their amphiphilic membrane targeting sequence (MTS). MinD attachment is highly cooperative [91], and so an initial accumulation on the membrane leads to a rapid increase in MinD density. In the meantime, MinE has two conformations: active and latent, and initially, MinE diffuses rapidly in solution in its latent state [82, 92]. As it comes into contact with MinD, MinE switches into a reactive conformation, where both their MTS as well as the MinD contact helix become fully exposed. MinE binding then stimulates the ATPase activity of MinD, leading to ATP hydrolysis. At this point MinD dissociates into monomers, which consequently weakens its membrane attachment. Thus, MinD detaches from the membrane, and after a short residence time, MinE also unbinds and diffuses back into the bulk. This delayed negative feedback cycle of attachment and detachment of Min proteins from the membrane results in oscillations that are observed *in vivo* and *in vitro* (Fig 4.1a).

The exact appearance of the self-organisation patterns are governed by a complex interplay of reaction kinetics between the proteins and the membrane, as well as the rates of diffusion between the membrane surface and the bulk volume. Parameters such as absolute and relative protein concentrations [88], ionic strength [93], membrane composition [93, 94], macromolecular crowding [46, 89, 90] as well as the presence

of the MinE conformational switch [82, 92] play crucial roles in determining pattern formation. The positioning of the His-tag during MinE protein conformation is also important. Their C-terminal attachment resulted in their rate of MinD ATPase stimulation becoming more similar to the WT protein, and this resulted in a display of a wider range of Turing-like patterns [95].

4.1.2 Geometry sensing and Microfabrication

In addition to biochemical parameters that influence MinDE pattern formation, geometrical parameters also play a crucial role in their self-organisation. Key developments in the understanding of the Min system occurred from reconstituting the proteins in microfabricated environments, where spatial parameters could be systematically varied to investigate their influence.

The first *in vitro* demonstration that geometry plays a key role in its behaviour was with the use of patterned supported lipid bilayers [46]. Differently sized rectangular patches of membrane were deposited on a substrate, which was fabricated by evaporating thin films of gold on a mask patterned by photolithography. In this study, the MinDE travelling waves responded to the 2D boundaries by orientating themselves according to the shapes: the waves aligned on the diagonal of the rectangular shaped patches, consistently finding the long axis of these 2D geometries. Even on membrane strips shaped like an L or a serpentine, the waves were shown to be guided by the geometry. These experiments indicated that geometry sensing is an inherent property of Min pattern formation.

In an effort to more closely mimick the *in vivo* geometry of *E. coli* cells, microstructured compartments were fabricated by PDMS soft lithography, which were then coated with supported lipid membranes to imitate the membranous 3D volume inside a cell [96]. In these assays, the lithography-embossed structures were submerged in a larger reaction well filled with the reaction buffer, and the buffer was subsequently removed until the rim of the microwells, thus isolating each well as a quasi-microcompartment. In these volumes, the MinDE system was shown to perform pole- to-pole oscillations analogous to the *in vivo* observations, which indicated that the rod-like geometry and confinement are essential in giving rise to this characteristic behaviour. These compartments, however, were “open-top” and struggled to prevent the evaporation of reaction volumes. Protein concentrations are also likely to vary between chambers, due to the fact that Min bind to the membrane and start forming patterns as soon as they are loaded in. As a result, the proteins become inhomogeneously distributed by the time the buffer is finally lowered down to the compartment rim. Other systems that were developed thereafter, such as flow cells [97], and fully confined PDMS structures [90] also struggled to regulate the distribution of proteins while loading the system.

Another interesting approach to use microfabrication to harness Min patterns was explored *in vivo*, where cells were grown and molded into defined shapes created by soft lithography [23]. By inhibiting both cell division and shape maintenance via MreB by antagonistic drugs, cells grew in triangular, square or rectangular PDMS chambers. Min oscillations then preferentially oriented along the symmetry axis.

Such microfabrication techniques using PDMS, however, face the benefits as well as the drawbacks of using PDMS as a structural material. PDMS is a highly

moldable material that can be used to pattern desired shapes with relative technical ease [5]. For this reason, it has been used very widely in all areas of research including applications in *in vitro* reconstitution of proteins (section 1.2). However, PDMS is permeable to gases and faces persistent problems to prevent evaporation of water in micro-confined volumes. This can be a particular concern for confined volumes, where the compartments are not connected to a larger feeding channel where reaction volumes can be continuously replenished. It also has unfavourable optical properties which makes imaging through these materials difficult (section 1.2). Patterning bulky volumes of PDMS can severely distort images due to the unmatched refractive index with water. Therefore, there is a general need to develop alternative materials with more favourable chemical and optical properties for applications in life sciences.

The Min system has also been reconstituted inside encapsulated, non-supported 3D geometries. In spherical water- in-oil droplets with a lipid monolayer, MinDE exhibit distinct modes of oscillations: a pulsing mode, pole-to-pole oscillations and circling waves [98, 99]. More recently, the Min system was successfully encapsulated in GUVs [100]. The authors used a 3D printed rotating chamber to create centrifugal forces necessary for double emulsion transfer of lipids [58]. They observed similar oscillation modes that were seen in droplets, as well as dynamic shape transformations in vesicles that result from the rapid binding and detachment of Min proteins to the inner membrane of the vesicle. Deformation of these encapsulated Min droplets and vesicles towards more cell-like non-spherical geometry is still a pending experimental goal, although this has been demonstrated with other protein systems using microfluidic tools [29, 30].

There is also a drive to explore the geometry sensitivity of the Min system on much more complex 3D geometries. Recent theoretical analysis of the MinDE system has reported that the pattern formation of MinDE heavily depends on the surface to volume coupling, suggestive of even richer and partly unexplored MinDE pattern formation [101, 102]. In addition, MinDE were shown to not only form traveling waves, but they exhibits many more patterns such as quasi-stationary patterns [95] that so far have only been observed in quasi-infinite plane and bulk volume assays. In this thesis, we developed the toolbox necessary for this investigation using 2-photon lithography and membrane patterning.

5

Objective of This Thesis

Geometry plays a crucial role in many protein functions, and therefore, it is important to establish methods that can construct relevant shapes for *in vitro* reconstitution experiments.

As a target, I focused on the *E. coli* MinDE system, which is a paradigmatic biological reaction-diffusion system known to respond to geometrical features. Their self-organisation patterns are well studied but only on planar substrates and a limited number of confined, compartmentalised volumes [82]. Yet, theoretical as well as experimental evidence dictate that MinDE can potentially display a much wider range of pattern formation depending on the surface to volume ratio of their surrounding environment [95, 101, 102]. This called for a deeper exploration of their pattern formation in more complex, 3D environments where geometrical features could be systematically varied with a greater degree of freedom. To embark on this investigation, a method to pattern membranous structures in 3D needed to be developed.

To tackle this challenge, I posed the following questions:

1. To what extent can microfabrication be used for the recreation of membranous *in vitro* environments with variable geometry? For this, I needed to elucidate the lipid-substrate interactions that are required to pattern supported lipid membranes on different substrates. Suitable materials, for example, that are refractive index matched, as well as appropriate fabrication techniques needed to be identified that would improve on our current methodologies.
2. Can free-standing membranes, such as vesicles, be reliably deformed into shapes to study effects of geometry on protein function? Lipid mimics that can form more stable vesicles were available [103], but I needed to reengineer their biochemical properties and then to evaluate their functional analogy to the lipid bilayer, so that they could be established as a model membrane system for synthetic biology.
3. How far can emerging technologies, such as two-photon direct laser writing (2PP-DLW), be applied in our investigation? The technology can also efficiently template structures with high aspect ratios, and thus is an effective way to fabricate structures that are relevant for many areas of biology. Protein-based

hydrogels, for example, were established as stimuli-responsive microactuators [72] that could be used to deform vesicles.

While these investigations were primarily aimed at the study of the Min system, my goal for these methods extended to wider applications in synthetic biology. Membrane sculpting in 3D could potentially be used together with any membrane interacting or associated proteins for *in vitro* reconstitution experiments. The development of 3D printed, dynamic, shape-transforming structures also have implications beyond membranous systems, where we can anticipate further advancements that recapitulate more complex, biomimetic behaviours. Thus, the objective of this thesis was to demonstrate methodological advancements that sets a technological benchmark for bottom-up synthetic biology.

Part II

Results and Discussion

6

From 2D to 3D: Patterning membranes to study MinDE dynamics

In this chapter, I present a series of projects aimed at interrogating and controlling the geometry sensitivity of the *E. coli* MinDE system.

Geometrical features are part of an important basis by which Min proteins self-organise [23, 46, 101, 104]. Regulating shapes of membranes as well as the spatial extent of the reaction volume influence key parameters that govern MinDE pattern formation. In particular, they modulate the relative diffusion of Min molecules on the surface and in the volume, as well as the catalytic membrane area per volume on which Min proteins react. Different geometries have reportedly given rise to drastically varied self-organisation behaviours, such as the directed motion of travelling waves [46] and pole-to-pole oscillations [96]. Throughout this chapter, I used a range of microfabrication techniques to pattern and shape membranes in different dimensions, spanning from 2D patterning of membranes (section 5.1), compartments fabricated by 2.5D or embossed fabrication methods (section 5.2) and lipid-coated, fully 3D structures based on micron-scale 3D printing (section 5.3), and I examined how Min patterns can be controlled and probed by using these advanced microfabrication techniques. While these investigations primarily revolve around the study of the Min system, the methods developed in this thesis have wider applications in synthetic biology in general, where membrane interacting or associated proteins with geometry sensitive properties are concerned. Reliably creating arbitrary-shaped membranous environments is an ongoing challenge in synthetic biology, and here I present novel methods in this direction.

The range of geometries that can be created also depends on the membrane properties themselves. Thus, I turned to engineering membranes from synthetic lipid mimics, which form vesicles with increased stability that have the potential to be more robustly deformed in shape (section 5.4). I demonstrated that components of the cell division machinery, including MinDE and FtsZ, interact and self-organise on these synthetic molecules in a manner similar to on lipid membranes. They therefore constitute a free-standing model membrane system alternative to liposomes, which encapsulate and compartmentalise biochemical reaction volumes as a membranous cellular mimic. With their increased resistance to rupture from external forces, they promise future applications in studying membrane deformation that ultimately lead to one of the ultimate goals of synthetic biology: artificial cell division.

6.1 Directing diffusiophoretic transport of DNA nanostructures by the MinDE system through the use of 2D patterned lipid membranes

MinDE waves transport membrane-bound molecules by non-specific interactions [82]. Even in the absence of specific mediator proteins MinC and FtsZ, lipid-anchored streptavidin formed large-scale gradients according to the direction of MinDE travelling waves, indicating net transport. Deeper insights into the physical mechanisms behind this phenomenon, however, remained hindered by the lack of control over the directionality of the net transport. In previous assays, where membrane areas were unconstrained, MinDE waves originated from spiral centres that were spatially randomly distributed, and therefore the positions of large-scale gradients formed by cargo molecules were also unpredictable [82, 105]. In order to facilitate this investigation, I patterned defined patches lipid membranes on which Min pattern formation and cargo transport was restricted. Through reconstituting MinDE on diffusion limited, rectangular patches of membranes, we were able to control the directionality of MinDE waves, and thus direct the large-scale transport of membrane bound synthetic cargo. Combined experimental and theoretical analysis lead to the finding that MinDE transports molecules via diffusiophoresis, which is, as yet, a mechanism that is unreported in cell biology, and this is described in the associated publication P1.

The results of this section is from a collaboration with Beatrice Ramm (formerly of Schwille lab), parts of which were published as associated publication P1. H.E. and B.R. fabricated the chromium slides and performed initial membrane and MinDE experiments. Additional acknowledgements go to Jakob Schweizer (formerly of Schwille lab), who designed the initial chromium patterns, and Philipp Altpeter (Chair of Solid State Physics (N.N.), Ludwig-Maximilians-Universität München) for help with setting up the chromium patterning.

6.1.1 Introduction

Intracellular transport of molecules is one of the most fundamental processes for a living cell, and many of these mechanisms rely on coupling energy-dissipating NTPases, such as motor proteins [106] and self-assembly of cytoskeletal elements [107] to targeted cargo. This commonly occurs through specific protein-protein interactions, and in contrast, non-specific coupling of biomolecules to transport is less well understood in biology, and only a handful of studies have so far been reported [108–110].

On this note, the *E. coli* Min system was recently shown in an *in vitro* study [82] to transport membrane-bound molecules even in the absence of specific mediator proteins MinC and FtsZ (Fig 4.1). In this study, lipid-anchored streptavidin formed large-scale gradients according to the direction of MinDE travelling waves, and this indicated net transport of these molecules through non-specific interaction. This implied that MinDE oscillations have the capacity to further enhance cell division by repositioning membrane proteins to the cell middle. Such a discovery called for a deeper interrogation of this mechanism extending to different types of cargoes, as well as a more comprehensive understanding of the underlying physics. However, in previous assays, membrane areas were unconstrained, and MinDE waves originated from spiral centres that were spatially randomly distributed [82, 105]. Therefore, the

positions of large-scale gradients formed by cargo molecules were also unpredictable. This lack of control over the wave distribution means that the transport of cargo is difficult to analyse, which has made quantitative assessments tricky.

To facilitate this investigation, we took advantage of the geometry sensitivity of MinDE to direct the travelling waves using micro-patterned supported lipid bilayers. Using a method developed by Groves et al. [16], we formed lipid membranes on chromium-patterned glass coverslips. When we reconstituted MinDE on diffusion limited, rectangular patches of membranes, MinDE waves travelled directionally along the longest axis of a patterned bilayer, as previously reported [46]. Thus, we could regulate the directionality as well as the total amount of transported cargo, which allowed us to study their accumulation at the membrane boundaries.

Furthermore, we used DNA origami nanostructures as a synthetic cargo. Here, we could tune the effective size of the cargo, thus modulating their membrane footprint and diffusion coefficient on the membrane. We demonstrated that these parameters, as well as the different types of MinDE patterns, are crucial in determining how the cargoes are transported.

The advancement of these experimental tools aided our combined experimental and theoretical investigation into the underlying mechanisms behind the non-specific transport of MinDE. We showed that this is in fact a diffusiophoretic effect: an effective density-dependent inter-particle friction creates cargo transport along the diffusive fluxes of MinD proteins. We report this in the associated publication P1.

6.1.2 Methods

MICROFABRICATION OF CHROMIUM PATTERNED GLASS COVERSLEIPS

Chromium patterns were formed as described in [16, 17]. The patterns were designed on Autocad (Autodesk, USA). Glass coverslips (Menzel #1.5) were first cleaned by rinsing with ethanol and water, and then plasma treated with oxygen (50% power, 0.3 mbar for 60 s) to activate the surface. The vapour of Bis(trimethylsilyl)amine (HDMS) was deposited on the cover slide for 2 min as adhesion promoter. The photoresist (AZ ECI 3027, MicroChemicals GmbH, Ulm, Germany) was then spin-coated onto the cover slide for 40 s at 4000 rpm with an acceleration of 2000 rpm/s, to a layer thickness of approximately 3 μm . After pre-baking the cover slides for 90 s at 90 $^{\circ}\text{C}$, the photoresist was patterned using UV-lithography (μPG 101, Heidelberg Instruments, Heidelberg, Germany) with a 10 mm write head, 35mW nominal output power at a wavelength of 375 nm, before passing a 45% attenuation filter. Afterwards, the slides were post baked for 60 s at 110 $^{\circ}\text{C}$. The slides were then developed (AZ 351B, NaOH based, diluted 1:4 (v/v), MicroChemicals GmbH) for 4 min, and rinsed with water and dried with a nitrogen stream. Chromium was deposited onto these slides by evaporation at 22-33 mA at a rate of 1-2 $\text{\AA}/\text{s}$ to a final thickness of about 30 nm. After chrome deposition the photoresist was lifted off in acetone with sonication for 5 min in a sonicator bath. Afterwards slides were rinsed with isopropanol and dried with a nitrogen stream.

PREPARATION OF SUPPORTED LIPID BILAYERS

SLBs were prepared as described in [105]. All lipids, including 1,2-dioleoyl-sn-glycero-3-phosphocholine (DOPC) and 1,2-dioleoyl-sn-glycero-3-phospho-(1'-rac-glycerol (DOPG) were purchased from Avanti Polar Lipids (Alabaster, AL, USA), unless otherwise stated. To prepare SUVs, lipids were first dissolved in chloroform, with DOPC:DOPG:Atto655-DOPE (Atto-TEC GmbH, Siegen, Germany) in 7:3:0.005 molar ratio. The chloroform was dried under a nitrogen stream, and vials were placed in a desiccator to remove residual solvent for at least 2 h. Afterwards, lipids were rehydrated in Buffer M (25 mM Tris-HCl, 150 mM KCl, 5 mM MgCl₂, pH 7.5) to a concentration of 4 mgml⁻¹.

A chamber was constructed from a cut 0.5 ml eppendorf tube glued onto a the chromium patterned glass slides (as in Fig 6.1b). These chambers were then plasma treated with oxygen at 50 % power, flow rate 0.3 sccm for 40 s (model Zepto, Diener Electronic). SUVs were added to the chamber, and after 3 min incubation at 37 °C on a heating block, the supported bilayer membrane was gently washed with a total of 2 ml buffer S (25 mM Tris-HCl, 150 mM KCl, pH 7.5) to remove excess vesicles.

MICROSCOPY

Images were taken on a Zeiss LSM780 confocal laser scanning microscope using a Zeiss C-Apochromat 40x/1.20 water-immersion objective (Carl Zeiss AG, Oberkochen, Germany). EGFP-MinD was excited using the 488 nm Argon laser, and Atto655-DOPE using the 633 nm He-Ne laser. Obtained images were processed using Fiji [111].

FLUORESCENCE RECOVERY AFTER PHOTBLEACHING

On supported bilayer membranes, a circular spot of 5 μm diameter was illuminated with full laser power for 0.82 s (50 iterations on the Zen Black software (Carl Zeiss AG, Oberkochen, Germany)), and the average fluorescence intensity was recorded every second for 100 s. Measurements were taken at room temperature (23 °C). Intensity in a second area of the same dimensions was recorded in the same field of view, in order to correct for the intensity drift. The intensity trace was fit to the equation derived by Soumpasis [112].

$$f(t) = (I_0((\frac{2\tau_D}{t}) + I_1((\frac{2\tau_D}{t})))e^{-\frac{2\pi\tau_D}{t}}$$

Here, τ_D is the characteristic timescale for diffusion, and t is the time. $f(t)$ is the normalized fluorescence, and I_0 and I_1 are modified Bessel functions. The diffusion timescale for a bleached spot of radius r is $\tau_D = r^2/4D$ with D the diffusion coefficient. A custom script written in Python was used for curve fitting and data analysis.

MINDE SELF-ORGANISATION ASSAY

Self-organization assays were performed essentially as described in [105]. In short, they were performed on preformed SLBs in 200 μL reaction buffer (25 mM Tris-HCl pH 7.5, 150 mM KCl, 5 mM MgCl₂) supplemented with 2.5 mM Mg-ATP (stock: 100

mM ATP, in 100 mM MgCl₂, adjusted to pH 7.5) and at a constant room temperature of 23 °C. MinD was used at 1 μM with 3.0 μM His-MinE to generate regular traveling surface waves.

6.1.3 Results

MICROFABRICATION OF CHROMIUM PATTERNED GLASS COVERSLEIPS

Lipid membranes can be patterned by depositing thin films of chromium in defined areas, which partitions membranes into separate regions (schematic shown in Fig 6.1 a) [16]. This micropatterning process involves 3 main steps: 1) fabrication of a patterned mask by photolithography; 2) deposition of a thin film of chromium; and 3) lift off of the photomask to leave intact chromium patterns on glass (Fig 6.1).

In the photolithography step, I first deposited an adhesion promotor, HMDS (Bis(trimethylsilyl)amine), on plasma treated glass, which is essential to ensure that smaller features stay intact and do not lift off during development. I then spin coated a thin layer (3 μm) of the photoresist. Here, I used a positive-tone resist, since the area required for crosslinking (exposure) was smaller compared to the areas that are left uncrosslinked, and therefore would require less time for exposure. I exposed the resist to UV light using a laser writer and developed the sample to remove the uncrosslinked regions of the photoresist. Here, the developer must be well rinsed off to prevent delamination of the deposited metal in the subsequent steps. This process leaves a “mask” for the subsequent metal deposition.

For the metal deposition step, there are 2 commonly used methods: evaporation and sputtering. Evaporation involves heating the metal up to the vapour phase, which then deposit on surfaces, whereas in sputtering, high energy ions are directed onto a piece of metal, which then eject atoms from the metal surface and then coat the glass. Typically, evaporation results in a more even coating, whereas sputtering has the advantage that it is usually faster. To evaluate both methods, I deposited 30 nm of chromium onto the patterned glass coverslips. After deposition, there were differences in the initial appearances between the two methods, as seen in the brightfield images in Fig 6.1 c,d. With evaporation, the chromium deposited on top of the photoresist showed thin cracks. With sputtering, no cracks were visible, and the material visually looked darker. However, on regions directly on top of glass, the chromium showed no cracks for either method. The difference was more notable after lift off in acetone. On evaporated slides, the photoresist was cleanly dissolved away, and the chromium barriers remained intact Fig 6.1 e. Whereas on sputtered slides, the structures seem clean on the brightfield, but there were some “glitter” on the slides that could be detected by eye. Longer sonication times or multiple cleaning steps failed to remove this glitter. We therefore decided to proceed with evaporated slides for the next steps.

FORMATION OF SUPPORTED LIPID BILAYERS ON PATTERNED COVERSLEIPS

Once the glass coverslips were patterned with chromium, I constructed a chamber (as shown in Fig 6.1 b) to form lipid bilayers, which were then used for subsequent in vitro reconstitution assays. I first plasma treated the glass to expose hydroxyl groups on the surface. Their negative charges can be bridged by divalent cations (Ca²⁺ /Mg²⁺)

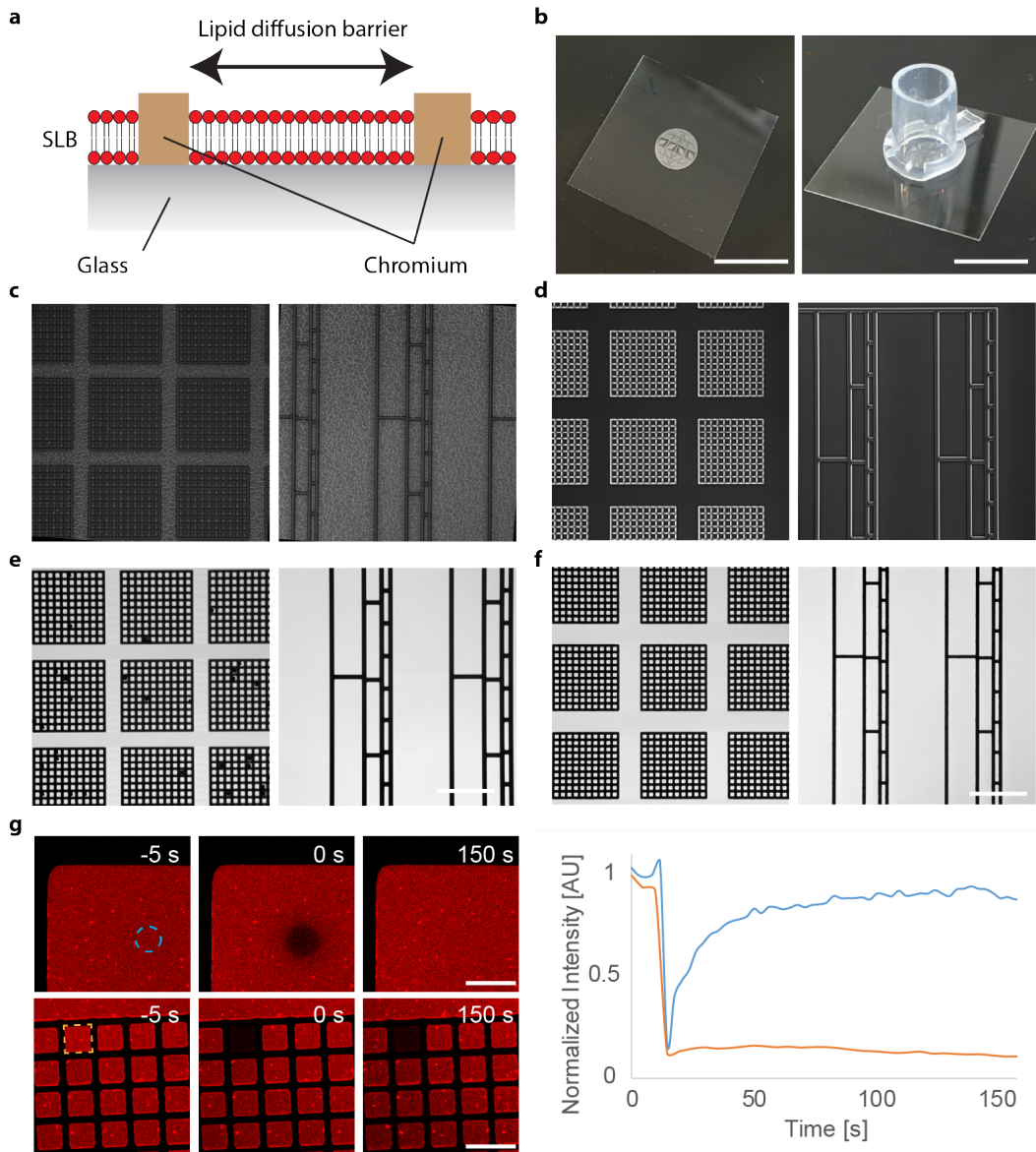


Figure 6.1. Fabrication of patterned SLBs by chromium deposition. a) Schematic of chromium patterned SLB. b) Example of a chromium patterned glass coverslip (left) with the chamber assembled for subsequent *in vitro* reconstitution assays (right). Scale bar 10 mm. Brightfield images of patterned glass coverslips directly after chromium deposition by c) evaporation and d) sputtering. Brightfield images after lift off for e) evaporation and f) sputtering. Scale bar 10 μm . g) Timelapse images of FRAP experiments performed on patterned SLBs (left) and intensity traces from the indicated regions of interest (right).

to promote fusion of negatively charged vesicles (DOPC:DOPG 7:3 molar ratio). Upon vesicle deposition, the vesicles fused with the surface and the lipids homogeneously covered the glass surfaces.

To check for lipid mobility, I performed fluorescence recovery after photobleaching (FRAP) on these membranes. When I bleached a small area of the membrane (Fig.6.1g, top panel), fluorescence recovered with a diffusion coefficient of $0.8 \pm 0.3 \mu\text{m}^2\text{s}^{-1}$, which falls between typical values observed for supported lipid bilayers on glass [113, 114]. It also has a high mobile fraction (0.97 ± 0.2), which suggests the presence of a fluid bilayer. When I bleached an entire patch of membrane enclosed by chromium barriers, the fluorescence did not recover (Fig.6.1g, bottom panel). This confirmed that adjacent membrane patches are diffusively independent from each other, as the chromium acts as a lipid diffusion barrier. Here, it is considered that lipid molecules are present on top of chromium, but are adhered to the surface and are immobile [17]. Therefore, mobile lipids from adjacent patches are prevented from diffusing over the chromium.

IN VITRO RECONSTITUTION OF MINDE ON PATTERNED MEMBRANES

Having confirmed the presence of fluid membranes on chromium patterned patches, I then proceeded to reconstitute MinDE proteins *in vitro*. MinDE self-organised into travelling waves with a period of ~ 1 min and wavelength $\sim 50 \mu\text{m}$, which is similar to those on planar surfaces. They also formed travelling waves on arbitrary shaped membrane patches (Fig.6.2).



Figure 6.2. MinDE self-organisation on arbitrary shaped membranes.

6.1.4 PUBLICATION P1: A diffusiophoretic mechanism for ATP-driven transport without motor proteins

In the associated publication P1, in order to investigate whether the non-specific molecular transport by MinDE is modulated by cargo properties, we turned to DNA origamis. By modulating the number of anchors to the membrane, their membrane footprint and diffusion coefficient on the membrane can be tuned, and thus vary the effective size of the cargo on the membrane.

When we reconstituted these DNA nanostructures together with MinDE, on the chromium patterned membranes. We exploited the geometry-sensitivity of MinDE waves that travel along the longest axis on geometrically patterned planar membranes. On these membranes, MinDE waves indeed transported cargo directionally along their wavevector, and cargo reproducibly accumulated at the membrane boundaries, forming long-range gradients. Thus, MinDE-dependent transport of DNA origami

species can be directed by exploiting the geometry sensitivity of MinDE pattern formation.

Through our combined approach of experiments and theoretical analysis, we showed that the non-specific transport of molecules by MinDE is in fact a diffusio-phoretic effect: an effective density-dependent inter-particle friction creates cargo transport along the diffusive fluxes of MinD proteins. This mechanism is, as yet, unreported in cell biology and points towards a more general way in which molecules are organised within living organisms.

A diffusiophoretic mechanism for ATP-driven transport without motor proteins

Beatrice Ramm, Andriy Goychuk, Alena Khmelinskaia, Philipp Blumhardt,
Hiromune Eto, Kristina A. Ganzinger, Erwin Frey and Petra Schuille

Author contributions:

B.R., A.G., E.F. and P.S. conceived the study. B.R. performed all experiments. H.E. and B.R. fabricated chromium-patterned slides. A.G. and E.F. designed the theoretical analysis. A.G. conducted the theoretical analysis. B.R., A.K. and P.B. designed experiments. A.K. designed DNA origami. A.K. and B.R. prepared origami. K.A.G. developed single-particle tracking code. B.R., A.G., P.B. and K.A.G. analysed data. B.R., A.G., E.F. and P.S. wrote the manuscript. All authors discussed and interpreted the results and revised the manuscript

published in

Nature Physics (2021)

*Reprinted from [115] under the Creative Commons Attribution 4.0 International License
(see <https://creativecommons.org/licenses/by/4.0/>)*



OPEN

A diffusio-phoretic mechanism for ATP-driven transport without motor proteins

Beatrice Ramm^{1,4,6}, Andriy Goychuk^{2,6}, Alena Khmelinskaia^{1,5}, Philipp Blumhardt¹, Hiromune Eto¹, Kristina A. Ganzinger³, Erwin Frey²✉ and Petra Schwille¹✉

The healthy growth and maintenance of a biological system depends on the precise spatial organization of molecules within the cell through the dissipation of energy. Reaction-diffusion mechanisms can facilitate this organization, as can directional cargo transport orchestrated by motor proteins, by relying on specific protein interactions. However, transport of material through the cell can also be achieved by active processes based on non-specific, purely physical mechanisms, a phenomenon that remains poorly explored. Here, using a combined experimental and theoretical approach, we discover and describe a hidden function of the *Escherichia coli* MinDE protein system: in addition to forming dynamic patterns, this system accomplishes the directional active transport of functionally unrelated cargo on membranes. Remarkably, this mechanism enables the sorting of diffusive objects according to their effective size, as evidenced using modular DNA origami-streptavidin nanostructures. We show that the diffusive fluxes of MinDE and non-specific cargo couple via density-dependent friction. This non-specific process constitutes a diffusio-phoretic mechanism, as yet unknown in a cell biology setting. This nonlinear coupling between diffusive fluxes could represent a generic physical mechanism for establishing intracellular organization.

Spatiotemporal organization of cells generally emerges through redistribution and transport of molecules via motor proteins¹, self-assembling cytoskeletal elements² or self-organizing reaction-diffusion systems³. Coupling of cargo to energy-dissipating NTPases that drive the transport is usually mediated by specific protein-protein interactions. Non-specific coupling of biomolecules, by contrast, is poorly explored in biology and, so far, only a few examples of molecular transport based on purely physical mechanisms have been reported. For example, a study in mouse oocytes showed that actin-coated vesicles generated a pressure gradient that positioned large objects like the nucleoid in the cell centre^{4,5}. In the *Caenorhabditis elegans* zygote, cortical flows were shown to couple to the PAR reaction-diffusion system via advective transport⁶. Another recent example comes from in vitro studies of the *Escherichia coli* Min system^{7,8}.

The Min system, a paradigmatic model for pattern formation in biology, regulates the site of cell division in *E. coli*^{9–12}. The core of this reaction-diffusion system consists of only two proteins, the ATPase MinD and the ATPase activating protein MinE, which interact and reversibly bind to the membrane^{11,13}. Despite this simple reaction scheme, the Min system exhibits rich dynamics that have been explored in vivo^{9–11,14}, reconstituted in vitro^{13,15,16} and described by physical theories^{17–21}. In the rod-shaped *E. coli*, MinDE oscillate from pole to pole^{10,11,14}. In vitro, MinDE proteins form travelling surface waves or quasi-stationary patterns on planar artificial membranes^{13,15,16} and exhibit oscillations when geometrically confined^{22,23}. These dynamics can provide spatial cues for particular proteins. MinC specifically binds to MinD and thus follows its movements^{10,22,24–26}. In turn, MinC constrains the localization of the main divisome protein FtsZ by inhibiting its polymerization^{27,28}.

Besides this well-described patterning by specific interactions with clear physiological evidence, MinDE self-organization has

recently shown an intriguing hidden function in vitro: MinDE regulated the localization of unrelated membrane-bound molecules in space and time in the absence of MinC/FtsZ^{7,8}. These results suggested that MinDE oscillations could further enhance cell division by prepositioning membrane proteins to the cell middle⁷. However, the underlying physics and the broader biological implications have remained unknown.

Here, through a joint experimental and theoretical investigation, we have deciphered the physical mechanism underlying this non-specific transport phenomenon. We quantitatively probed MinDE-dependent transport using a synthetic membrane-bound cargo based on composite DNA nanostructures. We discerned how the effective size (that is, membrane footprint) and diffusion coefficient of the cargo, as well as the type of MinDE patterns, determine the transport that takes place. Exploiting these effects, we revealed that MinDE can even spatially sort different cargo species. Theoretical analysis of these data demonstrated a diffusio-phoretic effect: an effective density-dependent inter-particle friction creates cargo transport along the diffusive fluxes of MinD proteins. This type of NTPase-driven diffusio-phoresis might represent a generic active transport mechanism in cells that neither requires motor proteins nor specific protein interactions. As such, it might be particularly important for prokaryotes and could have been prevalent in early stages of life on Earth.

Probing MinDE-induced transport with a synthetic cargo

We set out to understand how MinDE dynamics can spatiotemporally regulate other membrane-bound, yet unrelated molecules (henceforth referred to as non-specific ‘cargo’) into patterns and gradients^{7,8}. Specifically, we asked whether cargo transport can arise from MinDE patterns per se via thermodynamic forces, or whether it requires active processes and non-equilibrium particle fluxes.

¹Max Planck Institute of Biochemistry, Martinsried, Germany. ²Arnold-Sommerfeld-Center for Theoretical Physics and Center for NanoScience, Ludwig-Maximilians-Universität München, Munich, Germany. ³Living Matter Program, AMOLF, Amsterdam, Netherlands. ⁴Present address: Department of Physics, Princeton University, Princeton, NJ, USA. ⁵Present address: University of Washington, Institute for Protein Design, Seattle, WA, USA.

⁶These authors contributed equally: Beatrice Ramm, Andriy Goychuk. ✉e-mail: frey@lmu.de; schwille@biochem.mpg.de

To experimentally address this question and test possible mechanisms, we set up a highly controllable minimal *in vitro* platform. To this end, we reconstituted MinDE pattern formation on supported lipid bilayers (SLBs)¹³. For simplicity, we first chose conditions under which initially chaotic, laterally moving MinDE waves transition into quasi-stationary labyrinth patterns¹⁶. To quantitatively assess the interaction between MinDE and cargo molecules on the membrane, we employed a synthetic cargo: a composite object consisting of a DNA origami nanostructure as scaffold and streptavidin molecules that serve as modular building blocks and connectors to the membrane (Fig. 1a). In particular, the origami²⁹ featured 7 dyes on the upper facet for visualization and 42 sites at the bottom facet that could be specifically addressed for the incorporation of biotinylated oligonucleotide handles. These handles in turn bound to streptavidin coupled to biotinylated lipids in the SLB.

When we initiated MinDE self-organization with ATP in the presence of this synthetic cargo, the cargo components—that is, the origami structures and streptavidin—reorganized into patterns from an initially homogeneous state (Fig. 1b,c, Supplementary Fig. 1 and Supplementary Video 1). As expected, the origami and streptavidin co-localized. Accordingly, in the following, origami fluorescence serves as a proxy for cargo localization. For the entire duration of the experiment, cargo always gathered in MinD-depleted regions, forming patterns that were anti-correlated to the MinDE patterns (Fig. 1b,c). Similarly, when we altered the established MinDE/cargo patterns by adding more MinE, the cargo channel reflected the changes in MinDE patterns, moving in an anti-correlated fashion (Supplementary Fig. 2 and Supplementary Video 2). By contrast, when MinE (which stimulates MinD ATP hydrolysis) was omitted, MinD and the cargo molecules remained uniformly distributed (Extended Data Fig. 1). These findings indicate that the spatial heterogeneity of the cargo is not caused by depletion attraction, such as in filament bundling³⁰. For one, depletion attraction should lead to aggregation of large particles (cargo), even in a homogeneous field of smaller particles (MinD)³¹. Furthermore, depletion attraction would imply a preferred agglomeration of cargo in regions of high MinD density, which we also did not observe (Supplementary Information). Hence, our data demonstrate that cargo transport is active, because it requires the presence of MinDE and ATP, and thus active MinDE self-organization.

Effective cargo size determines the extent of cargo demixing

Having shown that MinDE redistribute our synthetic cargo, we next exploited the modular nature of our cargo to systematically vary its interaction with MinDE. MinD and lipid-anchored streptavidin both form a monomolecular layer of height ~ 5 nm on membranes^{32,33}, whereas the lower facet of the origami scaffold lies at ~ 5 – 11 nm above the membrane (Supplementary Note 1). MinDE thus move on the membrane below the altitude of the origami

scaffold and should mainly interact with the membrane-bound streptavidin. Hence, varying the number of streptavidin ($n \in \{1, 2, 5, 15, 28, 42\}$) bound to the origami scaffold enables fine control over a large dynamic range of the membrane footprint or effective size of the cargo (henceforth cargo- n , Fig. 1). In this way, we modulated the interaction of the cargo- n with MinDE, as well as its diffusion on the membrane.

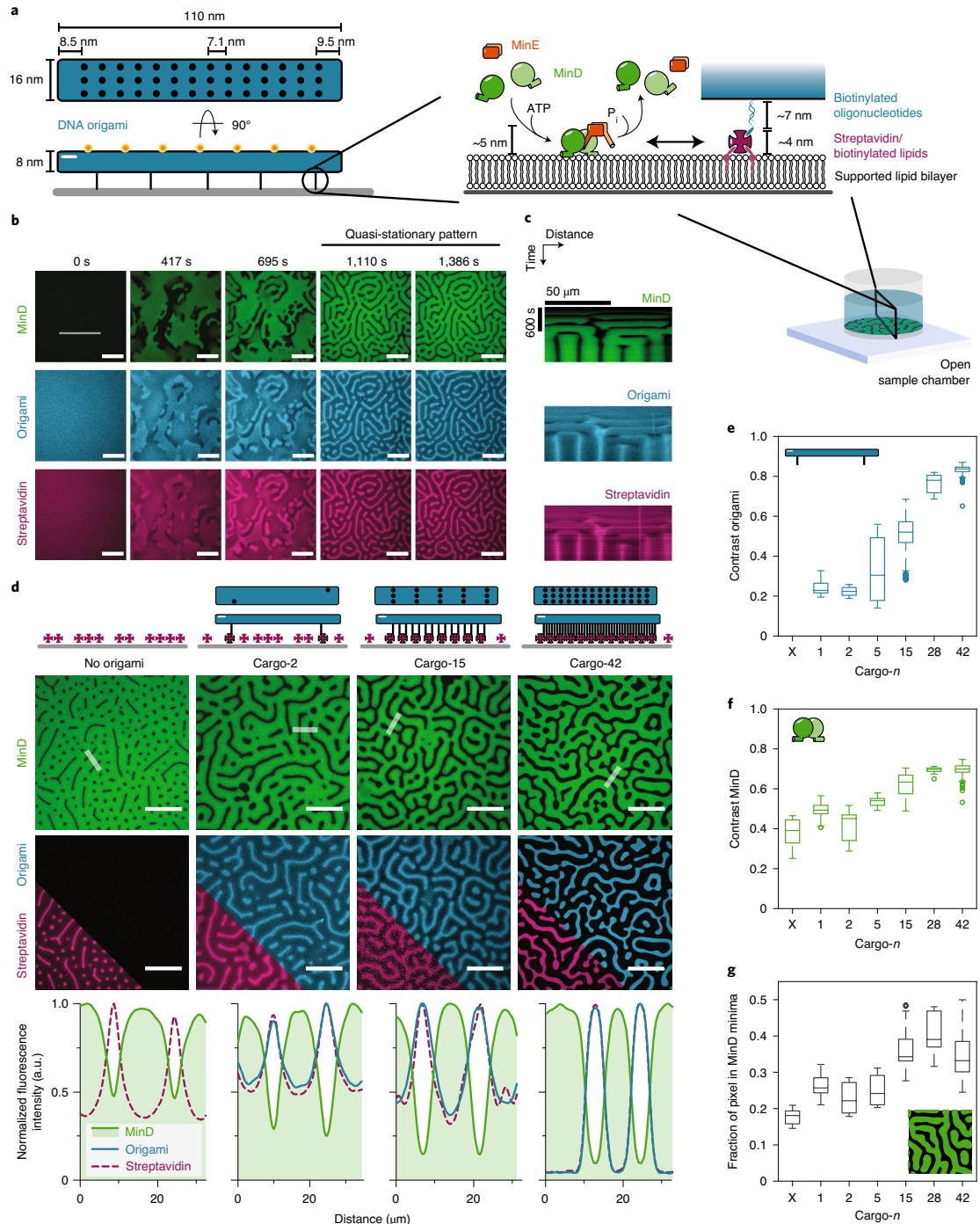
To quantitatively assess the interaction between MinDE and the respective cargo, we analysed the resulting, final quasi-stationary patterns (Fig. 1d and Extended Data Fig. 2). As a measure for molecule enrichment, we determined the Michelson contrast, $(I_{\max} - I_{\min}) / (I_{\max} + I_{\min})$, of the fluorescence images on a scale from zero for a homogeneous distribution to one for a binary distribution. Cargo patterns became much sharper with increasing cargo size (Fig. 1e and Extended Data Fig. 2). This increase in the contrast of cargo patterns was accompanied by sharper and also narrower MinDE patterns, as indicated by an increased region of pixels classified as MinD minima (Fig. 1f,g). Thus, MinDE dynamics dictate the localization of cargo on the membrane in a size-dependent manner, and are in turn also impacted by their presence. At first glance, these results could be interpreted as simply being a consequence of steric repulsion between cargo and MinDE. However, although a static gradient of accessible space would indeed induce a gradient of cargo molecules, this effect should be equal for all cargo species, irrespective of their effective size (Supplementary Information). Therefore, even though the diffusion of MinD on the membrane under the given conditions is very slow ($D = 0.013 \mu\text{m}^2 \text{s}^{-1}$)³⁵, we conclude that MinD proteins do not simply act as immobile obstacles on the membrane that would bias cargo diffusion via static volume exclusion, a second option for a thermodynamic force.

Thermodynamic forces cannot explain cargo transport by MinDE

As our experimental data disqualified both depletion attraction and static volume exclusion as possible explanations for cargo redistribution, we wondered whether mobile MinD proteins could effectively repel cargo in a size-dependent manner by imposing local constraints on the entropy of mixing. To test this third (thermodynamic) hypothesis, we formulated a fully quantitative Flory–Huggins theory (FH) without fitting parameters. Specifically, each origami scaffold crosslinks n streptavidin into a passive polymer-like cargo (Fig. 2a), while the remaining free streptavidin (for $n < 15$; Extended Data Fig. 2) behave independently (Supplementary Information). Given these constraints, we characterized the membrane in terms of local surface densities of c_c cargo, c_s free streptavidin and c_p MinD (Supplementary Table 1), assuming a well-mixed lattice gas on the microscopic scale. On the mesoscopic scale, we then asked ‘what is the equilibrium distribution of passive particles (cargo and free streptavidin) in the presence of a heterogeneous distribution of active MinD proteins?’ To answer this question, we used our FH model to calculate the corresponding chemical

Fig. 1 | MinDE-driven cargo demixing depends on the effective size (membrane footprint) of the cargo. **a**, Schematic of the synthetic membrane-anchored cargo consisting of a DNA origami scaffold (20-helix bundle; $110 \times 16 \times 8$ nm) and streptavidin building blocks. The DNA origami nanostructure illustrates the position of 7 dyes at the upper facet and 42 addressable sites for incorporation of biotinylated oligonucleotides at the lower facet. Biotinylated oligonucleotides bind to lipid-anchored streptavidin on the SLB. MinDE self-organize by concerted attachment and detachment to and from the membrane powered by ATP hydrolysis into ADP and P_i (inorganic phosphate). The self-organization assay is performed in an open chamber. **b, c**, Representative time series (**b**) and kymograph (along the line selection in **b**) (**c**) of MinDE self-organization inducing patterns of cargo-2 ($1 \mu\text{M}$ MinD (30% EGFP-MinD), $1.5 \mu\text{M}$ MinE-His, 0.1 nM origami-Cy5 with two biotinylated oligonucleotides, Alexa568-streptavidin). **d**, Representative images and fluorescence intensity line plots (smoothed) of established MinDE labyrinth patterns and anti-correlated DNA origami and streptavidin patterns when no origami, cargo-2, cargo-15 or cargo-42 is present. The contrast of the resulting patterns and size of the MinD minima increase with increasing number of incorporated streptavidin per cargo. **e–g**, Box plots of the contrast of cargo (**e**), MinD patterns (**f**) and the fraction of pixels classified as MinD minima (**g**) when no origami, cargo-1, cargo-2, ..., or cargo-42 is present. Lines in box plots are medians, box limits are quartiles 1 and 3, whiskers are $1.5 \times$ interquartile range (IQR) and points are outliers. Data are from at least two independent experiments with total numbers of analysed images per condition $N(\text{No origami}) = 32$, $N(\text{Cargo-1}) = 96$, $N(\text{Cargo-2}) = 41$, $N(\text{Cargo-5}) = 32$, $N(\text{Cargo-15}) = 94$, $N(\text{Cargo-28}) = 32$, $N(\text{Cargo-42}) = 87$. Scale bars, $50 \mu\text{m}$ (**b, c, d**).

potentials μ_i for each species (Supplementary Information). Furthermore, we assumed that the passive particles adopt a thermal equilibrium state with vanishing chemical potential gradients ($\nabla\mu_g = \nabla\mu_s = 0$) in an adiabatic response to the imposed steady-state distribution of active particles ($\nabla\mu_p \neq 0$). Our theoretical analysis shows that entropic mixing effects can, in principle, create a



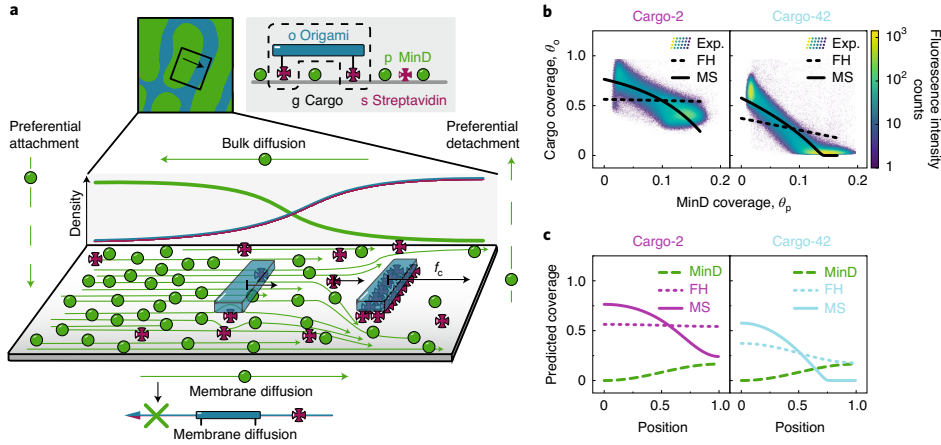


Fig. 2 | MinDE-dependent cargo transport is explained by mesoscopic friction between particle fluxes, not by mixing or volume exclusion. **a**, Schematic of the phenomenological MS-type model. MinD protein density gradients are determined by a closed cycle of reactive fluxes (MinD membrane attachment/detachment, dashed green arrows) and diffusive fluxes (green arrows). Mediated by hydrodynamic or direct interactions, the diffusive MinD membrane fluxes exert a frictional force f_c (black arrow) on the cargo molecules. Then, cargo density gradients are determined by a balance between these frictional forces and thermodynamic forces (entropic repulsion and mixing). **b**, Cross-correlation between MinD coverage ($\theta_p = a_p c_p$) and DNA origami coverage ($\theta_c = a_c c_c$), for two different cargo species, cargo-2 and cargo-42. Respective membrane footprints: MinD dimer $a_p = 25 \text{ nm}^2$, DNA origami $a_c = 1,760 \text{ nm}^2 \approx 70 a_p$. The colour-coded two-dimensional histogram represents the experimental data of selected days (Exp.), where the raw images were smoothed by a one-pixel-wide Gaussian kernel. Solid and dashed lines correspond to two candidate models. The FH-type model (dashed lines), whose parameters are fully determined by our experiments, fails to account for cargo transport: weak entropic sorting of streptavidin in an external gradient of MinD is not sufficient to overcome the strong repulsion of the bulky DNA origami scaffolds. Instead, we find that the MS model (solid lines), with an estimated interaction parameter, explains cargo transport. The MS model allows stronger reorganization of cargo than the FH model, because, in addition to thermodynamic forces, cargo transport is further driven by frictional coupling to MinD protein fluxes. **c**, Spatial distribution of cargo molecules in response to the (imposed) MinD profile, corresponding to the cross-correlation functions in **b**. Model parameters: (cargo-2) average coverages $\bar{\theta}_p = 0.0825$, $\bar{\theta}_c = 0.149$ and $\bar{\theta}_o = 0.55$; interaction parameter in terms of MinD coverage $\theta_x^{-1} = a_p^{-1} c_x^{-1} = 220$; (cargo-42) average coverages $\bar{\theta}_p = 0.0825$, $\bar{\theta}_c = 0$ and $\bar{\theta}_o = 0.28$; interaction parameter $\theta_x^{-1} = a_p^{-1} c_x^{-1} = 620$.

gradient of passive cargo in response to a gradient of active MinD, where the cargoes' crosslinked streptavidin experience a weak entropic bias towards MinD-depleted regions (due to volume exclusion effects). However, this effect will be partly compensated by the analogous entropic repulsion between origami scaffolds, which prevents high cargo densities, in stark contrast to our experimental observations (Fig. 2b,c and Extended Data Fig. 3). Consequently, we also rejected entropic mixing in fixed external (chemical potential) gradients as the mechanism underlying MinDE-dependent cargo transport.

Coupling between particle fluxes explains cargo transport

Taken together, thermodynamic mechanisms alone cannot explain MinDE-induced cargo transport in our experiments, suggesting that the underlying mechanism is genuinely non-equilibrium in nature. Therefore, we generalized our equilibrium FH model to consider the non-equilibrium dynamics of particles. Specifically, MinDE gradients build up due to particle exchange between the bulk solution and membrane (reactive fluxes)^{16,18,19,21,25}, leading to chemical potential gradients $\nabla\mu_i$ on the membrane (thermodynamic forces). According to Onsager's theory³⁴, thermodynamic forces imply particle fluxes \mathbf{j}_i . Conceptually, diffusive fluxes on the membrane then arise from an effective force balance of thermodynamic and friction forces between the different macromolecules and lipids (with friction coefficients ζ_{ik}). Furthermore, in a crowded environment such as the membrane surface in our experiments (mean free path of $\sim 50 \text{ \AA}$; Supplementary Information), hydrodynamic or also direct interactions between particles can mediate a 'mesoscopic friction'

that couples their respective fluxes (with coupling constants ζ_{ik}). Using these arguments, we formulated a phenomenological theory where each membrane-bound species obeys a Maxwell–Stefan (MS)-like effective force-balance equation^{35,36}:

$$\nabla\mu_i + \xi_i \frac{\mathbf{j}_i}{c_i} + \sum_k c_k \zeta_{ik} \left(\frac{\mathbf{j}_i}{c_i} - \frac{\mathbf{j}_k}{c_k} \right) = 0. \quad (1)$$

As before, the index $i \in \{p, g, s\}$ refers to MinD proteins, cargo with bound streptavidin and free streptavidin, respectively. Although our theory is intrinsically dynamic (Methods), we first analysed the non-equilibrium steady state, $\partial_t c_i = 0$, reflecting the quasi-stationary MinDE patterns. Then, cargo and streptavidin exhibit Brownian motion and relax to a thermal equilibrium state with vanishing fluxes $\mathbf{j}_g = \mathbf{j}_s = 0$. The MinD protein patterns maintain a non-equilibrium steady state and finite protein fluxes $\mathbf{j}_p \neq 0$ via off-equilibrium chemical reactions (ATPase activity). In the absence of mutual friction between the macromolecules ($\zeta_{ik} = 0$), equation (1) reduces to the FH model ($\nabla\mu_g = \nabla\mu_s = 0$), which readily implies weak cargo redistribution in a static gradient of active proteins. As a decisive factor in addition to these entropic demixing effects, the presence of frictional coupling ($\zeta_{ik} \neq 0$) between cargo and MinD leads to advective cargo transport by the non-equilibrium protein fluxes ($\mathbf{j}_p \neq 0$) of MinD (Fig. 2a). The additional bias conferred by these protein fluxes leads to cargo redistribution, which is much stronger than by equilibrium thermodynamic forces alone and thus quantitatively explains our experimental data (Fig. 2b,c and Extended Data Fig. 3).

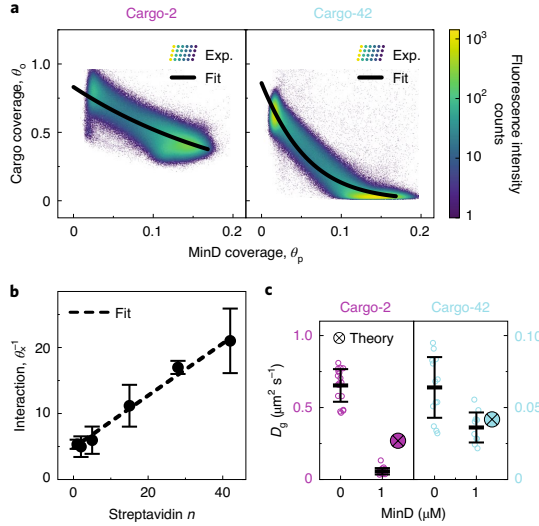


Fig. 3 | Reduced model predicts that large MinD densities slow down cargo diffusion. **a**, Cross-correlation between MinD coverage ($\theta_p = a_p c_p$) and DNA origami coverage ($\theta_c = a_c c_c$) for cargo-2 and cargo-42. Respective membrane footprints: MinD dimer $a_p = 25 \text{ nm}^2$, DNA origami $a_c = 1,760 \text{ nm}^2$. The colour-coded two-dimensional histogram represents experimental data for selected days (Exp.), identical to Fig. 2b, while the solid line (Fit) is a fit curve of our reduced model. **b**, Interaction parameter in terms of MinD coverage, $\theta_c^{-1} = a_p^{-1} c_p^{-1}$, obtained by the fitting procedure in **a**. The interaction linearly increases when more streptavidin is incorporated per cargo, starting from the base interaction of the origami scaffold. The dashed line indicates a linear fit of the interaction parameter $\theta_c^{-1} = (\zeta_{po} + n\zeta_{ps})/(a_p \xi_p)$ as a function of n . In contrast to our initial estimate (Fig. 2c), entropic repulsion between cargo molecules was neglected for simplicity, thus probably underestimating the interaction parameter. **c**, Cargo molecule diffusion coefficient in the absence or presence of $1 \mu\text{M}$ MinD ($1 \mu\text{M}$ MinD (30% EGFP-MinD), $0.1\text{-}1 \text{ pM}$ origami-Cy3b with 2 or 42 biotinylated oligonucleotides, non-labelled streptavidin, SLB: DOPC/DOPG/biotinyl-CAP-PE 70/30/0.01 mol%), measured via single-particle tracking and predicted with the fitted interaction parameters from **b**. Cargo-42 typically diffuses slower than cargo-2 (indicated by a smaller diffusion coefficient D_0 at $0 \mu\text{M}$ MinD). Increasing MinD density has a much stronger effect on cargo-2 than on cargo-42, both in theory and experiment. Points are mean values of individual measurements (M), line and error bars represent the mean value and standard deviation. Data were obtained from the number of sample chambers $S(\text{Cargo-2}) = 7$, $S(\text{Cargo-42}) = 5$, $S(\text{Cargo-2, MinD}) = 4$, $S(\text{Cargo-42, MinD}) = 3$; number of measurements $M(\text{Cargo-2}) = 18$, $M(\text{Cargo-42}) = 13$, $M(\text{Cargo-2, MinD}) = 19$, $M(\text{Cargo-42, MinD}) = 10$; number of analysed single-particle tracks $N(\text{Cargo-2}) = 15,755$, $N(\text{Cargo-42}) = 19,481$, $N(\text{Cargo-2, MinD}) = 7,924$, $N(\text{Cargo-42, MinD}) = 4,542$; average track length $\text{TL}(\text{Cargo-2}) = 339$, $\text{TL}(\text{Cargo-42}) = 546$, $\text{TL}(\text{Cargo-2, MinD}) = 772$, $\text{TL}(\text{Cargo-42, MinD}) = 647$; fraction of mobile DNA origami $\text{MF}(\text{Cargo-2}) = 0.81$, $\text{MF}(\text{Cargo-42}) = 0.67$, $\text{MF}(\text{Cargo-2, MinD}) = 0.70$, $\text{MF}(\text{Cargo-42, MinD}) = 0.63$.

MinDE impair cargo diffusion via mesoscopic friction

Next, we simplified our theoretical model by neglecting membrane saturation effects (Supplementary Information), reducing the chemical potential of particles with size a_i to $\mu_i \approx k_B T \ln(a_i c_i)$. The force-balance equation, equation (1), then becomes a generalized Fick's law:

$$j_p \approx -\frac{k_B T}{\zeta_p + \zeta_{pg} + \zeta_{ps}} \nabla c_p \equiv -D_p(c_g, c_s) \nabla c_p \quad (2)$$

where the density-dependent diffusion coefficient of MinD, $D_p(c_g, c_s)$, decreases through friction (that is, interactions) with cargo and streptavidin. For cargo with strong coupling ζ_{pg} , maintaining the diffusive fluxes that balance reactive protein turnover requires sharper protein gradients, which explains the progressively sharper and narrower MinDE patterns (Fig. 1f,g).

Assuming that the typically small number of free streptavidin (Supplementary Information) does not notably contribute to the dynamics, $c_s \zeta_{ps} \ll c_g \zeta_{pg}$, one obtains a closed expression for the cargo distribution:

$$c_g(c_p) = c_x W_0 \left[\frac{c_g(0)}{c_x} \exp\left(\frac{c_g(0) - c_p}{c_x}\right) \right], \quad (3)$$

with typical interaction density $c_x = \xi_p / \zeta_{pg}$. Fitting equation (3) to our experimental data (Fig. 3a,b and Extended Data Fig. 3), we demonstrate that the coupling constant ζ_{pg} between MinD and cargo- n has a contribution from the origami scaffold and from the n incorporated streptavidin, $\zeta_{pg} = \zeta_{po} + n\zeta_{ps}$, explaining why cargo transport increases with the number of streptavidin per cargo (Fig. 1d-g).

To test our theoretical model experimentally, we performed single-particle tracking of cargo-2 and cargo-42, both in the presence and absence of MinD. In the former case, we emulated high MinD membrane densities in the maxima of MinDE patterns by adding $1 \mu\text{M}$ MinD and ATP, but no MinE. We found that the diffusion coefficient of cargo-2 decreased from $0.65 \pm 0.12 \mu\text{m}^2 \text{s}^{-1}$ in the absence of MinD to $0.06 \pm 0.02 \mu\text{m}^2 \text{s}^{-1}$ at high MinD density (Fig. 3c). By contrast, the diffusion coefficient of cargo-42, which was already low in the absence of MinD ($0.06 \pm 0.02 \mu\text{m}^2 \text{s}^{-1}$), hardly changed at high MinD density ($0.036 \pm 0.011 \mu\text{m}^2 \text{s}^{-1}$) (Fig. 3c). Subsequently, we used our fitted interaction parameters to predict the diffusion coefficient of cargo at high protein densities, based on the experimental values in the absence of proteins (Supplementary Information). Our predictions were in good quantitative agreement with our experimental findings, validating our model. At first, it might seem counterintuitive that MinD affects cargo-42 diffusion less than that of cargo-2, despite stronger frictional coupling. However, even in the absence of MinD, cargo-42 diffuses much slower than cargo-2 due to the friction between its many streptavidin and the membrane, which dominates over the additional friction with MinD. This observation highlighted the parameter interdependence that arises due to streptavidin serving both as building block and connector to the membrane and raised the question whether cargo transport is affected more by its effective size or its diffusion coefficient. To answer this, we employed an alternative membrane attachment strategy for the DNA origami scaffolds via cholesteryl moieties (Extended Data Figs. 4 and 5 and Supplementary Note 2). We found that cargoes with a larger membrane footprint (that is, effective size) and at the same time similar diffusion as cargo-2 were strongly redistributed (Extended Data Fig. 5 and Supplementary Note 2), corroborating that it is indeed the effective cargo size that determines the interaction with MinD. In conclusion, the dependence of the cargo diffusion coefficient on the ambient protein density is a direct experimental proof of friction between MinD and cargo and that the effective cargo size governs the corresponding friction coefficient.

MinDE spatially sort different cargo species

Can we use our obtained knowledge to selectively position cargo molecules, that is, to sort them according to their properties, along protein gradients? To answer this question, we placed two differently labelled cargo species, cargo-2 and cargo-42, in the same assay (Fig. 4a). We found, as predicted by our model (Fig. 4d), that cargo-

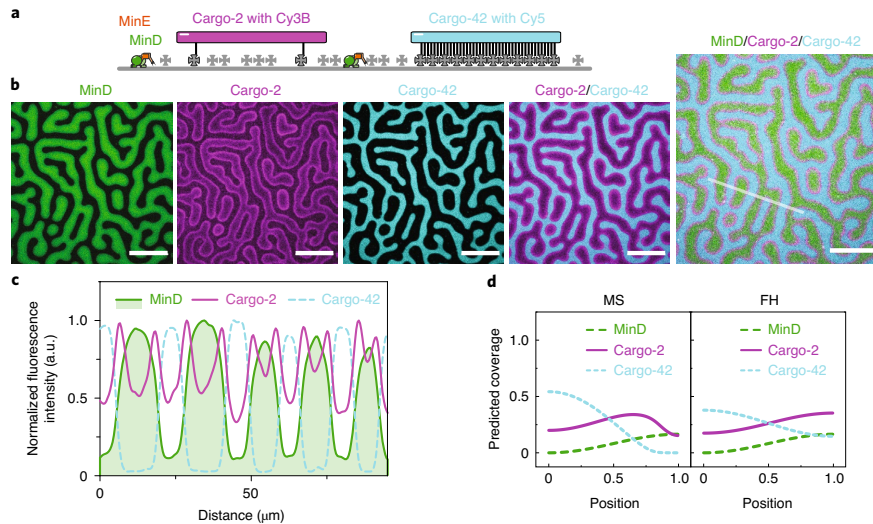


Fig. 4 | MinDE spatially sort cargo according to effective size. a, Schematic of the experimental set-up. MinDE self-organization was performed in the presence of two different cargo species with distinct fluorescent labels, cargo-2 with Cy3B and cargo-42 with Cy5 (1 μM MinD (30% EGFP-MinD), 1.5 μM MinE-His, 50 pM origami-Cy3b with two biotinylated oligonucleotides, and 50 pM origami-Cy5 with 42 biotinylated oligonucleotides, non-labelled streptavidin). **b, c**, Representative images of individual and overlaid channels (**b**) and line plot (**c**) (smoothed) of the indicated selection of MinDE-induced sorting of cargo species. Scale bars, 50 μm . The experiment was performed three times under identical conditions. **d**, Spatial distribution of two cargo species in response to the (imposed) MinD profile. The phenomenological MS-type model allows for stronger reorganization of cargo molecules than the FH-type model. In particular, the phenomenological MS-type model predicts that cargo-2 accumulates between cargo-42 and MinD. Model parameters: average coverage of MinD proteins $\theta_b = 0.0825$, streptavidin $\theta_s = 0$, cargo-2 $\theta_{o-2} = 0.26$ and cargo-42 $\theta_{o-42} = 0.26$; interaction parameter (in terms of MinD coverage: $\theta_x^{-1} = a_p^{-1}c_x^{-1}$) of cargo-2 $\theta_{x-2}^{-1} = 220$ and cargo-42 $\theta_{x-42}^{-1} = 620$. Respective membrane footprints: MinD dimer $a_p = 25 \text{ nm}^2$, streptavidin $a_s = 25 \text{ nm}^2$, DNA origami $a_o = 1,760 \text{ nm}^2 \approx 70a_p$.

42 gathered in MinD-free regions and was framed by cargo-2 (Fig. 4b,c, Supplementary Fig. 3 and Supplementary Video 3). Thus, cargo-42 exhibited a similar behaviour as when present in the assay alone. By contrast, the localization of cargo-2 relative to MinD changed when cargo-42 was also present (Figs. 1d and 4c). The observed spatial separation of cargo species was not an artefact due to fluorescent channel crosstalk, dye selection or quenching (Extended Data Fig. 6). Hence, the clear MinDE-induced spatial sorting of cargo species according to their effective size further refutes thermodynamic models (Fig. 4d), corroborating that MinDE indeed transport molecules via friction.

MinDE waves direct net cargo transport via diffusiophoresis

Having confirmed diffusiophoretic transport in the context of quasi-stationary MinDE patterns, we turned to conditions where MinDE form travelling surface waves^{7,8}. As in previous experiments with lipid-anchored streptavidin alone^{7,8}, MinDE waves induced anti-correlated patterns of our synthetic cargo-2 that were superimposed with macroscopic gradients across multiple MinDE wavelengths, indicating net transport (Fig. 5a). Consequently, cargo accumulated between opposing wavefronts (Fig. 5a and Supplementary Video 4). Despite their distinct appearance, stationary as well as moving MinDE patterns are maintained by the same kind of non-equilibrium reaction and diffusion fluxes^{6,18,19,21,25}. Thus, we could directly apply our theory to this dynamic setting, without further assumptions (Methods). We found that, in addition to the interaction between MinDE and cargo, macroscopic transport also requires matching timescales between MinDE

wave propagation and cargo diffusion: cargo with small mobility cannot keep up with the MinDE wave. In agreement with our simulations (Fig. 5b), the slowly diffusing cargo-42 hardly formed long-ranged gradients (Fig. 5c and Supplementary Fig. 4), despite its strong frictional coupling to MinDE, supporting our prediction that low cargo mobility can limit macroscopic transport. This was further corroborated by the emergence of macroscopic gradients for cholesterol-anchored cargo-chol-2 and cargo-chol-15 (Fig. 5c and Supplementary Fig. 4), which display similarly high coupling to MinDE, but diffuse faster than cargo-42 (Extended Data Fig. 5).

Next, we exploited the geometry-sensitivity of MinDE waves that travel along the longest axis on geometrically patterned planar membranes with chromium barriers³⁷. On these membranes, MinDE waves indeed transported cargo directionally along their wavevector, resulting in reproducible gradients (Fig. 5d,e, Extended Data Fig. 7 and Supplementary Videos 5 and 6). These density gradients are clearly visible on the macroscopic scale, while directed movement of single cargo molecules cannot be discerned from diffusion (Extended Data Fig. 8 and Supplementary Note 3). This observation highlights the difference between ATP-driven diffusiophoresis and translational motor proteins.

Our findings raised the question of whether MinDE-dependent transport via diffusiophoresis could occur in vivo. To our knowledge, no direct observation of this mechanism in *E. coli* has been reported, which may be attributed to bacterial sizes close to the optical resolution limit or specific interactions concealing such occurrence. Thus, we reconstituted MinDE oscillations together with inert model peripheral membrane proteins (mCh-MTS)⁷ in the evolutionary distant fission yeast *Schizosaccharomyces pombe*³⁸

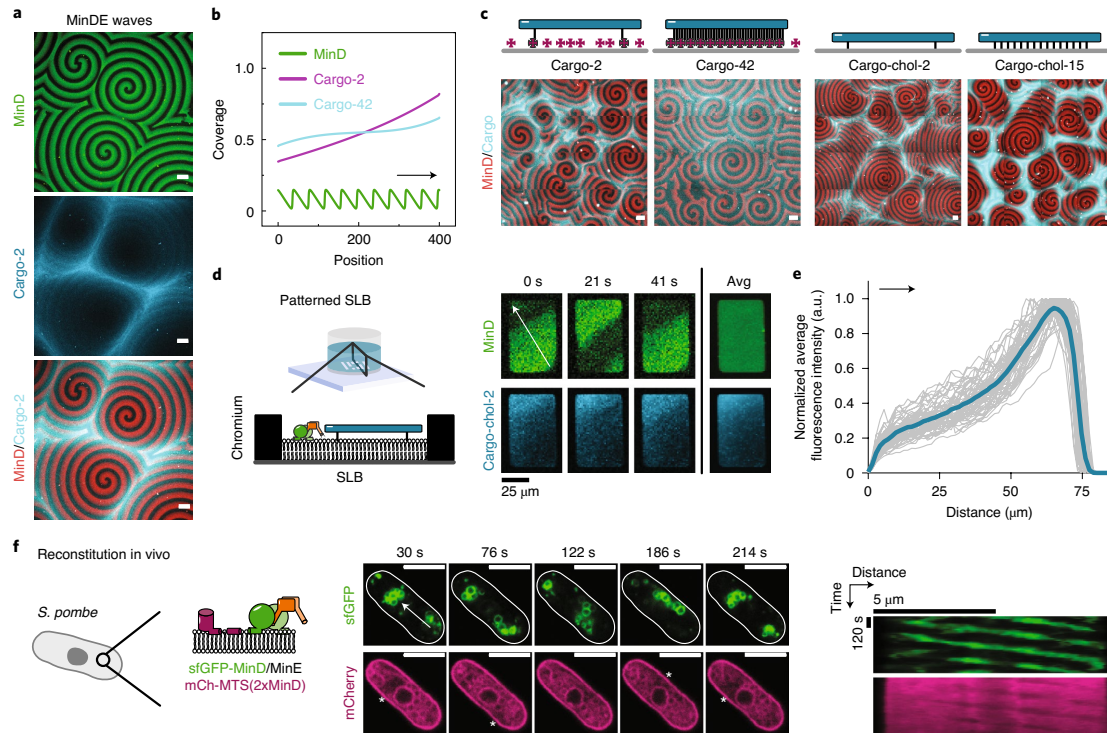


Fig. 5 | Directed net transport of cargo by MinDE waves via diffusiophoresis. **a**, Representative images of MinDE travelling surface waves that transport cargo-2 establishing long-range gradients (1 μM MinD, 5 μM His-MinE, 0.1 nM origami-Cy3b with two biotinylated oligonucleotides, non-labelled streptavidin). **b**, Simulation of cargo transport by a protein wave with skewed sinusoidal waveform (green, skewness $\gamma = -0.9$), which emulates MinD travelling waves (40 μm wavelength, 1.4 $\mu\text{m s}^{-1}$ velocity) in one-dimensional geometry (the black arrow indicates the wavevector). After a very long simulation time of 28 h, we find only weak redistribution of cargo-42 compared with the strong redistribution of cargo-2. Interaction parameters are as in Fig. 3b, (bare) cargo diffusion coefficients $D_c(0)$ as in Fig. 3c and the (bare) MinD diffusion coefficient is set to $D_p = 0.425 \mu\text{m}^2 \text{s}^{-1}$ (ref. 25). Both cargo coverages are set to $\theta_0 = 0.55$ (thus neglecting the reduced surface coverage of cargo-42) to improve comparability. Cargo coverages are averaged over the last 17 min. **c**, Representative images of MinDE inducing large-scale gradients of cargo-2, cargo-chol-2 and cargo-chol-15, but not of cargo-42 (1 μM MinD, 5 μM His-MinE, 0.1 nM origami-Cy5 with 2 or 42 biotinylated oligonucleotides, non-labelled streptavidin or 0.1 nM origami-Cy3b with 2 or 15 hybridizing oligonucleotides, 10 nM TEG-cholesteryl oligonucleotide). **d**, Representative time series and average of MinDE travelling surface waves transporting cargo-chol-2 along the wavevector when oriented along the longest axis on chromium-patterned SLBs **e**, Normalized average fluorescence intensity profiles of cargo along the wavevector in **d**. The bold coloured line represents the mean profile, generated from $N = 56$ membrane patches from three independent experiments. **f**, MinDE dynamics spatiotemporally regulates the model peripheral membrane proteins mCh-MTS(2xMinD) when reconstituted in the fission yeast *S. pombe*. Decreased fluorescence in the mCherry channel is highlighted by white asterisks. Arrows indicate wave direction. Scale bars, 50 μm (**a,c**), 25 μm (**d**) and 5 μm (**f**).

(Fig. 5f, Extended Data Figs. 9 and 10 and Supplementary Videos 7 and 8). We found that in this in vivo model system MinDE formed dynamic patterns with similar wavelength and velocity as in its native host *E. coli*^{11,12} (Supplementary Note 4) and, indeed, spatiotemporally regulated mCh-MTS proteins on intracellular membranes (Extended Data Fig. 10).

Diffusiophoresis drives molecular transport in biology

In conclusion, combining in vitro and in vivo reconstitution experiments with theoretical modelling and analysis, we showed that the prokaryotic MinDE proteins can non-specifically transport and even sort membrane-bound cargo molecules by a diffusiophoretic effect: the diffusive fluxes of MinD and cargo couple via friction in a mechanical rather than thermodynamic fashion (Fig. 6). This process is driven by ATP-consuming MinDE self-organization, which

generates a net diffusive flux of MinD towards low densities. This flux establishes an effective frictional force on cargo, driving diffusiophoretic cargo transport towards areas of low MinD density. Hence, the friction between cargo and MinD increases with the effective size of the cargo (for example, with the number of streptavidin building blocks). The bare diffusion coefficient of cargo only becomes relevant in the case of dynamic MinDE waves where cargo diffusion has to ‘keep up’ with the MinDE waves to induce macroscopic gradients.

Similar transport effects have been reported previously in a non-biological context: diffusiophoresis generally refers to particle transport in fluids, induced by concentration gradients of small solutes^{39–49}. Interestingly, diffusiophoresis was also treated in terms of particle fluxes⁴⁸, suggesting that a flux-centred viewpoint may be appropriate for multicomponent mixtures out of equilibrium.

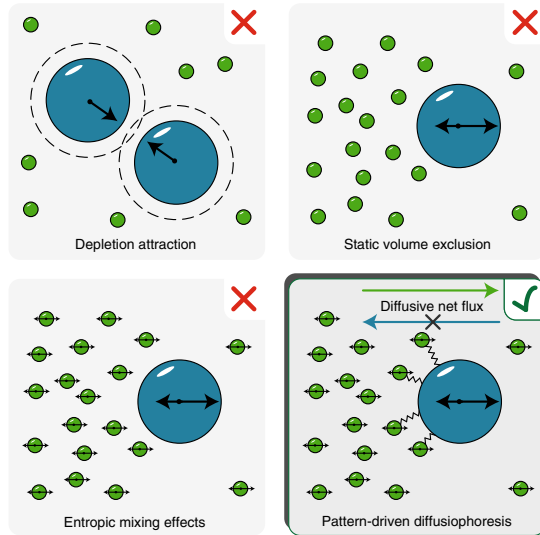


Fig. 6 | Diffusiophoresis explains cargo transport by protein self-organization.

Thermodynamic forces, such as depletion attraction, static volume exclusion or entropic mixing effects, cannot explain MinDE-dependent cargo transport in our experiments. However, it can be explained by diffusiophoresis: active protein self-organization generates gradients and hence net diffusive fluxes. As the proteins interact non-specifically with the cargo, the diffusive fluxes establish an effective frictional force, driving the accumulation of cargo in areas of low protein density.

A phenomenologically similar effect has been demonstrated in gases with the MS theory of diffusion^{35,36,50,51}. In a biologically relevant context, theoretical studies have suggested that diffusiophoresis might occur in enzyme chemotaxis⁵² and alignment⁵³, during ParABS-mediated chromosome segregation in bacteria⁵⁴ and that metabolism-dependent gradients of small molecules (for example, ATP) could induce transport of large particles⁵⁵. The here described diffusiophoresis driven by protein patterns that are maintained by NTPase cycles might constitute a novel mechanism of coupling energy dissipation to active spatiotemporal positioning in cell biology. Diffusiophoretic transport is presumably not a special feature of the *E. coli* MinDE system or reaction-diffusion systems in general, but can potentially be exerted by any active system producing concentration gradients. For example, such a mechanism could be underlying the secretion-induced protein patterning that has been observed in fission yeast⁵⁶ or be at play for the plethora of intracellular (actin) waves in eukaryotes whose purpose and mode of action has remained elusive⁵⁷. The mechanism might not even be limited to the membrane as a reaction surface, but potentially extends to other cellular surfaces and even cytosolic gradients. For example, the strong concentration gradients that are built up during liquid-liquid phase-separation processes could potentially similarly impact other molecules⁵⁸. We also propose that distinct pattern-forming systems sharing the same reaction space should align to minimize friction, even if their constituents are chemically independent. This could potentially link and synchronize pathways to increase their efficacy or provide a rescue mechanism against mutations affecting the chemical coupling via specific interactions (for example, between MinC and FtsZ). That this non-specific means of transport was discovered and described in an in vitro reconstitution assay is

not a coincidence, but highlights that the complexity of cells with more sophisticated and stronger specific interactions presumably masks such occurrence. Finally, simple as it is in comparison to eukaryotic, translational motor proteins, this mechanism could be interpreted as an alternative, more rudimentary mode of mechanochemical coupling and as such might be prevalent in prokaryotes and might have been present in early forms of life.

Online content

Any methods, additional references, Nature Research reporting summaries, source data, extended data, supplementary information, acknowledgements, peer review information; details of author contributions and competing interests; and statements of data and code availability are available at <https://doi.org/10.1038/s41567-021-01213-3>.

Received: 1 May 2020; Accepted: 22 February 2021;

Published online: 05 April 2021

References

- Vale, R. D. The molecular motor toolbox for intracellular transport. *Cell* **112**, 467–480 (2003).
- Theriot, J. A. The polymerization motor. *Traffic* **1**, 19–28 (2000).
- Halatek, J., Brauns, F. & Frey, E. Self-organization principles of intracellular pattern formation. *Phil. Trans. R. Soc. B* **373**, 20170107 (2018).
- Almonacid, M. et al. Active diffusion positions the nucleus in mouse oocytes. *Nat. Cell Biol.* **17**, 470–479 (2015).
- Colin, A. et al. Active diffusion in oocytes nonspecifically centers large objects during prophase I and meiosis I. *J. Cell Biol.* **219**, e201908195 (2020).
- Goehring, N. W. et al. Polarization of PAR proteins by advective triggering of a pattern-forming system. *Science* **334**, 1137–1141 (2011).
- Ramm, B. et al. The MinDE system is a generic spatial cue for membrane protein distribution in vitro. *Nat. Commun.* **9**, 3942 (2018).
- Shih, Y.-L. et al. Active transport of membrane components by self-organization of the Min proteins. *Biophys. J.* **116**, 1469–1482 (2019).
- de Boer, P. A. J., Crossley, R. E. & Rothfield, L. I. A division inhibitor and a topological specificity factor coded for by the minicell locus determine proper placement of the division septum in *E. coli*. *Cell* **56**, 641–649 (1989).
- Hu, Z. & Lutkenhaus, J. Topological regulation of cell division in *Escherichia coli* involves rapid pole to pole oscillation of the division inhibitor MinC under the control of MinD and MinE. *Mol. Microbiol.* **34**, 82–90 (1999).
- Raskin, D. M. & de Boer, P. A. J. Rapid pole-to-pole oscillation of a protein required for directing division to the middle of *Escherichia coli*. *Proc. Natl Acad. Sci. USA* **96**, 4971–4976 (1999).
- Ramm, B., Heermann, T. & Schwille, P. The *E. coli* MinCDE system in the regulation of protein patterns and gradients. *Cell. Mol. Life Sci.* **76**, 4245–4273 (2019).
- Loose, M., Fischer-Friedrich, E., Ries, J., Kruse, K. & Schwille, P. Spatial regulators for bacterial cell division self-organize into surface waves in vitro. *Science* **320**, 789–792 (2008).
- Wu, F., van Schie, B. G. C., Keymer, J. E. & Dekker, C. Symmetry and scale orient Min protein patterns in shaped bacterial sculptures. *Nat. Nanotechnol.* **10**, 719–726 (2015).
- Vecchiarelli, A. G. et al. Membrane-bound MinDE complex acts as a toggle switch that drives Min oscillation coupled to cytoplasmic depletion of MinD. *Proc. Natl Acad. Sci. USA* **113**, E1479–E1488 (2016).
- Glock, P. et al. Stationary patterns in a two-protein reaction-diffusion system. *ACS Synth. Biol.* **8**, 148–157 (2019).
- Huang, K. C., Meir, Y. & Wingreen, N. S. Dynamic structures in *Escherichia coli*: spontaneous formation of MinE rings and MinD polar zones. *Proc. Natl Acad. Sci. USA* **100**, 12724–12728 (2003).
- Halatek, J. & Frey, E. Highly canalized MinD transfer and MinE sequestration explain the origin of robust MinCDE-protein dynamics. *Cell Rep.* **1**, 741–752 (2012).
- Denk, J. et al. MinE conformational switching confers robustness on self-organized Min protein patterns. *Proc. Natl Acad. Sci. USA* **115**, 4553–4558 (2018).
- Glock, P., Brauns, F., Halatek, J., Frey, E. & Schwille, P. Design of biochemical pattern forming systems from minimal motifs. *eLife* **8**, e48646 (2019).
- Halatek, J. & Frey, E. Rethinking pattern formation in reaction-diffusion systems. *Nat. Phys.* **14**, 507–514 (2018).
- Zieske, K. & Schwille, P. Reconstitution of self-organizing protein gradients as spatial cues in cell-free systems. *eLife* **3**, e03949 (2014).
- Caspi, Y. & Dekker, C. Mapping out Min protein patterns in fully confined fluidic chambers. *eLife* **5**, e19271 (2016).

24. Raskin, D. M. & De Boer, P. A. J. MinDE-dependent pole-to-pole oscillation of division inhibitor MinC in *Escherichia coli*. *J. Bacteriol.* **181**, 6419–6424 (1999).
25. Loose, M., Fischer-Friedrich, E., Herold, C., Kruse, K. & Schwille, P. Min protein patterns emerge from rapid rebinding and membrane interaction of MinE. *Nat. Struct. Mol. Biol.* **18**, 577–583 (2011).
26. Hale, C., Meinhardt, H. & de Boer, P. Dynamic localisation cycle of the cell division regulator MinE in *Escherichia coli*. *EMBO J.* **20**, 1563–1572 (2001).
27. Hu, Z., Mukherjee, A., Pichoff, S. & Lutkenhaus, J. The MinC component of the division site selection system in *Escherichia coli* interacts with FtsZ to prevent polymerization. *Proc. Natl Acad. Sci. USA* **96**, 14819–14824 (1999).
28. Mcquillen, R. & Xiao, J. Insights into the structure, function and dynamics of the bacterial cytoskeletal FtsZ-ring. *Annu. Rev. Biophys.* **49**, 311–343 (2020).
29. Khmelinskaia, A., Franquelim, H. G., Petrov, E. P. & Schwille, P. Effect of anchor positioning on binding and diffusion of elongated 3D DNA nanostructures on lipid membranes. *J. Phys. D* **49**, 194001 (2016).
30. Marenduzzo, D., Finan, K. & Cook, P. R. The depletion attraction: an underappreciated force driving cellular organization. *J. Cell Biol.* **175**, 681–686 (2006).
31. Asakura, S. & Oosawa, F. On interaction between two bodies immersed in a solution of macromolecules. *J. Chem. Phys.* **22**, 1255–1256 (1954).
32. Miyagi, A., Ramm, B., Schwille, P. & Scheuring, S. High-speed AFM reveals the inner workings of the MinDE protein oscillator. *Nano Lett.* **18**, 288–296 (2018).
33. Scheuring, S., Müller, D. J., Ringler, P., Heymann, J. B. & Engel, A. Imaging streptavidin 2D crystals on biotinylated lipid monolayers at high resolution with the atomic force microscope. *J. Microsc.* **193**, 28–35 (1999).
34. Balian, R. *From Microphysics to Macrophysics* (Springer, 2007).
35. Maxwell, J. C. IV On the dynamical theory of gases. *Phil. Trans. R. Soc. Lond.* **157**, 49–88 (1866).
36. Stefan, J. Über das Gleichgewicht und die Bewegung, insbesondere die Diffusion von Gasgemengen. *Sitzber. Akad. Wiss. Wien.* **63**, 63–124 (1871).
37. Schweizer, J. et al. Geometry sensing by self-organized protein patterns. *Proc. Natl Acad. Sci. USA* **109**, 15283–15288 (2012).
38. Terbush, A. D., Porzondek, C. A. & Osteryoung, K. W. Functional analysis of the chloroplast division complex using *Schizosaccharomyces pombe* as a heterologous expression system. *Microsc. Microanal.* **22**, 275–289 (2016).
39. Anderson, J. L., Lowell, M. E. & Prieve, D. C. Motion of a particle generated by chemical gradients. Part 1. Non-electrolytes. *J. Fluid Mech.* **117**, 107–121 (1982).
40. Prieve, D. C., Anderson, J. L. & Lowell, M. E. Motion of a particle generated by chemical gradients. Part 2. Electrolytes. *J. Fluid Mech.* **148**, 247–269 (1984).
41. Prieve, D. C., Malone, S. M., Khair, A. S., Stout, R. F. & Kanj, M. Y. Diffusiophoresis of charged colloidal particles in the limit of very high salinity. *Proc. Natl Acad. Sci. USA* **116**, 18257–18262 (2019).
42. Shin, S. et al. Size-dependent control of colloid transport via solute gradients in dead-end channels. *Proc. Natl Acad. Sci. USA* **113**, 257–261 (2016).
43. Paustian, J. S. et al. Direct measurements of colloidal solvophoresis under imposed solvent and solute gradients. *Langmuir* **31**, 4402–4410 (2015).
44. Illien, P., Golestanian, R. & Sen, A. 'Fuelled' motion: phoretic motility and collective behaviour of active colloids. *Chem. Soc. Rev.* **46**, 5508–5518 (2017).
45. Abécassis, B., Cottin-Bizonne, C., Ybert, C., Ajdari, A. & Bocquet, L. Boosting migration of large particles by solute contrasts. *Nat. Mater.* **7**, 785–789 (2008).
46. Palacci, J., Abécassis, B., Cottin-Bizonne, C., Ybert, C. & Bocquet, L. Colloidal motility and pattern formation under rectified diffusiophoresis. *Phys. Rev. Lett.* **104**, 138302 (2010).
47. Marbach, S. & Bocquet, L. Osmosis, from molecular insights to large-scale applications. *Chem. Soc. Rev.* **48**, 3102–3144 (2019).
48. Shi, N., Nery-Azevedo, R., Abdel-Fattah, A. I. & Squires, T. M. Diffusiophoretic focusing of suspended colloids. *Phys. Rev. Lett.* **117**, 258001 (2016).
49. Golestanian, R. Phoretic active matter. Preprint at <https://arxiv.org/pdf/1909.03747v3.pdf> (2019).
50. Duncan, J. B. & Toor, H. L. An experimental study of three component gas diffusion. *AIChE J.* **8**, 38–41 (1962).
51. Krishna, R. & Wesselingh, J. A. The Maxwell–Stefan approach to mass transfer. *Chem. Eng. Sci.* **52**, 861–911 (1997).
52. Agudo-Canalejo, J., Illien, P. & Golestanian, R. Phoresis and enhanced diffusion compete in enzyme chemotaxis. *Nano Lett.* **18**, 2711–2717 (2018).
53. Adeleke-Larodo, T., Agudo-Canalejo, J. & Golestanian, R. Chemical and hydrodynamic alignment of an enzyme. *J. Chem. Phys.* **150**, 115102 (2019).
54. Banigan, E. J., Gelbart, M. A., Gitai, Z., Wingreen, N. S. & Liu, A. J. Filament depolymerization can explain chromosome pulling during bacterial mitosis. *PLoS Comput. Biol.* **7**, e1002145 (2011).
55. Sear, R. P. Diffusiophoresis in cells: a general nonequilibrium, nonmotor mechanism for the metabolism-dependent transport of particles in cells. *Phys. Rev. Lett.* **122**, 128101 (2019).
56. Gerganova, V. et al. Cell patterning by secretion-induced plasma membrane flows. Preprint at [bioRxiv](https://doi.org/10.1101/2020.12.18.423457) <https://doi.org/10.1101/2020.12.18.423457> (2020).
57. Yang, Y. & Wu, M. Rhythmicity and waves in the cortex of single cells. *Phil. Trans. R. Soc. B* **373**, 20170116 (2018).
58. Hyman, A. A., Weber, C. A. & Jülicher, F. Liquid–liquid phase separation in biology. *Annu. Rev. Cell Dev. Biol.* **30**, 39–58 (2014).

Publisher's note Springer Nature remains neutral with regard to jurisdictional claims in published maps and institutional affiliations.



Open Access This article is licensed under a Creative Commons Attribution 4.0 International License, which permits use, sharing, adaptation, distribution and reproduction in any medium or format, as long as you give appropriate credit to the original author(s) and the source, provide a link to the Creative Commons license, and indicate if changes were made. The images or other third party material in this article are included in the article's Creative Commons license, unless indicated otherwise in a credit line to the material. If material is not included in the article's Creative Commons license and your intended use is not permitted by statutory regulation or exceeds the permitted use, you will need to obtain permission directly from the copyright holder. To view a copy of this license, visit <http://creativecommons.org/licenses/by/4.0/>.

© The Author(s), under exclusive licence to Springer Nature Limited 2021

Methods

Theoretical description in the presence of travelling waves. We have formulated our theory, equation (1), in terms of particle fluxes. Given these fluxes \mathbf{j}_i , the spatiotemporal dynamics of each molecular species is determined by the balance equation

$$\partial_t c_i + \nabla \cdot \mathbf{j}_i = r_i(\dots), \quad (4)$$

where r_i signify reaction terms. We considered two species, passive cargo molecules c_g that do not engage in reactions, $r_g = 0$, and active MinD proteins c_p . Instead of considering specific reaction terms, we assumed that the interplay between diffusive and reactive fluxes of MinDE leads to travelling waves. Then, we took these travelling MinD protein waves with wavelength λ and speed v :

$$c_p(x, t) = c_p\left(2\pi \frac{x - vt}{\lambda}\right) \equiv c_p(z) \quad (5)$$

as a given. As specific waveform, we assumed a skewed sinusoidal curve (Fig. 5b):

$$c_p(z) = \frac{2}{\pi\gamma} \arctan\left[\frac{\gamma \cos z}{1 - \gamma \sin z}\right], \quad (6)$$

where the parameter $\gamma \in [-1, \dots, 1]$ determines the 'skewness' of the waveform. In principle, we could also choose a different waveform (for example, a sinusoidal curve that is skewed in the opposite direction). Choosing a different waveform does not change the general result of a macroscopic net transport along the wavevector, but it can change the magnitude of the transport because the local gradient magnitude is affected.

Furthermore, for simplicity, we neglected membrane saturation effects (Supplementary Information), so that the chemical potential of a particle with size a_i reduces to $\mu_i \approx k_B T \ln(a_i c_i)$. This is the same assumption as in the derivation of the fitting function for the stationary patterns, equation (3), and hence has the same limitations at high particle densities. Taken together, the spatiotemporal dynamics of the passive cargo species is determined by the following transport equation:

$$\partial_t c_g = -\nabla \cdot \mathbf{j}_g = \nabla \cdot \left[D_g \frac{(1 + c_g/c_p) \nabla c_g + (c_g/c_p) \nabla c_p}{1 + c_g/c_p + (D_g/D_p)(c_g/c_p)} \right], \quad (7)$$

where the interaction density is given by $c_i = \xi_i/\zeta_i$ and the two diffusion coefficients are given by $D_g = k_B T/\xi_g$ and $D_p = k_B T/\xi_p$. We used FEniCS⁵² to numerically solve equation (7) in a one-dimensional geometry with no-flux boundary conditions for the cargo.

Plasmids, strains and proteins. A list of all plasmids and primers is provided in Supplementary Tables 2 and 3. The plasmids pET28a-His-MinD_MinE¹³, pET28a-His-EGFP-MinD⁶⁰, pET28a-His-MinE¹³ and pET28a-MinE-His¹⁶ were used for purification of His-MinD, His-EGFP-MinD, His-MinE and MinE-His, respectively, as described in detail previously⁶¹. In brief, proteins were expressed in *E. coli* BL21 (DE3) and then purified via Ni-NTA affinity and size-exclusion chromatography in storage buffer (50 mM HEPES/KOH pH 7.2, 150 mM KCl, 10% glycerol, 0.1 mM EDTA, 0.4 mM tris(2-carboxyethyl)phosphine (TCEP)). Proteins were snap-frozen in liquid nitrogen and stored in small aliquots until further use at -80°C .

Plasmids for heterologous co-expression of MinD, MinE and model peripheral membrane proteins pREP41X-sfGFP-MinD, pREP42X-MinE, pREP41X_coex_sfGFP-MinD_MinE, pREP42X-mCherry-BsMTS, pREP42X-mCherry and pREP42X-mCherry-BsMTS were constructed analogously to plasmids devised by Terbush and colleagues³⁸. pREP41X and pREP42X, and the leucine and uracil auxotroph *S. pombe* strain FY61 [h- ura4-D18 leu1-32], were a kind gift from S. Forsburg, University of Southern California⁶². All constructs based on pREP41X and pREP42X express the respective proteins under the control of the inducible nmt1* promoter. For details see Supplementary Methods.

Reconstitution in *S. pombe*. Details of *S. pombe* culture and transformation are provided in the Supplementary Methods. For image acquisition, 5-ml cultures with selective medium were inoculated with the respective strains from glycerol stocks or plates and grown for 48–72 h at 30°C . Cover slides were rinsed with ethanol and ddH₂O, and further cleaned in a plasma cleaner with oxygen as the process gas. Subsequently, Grace Bio-LABs reusable culture well gaskets (diameter of 9 mm, GBL103240, Sigma-Aldrich) or sticky slides (#81818, ibidi) were attached to the clean cover slides. Poly-L-lysine solution (0.01%, P4707, Sigma-Aldrich) was added to the wells and incubated for more than 30 min. Wells were washed with the respective media once before 10–50 μl of cell suspension was added for microscopy at a constant room temperature of 23°C .

DNA origami nanostructures. The elongated DNA origami nanostructure used here was previously designed and described in ref. ²⁹. The 20-helix bundle with hexagonal lattice is based on the M13mp18 7,429-nucleotide-long scaffold plasmid (p7429; Bayou Biolabs) and was modified using CadNano⁶³. Staple oligonucleotides, 5'-Cy3B/Cy5-functionalized oligonucleotides, the

5'-cholesteryl-TEG functionalized oligonucleotides (high-purity, salt-free, Eurofins MWG Operon) and 5'-biotin-TEG functionalized oligonucleotides (Sigma-Aldrich) were purchased or diluted in Milli-Q ultrapure water at a concentration of 100 μM . Origami structures with 1–15 anchors were based on the previous design²⁹, which was further modified for functionalization with 42 anchors (Supplementary Fig. 5). The assembly of the origami structure was performed in a one-pot reaction mix as described previously²⁹. In brief, the components were mixed at a final concentration of 20 nM p7429 scaffold plasmid and 200 nM staple oligonucleotides in folding buffer (5 mM Tris-HCl, 1 mM EDTA, 20 mM MgCl₂, pH 8.0) and annealed in a thermocycler (Mastecycler) over a 41-h cooling scheme from 65 to 40°C . Folded nanostructures were purified to remove excess staple strands by centrifugation (14,000g, three cycles for 3 min, one cycle for 5 min) in Amicon Ultra 100kDa molecular weight cutoff filters (Merck Millipore) using reaction buffer (25 mM Tris-HCl pH 7.5, 150 mM KCl, 5 mM MgCl₂). The concentration of folded Cy5-labelled origami structures was estimated by fluorescence intensity measurements using a one-drop measurement unit of a Jasco FP-8500 spectrofluorometer and subsequent comparison with an intensity calibration curve obtained for free Cy5 dye corrected for the multiple labelling of the origami. Cy3B-labelled DNA origami concentration was measured by absorption at 260 nm on a NanoDrop spectrophotometer (ThermoFisher Scientific) and related to Cy5-labelled structures of known concentrations. Cy3B/Cy5-labelled DNA origami structures contained seven Cy3B/Cy5-labelled oligonucleotides attached to extended staples on the upper facet. At the lower facet, the biotin-functionalized origami contained multiple 18-nucleotide (nt) extensions that were hybridized with complementary 5' biotin-TEG-functionalized oligonucleotides (5' biotin-TEG-AACCAGACCACCCATAGC) at defined positions. DNA origami that were bound to the membrane via cholesteryl oligonucleotides contained single or multiple 18-nt extensions on the lower facet that can hybridize with the complementary 5' TEG-cholesteryl-functionalized oligonucleotides (5' chol-TEG-AACCAGACCACCCATAGC) supplied in the self-organization assay.

Preparation of SLBs. SLBs were prepared as described in detail in refs. ^{13,61}. In brief, cover slides were rinsed with ddH₂O and ethanol, and a plastic chamber was glued on top. Slides were further cleaned by plasma cleaning with oxygen as the process gas (model Zepto, Diener Electronic). Chloroform-dissolved lipids (Avanti Polar Lipids) were dried by a nitrogen stream and subsequently in a desiccator before slow rehydration at a concentration of 4 mg ml⁻¹ in reaction buffer (25 mM Tris-HCl pH 7.5, 150 mM KCl, 5 mM MgCl₂). Small unilamellar vesicles were generated by sonication in a bath sonicator and subsequently added to the cleaned reaction chambers at a concentration of 0.5 mg ml⁻¹. After 4 min of incubation on a 37°C warm heating block, the SLB was washed 10 times with a total of 2 ml of wash buffer (25 mM Tris-HCl pH 7.5, 150 mM KCl) to remove excess vesicles. All mentioned concentrations refer to the final volume of the reaction chamber of 200 μl . To prepare chambers for self-organization experiments with biotin-functionalized origami, the SLB was generated with a lipid composition of 69/30/1 mol% DOPC/DOPG/biotinyl-CAP-PE or with 70/30/0.01 mol% DOPC/DOPG/biotinyl-CAP-PE for single-particle tracking experiments and subsequently incubated with non-labelled or Alexa568-labelled streptavidin (ThermoFisher Scientific) at a final concentration of 1 $\mu\text{g ml}^{-1}$. After incubation for 5–10 min, unbound streptavidin was removed by washing five times with a total volume of 1 ml of reaction buffer. The buffer was adjusted to a volume of 100 μl and the origami was incubated at a final concentration of 0.1 nM for 10 min, before the buffer was adjusted to the final volume of 200 μl . To prepare chambers for self-organization experiments with cholesteryl-bound origami, the SLB was generated with a lipid composition of 70/30 mol% DOPC/DOPG. The buffer was adjusted to a volume of 100 μl and the 5' TEG-cholesteryl-functionalized oligonucleotides for binding were added at a final concentration of 10 nM. Subsequently, the origami was added at a final concentration of 0.1 nM and incubated for 10 min, before buffer adjustment to 200 μl . For experiments involving more than one type of DNA origami, DNA origami species were premixed in DNA LoBind tubes (Eppendorf) before addition to the sample chamber at a final concentration of 50 pM for each DNA origami, keeping the overall DNA origami concentration at 0.1 nM. Note that at these experimental conditions, DNA origami does not bind non-specifically to the lipid membrane in the absence of biotin-TEG-anchors/streptavidin or cholesteryl-TEG-anchors, due to the high net negative charge of both the SLB and DNA origami^{64,65}.

Chromium-patterned cover slides. Chromium-patterned cover slides for patterned SLBs^{66,67} were generated by photolithography and metal evaporation. Cover slides were first cleaned by rinsing with pure ethanol and ddH₂O and subsequently by plasma cleaning with oxygen as the process gas (model Zepto, 20–60 s, 40–50% power and 0.3 mbar). The vapour of bis(trimethylsilyl)amine (HDMS) was deposited on the cover slide for 2 min as adhesion promoter. Subsequently, positive photoresist (AZ ECI 3027, MicroChemicals) was spin-coated onto the cover slide (40 s, 4,000 r.p.m., start/stop acceleration 2,000 r.p.m. s⁻¹) resulting in an $\sim 3\text{-}\mu\text{m}$ -thick layer of photoresist. After pre-baking (90 s, 90°C) the photoresist was patterned using ultraviolet lithography ($\mu\text{PG}101$, Heidelberg Instruments) with a 10-mm write head, nominal output power

of 35 mW at a wavelength of 375 nm, before passing a 45% attenuation filter. Afterwards, the slides were post baked (60 s, 110°C) before applying developer (AZ 351B, NaOH-based, diluted 1:4 (vol/vol), MicroChemicals) for 4 min. Finally, slides were rinsed with ddH₂O and dried with a nitrogen stream. Chromium was deposited onto these slides by evaporation at 22–33 mA at a rate of $\sim 1 \text{ \AA s}^{-1}$ to a final thickness of $\sim 30 \text{ nm}$. After chromium deposition, the photoresist was lifted off in acetone with sonication for 5 min in a sonicator bath. Afterwards, slides were rinsed with isopropanol and dried with a nitrogen stream. SLBs were formed on the chromium-patterned slides as described above.

Self-organization assay. Self-organization assays were performed essentially as described in detail in ref. ⁶¹. In short, they were performed on preformed SLBs in 200 μl of reaction buffer (25 mM Tris-HCl pH 7.5, 150 mM KCl, 5 mM MgCl₂) supplemented with 2.5 mM Mg-ATP (stock: 100 mM ATP, in 100 mM MgCl₂, adjusted to pH 7.5) and at a constant room temperature of 23 °C. MinD was typically used at 1 μM (0.3 μM EGFP-MinD, 0.7 μM MinD) with either 1.5 μM MinE-His⁶² to generate quasi-stationary labyrinth patterns or 5 μM His-MinE²¹³ to generate regular travelling surface waves. Time series showing the initial development of patterns were acquired by starting the self-organization with Mg-ATP directly before image acquisition. Tile scans used for quantification of quasi-stationary patterns or gradients induced by regular travelling waves on unconstrained and patterned SLBs were acquired 30–60 min after the start of self-organization, in areas of the chamber that had not been imaged previously.

Single-particle tracking. Single-particle tracking of DNA origami was conducted at a concentration of DNA origami and anchors that can be described as diluted, so that interaction between individual DNA origami was minimized⁶³. DNA origami was diluted in DNA LoBind tubes (Eppendorf) and added to a chamber at a final concentration of 0.1–1 pM (biotin-functionalized origami, SLB with 70/30/0.01 mol% DOPC/DOPG/biotinyl-CAP-PE; cholesterol-functionalized origami, SLB with 70/30 mol% DOPC/DOPG, 0.1 nM 5' TEG-cholesterol-functionalized oligonucleotides). Owing to the superior brightness and photostability, single-particle tracking was exclusively performed using Cy3B-labelled DNA origami. To further reduce photobleaching and blinking as well as photopolymerization of MinD, single-particle tracking was performed in the presence of an oxygen scavenger system (3.7 U ml⁻¹ pyranose oxidase, 90 U ml⁻¹ catalase, 0.8% glucose)⁶⁴ and trolox. Experiments were performed in the absence of any protein or in the presence of 1 μM MinD (30% EGFP-MinD) and 2.5 mM ATP to emulate conditions in the MinD maxima in a simplified fashion. For single-particle tracking of cargo in the presence of MinDE travelling waves, 1 μM MinD (30% EGFP-MinD) and 5 μM His-MinE were used and tracking was performed more than 30 min after starting the reaction with 2.5 mM ATP to obtain regular waves.

Microscopy. All images, except for single-particle tracking, were taken on a Zeiss LSM780 confocal laser scanning microscope using a Zeiss C-Apochromat $\times 40/1.20$ water-immersion objective, $\times 20$ air objective for chromium-patterned SLBs or $\times 60/1.4$ differential interference contrast (DIC) oil-immersion objective for *S. pombe* cells (all Carl Zeiss). Longer time series were acquired using the built-in autofocus system. All two- or three-colour images were acquired with alternating illumination for the 488/633 nm and 561 nm laser lines to avoid crosstalk. EGFP-MinD or sfGFP-MinD was excited using a 488 nm argon laser; Cy3B-labelled origami, Alexa568-streptavidin or mCherry in *S. pombe* were excited using a 561 nm diode-pumped solid-state (DPSS) laser and Cy5-labelled origami using a 633 nm He-Ne laser. Images were typically recorded with a pinhole size of 2.6–4 Airy units for the EGFP and origami channels, 1 Airy unit for the streptavidin channel, 512 \times 512-pixel resolution and a pixel dwell time of 1.27 μs . Time series were typically acquired with ~ 14 -s intervals for unconstrained SLBs or 4-s intervals for chromium-patterned SLBs and *S. pombe* cells. For single-particle tracking of DNA, origami images were acquired on a custom-built total internal reflection fluorescence microscope (TIRFM)⁶⁵ using a NIKON SR Apo TIRF $\times 100/1.49$ oil-immersion objective, constructed around a Nikon Ti-S microscope body (both Nikon). Two laser lines (490 nm (Cobolt Calypso, 50 mW nominal) and 561 nm (Cobolt Jive, 50 mW nominal), Cobolt AB)) were controlled in power and timing (AOTE, Gooch & Housego TF-525-250) and spatially filtered (kineFLEX-P-3-S-405.640-0.7-FCS-P0, Qioptiq). The beam was further collimated, expanded (10 \times) and focused on the objective's back aperture by standard achromatic doublet lenses. The TIRF angle was controlled by precise parallel offset of the excitation beam (Q545, PI). The emission light was notch-filtered to remove residual excitation light, spectrally separated by a dichroic beamsplitter (T555lpxr-UF1, Chroma Technology Cooperation), bandpass-filtered 525/50 and 593/46 (both Chroma), respectively, and repositioned on two halves of the electron-multiplying charge-coupled device (EMCCD) camera (Andor iXon Ultra 897, Andor Technologies). Images were recorded with Andor Solis software (version 4.28, Andor Technologies).

Image analysis. All images were processed using Fiji (version v1.52p), MATLAB (R2018a, The Math-Works) or Python (Python Software Foundation). Brightness or contrast adjustments of all displayed images were applied homogeneously.

For line plots, the images were smoothed with a Gaussian filter with pixel width of 2 in Fiji.

For the cross-correlation plots, the images were smoothed with a Gaussian kernel of pixel width 1. The theoretical models were formulated as boundary-value problems and solved in a one-dimensional geometry using a finite-difference scheme using SciPy⁷¹. Curve fitting was performed with lmfit⁷².

Single-particle tracking analysis. Analysis of single-particle tracking was conducted as described previously using previously established code⁷³. In brief, a custom-written MATLAB code was used to detect DNA origami fluorescence in each frame and extract its position. Origami trajectories on the membrane were analysed using jump-distance analysis^{74,75}. The distances between particle locations between subsequent frames were analysed and diffusion coefficients of particle ensembles were obtained by fitting the cumulative histograms. As, usually, some of the origami in the field of view were immobile and did not diffuse, cumulative histograms of obtained jump distances were fitted with two components, where for the second component the upper boundary was set to $0.1 \mu\text{m}^2 \text{ s}^{-1}$, and usually resulted in diffusion coefficients of less than $0.01 \mu\text{m}^2 \text{ s}^{-1}$.

Analysis of MinDE-dependent transport. Analysis of fluorescence intensities and contrast was essentially performed as described earlier⁷⁶. In brief, tile scans were imported into Fiji, where the EGFP-MinD channel was used for segmentation to generate a binary mask of the patterns. The original non-modified images from the two or three spectral channels were analysed based on the binary mask using a custom-written MATLAB code. The average fluorescence intensity in the Alexa568-streptavidin or origami-Cy5 and EGFP-MinD spectral channel was obtained by pooling the means of individual images from one independent experiment. All means from one independent experiment and condition were pooled together. All fluorescence intensity values from one experimental set were normalized to the fluorescence intensity values obtained for the respective origami with one anchor. The Michelson contrast of the resulting cargo patterns was calculated for every individual image as the difference between the average intensity in the MinD minima and MinD maxima divided by the sum of the average intensities in the MinD maxima and minima. The contrast of the MinD patterns was calculated for every individual image as the difference between the average intensity in the MinD maxima and MinD minima divided by the sum of the average intensities in the MinDE minima and maxima.

Analysis of fluorescence profiles on chromium-patterned SLBs. Time-series from chromium-patterned SLB patches with regular travelling MinDE waves that aligned along the longest axis of the patch were selected and averaged in Fiji. The resulting average intensity of the cargo was plotted along the wavevector of the MinDE waves (that is, the longest axis of the patch) and exported as csv files. Subsequently, using MATLAB, the fluorescence intensity profiles were aligned at the beginning based on the increase of the signal, and the average profile was generated.

Reporting Summary. Further information on research design is available in the Nature Research Reporting Summary linked to this Article.

Data availability

The raw images that support the findings of this study are available at Edmond with the identifier <https://dx.doi.org/10.17617/3.5n> or from the corresponding authors upon request. Source data are provided with this paper.

Code availability

The code for the analysis is available at Edmond with the identifier <https://dx.doi.org/10.17617/3.5n> or from the corresponding authors upon request.

References

- Logg, A., Mardal, K. A. & Wells, G. N. *Automated Solution of Differential Equations by the Finite Element Method* (Springer, 2012).
- Zieske, K., Schweizer, J. & Schwille, P. Surface topology assisted alignment of Min protein waves. *FEBS Lett.* **588**, 2545–2549 (2014).
- Ramm, B., Glock, P. & Schwille, P. In vitro reconstitution of self-organizing protein patterns on supported lipid bilayers. *J. Vis. Exp.* **137**, 58139 (2018).
- Forsburg, S. L. Comparison of *Schizosaccharomyces pombe* expression systems. *Nucleic Acids Res.* **21**, 2955–2956 (1993).
- Douglas, S. M. et al. Rapid prototyping of 3D DNA-origami shapes with caDNA. *Nucleic Acids Res.* **37**, 5001–5006 (2009).
- Czogalla, A. et al. Switchable domain partitioning and diffusion of DNA origami rods on membranes. *Faraday Discuss.* **161**, 31–43 (2013).
- Khmelnikskaya, A., Mücksch, J., Petrov, E. P., Franquelim, H. G. & Schwille, P. Control of membrane binding and diffusion of cholesterol-modified DNA origami nanostructures by DNA spacers. *Langmuir* **34**, 14921–14931 (2018).
- Groves, J. T., Ulman, N. & Boxer, S. G. Micropatterning fluid lipid bilayers on solid supports. *Science* **275**, 651–653 (1997).
- Groves, J. T., Ulman, N., Cremer, P. S. & Boxer, S. G. Substrate-membrane interactions: mechanisms for imposing patterns on a fluid bilayer membrane. *Langmuir* **14**, 3347–3350 (1998).

ARTICLES

NATURE PHYSICS

68. Czogalla, A., Kauert, D. J., Seidel, R., Schwille, P. & Petrov, E. P. DNA origami nanoneedles on freestanding lipid membranes as a tool to observe isotropic-nematic transition in two dimensions. *Nano Lett.* **15**, 649–655 (2015).
69. Swoboda, M. et al. Enzymatic oxygen scavenging for photostability without pH drop in single-molecule experiments. *ACS Nano* **6**, 6364–6369 (2012).
70. Mücksch, J. et al. Quantifying reversible surface binding via surface-integrated fluorescence correlation spectroscopy. *Nano Lett.* **18**, 3185–3192 (2018).
71. Virtanen, P. et al. SciPy 1.0: fundamental algorithms for scientific computing in Python. *Nat. Methods* **17**, 261–272 (2020).
72. Newville, M. et al. lmfit/lmfit-py 1.0.0 (2019); <https://doi.org/10.5281/ZENODO.3588521>
73. Weimann, L. et al. A quantitative comparison of single-dye tracking analysis tools using Monte Carlo simulations. *PLoS ONE* **8**, e64287 (2013).
74. Schütz, G. J., Schindler, H. & Schmidt, T. Single-molecule microscopy on model membranes reveals anomalous diffusion. *Biophys. J.* **73**, 1073–1080 (1997).
75. Kues, T., Peters, R. & Kubitscheck, U. Visualization and tracking of single protein molecules in the cell nucleus. *Biophys. J.* **80**, 2954–2967 (2001).

Acknowledgements

We thank P. Altpeter (CeNS Munich) for supporting us with the fabrication of chromium-patterned slides. We thank MPIB Core Facility for assistance in protein purification and S. Forsburg (University of Southern California) for supplying *S. pombe* strains and plasmids. We further thank F. Brauns, H. Franquelim and J. Mücksch for helpful discussions. We acknowledge financial support by the German Research Foundation (DFG) through TRR 174 (Project ID No. 269423233) and SFB1032 (Project ID No. 201269156) and the Excellence Cluster ORIGINS under Germany's Excellence

Strategy (EXC-2094-390783311). B.R., A.K. and A.G. were supported by a DFG fellowship through the Graduate School of Quantitative Biosciences Munich (QBM). P.S. acknowledges the support of the research network MaxSynBio via a joint funding initiative of the German Federal Ministry of Education and Research (BMBF) and the Max Planck Society.

Author contributions

B.R., A.G., E.F. and P.S. conceived the study. A.G. and E.F. designed the theoretical analysis. A.G. conducted the theoretical analysis. B.R., A.K. and P.B. designed experiments. B.R. performed all experiments. A.K. designed DNA origami. A.K. and B.R. prepared origami. H.E. and B.R. fabricated chromium-patterned slides. K.A.G. developed single-particle tracking code. B.R., A.G., P.B. and K.A.G. analysed data. B.R., A.G., E.F. and P.S. wrote the manuscript. All authors discussed and interpreted the results and revised the manuscript.

Competing interests

The authors declare no competing interests.

Additional information

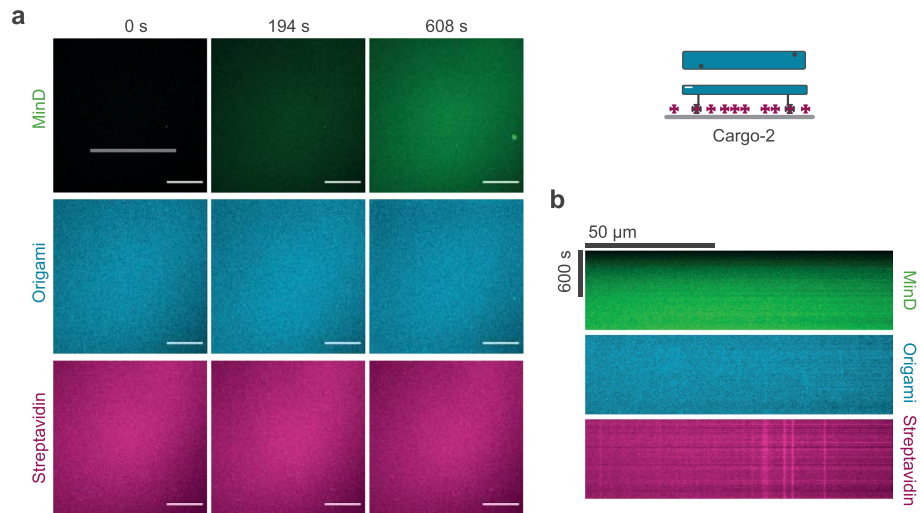
Extended data is available for this paper at <https://doi.org/10.1038/s41567-021-01213-3>.

Supplementary information The online version contains supplementary material available at <https://doi.org/10.1038/s41567-021-01213-3>.

Correspondence and requests for materials should be addressed to E.F. or P.S.

Peer review information *Nature Physics* thanks Jodi Camberg and the other, anonymous, reviewer(s) for their contribution to the peer review of this work.

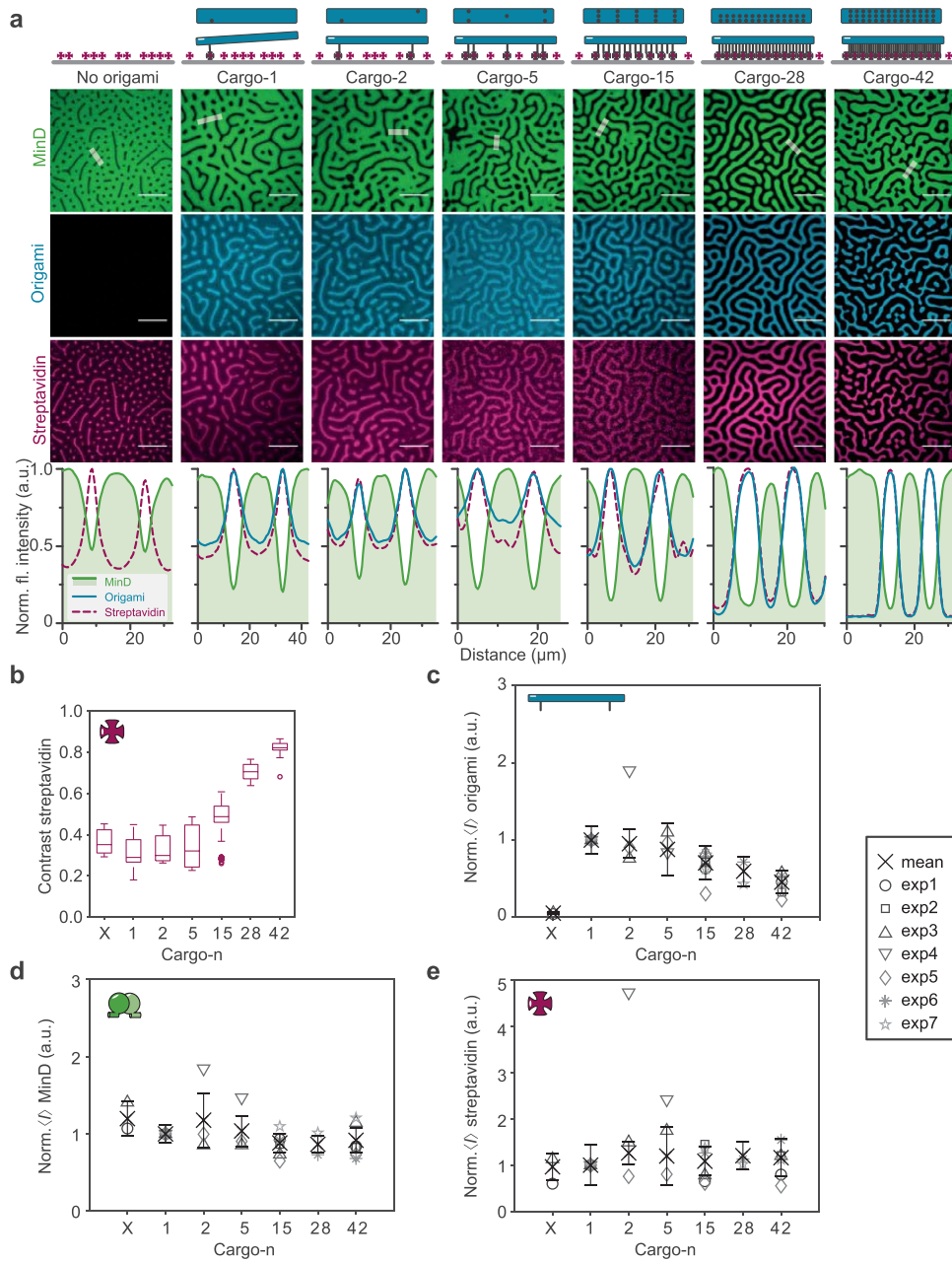
Reprints and permissions information is available at www.nature.com/reprints.



Extended Data Fig. 1 | Pattern formation of cargo depends on active self-organization by MinDE. **a**, Representative time series of MinD membrane binding on SLBs in the presence of cargo-2 and ATP, but in the absence of MinE (1 μ M MinD (30% EGFP-MinD), 0.1 nM origami-Cy5 with 2 biotinylated oligonucleotides, Alexa568-streptavidin, ATP). Scale bars, 50 μ m. **b**, Kymographs of the line selection indicated in **a**.

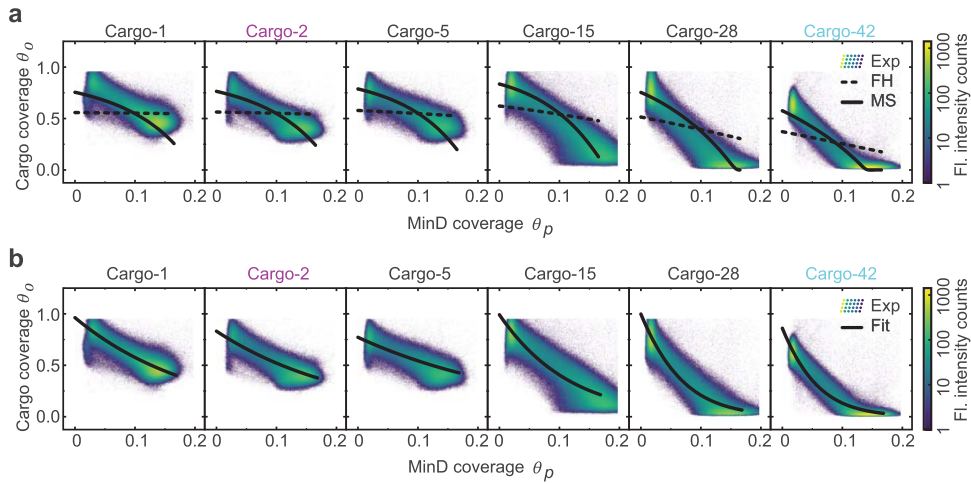
ARTICLES

NATURE PHYSICS

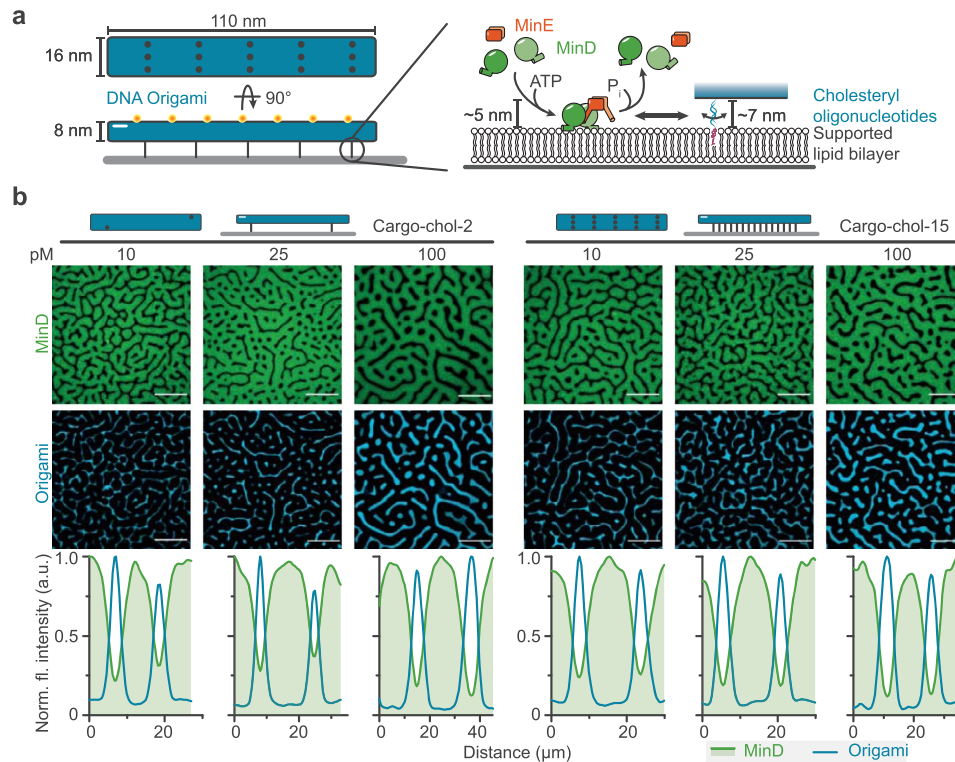


Extended Data Fig. 2 | See next page for caption.

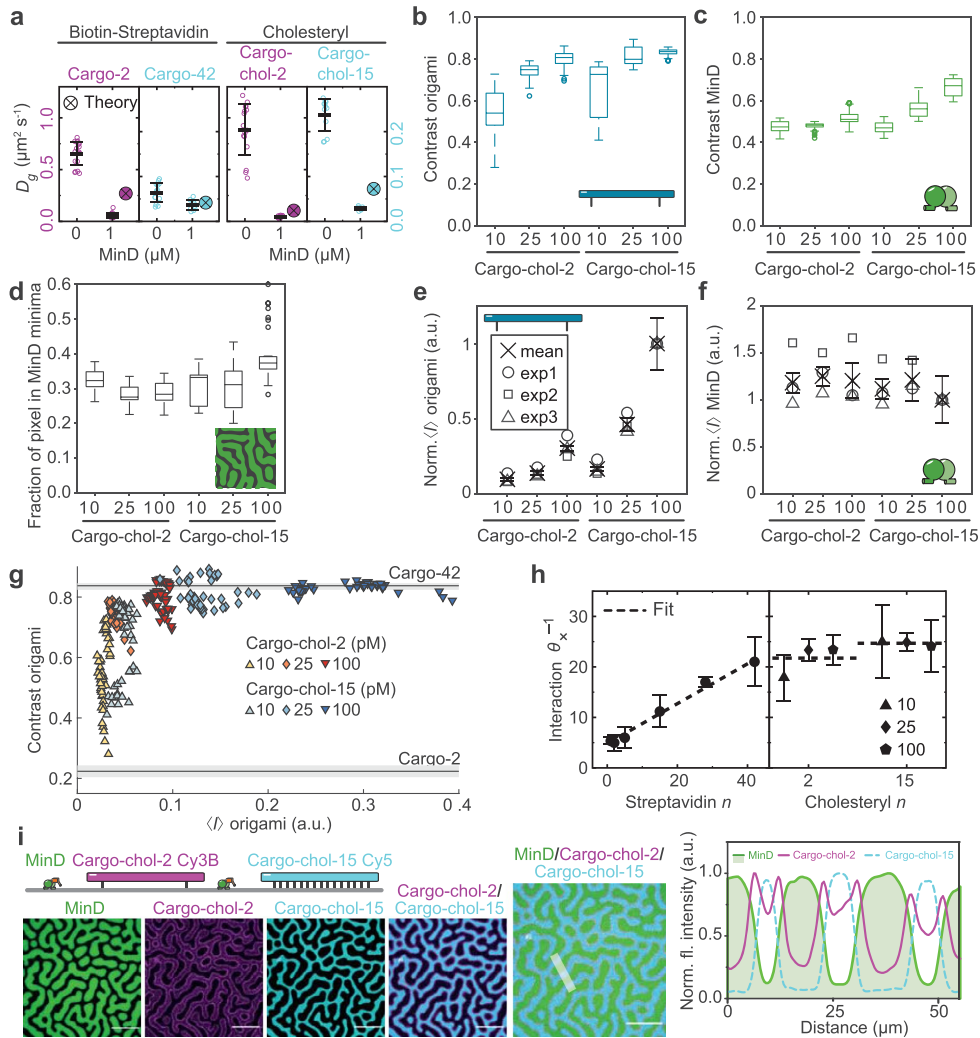
Extended Data Fig. 2 | Extent of the MinDE-driven cargo demixing depends on the effective size (that is, membrane footprint) of the cargo. a, Representative images and fluorescence intensity line plots (smoothed) of established MinDE labyrinth patterns and anti-correlated DNA origami and streptavidin patterns when no origami or cargo-1, cargo-2, ..., cargo-42 is present (1 μ M MinD (30% EGFP-MinD), 1.5 μ M MinE-His, with or without 0.1 nM origami-Cy5 with n biotinylated oligonucleotides, Alexa568-streptavidin). Panels "no origami, cargo-2, cargo-15 and cargo-42" are identical to Fig. 1d. Scale bars, 50 μ m. **b**, Contrast of the resulting streptavidin patterns increases with increasing number of streptavidin incorporated into the cargo. Box plot lines are median, box limits are quartiles 1 and 3, whiskers are 1.5x interquartile range (IQR) and points are outliers. Mean fluorescence intensity of **c**, DNA origami, **d**, EGFP-MinD and **e**, Alexa568-streptavidin of patterns formed when no origami or cargo-1, cargo-2, ..., cargo-42 is present; data is taken from the full image and normalised to the intensity of experiments containing cargo-1. Cross and error bars represent the mean value and standard deviation of two or more independent experiments with total number of analysed images per condition N(No origami)=32, N(Cargo-1)=96, N(Cargo-2)=41, N(Cargo-5)=32, N(Cargo-15)=94, N(Cargo-28)=32, N(Cargo-42)=87.



Extended Data Fig. 3 | Comparison between theory and experiment for different cargo molecules. a, Cross-correlation function between MinD coverage (θ_p) and DNA origami coverage (θ_o), for different cargo species. The color-coded 2D-histogram represents our experimental data of selected days (Exp), where the images were smoothed by a one-pixel-wide gaussian kernel. Solid and dashed lines correspond to two candidate models. The Flory-Huggins type model (FH), whose parameters are fully determined by our experiments, fails to account for cargo transport: the weak entropic sorting of streptavidin in an external gradient of proteins is not sufficient to overcome the strong repulsion of the bulky DNA origami scaffolds. Instead, we find that the phenomenological MS-type model, with an estimated interaction parameter, explains cargo transport. Model parameters: (cargo- n) average coverages $\bar{\theta}_p = 0.0825$, $\bar{\theta}_s = \max(0.165 - 0.55n/70, 0)$ and $\bar{\theta}_o = \min(11.55/n, 0.55)$; interaction parameter (in terms of MinD coverage) $\theta_x^{-1} = 200 + 10n$. Surface coverages $\theta = ac$ and surface densities c are related via the particle size a . **b**, The color-coded 2D-Histogram represents our experimental data of selected days (Exp), while the solid line (Fit) is a fit curve of our reduced model (Supplementary Information section I.5 "Analytic solution and fitting of reduced model").



Extended Data Fig. 4 | MinDE induces pattern formation of cargo that is bound to the membrane via cholesteryl oligonucleotides. **a**, Schematic of the synthetic cargo consisting of a DNA origami scaffold that is bound to the membrane via cholesteryl moieties. DNA origami are bound via hybridization of DNA oligonucleotides at the indicated positions with the complementary TEG-cholesteryl oligonucleotides in the lipid membrane. **b**, Representative images and fluorescence intensity line plots (smoothed) of established MinDE labyrinth patterns and anti-correlated DNA origami patterns when 10, 25 or 100 pM of cargo-chol2 or cargo-chol-15 are present (1 μM MinD (30% EGFP-MinD), 1.5 μM MinE-His with 10, 25 or 100 pM origami-Cy3b with 2 or 15 hybridizing oligonucleotides, 10 nM TEG-cholesteryl oligonucleotide). Scale bars, 50 μm.

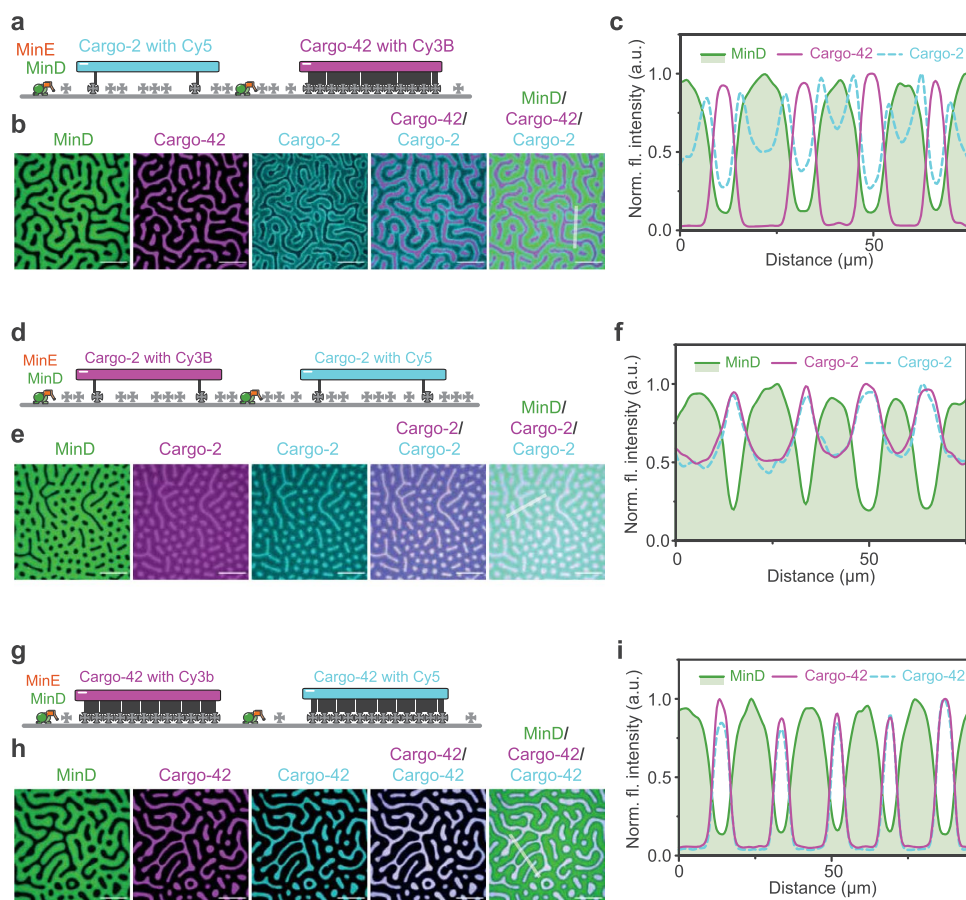


Extended Data Fig. 5 | See next page for caption.

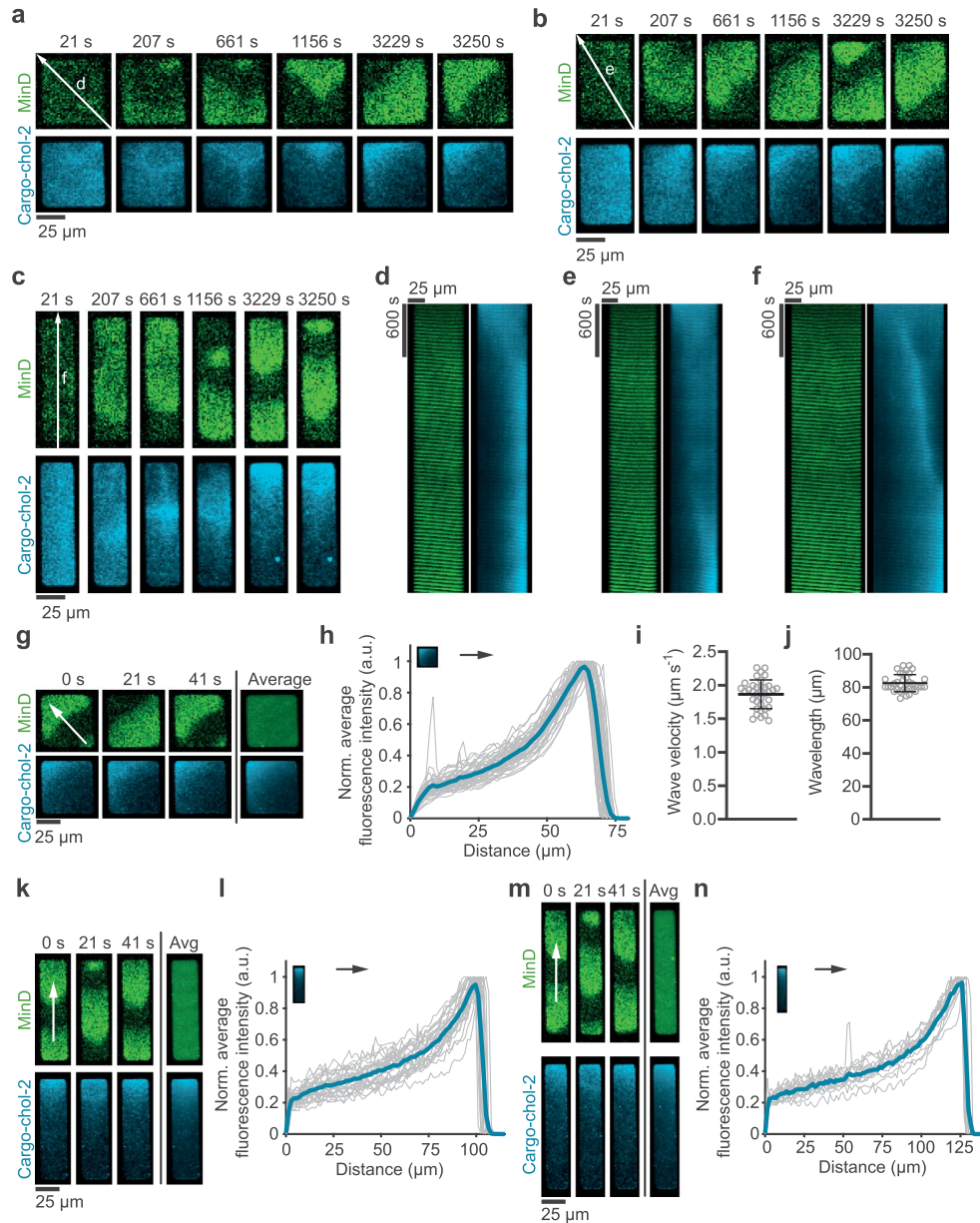
Extended Data Fig. 5 | MinDE-driven cargo demixing indeed depends on the effective size (membrane footprint) of the cargo and not on the diffusion coefficient. **a**, Cargo molecule diffusion coefficient in absence or presence of $1\ \mu\text{M}$ MinD (with or without $1\ \mu\text{M}$ MinD (30% EGFP-MinD), $0.1\text{-}1\ \text{pM}$ origami-Cy3b with 2 or 15 hybridizing oligonucleotides, $0.1\ \text{nM}$ TEG-cholesteryl oligonucleotide), as obtained from single particle tracking and predicted with the fitted interaction parameters obtained in **h**. Points are mean values of individual measurements (M), line and error bars represent the mean value and standard deviation. Left part identical to Fig. 3c. Data obtained from number of sample chambers $S(\text{Cargo-cho1-2})=7$, $S(\text{Cargo-cho1-15})=5$, $S(\text{Cargo-cho1-2, MinD})=3$, $S(\text{Cargo-cho1-15, MinD})=2$; number of measurements $M(\text{Cargo-cho1-2})=16$, $M(\text{Cargo-cho1-15})=12$, $M(\text{Cargo-cho1-2, MinD})=14$, $M(\text{Cargo-cho1-15, MinD})=6$; number of analysed single particle tracks $N(\text{Cargo-cho1-2})=19,647$, $N(\text{Cargo-cho1-15})=23,365$, $N(\text{Cargo-cho1-2, MinD})=1,879$, $N(\text{Cargo-cho1-15, MinD})=8,338$; average track-length $TL(\text{Cargo-cho1-2})=303$, $TL(\text{Cargo-cho1-15})=353$, $TL(\text{Cargo-cho1-2, MinD})=964$, $TL(\text{Cargo-cho1-15, MinD})=749$; fraction of mobile DNA origami $MF(\text{Cargo-cho1-2})=0.85$, $MF(\text{Cargo-cho1-15})=0.87$, $MF(\text{Cargo-cho1-2, MinD})=0.73$, $MF(\text{Cargo-cho1-15, MinD})=0.67$. Box plot of the contrast of **b**, cargo, **c**, MinD patterns, and **d**, of the fraction of pixels classified as MinD minima, when 10, 25 or 100 pM of cargo-cho1-2 or cargo-cho1-15 are present ($1\ \mu\text{M}$ MinD (30% EGFP-MinD), $1.5\ \mu\text{M}$ MinE-His with 10, 25 or 100 pM origami-Cy3b with 2 or 15 hybridizing oligonucleotides, $10\ \text{nM}$ TEG-cholesteryl oligonucleotide). Box plot lines are median, box limits are quartiles 1 and 3, whiskers are $1.5\times$ interquartile range (IQR) and points are outliers. Mean fluorescence intensity of **e**, DNA origami and **f**, EGFP-MinD of the full image, normalised to the intensity of experiments with 100 pM cargo-cho1-15. Cross and error bars represent the mean value and standard deviation. **g**, Increased membrane density leads to an apparent increase in contrast. Data from three independent experiments with total number of analysed images per condition $N(\text{Cargo-cho1-2, 10 pM})=48$, $N(\text{Cargo-cho1-2, 25 pM})=48$, $N(\text{Cargo-cho1-2, 100 pM})=64$, $N(\text{Cargo-cho1-15, 10 pM})=45$, $N(\text{Cargo-cho1-15, 25 pM})=48$, $N(\text{Cargo-cho1-15, 100 pM})=41$. Lines represent median and quartiles 1 and 3 of cargo-2 and cargo-42 contrast for comparison. **h**, Interaction parameter (in terms of MinD coverage; surface coverages $\theta = ac$ and surface densities c are related via the particle size a) as obtained from our fitting procedure. The interaction for cargo-cho1-2 and cargo-cho1-15 is larger than for cargo with streptavidin building blocks. Left part is identical to Fig. 3b. The dashed line indicates a linear fit of the interaction parameter θ_x^{-1} as a function of n . **i**, Representative images of individual and overlaid channels, and line plot of indicated selection of MinDE-induced sorting of cargo-cho1-2 and cargo-cho1-15 ($1\ \mu\text{M}$ MinD (30% EGFP-MinD), $1.5\ \mu\text{M}$ MinE-His with 50 pM origami-Cy3b with 2 and 50 pM origami-Cy5 with 15 hybridizing oligonucleotides, $10\ \text{nM}$ TEG-cholesteryl oligonucleotide). Scale bars, $50\ \mu\text{m}$.

ARTICLES

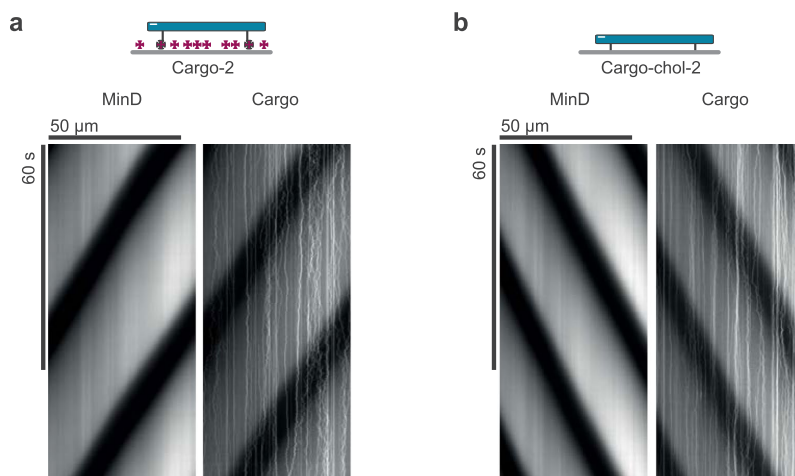
NATURE PHYSICS



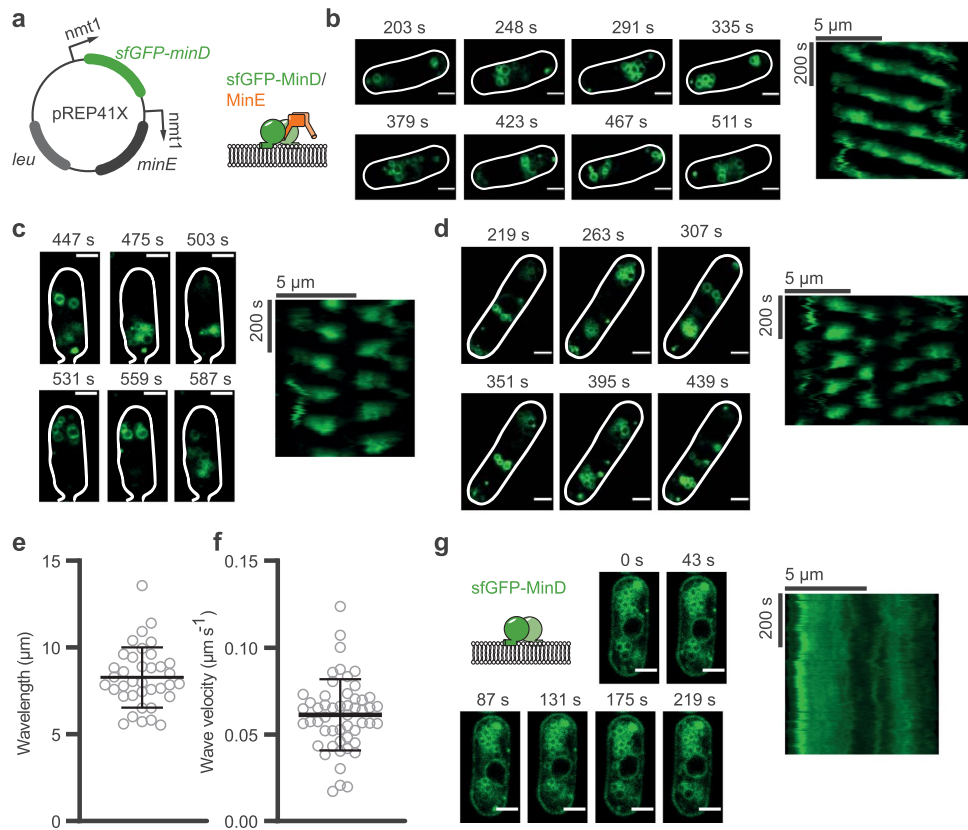
Extended Data Fig. 6 | The spatial sorting of cargo by MinDE according to the effective cargo size is not an artefact. **a-c**, Spatial sorting of cargo-2 and cargo-42 by MinDE also occurs when dyes are swapped. **a**, Schematic of the experimental setup. MinDE self-organization was performed in presence of two different cargo species with distinct fluorescent labels, cargo-2 with Cy5 and cargo-42 with Cy3B. **b**, Representative images and **c**, line plots of MinDE-induced sorting of cargo-2 and cargo-42 ($1\ \mu\text{M}$ MinD, $1.5\ \mu\text{M}$ MinE-His, $50\ \text{pM}$ origami-Cy5 with 2 biotinylated oligonucleotides, $50\ \text{pM}$ origami-Cy3B with 42 biotinylated oligonucleotides, non-labelled streptavidin). Experiment was performed three times under identical conditions. **d-i**, MinDE-induced distributions of differentially labelled, but otherwise identical cargo are superimposable. **d**, and **g**, Schematic of the experimental setup: two identical cargoes are labelled with distinct dyes. Pattern formation is induced by addition of MinDE ($1\ \mu\text{M}$ MinD, $1.5\ \mu\text{M}$ MinE-His, $50\ \text{pM}$ origami-Cy5 and $50\ \text{pM}$ origami-Cy3B with either both 2 or both 42 biotinylated oligonucleotides, non-labelled streptavidin). Representative images and line plot of pattern formation in presence of **e**, **f**, two differently labelled cargo-2 and **h**, **i**, two differently labelled cargo-42. Experiments were performed two times under identical conditions. Scale bars, $50\ \mu\text{m}$.



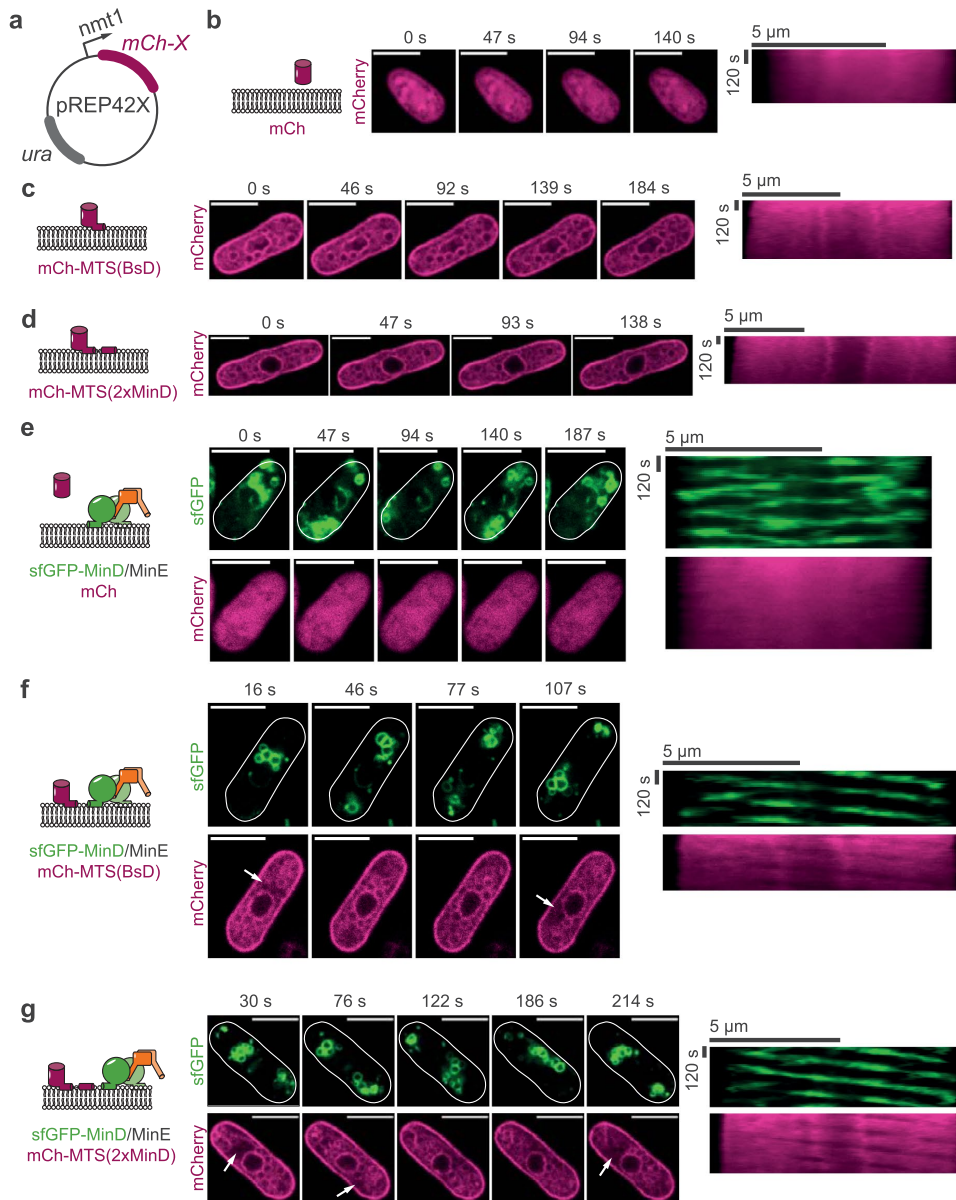
Extended Data Fig. 7 | Directed cargo transport by MinDE on chromium patterned bilayers. **a,b,c**, Representative time series and **d,e,f**, corresponding kymograph of MinDE traveling surface waves establishing cargo-chol-2 gradients from an initially homogeneous distribution on chromium patterned SLBs ($1\ \mu\text{M}$ MinD, $5\ \mu\text{M}$ His-MinE, $0.1\ \text{nM}$ origami-Cy3b with 2 hybridizing oligonucleotides, $10\ \text{nM}$ TEG-cholesteryl oligonucleotide). **g,k,m**, Representative time-series and average of MinDE traveling surface waves and cargo-chol-2 gradient along the wave vector after regular waves have formed (>30 minutes of incubation), along the longest axis on chromium-patterned bilayers for three geometries and **h,l,n**, the respective normalised average fluorescence intensity profiles of cargo along the wave vector in **g,k,m**. Bold, colored line represents the mean profile, generated from $N=44$, $N=27$ and $N=13$ membrane patches, respectively. **i**, Wave velocity and **j**, wavelength of MinDE waves on chromium patterned bilayers in presence of cargo-chol-2 or cargo-chol-15 with $N=52$ analysed membrane patches. Arrows indicate wave direction. Scale bars, $25\ \mu\text{m}$.



Extended Data Fig. 8 | No directed cargo movement can be observed on the single particle level. Representative kymographs of MinD waves and **a**, single cargo-2 and **b**, single cargo-chol-2 molecules in presence of regular directional MinDE travelling waves ($1\ \mu\text{M}$ MinD (30% EGFP-MinD), $5\ \mu\text{M}$ His-MinE, $0.1\text{-}1\ \text{pM}$ origami-Cy3b with 2 hybridizing oligonucleotides and $0.1\ \text{nM}$ TEG-cholesteryl oligonucleotide or with 2 biotinylated oligonucleotides, non-labelled streptavidin, SLB: DOPC/DOPG/Biotinyl-CAP-PE 70/30/0.01 mol%).



Extended Data Fig. 9 | MinDE self-organize in the fission yeast *S. pombe* at a similar spatiotemporal scale as in *E. coli*. **a**, Schematic of the plasmid employed for co-expression of sfGFP-MinD and MinE. **b-d**, Representative time-series and kymograph of *S. pombe* cells harbouring the co-expression plasmid for sfGFP-MinD and MinE, displaying MinD dynamics: **b**, travelling waves, **c**, pole-to-pole like oscillations and **d**, more complex dynamics. Analysis of **e**, the wavelength and **f**, wave velocity obtained from manually fitting the kymographs of cells displaying MinDE travelling waves. Lines represent the median and standard deviation. Data from three experiments with in total analysed cells **e**, $N = 37$ and **f**, $N = 52$. White boundaries represent cell outline obtained from average fluorescence images. **g**, No MinD dynamics can be observed when sfGFP-MinD is expressed in *S. pombe* in the absence of MinE. Scale bars, 2 µm.



Extended Data Fig. 10 | MinDE spatiotemporally regulate model peripheral membrane proteins when reconstituted in *S. pombe*. **a**, Schematic of the plasmid used for expression of mCherry versions in *S. pombe*. Representative time-lapse and kymographs (over the entire cell length) of *S. pombe* cells expressing **b**, soluble mCherry, mCh which remains cytoplasmic, or a model peripheral membrane protein **c**, mCh-MTS(BsD) and **d**, mCh-MTS(2xMinD) which bind to membranes. Representative time-lapse and kymographs of *S. pombe* cells heterologously expressing sfGFP-MinD, MinE and **e**, mCh or **f**, mCh-MTS(BsD) or **g**, mCh-MTS(2xMinD). MinDE self-organization spatiotemporally regulates the model peripheral membrane proteins mCh-MTS(BsD) and mCh-MTS(2xMinD) highlighted by white arrows, but not mCh. Panel g is identical to Fig. 5f. White boundaries represent cell outline obtained from average fluorescence images. Scale bars, 5 μ m.

Reporting Summary

Nature Research wishes to improve the reproducibility of the work that we publish. This form provides structure for consistency and transparency in reporting. For further information on Nature Research policies, see our [Editorial Policies](#) and the [Editorial Policy Checklist](#).

Statistics

For all statistical analyses, confirm that the following items are present in the figure legend, table legend, main text, or Methods section.

n/a Confirmed

- The exact sample size (n) for each experimental group/condition, given as a discrete number and unit of measurement
- A statement on whether measurements were taken from distinct samples or whether the same sample was measured repeatedly
- The statistical test(s) used AND whether they are one- or two-sided
Only common tests should be described solely by name; describe more complex techniques in the Methods section.
- A description of all covariates tested
- A description of any assumptions or corrections, such as tests of normality and adjustment for multiple comparisons
- A full description of the statistical parameters including central tendency (e.g. means) or other basic estimates (e.g. regression coefficient) AND variation (e.g. standard deviation) or associated estimates of uncertainty (e.g. confidence intervals)
- For null hypothesis testing, the test statistic (e.g. F , t , r) with confidence intervals, effect sizes, degrees of freedom and P value noted
Give P values as exact values whenever suitable.
- For Bayesian analysis, information on the choice of priors and Markov chain Monte Carlo settings
- For hierarchical and complex designs, identification of the appropriate level for tests and full reporting of outcomes
- Estimates of effect sizes (e.g. Cohen's d , Pearson's r), indicating how they were calculated

Our web collection on [statistics for biologists](#) contains articles on many of the points above.

Software and code

Policy information about [availability of computer code](#)

- Data collection
- Data analysis

For manuscripts utilizing custom algorithms or software that are central to the research but not yet described in published literature, software must be made available to editors and reviewers. We strongly encourage code deposition in a community repository (e.g. GitHub). See the Nature Research [guidelines for submitting code & software](#) for further information.

Data

Policy information about [availability of data](#)

All manuscripts must include a [data availability statement](#). This statement should provide the following information, where applicable:

- Accession codes, unique identifiers, or web links for publicly available datasets
- A list of figures that have associated raw data
- A description of any restrictions on data availability

The raw images that support the findings of this study are available at Edmond with the identifier <https://dx.doi.org/10.17617/3.5n> or from the corresponding author upon request.

Field-specific reporting

Please select the one below that is the best fit for your research. If you are not sure, read the appropriate sections before making your selection.

Life sciences Behavioural & social sciences Ecological, evolutionary & environmental sciences

For a reference copy of the document with all sections, see [nature.com/documents/nr-reporting-summary-flat.pdf](https://www.nature.com/documents/nr-reporting-summary-flat.pdf)

Life sciences study design

All studies must disclose on these points even when the disclosure is negative.

Sample size	No sample size was calculated. Due to the large magnitude of the observed effects, we assume that our sample size is adequate.
Data exclusions	Images were only excluded from analysis when supported lipid bilayers were defective or when the MinDE patterns were dynamic and not in the quasi-stationary state. For directed transport on chromium patterned membranes, membrane patches that did not show alignment of MinDE waves along the longest axis were excluded.
Replication	The numbers of experimental repeats are indicated in the respective figure legends. All experiments were performed at least in two or more independent experiments with at least one sample chamber each under the same conditions, so that the total sample number was always ≥ 2 .
Randomization	This study does not include work with participants or living organisms.
Blinding	This study does not include work with participants or living organisms.

Reporting for specific materials, systems and methods

We require information from authors about some types of materials, experimental systems and methods used in many studies. Here, indicate whether each material, system or method listed is relevant to your study. If you are not sure if a list item applies to your research, read the appropriate section before selecting a response.

Materials & experimental systems	Methods
n/a <input checked="" type="checkbox"/> Involved in the study	n/a <input checked="" type="checkbox"/> Involved in the study
<input checked="" type="checkbox"/> <input type="checkbox"/> Antibodies	<input checked="" type="checkbox"/> <input type="checkbox"/> ChIP-seq
<input checked="" type="checkbox"/> <input type="checkbox"/> Eukaryotic cell lines	<input checked="" type="checkbox"/> <input type="checkbox"/> Flow cytometry
<input checked="" type="checkbox"/> <input type="checkbox"/> Palaeontology and archaeology	<input checked="" type="checkbox"/> <input type="checkbox"/> MRI-based neuroimaging
<input checked="" type="checkbox"/> <input type="checkbox"/> Animals and other organisms	
<input checked="" type="checkbox"/> <input type="checkbox"/> Human research participants	
<input checked="" type="checkbox"/> <input type="checkbox"/> Clinical data	
<input checked="" type="checkbox"/> <input type="checkbox"/> Dual use research of concern	

6.2 PUBLICATION P2: Design of Sealable Custom-Shaped Cell Mimicry Based on Self-Assembled Monolayers on CYTOP Polymer

Having patterned membranes into planar, yet constrained geometries, in this section I present the fabrication of compartmentalised membranous structures that mimic cellular geometries. This is outlined in the associated publication P2.

With lipid membranes playing an important role in many cellular functions, an ongoing challenge in synthetic biology is to reliably recreate cell-sized membranous compartments that can harbour biochemical reactions in their interior [116]. Systems such as water-in-oil droplets and liposomes have been widely employed, since they mimic cells in their size, their overall shape as well as in their basic biochemical functionality by providing a fluid, lipid mono- or bilayer interface [39]. However, deforming them from their spherical, equilibrium shape is a technological challenge, due to either their high surface tension in the case of droplets, or instability to external forces for liposomes [29]. They are therefore limited in their applications where aspherical, or even complex, geometry is required.

In this regard, microfabricating solid materials into cellular mimics, and coating the surfaces of such structures with supported lipid membranes, is an attractive method to study how proteins function according to the shape of their environment. A notable example of this is the PDMS microcompartment in the shape of “bathtubs”, which was used to recapitulate the pole-to-pole oscillations of MinDE *in vitro* [96]. However, the use of PDMS as a structural material can be problematic, especially since the refractive index is not matched to that of water that cause distortions during imaging. Moreover, these compartments are not fully sealed and the reaction volume evaporates away, which prevents long timelapse imaging [96].

In this work, we turned to CYTOP, a fluorinated polymer that is non-cytotoxic, chemically inert, and is, crucially, refractive index matched to water, thus significantly improving imaging quality. Here, previously employed techniques to pattern CYTOP involved reactive ion etching, which required expensive equipment and specialised cleanroom facilities. Instead, I demonstrated that CYTOP can be patterned by negative molding, which requires only a lithography-patterned template and can be handled in a standard laboratory setting.

By forming lipid monolayers on the surfaces of these patterned CYTOP structures, and then subsequently sealing each of the compartments in a flow cell, I created an alternative compartmentalised model membrane platform, on which parallelized assays can be run on custom-shaped geometries. As a demonstration of their versatility, GFP was expressed in these compartments by cell-free protein synthesis. Pole-to-pole oscillations of MinDE were also recapitulated in these fully-closed compartments, which validates the use of these microcompartments as a suitable cell mimic for *in vitro* reconstitution experiments.

This work is in line with ongoing efforts in the field to find alternative materials, with physicochemical properties that are more suitable for specific biological applications. The robust patterning methods ensure that compartments can be custom-shaped, which opens up future applications to study membrane associating or interactive proteins in encapsulated geometries.

Design of Sealable Custom-Shaped Cell Mimicried Based on Self-Assembled Monolayers on CYTOP Polymer

Hirumune Eto, Naoki Soga, Henri G. Franquelim, Philipp Glock, Alena Khmelinskaia, Lei Kai, Michael Heymann, Hiroyuki Noji, Petra Schuille

Author contributions:

H.E., M.H., N.S., H.N. and P.S. conceived the project. **H.E.** conducted all experiments and wrote the article. **H.E.** and N.S. conducted experiments on chamber fabrication. **H.E.** and H.G.F. conducted experiments on GUV hemifusion and FRAP analysis and wrote the article. L.K. contributed to experiments on CFPS and wrote the article. **H.E.**, P.G. and A.K. conducted experiments on monolayer preparation and wrote the article. P.G. also contributed to experiments on dynamic protein reconstitution assays. All authors discussed and interpreted the results and revised the manuscript.

published in

ACS Applied Materials and Interfaces (2019), 11, 21372-21380

Reprinted from [117] under the Creative Commons Attribution 4.0 International License
(see <https://creativecommons.org/licenses/by/4.0/>)

This is an open access article published under a Creative Commons Attribution (CC-BY) License, which permits unrestricted use, distribution and reproduction in any medium, provided the author and source are cited.



Design of Sealable Custom-Shaped Cell Mimicries Based on Self-Assembled Monolayers on CYTOP Polymer

Hirumune Eto,[†] Naoki Soga,[‡] Henri G. Franquelim,[†] Philipp Glock,[†] Alena Khmelinskaia,^{†,§} Lei Kai,^{†,||} Michael Heymann,[†] Hiroyuki Noji,[‡] and Petra Schwille^{*,†}

[†]Max Planck Institute of Biochemistry, Am Klopferspitz 18, D-82152 Martinsried, Germany

[‡]Department of Applied Chemistry, Graduate School of Engineering, The University of Tokyo, Bunkyo-ku, Tokyo 113-8656, Japan

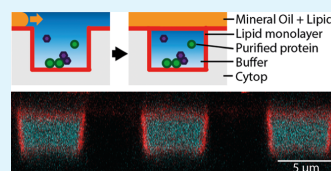
[§]Institute for Protein Design, University of Washington, Seattle 98195, Washington, United States

^{||}School of Life Sciences, Jiangsu Normal University, Shanghai Road 101, 221116 Xuzhou, P. R. China

Supporting Information

ABSTRACT: In bottom-up synthetic biology, one of the major methodological challenges is to provide reaction spaces that mimic biological systems with regard to topology and surface functionality. Of particular interest are cell- or organelle-shaped membrane compartments, as many protein functions unfold at lipid interfaces. However, shaping artificial cell systems using materials with non-intrusive physicochemical properties, while maintaining flexible lipid interfaces relevant to the reconstituted protein systems, is not straightforward. Herein, we develop micropatterned chambers from CYTOP, a less commonly used polymer with good chemical resistance and a refractive index matching that of water. By forming a self-assembled lipid monolayer on the polymer surface, we dramatically increased the biocompatibility of CYTOP-fabricated systems. The phospholipid interface provides an excellent passivation layer to prevent protein adhesion to the hydrophobic surface, and we succeeded in cell-free protein synthesis inside the chambers. Importantly, the chambers could be sealed after loading by a lipid monolayer, providing a novel platform to study encapsulated systems. We successfully reconstituted pole-to-pole oscillations of the *Escherichia coli* MinDE system, which responds dramatically to compartment geometry. Furthermore, we present a simplified fabrication of our artificial cell compartments via replica molding, making it a readily accessible technique for standard cleanroom facilities.

KEYWORDS: micropatterning, bottom-up biology, lab-on-a-chip, synthetic biology, self-assembled monolayers, lipids, polymer, CYTOP



INTRODUCTION

Functional encapsulation of biochemical reactions inside artificial biomimetic compartments is one of the most fundamental challenges in bottom-up synthetic biology. Many cellular reactions depend dramatically on volume size and topology as well as surface properties of the reaction spaces they are enclosed to. Often, binding to and from membranes, membrane insertion, or membrane transformation is part of their cellular functionality. Mimicking membrane-enclosed compartments of a particular shape and at the same time retaining structural flexibility are a daunting task that has so far not been conclusively solved. On the one hand, there is a strong motivation to maintain the classical advantages of in vitro techniques, such as high throughput, controllability, and accessibility of experiments. Examples of preferred compartments include water-in-oil droplets and liposomes, which can be produced in large numbers and feature cell-sized volumes with phospholipid mono- or bilayer interfaces. Through their mimicry of the cellular phospholipid interface, these compartments can support not only cytosolic reactions, but also those that involve membranes.^{1,2} On the other hand, deforming them to any other shape than their equilibrium spherical geometry remains a challenge,^{3,4} and thus, there is an ongoing

quest to develop new platforms that support the custom design of reaction spaces other than spheres.^{5,6} In this regard, the most prominent developments have been through micro-fabrication and photolithography techniques to pattern materials into any custom shape, including cell mimics.^{6–8} However, their effectiveness in biological studies depends greatly on the biocompatibility of the materials used to fabricate such structures. Cytotoxicity, poor compatibility with reagents, and a large refractive index mismatch with water (rendering their analysis by common microscopy techniques problematic) are notorious problems faced with commonly used materials. At the same time, standardized production routines and reasonable costs should support the development into a robust, widely accessible platform. In the past years, one of the most widely used polymers for the design of biomimetic reaction spaces has been PDMS (polydimethylsiloxane).⁹ Prepolymer of PDMS is commercially available, inexpensive, and easy to prepare. It is also biocompatible and unreactive. Membrane-coated PDMS chambers have been successfully

Received: March 21, 2019

Accepted: May 28, 2019

Published: May 28, 2019

employed to mimic the elongated shape of bacteria for the reconstitution of oscillatory dynamics, resulting from the self-organization of geometry-sensitive MinCDE proteins involved in bacterial cell division.¹⁰ However, constructing fully membrane-enclosed reaction volumes based on PDMS support⁷ is tedious and bears the risk of artifact generation under non-ideal optical conditions.

In this study, we turn our attention to CYTOP, an amorphous perfluorinated polymer, whose unique physico-chemical properties make it a material for a wide range of applications. In particular, with its low autofluorescence and refractive index ($n = 1.34$)¹¹ similar to that of water ($n = 1.33$), CYTOP can be readily used in combination with optical microscopy.¹² It has high chemical resistance and therefore a high compatibility with many reagents, including organic solvents and oils that could otherwise dissolve or swell conventionally used microfabrication materials, such as PDMS.¹³ As a hydrophobic material, it has a notably low surface energy (19 mN m^{-1}),¹¹ which makes it a useful coating material as a release layer in microfluidic applications.^{14,15}

Compartmentalized structures fabricated with CYTOP have been used for biological applications in the past. Particularly noteworthy are the attoliter-sized arrayed lipid bilayer chamber systems (ALBiC),¹⁶ developed by Noji et al., that are powerful tools to study functions of water-soluble enzymes or membrane-associated proteins. Although CYTOP has an excellent compatibility with many water-soluble proteins, its very low surface energy (and high hydrophobicity) result in enhanced adsorption and, consequently, often denaturation of more hydrophobic proteins coming into contact with the surface. Peripheral membrane proteins, transmembrane proteins, or proteins that generally contain hydrophobic moieties that are either exposed or not well shielded cannot usually be studied in combination with CYTOP surfaces.

To overcome this problem, we developed a supported lipid–CYTOP interface, where the CYTOP surface is coated with a phospholipid monolayer. The stable layer of lipids not only provides an effective passivation of the surface against the adsorption of hydrophobic molecules and residues, but also converts the interface into a model membrane platform to study lipid–lipid interactions, the functional role of membrane proteins, membrane–protein interactions, as well as other biochemical processes, such as molecular transport, signaling, and catalysis.¹⁷

Furthermore, we introduce replica molding to simplify compartment fabrication.¹⁸ Instead of lithographic patterning of each CYTOP chip independently, our process requires an SU8 master to be prepared in the cleanroom only once, as subsequent replica chips can be patterned using inexpensive tools outside of the cleanroom.

MATERIALS AND METHODS

Chamber Fabrication by Photolithography. Chambers were patterned as described previously.¹⁹ CYTOP 816AP (Asahi-Glass, Japan) was coated on a glass cover slide (32 mm × 24 mm; Matsunami) by spin-coating at 4000 rpm for 30 s and baked for 1 h at 180 °C. Note that the different grades of CYTOP used in the subsequent methods differ only in their functional groups, which is important in how they couple to their various substrates (e.g., glass), but not in the overall material properties, such as refractive index, surface energy, or cross-linking density.¹¹ The thickness of the CYTOP layer was 3 μm, as determined by an optical profiler (VK-X1000; Keyence). Photolithography was then performed using a positive photoresist (AZP4903; AZ Electronic Materials) to pattern

mask structures on the CYTOP layer. Subsequently, the resist-patterned substrate was dry etched with O₂ plasma using a reactive ion-etching system (RIE-10NR; Samco). For photoresist lift-off, the substrate was sonicated in acetone for 10 min and rinsed with 2-propanol and deionized water.

Chamber Fabrication by Replica Molding. Replica-molded CYTOP chamber fabrication was adopted from an X-ray chip fabrication method that used solvent-diluted epoxy resin.¹⁸ First, an SU8 master was fabricated by standard photolithography methods: on a 2" silicon wafer, a 3 μm thickness SU8 3005 (Microchem, USA) was spin coated, subsequently exposed to UV, and developed. To fabricate the stamp, PDMS was mixed with a cross linker in 10:1 weight ratio, cast on the SU8 master, and cured at 75 °C over 2 h. The PDMS was then peeled off the master. Subsequently, CYTOP 109AE was drop-cast on a clean glass cover slide, and the stamp was pressed down with a weight of ~65 mg mm⁻². CYTOP was gently cured on a hotplate at 50 °C over 20 min, until full solvent evaporation. Finally, the stamp was gently peeled off.

Giant Unilamellar Vesicles Preparation and Hemifusion with CYTOP Surface. Giant unilamellar vesicles (GUVs) composed of DOPC (1,2-dioleoyl-*sn*-glycero-3-phosphocholine), containing additional 0.005 mol % Atto655-DOPE (1,2-dioleoyl-*sn*-glycero-3-phosphoethanolamine), were produced by electroformation in polytetrafluoroethylene chambers with platinum electrodes 4 nm apart, as described previously.^{20,21} Briefly, 6 μL of the lipid mixture (2 mg mL⁻¹ in chloroform) was spread onto two platinum wires and dried in a desiccator for 30 min. The chamber was then filled with 370 μL of a 250 mOsm kg⁻¹ aqueous solution of sucrose. An AC electric field of 2 V (RMS) was applied at a frequency of 10 Hz for 1.5 h, followed by 2 Hz for 45 min. The obtained solution was diluted 1:10 in volume in 250 mOsm kg⁻¹ sucrose and further diluted 1:7 in volume in buffer M (25 mM Tris-HCl, 150 mM KCl, 5 mM MgCl₂, pH 7.5).

A flat CYTOP was prepared by spin-coating a film of CYTOP (809M); diluted 1:10 in volume in solvent CT-SOLV180, at 3000 rpm for 40 s; and a reaction chamber assembled, as described previously.²²

Monolayer Preparation on CYTOP Surface. All lipids were purchased from Avanti Polar Lipids (Alabaster, AL, USA), unless otherwise stated. Small unilamellar vesicles (SUVs) composed of DOPC or DOPC/DOPG (1,2-dioleoyl-*sn*-glycero-3-phospho-(1'-*rac*-glycerol)) (7:3 molar ratio), containing additional 0.005 mol % Atto655-DOPE (Atto-TEC GmbH, Siegen, Germany), were prepared at a concentration of 4 mg mL⁻¹ in buffer M, as described elsewhere.²² Shortly, lipids dissolved in chloroform were dried under a nitrogen stream, and vials were placed in a desiccator to remove residual chloroform for at least 30 min. Afterward, lipids were slowly rehydrated in buffer M and SUVs were generated by sonication in a water bath (model 1510; Branson) until the solution appeared clear.

To deposit self-assembled monolayers (SAM) on a planar surface, we first spin-coated a film of CYTOP (809M); diluted 1:10 in volume in solvent CT-SOLV180, at 3000 rpm for 40 s; and assembled a reaction chamber, as described previously.²² SUVs were added to the chamber at a concentration of 0.5 mg mL⁻¹ in buffer M. After 10 min incubation at 37 °C on a heating block, the SAM was gently washed with a total of 600 μL buffer S (25 mM Tris-HCl, 150 mM KCl, pH 7.5) to remove excess vesicles.

CYTOP Chamber Loading and Sealing. A flow cell was constructed, as described elsewhere.¹⁹ To prepare SAM on the fabricated chamber surface, SUVs were added to the flow cell at a concentration of 0.5 mg mL⁻¹ in buffer M. After 10 min incubation on a 37 °C warm heating block, the SAM was washed by exchanging the volume inside the flow cell 3 times with buffer S to remove excess vesicles. After coating the surface with lipids, the desired reaction mixture was flushed in to fill up the chambers.

To seal the chambers, we first prepared a lipid–mineral oil mixture. A DOPC/DOPG mixture (7:3 molar ratio), dissolved in chloroform, was partially evaporated in a glass vial until the meniscus touched the bottom. Mineral oil (Art-Nr. HP50.1; Carl Roth) was added and

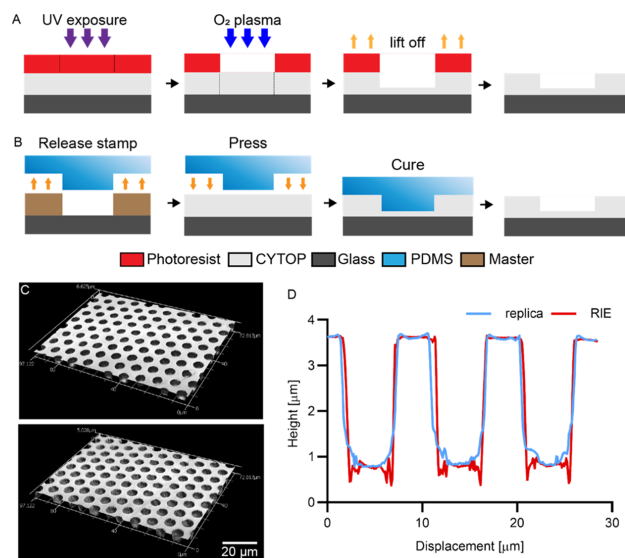


Figure 1. CYTOP chambers microfabricated by (A) photolithography involving reactive ion etching (RIE) and (B) replica molding. Fabricated chambers were imaged on a laser profiler (C, above): RIE; (C, below): replica molded. Chambers were fabricated with height $\sim 3 \mu\text{m}$ and width $\sim 5 \mu\text{m}$, and their height profiles are plotted in (D), which reveals that replica-molded chambers can be fabricated with remarkable similarity to those made by RIE.

vortexed, with the final concentration of lipid in the mixture at 2.5 mg mL^{-1} . Handling of mineral oil was done in a nitrogen chamber ($<10\%$ relative humidity). This mixture was then flushed in to the flow cell to seal the chambers.

Fluorescence Microscopy Imaging and Fluorescence Recovery after Photobleaching. Z-stack images of loaded chambers were obtained on a Zeiss LSM780 confocal laser scanning microscope using a Zeiss C-Apochromat $40\times/1.20$ water-immersion objective (Carl Zeiss AG, Oberkochen, Germany). Alexa 488 was excited using the 488 nm argon laser, and Atto655-DOPE using the 633 nm He-Ne laser.

Surface images were taken on Nikon Eclipse Ti2 in a TIRF (total internal reflection fluorescence) set-up using a Nikon Apo TIRF $60\times/1.4$ oil immersion objective, and for imaging chambers, we used Nikon Eclipse Ti in a spinning disk confocal set-up, with the Nikon Plan Fluor $20\times/0.75$ water immersion objective (both Nikon GmbH, Düsseldorf, Germany). We used the 490 and 640 nm diode laser lines to image GFP and Atto655-DOPE, respectively. All images were processed using Fiji with the standard set of packaged plugins sufficient for basic analysis.²³

For fluorescence recovery after photobleaching (FRAP) analysis, a circular spot of $5 \mu\text{m}$ diameter was illuminated with full laser power for 20 ms, and the average intensity was recorded every 3 s over 300 s. Measurements were taken at room temperature (23°C). Intensity in a second area of the same dimensions was recorded in the same field of view, in order to correct for the intensity drift. The intensity trace was fit to the equation derived by Soumpasis²⁴

$$f(t) = e^{-2\tau_D/t} \left(I_0 \left(\frac{2\tau_D}{t} \right) + I_1 \left(\frac{2\tau_D}{t} \right) \right)$$

Here, τ_D is the characteristic timescale for diffusion, and t is the time. $f(t)$ is the normalized fluorescence, and I_0 and I_1 are modified Bessel functions. The diffusion timescale for a bleached spot of radius r is $\tau_D = r^2/4D$ with D the diffusion coefficient. A custom code written in Python was used for curve fitting and data analysis.

Cell-Free Extract. S30 cell extracts were prepared from either *Escherichia coli* strain BL21 (DE3) or A19 according to previous protocols described by Kigawa et al.²⁵ and Kai et al.^{26,27} The basic cell-free reactions for batch configuration was set up according to previous protocols by Kigawa with modifications as follows: 17 mM of HEPES/KOH (pH 7.5); 3.2 mM of ATP; 1.6 mM of CTP, GTP, and UTP; 1 mM of DTT; 0.175 mg mL^{-1} of *E. coli* total tRNA mixture; 0.64 mM of cAMP; 210 mM of potassium glutamate; 8.7 mM of ammonium acetate; 21 mM of magnesium acetate; $34 \mu\text{g mL}^{-1}$ of L-5-formyl-5,6,7,8-tetrahydrofolic acid (folinic acid); 2.0 mM each of 20 amino acids; 2% PEG (8000); 100 mM of creatine phosphate; 250 mM of creatine kinase; 15 ng mL^{-1} of plasmid DNA template; 30% (v/v) of S30 extract from *E. coli* BL21 (DE3); and $10 \mu\text{g mL}^{-1}$ T7 RNA polymerase.

To estimate the concentration of purified eGFP, an absorption spectrum of a 1:100 dilution in buffer M was recorded from 300 to 600 nm using a Jasco V-650 spectrophotometer (Jasco Deutschland GmbH, Germany). The absorption peak at 489 nm was used in combination with the Lambert–Beer relation, $A = \epsilon cl$ (A = measured absorption, $\epsilon = 55\,000 \text{ M}^{-1} \text{ cm}^{-1}$ for eGFP, path length = 10 mm), to estimate the concentration c of the dilute solution. We took a dilution series of this solution to create an intensity standard, which we used to estimate the concentration of our expressed protein.

MinDE Self-Organization Assays. For the reconstitution of the MinDE assay on planar surfaces, we used protocols as described in earlier literature.²² For reconstitution in the chambers, a mixture of $0.5 \mu\text{M}$ MinD (doped with 30% EGFP-MinD), $1 \mu\text{M}$ MinE, and 2.5 mM ATP (from 100 mM ATP stock in 100 mM MgCl_2 , pH 7.5) in buffer M was first prepared. The mixture was then loaded onto the flow cell and incubated for 30 min at room temperature (23°C). The chambers were then sealed, as described previously.

RESULTS AND DISCUSSION

CYTOP Chambers Fabricated by Reactive Ion Etching and Replica Molding. Photolithography is a commonly used method to pattern materials, including CYTOP, that are

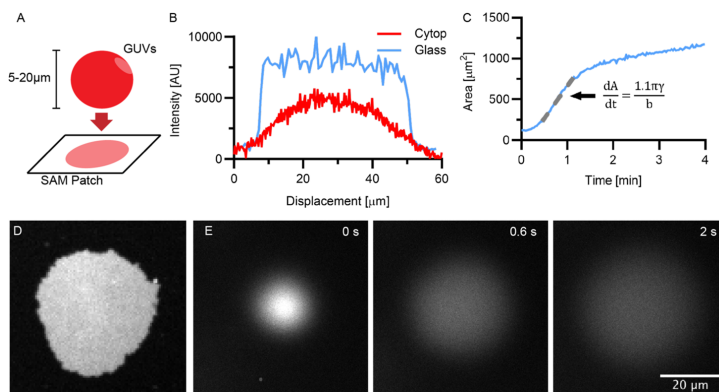


Figure 2. (A) GUVs hemifuse with CYTOP to form SAM patches. (B) Intensity profile of lipid membrane patches (taken through the diameter) formed by GUV fusion on glass (D) and on CYTOP (E). (C) Area of the membrane patch was plotted over time [from time lapse image, (E)]. From the initial gradient, we calculated the surface energy of the material ($21 \pm 3 \text{ mN m}^{-1}$).

themselves not photo-reactive (Figure 1A). A photoresist is first deposited on top of the material and patterned by UV light, which then becomes a mask for the subsequent chemical or plasma treatment that etches away the material in the regions that are exposed. The photoresist is then lifted off to reveal the patterned structures.

With CYTOP, the etching step is done with a high-power oxygen plasma, which requires a reactive ion etcher (RIE). Although this is a reliable and effective technique, the equipment is costly and many cleanroom facilities do not offer respective procedures. We therefore present an alternative fabrication method by replica molding (Figure 1B), which requires significantly less technical expertise and lowers equipment costs. In replica molding,¹⁸ we first require a master or a template. The master can be either purchased or fabricated by patterning a photoresist, such as SU8, by UV exposure. Then, a PDMS stamp is cast out of the master mold and pressed down on uncured CYTOP. The CYTOP is cured with the stamp in place, taking its form. Once the stamp is lifted off, a high-fidelity replica of the master remains.

The fabricated chambers by both methods were imaged on a profiler (Figure 1C, top: RIE, bottom: replica molding), and the height profile (Figure 1D) shows little difference between the two methods. In the subsequent encapsulation experiments, we used chambers produced with both methods and compared the obtained results. Replica molding is a low-cost alternative to the highly reliable photolithography method using RIE. It can, however, lead to small variations across samples. For example, there can be small damages in parts when the stamp is peeled off, and variations in the way the stamp is pressed down onto the uncured CYTOP can sometimes cause deformed structures. A rigid frame around the PDMS stamp²⁸ would reduce deformations and increase the fidelity of the replica, and thus should be attempted in the next iteration to improve this technique.

Hemifusion of GUVs on CYTOP Confirms the Formation of SAM. To address the issue of CYTOP's biocompatibility, we attempted to coat the surface of CYTOP with lipid membrane. On hydrophobic surfaces, such as that of CYTOP, vesicles are thought to undergo the process of hemifusion,²⁹ during which the lipids in the vesicle bilayer

reorganize themselves such that the hydrophobic tails (of both the inner and outer leaflets of the vesicle) come into contact with the surface. This forms a low-energy interface between the hydrophobic substrate and the surrounding buffer, as a result of the formation of a lipid SAM.

To test the hypothesis that vesicles form a lipid monolayer upon hemifusion on the CYTOP surface, we utilized GUVs (Figure 2A). Typically with diameters 5–20 μm , these membrane structures are large enough to be well resolved by optical microscopy, making them ideal test substrates for detailed analyses of the fusion process and the formed lipid patch.

We prepared a flat spin-coated CYTOP and deposited a solution containing GUVs on top of the CYTOP surface. We then observed the hemifusion process by TIRF microscopy. The SAM patch formed through GUV hemifusion resulted in a unique intensity profile on the CYTOP surface (Figure 2B) that is markedly different from that of a supported lipid bilayer (SLB) formed on glass (Figure 2D). The formed SAM patch appeared fuzzy, with a less-defined edge because of a gradual intensity fall-off that implies a sparser lipid density away from the center of the fusion site. In contrast, an SLB patch had a very defined edge with a sharp intensity fall-off, and the lipids formed a homogeneous coverage. A previous study on the hemifusion of GUVs on a hydrophobically functionalized glass surface showed that GUV-fused SAM patches have a characteristic morphology and behavior, from which we could draw close comparisons with our observations.²⁹

We observed the hemifusion of a GUV in high time resolution (30 ms time intervals) by TIRF microscopy; we can see the vesicle coming into contact, fusing, and spreading on the CYTOP surface (Figure 3E) and plotted the area increase over time (Figure 3C). We also observe the same by spinning disk confocal microscopy (Figure S1), where we can more clearly see the vesicle outline during fusion, which shrinks as lipids are reorganized and the SAM spreads over the surface. A physical model was developed by Zan et al.,²⁹ in which the instantaneous free energy gain because of the lipids spreading and the covering of the hydrophobic surface by the lipid tails is balanced by the frictional losses of the lipids flowing from the center of the hemifusion toward the edge of the covered area.

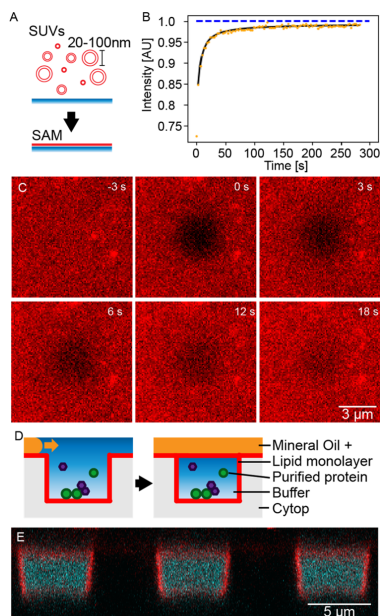


Figure 3. Lipid preparation on CYTOP surface. (A) Schematic of SAM formation. SUVs were incubated on the CYTOP surface, where they fuse to form a homogeneous SAM. (B,C) Subsequent FRAP analysis shows fluorescence recovery. (D) After coating the surface with SAM, the chambers can be sealed by flushing in mineral oil containing lipids through a flow cell. (E) Z-stacks of the sealed chambers were taken with a confocal microscope. The lipids are labeled red (DOPE-Atto655) and soluble Alexa 488 dye in the encapsulated volume (cyan).

For vesicles with radii $R \approx 10 \mu\text{m}$, the initial rate of area expansion can be approximated by a linear equation²⁹

$$\frac{dA}{dt} \approx \frac{1.1\pi\gamma}{b}$$

where γ is the surface energy, b is the friction coefficient, and A is the area over which the lipid layer spreads. Using the value $b \approx 10^8 \text{ N s m}^{-3}$ (based on Zan et al.²⁹) and taking the initial linear gradient from the first ~ 500 ms of area expansion after fusion occurs, we calculated the surface energy of the material ($21 \pm 3 \text{ mN m}^{-1}$), which is in good agreement with previous measurements (19 mN m^{-1}), published by Asahi-Glass.¹¹ Taken together, our results support that the CYTOP-supported lipid membrane is indeed a monolayer.

Self-Assembled Lipid Monolayers Formed on CYTOP through SUV Fusion. Having obtained strong evidence for the formation of SAMs on CYTOP, we attempted to form a uniform coating of lipids on the fabricated chamber surface. For this purpose, we deposited a solution containing a high concentration of SUVs on top of the CYTOP surface (Figure 3A). We prepared the SUVs with two lipid compositions: one containing DOPC and another with a DOPC/DOPG mixture (7:3). The latter has a net negative charge, which is crucial for the function of many membrane-interacting proteins, such as *E. coli* MinDE.

Both RIE-prepared and replica-molded structures were successfully coated with a homogeneous SAM (Figure S2), whose membrane mobility was assessed by FRAP (Figure 3B,C). In all cases, the obtained lipid diffusion coefficients were between 1.0 and $1.5 \mu\text{m}^2 \text{ s}^{-1}$ (Table 1), which are

Table 1. Calculated Diffusion Coefficients from FRAP Analysis^a

	diffusion coefficient ($\mu\text{m}^2 \text{ s}^{-1}$)		mobile fraction (%)	
	RIE	replica	RIE	replica
DOPC	1.3 ± 0.3	1.5 ± 0.7	98 ± 2	97 ± 3
DOPC/DOPG	1.0 ± 0.2	1.3 ± 0.5	97 ± 3	97 ± 2

^aError represents standard deviation of measurement values from $n = 15$ independent experiments.

comparable to those of other SAM systems ($0.2\text{--}2 \mu\text{m}^2 \text{ s}^{-1}$),^{30,31} and still in the range of those measured for SLBs ($1\text{--}6 \mu\text{m}^2 \text{ s}^{-1}$).^{32,33} More importantly, the immobile fraction was negligible, indicating the lack of major lipid aggregates and other surface artifacts.

Having fabricated the chambers and coated their surfaces with lipid membranes, we encapsulated biochemical reactions. The loading of the chambers was done in a flow cell, as shown in the schematic (Figure 3D). The confocal cross-sectional image (Figures 3E and S3) shows Alexa 488 dye successfully encapsulated in these lipid-coated chambers.

SAM on CYTOP Improves Biocompatibility. The native CYTOP surface is incompatible with many biological systems. Here, we show that SAM coverage can provide adequate passivation, which increases the biocompatibility of our CYTOP system. We first used water-soluble eGFP as a model protein. Despite its apparent hydrophilicity, eGFP adheres to and denatures upon contact with the CYTOP surface (Figure S4). Hence, we attempted to show that the SAM passivation is sufficient to shield the protein from CYTOP's hydrophobic surface.

A solution containing 50 nM eGFP was incubated on top of CYTOP (Figure S4A). Without the SAM, the fluorescence intensity on the surface was almost 16-fold higher than in the solution (Figure S4C,D), and we also saw aggregates forming on the surface. We verified that there was almost no recovery after photobleaching, suggesting that the eGFP attached permanently to the surface (Figure S4E,F). We then formed the SAM (DOPC) prior to depositing the eGFP solution. In this case, the fluorescence intensity on the surface could be dramatically reduced (Figure S4B–D). We still found a slight increase in the fluorescence on the membrane, which could point to a weak interaction between eGFP and the lipid. In contrast to the non-passivated CYTOP surface, eGFP was not permanently bound, as seen from the complete fluorescence recovery after bleaching on the surface.

To further verify the enhanced biocompatibility, we attempted cell-free protein synthesis (CFPS) inside the SAM-covered CYTOP chambers. The encapsulation of cell-free extracts has recently caught much attention,³⁴ because proteins can be expressed in defined volumes without the need of any additional protein purification steps.³⁵ The cell-free extract is an extremely complex mixture of proteins and co-factors and can therefore be compromised by the incompatibility of its constituents with their surrounding material. Moreover, encapsulating volumes inside small chambers,

whose surface area-to-volume ratio is high, emphasizes this problem; adsorption onto the larger surface to available volume can lead to a more significant depletion of components away from the reaction volume. Here, we show that GFP can be readily expressed within SAM-covered chambers, as the increased biocompatibility because of the SAM allows protein synthesis to occur efficiently.

The chambers were fabricated by the two alternative methods outlined before (photolithography and replica molding). The SAM was formed on the surface, and the chambers were subsequently loaded with the cell-free extract. After sealing the chambers, we incubated them at 37 °C over 5 h, monitoring the GFP expression levels by measuring the fluorescence intensity in the fabricated wells every 30 min (Figure 4).

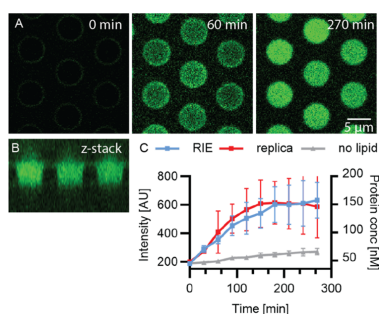


Figure 4. GFP expression by CFPS in sealed CYTOP chambers. (A) Time lapse images of the chambers, with time intervals of 30 min. (B) Z-stack image of the sealed chambers. (C) GFP expression levels against incubation time at 37 °C. Error bars represent standard deviation of measurement values from $n = 5$ independent experiments.

In our chambers, GFP was expressed almost linearly for the first 2 h of incubation, after which the expression slowed down. Without lipid passivation, GFP levels stayed low even after 5 h of incubation. This is a strong indication that the SAM's passivation is effective at preventing essential cell-free components from adsorbing to the CYTOP surface.

In this experimental set-up, each glass slide contains around 100 000 chambers of picoliter-sized reaction volumes. In our flow cell, the required sample volume used for loading was as low as 40 μL . The high-throughput, yet highly efficient, nature of these microfabricated systems can be further improved by connecting it to a microfluidic set-up, and this could also allow more complex exchange of solutions, to enable, for example, the generation of concentration gradients over the slide.³⁶

The expression of proteins using cell-free extracts in such high-throughput systems can be a powerful technique. Directed evolution of enzymes, where DNA from a DNA library could be introduced to each chamber and directly expressed in the cell-free extract, is an example. We also speculate that this technique can be combined with ALBiC-style chambers, developed by Noji et al.,³⁷ where, instead of having a mineral oil seal, the chambers have a free-standing bilayer interface sealing the top of the chamber.

SAM on CYTOP as a Platform for the Study of Membrane-Interacting Protein Systems: *E. coli* MinDE. We investigated whether the lipid interface formed on CYTOP

can be used as a platform to study membrane-interacting proteins. In particular, we investigated the *E. coli* MinDE system, which is known to form dynamic patterns when reconstituted on supported lipid membranes.³⁸ The reconstitution of the Min system on planar surfaces, as well as encapsulation in aspherical compartments, has been well studied,^{6,10,39,40} and therefore, it is an ideal model protein system to test our new platform. Importantly, either the micropatterning methods employed in previous studies have not succeeded in fully sealing the reaction volume¹⁰ or the structural material they have used can have unfavorable chemical or optical properties,⁷ particularly in the case of PDMS.

The *E. coli* MinDE system involves two proteins, MinD and MinE: MinD forms a dimer in the presence of ATP, upon which it attaches cooperatively to the membrane. At higher local concentrations on the membrane, it recruits MinE. MinD's ATPase activity gets activated when MinE is bound to it, which in turn triggers its detachment from the membrane.⁴¹ The time delay between the accumulation of MinD on the membrane and MinE-triggered detachment, or in other words, the delayed negative feedback,^{39,40} results in traveling waves of Min proteins on a planar surface,^{39,40} and pole-to-pole oscillations when confined in a cylindrical geometry,¹⁰ which has been shown to position the cell division ring in *E. coli*.⁴²

First, we prepared a planar CYTOP surface by spin-coating and coated the surface by SUV hemifusion (lipid composition DOPC/DOPG in 7:3 ratio). We then incubated purified MinDE proteins and observed their dynamics. Dynamic spiral patterns were observed on the surface (Figures S5A and S5), in good qualitative agreement with observations made in previous studies on supported bilayers.³⁹ The measured period (1–2 min) and wavelength ($\sim 30 \mu\text{m}$) compare well with previous studies on bilayers (period 0.6–2 min, wavelength 50–110 μm)^{39,40,43} as well as on monolayer surfaces at the air–water interface (period 0.5–1 min, wavelength 30–60 μm).⁴⁴ The Min wavelength is known to vary according to the substrate and its preparation,⁴³ and a different wavelength on CYTOP can therefore be expected.

As a control, we checked that MinD is indeed adhering to and denaturing on CYTOP without the SAM (Figure 5B). Without MinE and in the presence of ATP, MinD still has a basal on/off rate from the membrane that is not catalyzed by MinE binding. Without the SAM, FRAP analysis on this system shows only partial recovery, which suggests that most of the MinD is permanently bound to the CYTOP surface. With the SAM, MinD fluorescence almost fully recovers, which indicates a healthy cycling of MinD from the membrane into the bulk volume.

We fabricated chambers as bacteria mimics—in elongated chambers with aspect ratios (width/length) ranging from 1:1 to 1:5. Both photolithography (Figure 5) and replica molding (Figure S6) methods were tested, and we confined the MinDE proteins within these chambers and observed their dynamics.

After encapsulation, MinDE performed pole-to-pole oscillations in the longer chambers, in good agreement with previous in vitro studies.^{6,10} These standing waves determine midcell in *E. coli*:⁴⁵ the time-averaged concentration of MinD is depleted in the middle, and this is where the FtsZ ring can form and act as a scaffold for subsequent assembly of the cell division machinery. In small aspect ratio chambers, we also observed volume oscillations or “blinking” of Min proteins, where the Min proteins are periodically either attached to or

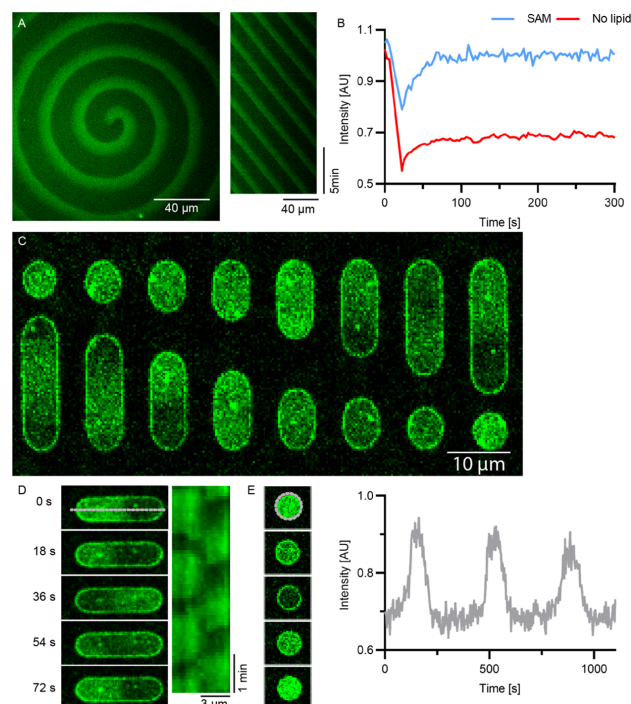


Figure 5. MinDE system dynamics reconstituted on CYTOP-SAM. (A) Min proteins form spiral waves on a planar surface. (B) As a control, MinD activity on the surface was checked by FRAP with and without the SAM. (C) Min proteins can be encapsulated in rod-shaped chambers, with aspect ratios ranging from 1:1–5. (D) Time lapse images of pole-to-pole oscillations in rod-shaped chambers and (E) “blinking” dynamics in symmetrical compartments.

dissociated from the membrane. This behavior was also seen previously in spherical vesicles and in systems with high surface/volume ratios.^{44,46}

The successful encapsulation of the MinDE system conveys two important messages with regard to other potential applications of the CYTOP structures described here. The first is that complex protein systems, whose function is dependent on geometry, can be readily studied in these confined and asymmetrical chambers when they are passivated by a lipid membrane. The second is that a negatively charged lipid membrane can be formed on the surface, providing an active and catalytic interface that is essential for the function of many proteins. Indeed, most prokaryotic cell membranes are negatively charged, and therefore, many bacterial protein systems are adapted to work on this type of membrane. A more comprehensive investigation of lipid species, such as PIP₂ or DOPS, could further extend the range of protein systems (e.g., eukaryotic) that CYTOP-SAM chambers can be utilized for.

CONCLUSIONS

In the search for new materials for the fabrication of biomimetic and biocompatible compartments to encapsulate complex protein systems, we turned our attention to CYTOP, an amorphous fluorinated polymer that has good chemical resistance and ideal optical properties for imaging with standard fluorescence microscopy methods. We demonstrated

that CYTOP chambers can be fabricated by two methods: one, by photolithography using RIE, and second, by replica molding. In order to increase the range of compatible biosystems, we deposited an SAM on the CYTOP surface by SUV fusion. By coating it with lipid monolayers, the surface can be efficiently passivated against adhesion and subsequent denaturation of proteins. Importantly, the structures can be fully sealed by a lipid monolayer, enabling the design of closed membrane compartments of defined 3D geometry. Furthermore, we demonstrate that the CYTOP-SAM is an improved model membrane platform to study membrane-interacting proteins, in particular the dynamic MinDE system.

ASSOCIATED CONTENT

Supporting Information

The Supporting Information is available free of charge on the ACS Publications website at DOI: 10.1021/acsami.9b05073.

GUV hemifusion time lapse, homogeneous SAM on CYTOP, Z-stack images of sealed chambers, eGFP adhesion on CYTOP, MinDE oscillation on planar surface, and MinDE oscillations on replica molded chambers (PDF)

Movie of GUV hemifusion on CYTOP (AVI)

AUTHOR INFORMATION

Corresponding Author

*E-mail: schwille@biochem.mpg.de.

ORCID

Hiromune Eto: 0000-0001-8737-2939

Henri G. Franquelim: 0000-0001-6229-4276

Philipp Glock: 0000-0002-0238-2634

Alena Khmelinskaia: 0000-0003-1584-9800

Hiroyuki Noji: 0000-0002-8842-6836

Petra Schwille: 0000-0002-6106-4847

Author Contributions

H.E. contributed to the project design, conducted experiments, analyzed data, and wrote the article. N.S. conducted experiments on chamber fabrication. H.G.F. conducted experiments on GUV hemifusion and FRAP analysis and wrote the article. L.K. conducted experiments on CFPS and wrote the article. M.H. contributed to the project design. P.G. and A.K. conducted experiments on monolayer preparation and wrote the article. P.G. also conducted experiments on dynamic protein reconstitution assays. H.N. and P.S. contributed to the project design and wrote the article.

Notes

The authors declare no competing financial interest.

ACKNOWLEDGMENTS

We thank Allen Liu for discussion and helpful comments on the article, the Biochemistry Core Facility of the Max Planck Institute of Biochemistry for assistance with protein purification, as well as the support from Center for Nano-sciences, Munich. P.G. acknowledges support from the DFG-funded GRK 2062—Molecular Principles of Synthetic Biology as well as support from International Max Planck Research School for Molecular Life Sciences. A.K. acknowledges the support of the Graduate School of Quantitative Biosciences Munich. P.S. acknowledges the financial support from the Max Planck Society (MPG) and from the DFG through the project A09 of the SFB1032 “Nanoagents for the spatiotemporal control of molecular and cellular reactions”. H.G.F. and P.S. acknowledge the financial support from project B10 of the SFB863 “Forces in Biomolecular Systems”. L.K., M.H., and P.S. have received funding from the MaxSynBio Consortium, which is jointly funded by the Federal Ministry of Education and Research of Germany (BMBF) and MPG. N.S. acknowledges the financial support from Grants-in-Aid for Scientific Research (KAKENHI) 17H05717 from the Japan Society for the Promotion of Science. H.N. acknowledges the financial support from the Japan Science and Technology Agency for ImPACT Program of Council for Science, Technology, and Innovation (Cabinet Office, Government of Japan) to K. V. T. (grant number: 15808948) as well as from JST CREST grant number JPMJCR18S6.

REFERENCES

- (1) Sezgin, E.; Levental, I.; Mayor, S.; Eggeling, C. The Mystery of Membrane Organization: Composition, Regulation and Roles of Lipid Rafts. *Nat. Rev. Mol. Cell Biol.* **2017**, *18*, 361–374.
- (2) Dezi, M.; Di Cicco, A.; Bassereau, P.; Levy, D. Detergent-mediated incorporation of transmembrane proteins in giant unilamellar vesicles with controlled physiological contents. *Proc. Natl. Acad. Sci. U.S.A.* **2013**, *110*, 7276–7281.

(3) Yamada, A.; Lee, S.; Bassereau, P.; Baroud, C. N. Trapping and Release of Giant Unilamellar Vesicles in Microfluidic Wells. *Soft Matter* **2014**, *10*, 5878–5885.

(4) Korlach, J.; Reichle, C.; Müller, T.; Schnelle, T.; Webb, W. W. Trapping, Deformation, and Rotation of Giant Unilamellar Vesicles in Octode Dielectrophoretic Field Cages. *Biophys. J.* **2005**, *89*, 554–562.

(5) Yeaman, C.; Grindstaff, K. K.; Nelson, W. J. New Perspectives on Mechanisms Involved in Generating Epithelial Cell Polarity. *Physiol. Rev.* **1999**, *79*, 73–98.

(6) Zieske, K.; Schwille, P. Reconstitution of Self-Organizing Protein Gradients as Spatial Cues in Cell-Free Systems. *eLife* **2014**, *3*, No. e03949.

(7) Caspi, Y.; Dekker, C. Mapping out Min Protein Patterns in Fully Confined Fluidic Chambers. *eLife* **2016**, *5*, No. e19271.

(8) Bao, M.; Xie, J.; Piruska, A.; Huck, W. T. S. 3D Microniches Reveal the Importance of Cell Size and Shape. *Nat. Commun.* **2017**, *8*, 1–12.

(9) Weibel, D. B.; Diluzio, W. R.; Whitesides, G. M. Micro-fabrication Meets Microbiology. *Nat. Rev. Microbiol.* **2007**, *5*, 209–218.

(10) Zieske, K.; Schwille, P. Reconstitution of Pole-to-Pole Oscillations of Min Proteins in Microengineered Polydimethylsiloxane Compartments. *Angew. Chem., Int. Ed.* **2013**, *52*, 459–462.

(11) Asahi Glass Co. Ltd. *J. Cytop Technical Report*.

(12) Nakahara, A.; Shirasaki, Y.; Kawai, K.; Ohara, O.; Mizuno, J.; Shoji, S. Fabrication of High-Aspect-Ratio Amorphous Perfluorinated Polymer Structure for Total Internal Reflection Fluorescence Microscopy. *Microelectron. Eng.* **2011**, *88*, 1817–1820.

(13) Lee, J. N.; Park, C.; Whitesides, G. M. Solvent Compatibility of Poly(dimethylsiloxane)-Based Microfluidic Devices. *Anal. Chem.* **2003**, *75*, 6544–6554.

(14) Kimura, H.; Yamamoto, T.; Sakai, H.; Sakai, Y.; Fujii, T. An Integrated Microfluidic System for Long-Term Perfusion Culture and on-Line Monitoring of Intestinal Tissue Models. *Lab Chip* **2008**, *8*, 741–746.

(15) Heymann, M.; Ophthalge, A.; Wierman, J. L.; Akella, S.; Szebenyi, D. M. E.; Gruner, S. M.; Fraden, S. Room-Temperature Serial Crystallography Using a Kinetically Optimized Microfluidic Device for Protein Crystallization and on-Chip X-Ray Diffraction. *IUCr* **2014**, *1*, 349–360.

(16) Watanabe, R.; Soga, N.; Fujita, D.; Tabata, K. V.; Yamauchi, L.; Hyeon Kim, S.; Asanuma, D.; Kamiya, M.; Urano, Y.; Suga, H.; Noji, H. Arrayed Lipid Bilayer Chambers Allow Single-Molecule Analysis of Membrane Transporter Activity. *Nat. Commun.* **2014**, *5*, 4519.

(17) Lagny, T. J.; Bassereau, P. Bioinspired Membrane-Based Systems for a Physical Approach of Cell Organization and Dynamics: Usefulness and Limitations. *Interface Focus* **2015**, *5*, 20150038.

(18) Gicquel, Y.; Schubert, R.; Kapis, S.; Bourenkov, G.; Schneider, T.; Perbandt, M.; Betzel, C.; Chapman, H. N.; Heymann, M. Microfluidic Chips for In Situ Crystal X-Ray Diffraction and In Situ Dynamic Light Scattering for Serial Crystallography. *J. Visualized Exp.* **2018**, *134*, No. e57133.

(19) Watanabe, R.; Soga, N.; Ohdate, S.; Noji, H. Single-Molecule Analysis of Membrane Transporter Activity by Means of a Microsystem. In *Bacterial Multidrug Exporters: Methods and Protocols*; Yamaguchi, A., Nishino, K., Eds.; Springer New York: New York, NY, 2018; pp 321–330.

(20) Angelova, M. I.; Dimitrov, D. S. Liposome Electroformation. *Faraday Discuss. Chem. Soc.* **1986**, *81*, 303–311.

(21) García-Sáez, A. J.; Carrer, D. C.; Schwille, P. Fluorescence Correlation Spectroscopy for the Study of Membrane Dynamics and Organization in Giant Unilamellar Vesicles. In *Liposomes: Methods and Protocols, Volume 2: Biological Membrane Models*; Weissig, V., Ed.; Humana Press: Totowa, NJ, 2010; pp 493–508.

(22) Ramm, B.; Glock, P.; Schwille, P. In Vitro Reconstitution of Self-Organizing Protein Patterns on Supported Lipid Bilayers. *J. Visualized Exp.* **2018**, *137*, No. e58139.

(23) Schindelin, J.; Arganda-Carreras, I.; Frise, E.; Kaynig, V.; Longair, M.; Pietzsch, T.; Preibisch, S.; Rueden, C.; Saalfeld, S.;

- Schmid, B.; Tinevez, J. Y.; White, D. J.; Hartenstein, V.; Eliceiri, K.; Tomancak, P.; Cardona, A. Fiji: An Open-Source Platform for Biological-Image Analysis. *Nat. Methods* **2012**, *9*, 676–682.
- (24) Soumpasis, D. Theoretical Analysis of Fluorescence Photo-bleaching Recovery Experiments. *Biophys. J.* **1983**, *41*, 95–97.
- (25) Kitagawa, T.; Yabuki, T.; Yoshida, Y.; Tsutsui, M.; Ito, Y.; Shibata, T.; Yokoyama, S. Cell-Free Production and Stable-Isotope Labeling of Milligram Quantities of Proteins. *FEBS Lett.* **1999**, *442*, 15–19.
- (26) Kai, L.; Roos, C.; Habersack, S.; Proverbio, D.; Ma, Y.; Junge, F.; Karbyshev, M.; Dötsch, V.; Bernhard, F. Systems for the Cell-Free Synthesis of Proteins. In *Chemical Genomics and Proteomics: Reviews and Protocols*; Zanders, E. D., Ed.; Humana Press: Totowa, NJ, 2012; pp 201–225.
- (27) Kai, L.; Dötsch, V.; Kaldenhoff, R.; Bernhard, F. Artificial Environments for the Co-Translational Stabilization of Cell-Free Expressed Proteins. *PLoS One* **2013**, *8*, No. e56637.
- (28) Aghvami, S. A.; Opathalage, A.; Zhang, Z. K.; Ludwig, M.; Heymann, M.; Norton, M.; Wilkins, N.; Fraden, S. Rapid Prototyping of Cyclic Olefin Copolymer (COC) Microfluidic Devices. *Sens. Actuators, B* **2017**, *247*, 940–949.
- (29) Zan, G. H.; Tan, C.; Deserno, M.; Lanni, F.; Lösche, M. Hemifusion of Giant Unilamellar Vesicles with Planar Hydrophobic Surfaces: A Fluorescence Microscopy Study. *Soft Matter* **2012**, *8*, 10877–10886.
- (30) Yang, Z.; Yu, H. Biomembrane Mimetic Surfaces by Phospholipid Self-Assembled Monolayers on Silica Substrates. *Langmuir* **1999**, *15*, 1731–1737.
- (31) Yeung, S. Y.; Ederth, T.; Pan, G.; Cicenaite, J.; Cárdenas, M.; Arnebrant, T.; Sellergren, B. Reversible Self-Assembled Monolayers (rSAMs) as Robust and Fluidic Lipid Bilayer Mimics. *Langmuir* **2018**, *34*, 4107–4115.
- (32) Chiantia, S.; Ries, J.; Kahya, N.; Schwille, P. Combined AFM and Two-Focus SFCS Study of Raft-Exhibiting Model Membranes. *ChemPhysChem* **2006**, *7*, 2409–2418.
- (33) Tamm, L. K.; McConnell, H. M. Supported Phospholipid Bilayers. *Biophys. J.* **1985**, *47*, 105–113.
- (34) Jia, H.; Heymann, M.; Bernhard, F.; Schwille, P.; Kai, L. Cell-Free Protein Synthesis in Micro Compartments: Building a Minimal Cell from Biobricks. *New Biotechnol.* **2017**, *39*, 199–205.
- (35) Majumder, S.; Garamella, J.; Wang, Y.-L.; Denies, M.; Noireaux, V.; Liu, A. P. Cell-Sized Mechanosensitive and Biosensing Compartment Programmed with DNA. *Chem. Commun.* **2017**, *53*, 7349–7352.
- (36) Jeon, N. L.; Dertinger, S. K. W.; Chiu, D. T.; Choi, I. S.; Stroock, A. D.; Whitesides, G. M. Generation of Solution and Surface Gradients Using Microfluidic Systems. *Langmuir* **2000**, *16*, 8311–8316.
- (37) Watanabe, R.; Soga, N.; Hara, M.; Noji, H. Arrayed Water-in-Oil Droplet Bilayers for Membrane Transport Analysis. *Lab Chip* **2016**, *16*, 3043–3048.
- (38) Loose, M.; Fischer-Friedrich, E.; Ries, J.; Kruse, K.; Schwille, P. Spatial Regulators for Bacterial Cell Division Self-Organize into Surface Waves in Vitro. *Science* **2008**, *320*, 789–792.
- (39) Loose, M.; Fischer-Friedrich, E.; Ries, J.; Kruse, K.; Schwille, P. Spatial Regulators for Bacterial Cell Division Self-Organize into Surface Waves in Vitro. *Science* **2008**, *320*, 789–792.
- (40) Loose, M.; Fischer-Friedrich, E.; Herold, C.; Kruse, K.; Schwille, P. Min Protein Patterns Emerge from Rapid Rebinding and Membrane Interaction of MinE. *Nat. Struct. Mol. Biol.* **2011**, *18*, 577–583.
- (41) Kretschmer, S.; Schwille, P. Pattern Formation on Membranes and Its Role in Bacterial Cell Division. *Curr. Opin. Cell Biol.* **2016**, *38*, 52–59.
- (42) Raskin, D. M.; de Boer, P. A. J. Rapid Pole-to-Pole Oscillation of a Protein Required for Directing Division to the Middle of Escherichia Coli. *Proc. Natl. Acad. Sci. U.S.A.* **1999**, *96*, 4971–4976.
- (43) Martos, A.; Petrasek, Z.; Schwille, P. Propagation of MinCDE Waves on Free-Standing Membranes. *Environ. Microbiol.* **2013**, *15*, 3319–3326.
- (44) Zieske, K.; Chwastek, G.; Schwille, P. Protein Patterns and Oscillations on Lipid Monolayers and in Microdroplets. *Angew. Chem., Int. Ed.* **2016**, *55*, 13455–13459.
- (45) Raskin, D. M.; de Boer, P. A. J. Rapid Pole-to-Pole Oscillation of a Protein Required for Directing Division to the Middle of Escherichia Coli. *Proc. Natl. Acad. Sci. U.S.A.* **1999**, *96*, 4971–4976.
- (46) Litschel, T.; Ramm, B.; Maas, R.; Heymann, M.; Schwille, P. Beating Vesicles: Encapsulated Protein Oscillations Cause Dynamic Membrane Deformations. *Angew. Chem., Int. Ed.* **2018**, *57*, 16286–16290.

Supporting Information

Design of Sealable Custom-Shaped Cell Mimicries Based on Self-Assembled Monolayers on CYTOP Polymer

Hirumune Eto¹, Naoki Soga², Henri G. Franquelim¹, Philipp Glock¹, Alena Khmelinskaia^{1,3}, Lei Kai^{1,4}, Michael Heymann¹, Hiroyuki Noji², Petra Schwille*¹

- 1- Max Planck Institute of Biochemistry, Am Klopferspitz 18, D-82152 Martinsried, Germany
 - 2- Department of Applied Chemistry, Graduate School of Engineering, The University of Tokyo, Bunkyo-ku, Tokyo 113-8656, Japan.
 - 3- Institute for Protein Design, University of Washington, Seattle, WA, USA.
 - 4- School of Life Sciences, Jiangsu Normal University, Shanghai Road 101, 221116, Xuzhou, P.R. China
- * Corresponding author: schwille@biochem.mpg.de

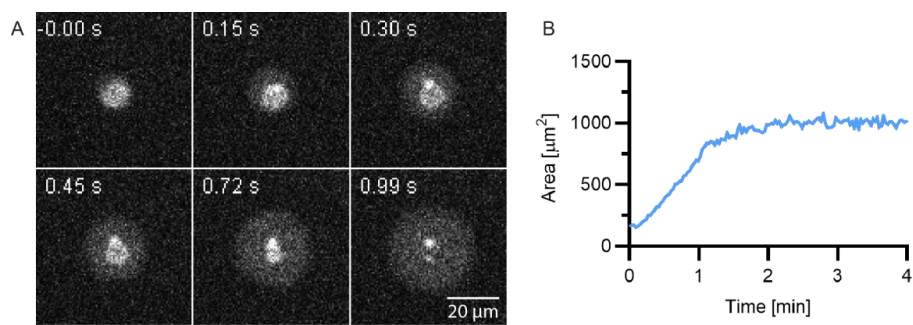


Figure S1: (A) Time lapse of GU hemifusion with CYTOP (Movie 1); (B) corresponding SAM area over time.

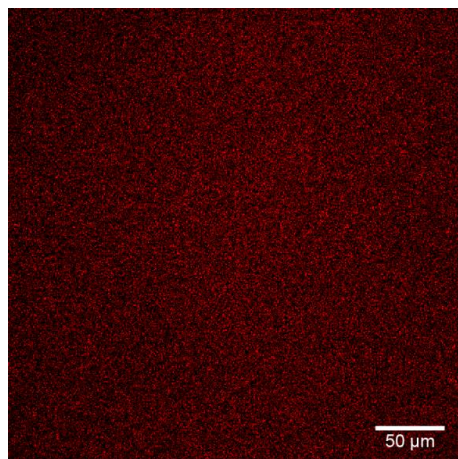


Figure S2: Homogeneous SAM coverage over 354.25 μm x 354.25 μm field of view. Lipids are labelled red with ATTO655-DOPE.

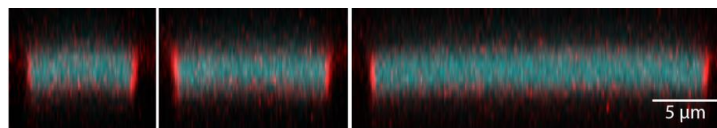


Figure S3: z-stack of sealed chambers with aspect ratios 1:1.5, 1:2.5, 1:5.

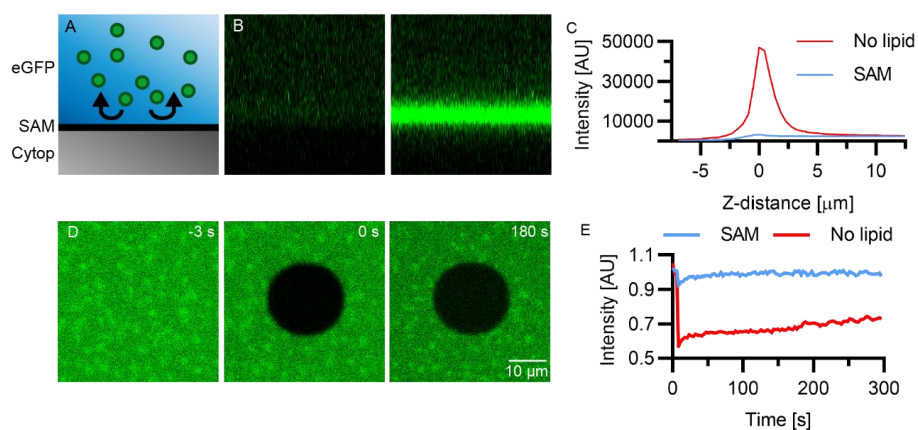


Figure S4: Passivation of eGFP against adhesion onto CYTOP surface (A). A confocal z-stack image was taken at the CYTOP surface with (B, left) and without (B, right) SAM, and intensity in Z was plotted in (C). Without the SAM passivation, intensity on the surface was 16-fold higher than in solution. FRAP analysis on the surface (D,E) showed permanent adhesion of eGFP on the CYTOP surface without SAM, as well as some aggregates.

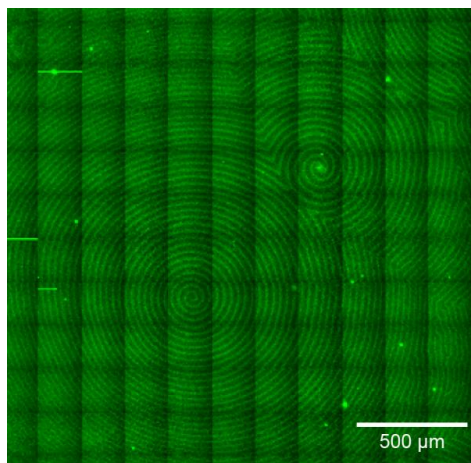


Figure S5: MinDE patterns over an extended area of 2 mm x 2 mm. Concentrations MinD 0.5 μM, MinE 0.5 μM.

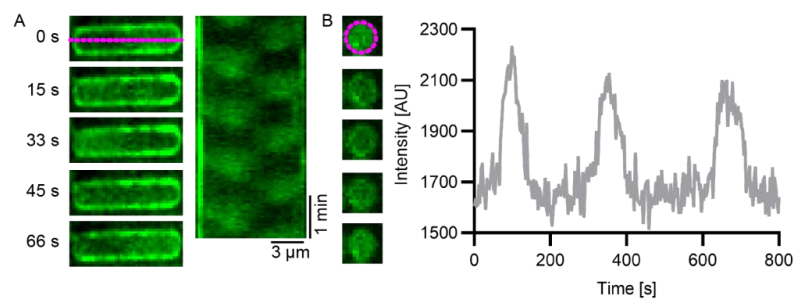


Figure S6: MinDE encapsulation in replica molded chambers. As with RIE-fabricated chambers, the longer chambers performed pole-to-pole oscillations (A) while the more symmetric chambers showed “blinking” (B), showing little difference in their behavior between the two fabrication methods.

6.3 PUBLICATION P3: Membrane-coated 3D architectures for bottom-up synthetic biology

Having explored methods to pattern membranes in 2D (section 5.1), and in compartmentalised structures fabricated from negatively molded, embossed structures (section 5.2), I turned to fabrication methods that allow us to pattern lipid membranes in fully 3D geometries. This is outlined in the associated publication P3.

In a reaction-diffusion system that involves the attachment of proteins to the lipid surface, their subsequent detachment as well as their diffusion in the bulk volume, self-organisation of the Min system is inherently dependent on spatial features in three dimensions. In order to interrogate this additional parameter space, generating fully 3D shapes that are not simply extrusions of 2D patterns, is crucial. This would give us the opportunity to engineer and systematically vary the local surface to volume ratios to study their effects on the Min pattern formation.

To achieve this, I employed two-photon laser lithography - a 3D printing technique with sub-micron spatial resolution and is thus capable of generating structures on length scales relevant to the Min system. To create membranous structures, I formed supported lipid bilayers on the surfaces of these 3D printed objects. Significantly, I undertook a thorough investigation of the lipid-substrate interaction that can be tuned in order to reliably deposit membranes on 3D printable materials.

As a proof of concept, I then printed rod-like structures as the most conceivably simple 3D object to reconstitute the MinDE system. On these structures, I found that the width of the rods compared to the typical wavelengths of Min waves is a critical parameter in giving directionality to the waves along the axis of the rods. This behaviour is similar to the observations made on 2D chromium patterned membranes, which I investigated in section 5.1.

In this work, I created a toolbox that allows us to investigate the 3D geometry dependence of membrane-interacting proteins in general. This work also outlines a robust framework by which supported membranes from different types of lipids can be formed on any material, anticipating the development of new 3D printable materials for future biological applications. This goes in line with continuous efforts in the field to imitate and recapitulate the complex 3D organisation of cells and organelles *in vitro*, to gain a better understanding of how 3D geometries affect biochemical functions.

Membrane-coated 3D architectures for bottom-up synthetic biology

Hirumune Eto, Henri G. Franquelim, Michael Heymann and Petra Schuille

Author contributions:

H.E., M.H. and P.S. conceived the project. **H.E.** performed all experiments and analysed the data. **H.E.** and H.G.F performed the GUV experiments and analysed the data. **H.E.**, H.G.F. and P.S. wrote the manuscript. All authors discussed the content and commented on the manuscript.

published in

Soft Matter (2021), 76, 4245–4273

Reprinted from [Eto2021] under the Creative Commons Attribution 3.0 Unported License
(see <https://creativecommons.org/licenses/by/3.0/>)



Membrane-coated 3D architectures for bottom-up synthetic biology†

Cite this: DOI: 10.1039/d1sm00112d

Hiromune Eto,^a Henri G. Franquelim,^a Michael Heymann^{ab} and Petra Schwille^{ab*}

One of the great challenges of bottom-up synthetic biology is to recreate the cellular geometry and surface functionality required for biological reactions. Of particular interest are lipid membrane interfaces where many protein functions take place. However, cellular 3D geometries are often complex, and custom-shaping stable lipid membranes on relevant spatial scales in the micrometer range has been hard to accomplish reproducibly. Here, we use two-photon direct laser writing to 3D print microenvironments with length scales relevant to cellular processes and reactions. We formed lipid bilayers on the surfaces of these printed structures, and we evaluated multiple combinatorial scenarios, where physiologically relevant membrane compositions were generated on several different polymer surfaces. Functional dynamic protein systems were reconstituted *in vitro* and their self-organization was observed in response to the 3D geometry. This method proves very useful to template biological membranes with an additional spatial dimension, and thus allows a better understanding of protein function in relation to the complex morphology of cells and organelles.

Received 21st January 2021,
Accepted 17th March 2021

DOI: 10.1039/d1sm00112d

rsc.li/soft-matter-journal

Introduction

Many protein functions take place at lipid interfaces; and often, geometrical features are key in regulating this interaction. For example, membrane curvature,^{1,2} compartmentalisation into droplets and vesicles,^{3,4} and formation of domains that pattern lipid surfaces^{5,6} all govern pathways by influencing protein localization and behaviour. Consequently, engineering membrane geometry to mimic cellular features, in order to faithfully reconstruct biological functionality *in vitro*, is one of the most fundamental challenges in bottom-up synthetic biology.

Over the past years, many techniques have been developed to generate artificial membranes and modulate their geometry. They often start from spherical membrane mimics, such as water-in-oil droplets and liposomes,⁷ which can be produced in large numbers and feature cell-sized volumes with phospholipid mono- or bilayer interfaces. By varying membrane curvature or surface tension through buffer exchange or membrane-transforming agents, the geometry of these delicate free-standing

vesicles can be deformed into rod- or tubular-like shapes, mimicking certain cellular geometries.^{4,8,9} However, the resulting morphologies are either ill-controlled or require sophisticated techniques that are technically challenging. In particular, since non-spherical shapes are rarely in equilibrium, they tend to be temporally unstable and hard to control. Hence, the variety of shapes that free-standing vesicle membranes can adapt to is limited. Other bilayer systems, such as black lipid membranes^{10–12} and other emulsion transfer methods¹³ also suffer from this limitation; their membrane topology and topography cannot be easily varied beyond their equilibrium state.

In this regard, supported lipid membranes on substrates provide an attractive alternative, featuring high stability of membranes and facile preparation methods.¹⁴ They can be formed on planar surfaces, but their geometry can also be varied by forming them on patterned substrates^{15–19} or on the surfaces of microfabricated compartments.^{20,21} Here, the range and size of possible geometries depends on the underlying pattern or the shape of the supporting material, which allows much greater flexibility. However, accurately recreating cellular geometries often requires complex 3D features, which conventional 2D patterning methods cannot achieve.

In order to explore more complex 3D structures for membrane sculpting, we turned to two-photon direct laser writing (2PP-DLW) – a light-initiated 3D printing technology, based on photoresist polymerisation upon the quasi-simultaneous absorption of 2 photons. Owing to the higher definition of the 2-photon point spread function, structures can be printed with

^a Department for Cellular and Molecular Biophysics, Max Planck Institute for Biochemistry, Am Klopferspitz 18, D-82152, Martinsried, Germany.
E-mail: schwille@biochem.mpg.de

^b Department of Intelligent Biointegrative Systems, Institute of Biomaterials and Biomolecular Systems, University of Stuttgart, Pfaffenwaldring 57, 70569, Stuttgart, Germany

† Electronic supplementary information (ESI) available. See DOI: 10.1039/d1sm00112d

sub-micron resolution,²² and custom-shaped 3D microenvironments can be accurately fabricated with length scales relevant to cellular processes. 2PP-DLW has been successfully employed in optics,²³ microfluidics,²⁴ soft robotics^{25–27} and biological applications,^{26,28–30} and a variety of photoresists and post-modification methods have been developed to further increase the range of chemical functionalities for the different applications.^{31–33}

To form supported lipid membranes on materials suitable for 3D lithography, Ormocomp, pentaerythritol triacrylate (PETA) and trimethylolpropane ethoxylate triacrylate (TPETA) are of particular interest. They are well established polymer systems in bio-applications because they have low cytotoxicity, are easy to handle, and show minimal autofluorescence with good transmittance of light for imaging.^{31,32,34} They are chemically and mechanically stable, with low swelling unlike typical hydrogels,³⁵ and their elastic moduli are typical for stiff polymers (Ormocomp ~ 1 GPa, PETA ~ 3 GPa and TPETA ~ 10 MPa).^{36,37} Their chemical compositions are also ideal for manipulating membranes: PETA includes an exposed hydroxyl group that aid in lipid membrane formation, whilst TPETA has a PEG-like chain that passivates against membrane fusion. Ormocomp is accessible to a wide range of available post-modification methods,^{29,38} including silanization, that can render the surface favourable for membrane formation. Therefore, these materials are ideal candidates to fabricate 3D-lipid bilayer architectures.

In this paper, we introduce a new method for generating custom-shaped membrane morphologies based on 2PP-DLW. We specifically tailor 3D printed structures that are templates for biomimetic lipid membranes – different lipid compositions can be deposited, based on charge interaction between lipids and support structures. We apply our membrane architectures to investigate the influence of particular spatial features on *in vitro* reconstituted protein systems. These include a membrane attached minimal actin cortex and the pattern forming MinDE protein system from *E. coli*, which displays dynamic self-organization in response to 3D spatial patterning. Although 2D structuring of membrane surfaces has previously been shown to alter the obtained patterns,³⁹ adding another spatial dimension will bring us an important step closer towards studying true biomimetic functionality.

Experimental

Fabrication of 3D microstructures

To enhance the adhesion of the microscaffolds to the glass substrate surface for pentaerythritol triacrylate (PETA, Sigma-Aldrich) and trimethylolpropane ethoxylate triacrylate (TPETA, Sigma-Aldrich, $M_n \sim 692$, Sigma-Aldrich), glass coverslips (22 mm \times 22 mm, borosilicate, Menzel) were initially treated with O₂ plasma (Zepto, Diener Electronic) (power 30%, pressure 0.3 mbar for 1 min), then immersed in 3-(trimethoxysilyl)propyl methacrylate (Sigma-Aldrich, $\geq 98\%$) (0.1 mL in 20 mL ethanol) overnight, rinsed in water, and dried with nitrogen. At this

point, the coverslips should be slightly hydrophobic – a visual inspection of the contact angle of a small water droplet with the surface ($>45^\circ$) should suffice. For Ormocomp (Microchem, USA), similarly plasma treated coverslips were spin-coated with OrmoPrime (Microchem, USA) for 40 s at 6000 rpm and then baked on a hotplate for 5 min at 150 °C.

For lipid assays, plane surfaces of Ormocomp and PETA were spin-coated (60 s at 6000 rpm) and UV exposed (FormCure, Formlabs) for 15 min at room temperature. As TPETA requires either an overnight exposure, or cures more efficiently with O₂-free atmosphere – a slab of PDMS was gently pressed down on a drop of photoresist and exposed to UV for 15 min at RT.

For the Min assays, treated coverslips were further spin-coated with a drop of Ormocomp and UV exposed, so that the glass surface is also coated with Ormocomp (thickness ~ 10 μm).

For 3D printing, scaffold geometries were designed in Solidworks (Dassault Systèmes, France), and print parameters then specified in Describe (Nanoscribe GmbH, Germany) and fabricated on a commercial DLW system (Photonic Professional, Nanoscribe GmbH, Germany) with a Zeiss LCI “Plan-Neofluar” 25 \times /0.8 objective, corr-ring set on oil immersion. The photoresist was drop-cast onto the coverslip and the 3D microscaffolds were printed with an oil immersion (Carl Zeiss Immersol 518F). After exposure, the structures were developed and rinsed with isopropyl alcohol (for PETA and TPETA) or OrmoDev (Microchem, USA) and then isopropyl alcohol (for Ormocomp). The structures were kept submerged in isopropyl alcohol (IPA) and dried using a critical point dryer (Leica EM CPD300). This was because drying the beam structures directly in air would lead to them collapsing due to surface tension – for larger, sturdier structures, drying in air would be sufficient.

For composite printing, PETA was dropcast on spin-coated TPETA. The grids were printed at 80% laser power and 15 000 $\mu\text{m s}^{-1}$. The sample was then developed and rinsed with isopropyl alcohol and dried in a stream of air.

Scanning electron microscopy

Samples were first sputter-coated with platinum/palladium on a high-resolution automatic sputter coater (Cressington 208HR) at 20 mA and 0.1 mbar Argon for 3 \times 20 s. The thickness of the applied coatings was measured with a built-in thickness controller to be 2.0 nm. They were then imaged using TESCAN MIRA3 FESEM operating at an accelerating voltage of 10 kV in SE mode.

Homogeneous bilayer formation by small unilamellar vesicles (SUV) fusion

All lipids were purchased from Avanti Polar Lipids (Alabaster, AL, USA), unless otherwise stated. Small unilamellar vesicles (SUVs) composed of DOPC (1,2-dioleoyl-*sn*-glycero-3-phosphocholine) for neutral lipid membranes, DOPC/DOPG (1,2-dioleoyl-*sn*-glycero-3-phospho-(1'-rac-glycerol)) for negatively charged membranes, or DOPC/DOTAP (1,2-dioleoyl-3-trimethylammonium-propane) for positively charged membranes, containing Atto655-DOPE (Atto-TEC GmbH, Siegen, Germany) in 7:3:0.005 molar ratio. Lipids dissolved in chloroform were dried under a nitrogen stream, and



vials were placed in a desiccator to remove residual chloroform for at least 2 h. Afterwards, lipids were rehydrated in a buffer to a concentration of 4 mg mL⁻¹. One of two types of buffer was used, depending on the required conditions. pH Buffer (0.1 M Na₂CO₃ and 0.1 M Na₂HCO₃ mixed in 6:4 volume ratio, pH 10.1) was prepared to provide basic conditions for deprotonation of hydroxyl groups. Buffer M (25 mM Tris-HCl, 150 mM KCl, 5 mM MgCl₂, pH 7.5) was used for APTES-treated Ormocomp structures. SUVs were then generated by sonication in a water bath (model 1510; Branson) until the solution appeared clear.

SUVs were added to a chamber, assembled from a silicone isolator chamber (Thermo Fisher Scientific, 0717104) pressed on to the coverslip, at a concentration of 0.5 mg mL⁻¹ diluted in the buffer of choice. After 3 min incubation at 37 °C on a heating block, the supported lipid bilayer (SLB) was gently washed with a total of 600 µL buffer S (25 mM Tris-HCl, 150 mM KCl, pH 7.5) to remove excess vesicles.

For the silanisation treatment of Ormocomp, the samples were first plasma treated with argon plasma (Model 950 Advanced Plasma System, Gatan), and then incubated in (3-aminopropyl)triethoxysilane (Sigma-Aldrich) at a dilution of 0.1 mL in 25 mL ethanol for 5 min. The samples were then rinsed in IPA and water. For delicate structures, the chamber was assembled with the sample still submerged in water so that the structures did not collapse under surface tension during drying. The water was exchanged with buffer, and the SUV concentration was adjusted to 0.5 mg mL⁻¹.

Lipid patch formation by giant unilamellar vesicle (GUV) fusion

Giant unilamellar vesicles (GUVs) composed either of DOPC (neutral), DOPC/DOPG (negative) or DOPC/DOTAP (positive) mixtures with Atto655-DOPE (1,2-dioleoyl-*sn*-glycero-3-phosphoethanolamine) in 8:2:0.0005 molar ratio were produced by electroformation in polytetrafluoroethylene chambers with platinum electrodes 4 mm apart, as described previously.^{40,41} Briefly, 6 µL of the lipid mixture (2 mg mL⁻¹ in chloroform) was spread onto two platinum wires and dried in a desiccator for 30 min. The chamber was then filled with 370 µL of a 250 mOsm kg⁻¹ aqueous solution of sucrose. An AC electric field of 2 V (RMS) was applied at a frequency of 10 Hz for 1.5 h, followed by 2 Hz for 45 min. The obtained solution was diluted 1:10 in volume in 250 mOsm kg⁻¹ sucrose and further diluted 1:7 in volume in their respective buffers. The vesicle solution was then deposited directly onto the polymer surface, and left for several minutes until the vesicles sank to the bottom and came into contact with the surface.

Fluorescence microscopy

FRAP experiments on plane surfaces were done on Nikon Eclipse Ti2 in a TIRF (total internal reflection fluorescence) set-up using a Nikon Apo TIRF 60×/1.4 oil immersion objective. We used the 640 nm diode laser lines to image Atto655-DOPE. FRAP experiments on patterned membrane patches were done on a Zeiss LSM780 confocal laser scanning microscope using a C-Apochromat 40×/1.20 water-immersion objective (Carl Zeiss

AG, Oberkochen, Germany). Atto655-DOPE was excited by the 633 nm He-Ne laser.

Likewise, F-actin filament and MinDE self-organisation assays were imaged on a Zeiss LSM780 confocal laser scanning microscope using a Zeiss C-Apochromat 40×/1.20 water-immersion objective (Carl Zeiss AG, Oberkochen, Germany). Alexa488 was excited using the 488 nm argon laser, Alexa568 on the 561 nm DPSS laser and Atto655-DOPE using the 633 nm He-Ne laser. Obtained images were processed using Fiji.⁴²

4D images were taken with Nikon Eclipse Ti in a spinning disk confocal set-up, with the Nikon Plan Fluor 20×/0.75 water immersion objective (both Nikon GmbH, Düsseldorf, Germany). We used the 490 and 640 nm diode laser lines to image GFP and Atto655-DOPE, respectively. We then used a custom written script to reconstruct the 4D images. Briefly, the images were first processed by successive filters: Gaussian 3D Blur ($x = 3, y = 3, z = 10$; Subtract Background (rolling ball radius = 20, sliding paraboloid); Median 3D ($x = 3, y = 3, z = 1$). The 3D timelapse images from different fluorescence channels were then merged into one composite color hyperstack, and visualized using 3D Viewer (Display as = Volume, Color = None, Threshold = 0, Resampling factor = 2).

Fluorescence recovery after photobleaching (FRAP)

For FRAP on plane surfaces, a circular spot of 5 µm diameter was illuminated with full laser power for 260 ms, and the average fluorescence intensity was recorded every 3 s over 300 s. For FRAP on patterned membrane patches, the defined regions of interest were illuminated with full laser power for 0.82 s (50 iterations on the Zen Black software (Carl Zeiss AG, Oberkochen, Germany)), and the average fluorescence intensity was recorded every second for 100 s for the 2.5 µm diameter circular region, and every 3 s for 300 s for the entire square patch. Measurements were taken at room temperature (23 °C). Intensity in a second area of the same dimensions was recorded in the same field of view, in order to correct for the intensity drift. The intensity trace was fit to the equation derived by Soumpasis.⁴³

$$f(t) = e^{-\frac{2\pi r^2}{t}} \left(I_0 \left(\frac{2\tau_D}{t} \right) + I_1 \left(\frac{2\tau_D}{t} \right) \right) \quad (1)$$

Here, τ_D is the characteristic timescale for diffusion, and t is the time. $f(t)$ is the normalized fluorescence, and I_0 and I_1 are modified Bessel functions. The diffusion timescale for a bleached spot of radius r is $\tau_D = r^2/4D$ with D the diffusion coefficient. A custom script written in Python was used for curve fitting and data analysis.

Atomic force microscopy

AFM was performed on a JPK Instruments Nanowizard III BioAFM mounted on a Zeiss LSM510 Meta laser scanning confocal microscope (Jena, Germany). AFM measurements were taken after locating the membrane patch by confocal microscopy. Cantilevers (BL-AC40TS-C2, Biolever Mini, Olympus) were used for the quantitative imaging (QI) mode, with typical



spring constants of 0.09–0.1 N m⁻¹. Setpoint force was set to 200–250 pN, acquisition speed to 61.1 μm s⁻¹, Z-length to 110 nm and image resolution to 256 × 256 pixels. Data was analyzed using JPK data processing software Version 5.1.4 (JPK Instruments).

F-Actin filament assays

Actin filaments were prepared according to the published protocol.^{44,45} Briefly, rabbit skeletal muscle actin monomers (Molecular Probes) and biotinylated rabbit actin monomers (tebu-bio, Cytoskeleton Inc.) were mixed in a 5 : 1 (actin : biotin-actin) ratio. Polymerization of the mixture (39.6 μM) was induced in Buffer F containing 50 mM KCl, 2 mM MgCl₂, 1 mM DTT, 1 mM ATP, 10 mM Tris-HCl buffer (pH 7.5). The biotinylated actin filaments were labelled and stabilized with Alexa-Fluor 647 Phalloidin (Molecular Probes) according to the manufacturer protocol.

We formed the SLB as described previously, with DOPC/DOTAP (1,2-dioleoyl-3-trimethylammonium-propane), 1,2-dioleoyl-*sn*-glycero-3-phosphoethanolamine-*N*-(cap biotinyl) and Atto655-DOPE (Atto-TEC GmbH, Siegen, Germany) mixed in 6.75 : 2.75 : 0.5 : 0.0005 molar ratio. Streptavidin Alexa 568-conjugate (Thermo Fischer Scientific) was subsequently added at 10 nM concentration and incubated for at least 30 min. After washing away the excess streptavidin with Buffer F, F-actin filaments were added at a final concentration of 200 nM. Filaments were incubated for at least 1 h at room temperature, and the unattached filaments gently washed away with Buffer F before imaging.

MinDE self-organisation assays

MinDE dynamics were reconstituted as previously described.⁴⁶ Briefly, a mixture of 1 μM MinD (doped with 30% EGFP-MinD), 2 μM MinE, and 5 mM ATP (from 100 mM ATP stock in 100 mM MgCl₂, pH 7.5) in buffer M was first prepared. The mixture was then loaded onto the chambers to a final concentration of 0.5 μM MinD (doped with 30% EGFP-MinD), 1 μM MinE, and 2.5 mM ATP (*i.e.*, to half the concentration) and incubated for at least 30 min at room temperature (23 °C) before imaging.

2. Results and discussion

2.1. 3D laser lithography of microstructures

Engineering functional lipid-coated 3D geometries before a possible *in vitro* reconstitution of membrane proteins involves three main steps: (1) microfabrication of the 3D structures, (2) surface modification of the polymers to specifically tune lipid-polymer interactions, and (3) lipid deposition to prepare supported lipid membranes (schematic shown in Fig. 1A). In the microfabrication step, we performed a 4-dimensional parameter sweep (laser power, scan speed, z-slicing and xy-hatching), and analysed the outcome for quality by scanning electron microscopy (SEM). All these parameters contribute to the deposited energy density, which regulates the degree of polymerisation. The slicing and hatching parameters with respect to the polymerisation voxel (determined by the optical

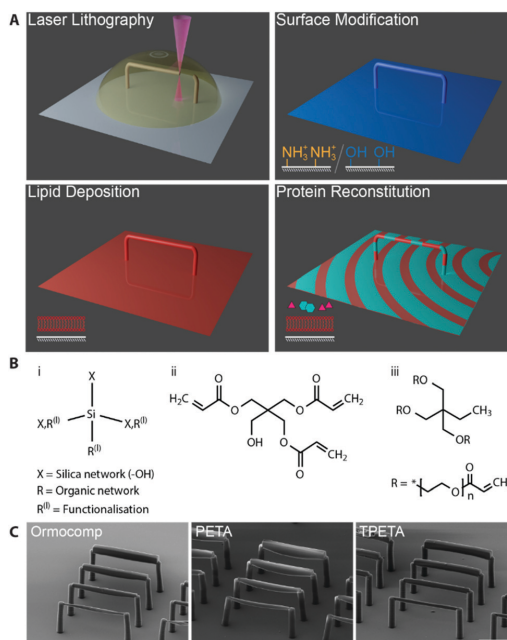


Fig. 1 (A) Schematic of the work flow. Microstructures are printed by two-photon lithography. The microstructure surface is then modified to promote lipid membrane fusion, and coated by a supported lipid membrane. Afterwards, purified proteins are reconstituted *in vitro*. (B) Chemical structures of (i) Ormocomp and (ii) PETA, which allow SLB formation, and (iii) TPETA, which passivates against SLB formation. (C) scanning electron microscopy images of beam structures printed with (left to right) Ormocomp, PETA and TPETA at their near-optimum settings (see Fig. S1 for a detailed parameter sweep, ESI[†]). Scale bar 50 μm.

set up, chemical composition, laser power and scan speed⁴⁷) also affect the structure quality. For example, a very coarse hatching with a small polymerisation voxel could lead to rough surface quality as well as underexposure.

We printed rod-like structures (length 100 μm, and widths 2–10 μm), as a minimal complexity design to first test out our printing parameters, (see Fig. S1 for parameter sweep, ESI[†]), and we subsequently used them in our *in vitro* reconstitution experiments. No stable structure could be printed below 2 μm width. For each of the resists (chemical structures shown in Fig. 1B), we found that the optimum writing conditions were: Ormocomp (power 80% speed 10 000 μm s⁻¹ slicing 0.1 μm hatching 0.5 μm), PETA (power 80% speed 10 000 μm s⁻¹ slicing 0.3 μm hatching 0.1 μm) and TPETA (power 100% speed 10 000 μm s⁻¹ slicing 0.3 μm hatching 0.1 μm), all with XY hatching at 90° (perpendicular) to the axis of the rods (Fig. 1C). We found that the dynamic range (range of parameters from where polymerisation starts to occur up to where resist explodes due to overexposure) of Ormocomp is narrow compared to PETA and TPETA. The narrow range of Ormocomp is consistent with previously reported results,⁴⁸ and could potentially be broadened by use of additional photoinitiators.



We also found that hatching at 90° (perpendicular) to the axis of the beams provided much better results as compared to hatching at 0° (parallel) to the axis (Fig. S2, ESI†). For structures with high *xy* aspect ratios (length much longer compared to width), the time taken between adjacent hatchlines is much shorter with perpendicular hatching. Each hatchline is immediately stabilised by the adjacent hatchline before it has time to deform under gravity or drift, which resulted in much more stable layers of print being formed.

2.2 Surface modification of polymers for membrane fusion

After the fabrication, we went on to coat the surfaces of our printed structures with lipid membranes. Supported lipid membranes can be formed by vesicle fusion,⁴⁶ whereby an attractive interaction between the lipid and the surface promotes vesicles to rupture and spread on the surface. A more detailed understanding of this process is extremely complex, as it involves a large set of parameters on both the surface and the membrane, including higher order molecular interactions, charge density on both membrane and polymer surface, as well as surface roughness.^{49,50} However, we can gain qualitative insights into the probable lipid behaviour by considering the charge interaction between the lipid headgroups and the functional groups on the polymer surface.⁵¹ Thus, by considering the molecular structures, we formulated lipid-polymer combinations that would form supported lipid bilayers (SLBs).

PETA has hydroxyl groups which can be deprotonated under alkaline conditions (Fig. 1B). The presence of negative charges on the surface promotes fusion of positively charged lipid vesicles *via* direct electrostatic interaction. Ormocomp is a commercially available polymer consisting of an organic/inorganic (silica) hybrid network, in which hydroxyl groups are also present. However, the detailed chemical composition is undisclosed. Similar to PETA, these hydroxyl groups can also be deprotonated at high pH, and thus likely a useful support for membranes with an overall positive charge. In order to support negative or neutrally charged lipids, deprotonated hydroxyl groups on PETA and Ormocomp can often be bridged by positively charged divalent ions such as calcium, which is also commonly used to support negatively charged lipids on glass.⁵²

In addition to the native properties of the polymers, there is a range of well-documented post-functionalisation methods for Ormocomp.^{32,38} The presence of the inorganic backbone in its chemical structure means that many treatments can be done similarly to treating glass or silicon dioxide. It can first be plasma-treated, which exposes more hydroxyl groups. This can again be used to support positively charged membranes or be bridged by divalent ions to support negative or neutral lipids. Ormocomp can further be silanized, by which positively charged amine groups are incorporated on the surface of the material by (3-aminopropyl)triethoxysilane (APTES) treatment.⁵³ Hence, silanization allows negatively charged vesicles to fuse with the surface. Note that oxygen plasma cannot be used with Ormocomp, since it reacts with the inorganic component in the polymer network and forms porous structures.⁵⁴ Hence, we have several possibilities to manipulate charge interactions that

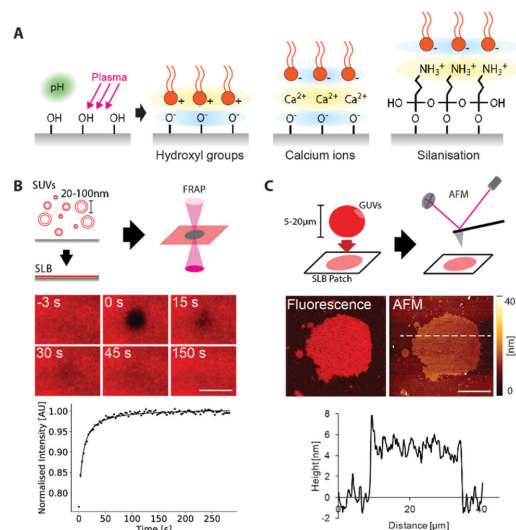


Fig. 2 Lipid interactions with polymer surfaces. (A) Functional groups on the polymer surface promotes membrane fusion with positive or negative lipid headgroups. (B) Homogeneous lipid membranes were formed by SUV fusion. Fluidity of the SLB was measured by FRAP. Time lapse images of FRAP, and the associated intensity trace, performed on Ormocomp with APTES treatment with DOPC:DOPG lipids doped with 0.005 mol% Atto655-DOPE. Scale bar 5 μm (C) Bilayer verification on Ormocomp. Membrane patches were prepared by fusing GUVs to the polymer surface. The membrane height (4.7 ± 0.7 nm) was measured by atomic force microscopy. Scale bar 20 μm , colour bar range 0–40 nm.

would favour fusion with vesicles of the desired lipid type with PETA and Ormocomp (Fig. 2A).

TPETA, on the other hand, has PEG-like chains in their structure, which is a known passivation agent against molecular adhesion and adsorption,³² and can also prevent vesicle fusion. This passivating property of TPETA, when combined with the lipophilic property PETA and Ormocomp, could allow us to print composite structures, where we can selectively target membrane supported regions. Thus, based on simple chemistry, we evaluated multiple combinatorial scenarios to generate 3D membrane geometries with desired membrane affinity.

These charge-based considerations do not only apply to the materials investigated here, but could also be used as starting points for forming membranes on any newly developed material. As more and more photoresins are being developed for 3D printing, materials with improved physical and chemical properties would significantly widen the scope of our biological research. For example, soft materials such as shape-shifting hydrogels²⁶ and protein-based hydrogels^{55–57} would allow us to create flexible and deformable structures, potentially enabling us to investigate how cytoskeletal proteins deform membranes. Materials with better optical properties are also crucial. With fluorescence-based, dynamic imaging of biological samples, the resolution and the image quality of membrane processes rely heavily on refractive index matching between the sample



and the surrounding medium. Materials such as CYTOP⁵⁸ and MyPolymer⁵⁹ have similar refractive indices to water, which would allow super-resolution imaging, and this would give us the chance to probe biological samples at a higher level of detail.

2.3. Supported lipid membrane formation on polymer surfaces

Next, we tested how well the different combinations of polymer and surface modifications support lipid membranes of different charges. We generated small unilamellar vesicles for vesicle fusion at a high concentration of vesicles (with the amount of lipid much greater than needed to completely cover all surfaces) and deposited them on planar, spin-coated polymer surfaces. Subsequently, we checked for homogeneous, fluid bilayers indicative of continuous membranes with no defects by fluorescence recovery after photobleaching (FRAP) of labelled lipids (Fig. 2B). Diffusion coefficients are summarised in Table 1, and immobile fractions in Table S1 (ESI[†]).

We found that for negative and neutrally charged lipids, Ormocomp with plasma treatment and silanization, or with divalent ion bridging, resulted in membranes with the highest fluidity ($0.6 \pm 0.4 \mu\text{m}^2 \text{s}^{-1}$), comparable to those of membranes on the commonly employed substrate, glass ($0.9 \pm 0.4 \mu\text{m}^2 \text{s}^{-1}$).^{60,61} Even though the fluidity of supported bilayers is typically slower than those of free-standing bilayers (which can be up to $20 \mu\text{m}^2 \text{s}^{-1}$),⁶² the support does not significantly interfere with biological functions of many membrane proteins, as shown in previous studies.^{16,63} Untreated Ormocomp or PETA with divalent ion bridging showed very little fluorescence recovery in the timescale of our experiments, indicative of immobile membranes. For positively charged lipids, Ormocomp with plasma treatment, as well as untreated PETA, formed fluid bilayers (Fig. S3, ESI[†]), whilst untreated Ormocomp formed immobile membranes. On TPETA, supported lipid membranes were not formed, indicated by the lack of fluorescence on the polymer surface after vesicle deposition (Fig. S3, ESI[†]).

Table 1 Lipid diffusion coefficients obtained from FRAP experiments on supported membranes. Units in $\mu\text{m}^2 \text{s}^{-1}$. Fluid bilayers are indicated in bold, which have values comparable to or faster than those formed on glass. Immobile bilayers are indicated in italics. Errors are standard deviations calculated from 9 measurements (3 samples at 3 different locations on the membrane each)

Negative/neutral charged lipids			
Material	Surface modifications	DOPC/DOPG	DOPC
Ormocomp	Plasma + APTES	0.6 ± 0.1	0.7 ± 0.4
	Plasma + pH buffer + $\text{Ca}^{2+}/\text{Mg}^{2+}$	0.6 ± 0.4	0.7 ± 0.3
	pH buffer + Ca/Mg	<i>0.2 ± 0.05</i>	<i>0.1 ± 0.03</i>
PETA	pH buffer + Ca/Mg	<i>0.006 ± 0.0004</i>	<i>0.05 ± 0.003</i>
Positive charged lipids			
Material	Surface modifications	DOTAP	
Ormocomp	Plasma + pH buffer	2.3 ± 1.3	
	pH buffer	<i>0.3 ± 0.03</i>	
PETA	pH buffer	1.1 ± 0.1	

Having determined the fluidity of the respective membranes, we confirmed whether the membrane was indeed a lipid bilayer and not a lipid monolayer, as for the case of some other polymer-supported membranes.²⁰ For this, we prepared giant unilamellar vesicles (GUVs), sized typically 5–20 μm , which form large membrane patches when they fuse onto the surface. These patches were individually imaged, by both fluorescence microscopy and atomic force microscopy, which allowed us to simultaneously verify the presence of the membrane patch, and also to directly measure the membrane height.

We measured the height of the bilayer patch for Ormocomp ($4.7 \pm 0.7 \text{ nm}$, Fig. 2C) and PETA ($4.7 \pm 0.9 \text{ nm}$, Fig. S4, ESI[†]). The error was calculated as a standard deviation from 3 cross-sections taken from 2 independent bilayer patches (total 6 cross-sections). Typical lipid membranes with di-oleyl acyl-chained lipids have an approximate thickness of 5 nm in height.⁶⁴ Both measurements are therefore well within the height range of bilayers. When GUVs were deposited on TPETA, GUVs did not rupture and remained intact, which was confirmed by confocal microscopy (Fig. S5, ESI[†]).

We conclude that, on PETA and Ormocomp, lipid bilayers of different charged lipids can be formed, with membrane fluidity comparable to those formed on glass. In contrast, TPETA does not support membrane formation, and passivates against membrane fusion.

The processes we employed here to investigate membrane formation can be applied to other material, surface modification and lipid combinations that are more application specific. In many cases, synthetic lipids are suitable mimics for natural lipids – for example, most prokaryotic cell membranes are negatively charged, and therefore, many bacterial protein systems can be reconstituted on membranes containing DOPG.^{65–67} A wider variety of lipid species, such as PIP₂ or DOPS, could be investigated to further extend the range of protein systems to be recruited. Membranes could also be formed on polymer cushions, *e.g.*, polyethylene glycol (PEG)-silanes, and this would allow the *in vitro* reconstitution of transmembrane proteins.^{68,69} Such investigations would support us to further improve the biomimicry of our fabricated microenvironment.^{31,70}

2.4. Lipid patterning by composite printing

One of the most attractive features of engineering microenvironments is the ability to spatially position molecules to mimic the spatial order and organisation within a living cell. Having found the polymer–lipid composition combinations that either allow or passivate against vesicle fusion, we printed composite structures that allowed selective membrane deposition. For these structures, we utilised PETA and TPETA (without post-modifications), where untreated PETA supports positively charged membranes in alkaline conditions, whereas TPETA passivates against them. We designed 10 μm grids consisting of PETA, with 10 μm spacing, that were printed on top of a planar TPETA surface.

We deposited labelled lipids (DOPC : DOTAP 7 : 3 molar ratio doped with 5 mol% biotinylated lipid and 0.005 mol% Atto655-DOPE) on these structures and observed lipid–dye fluorescence



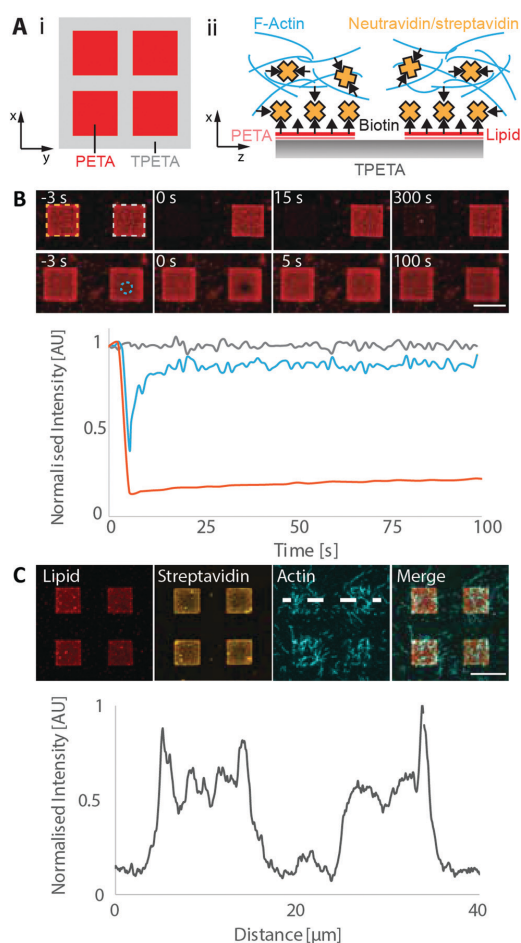


Fig. 3 Lipid patterning by composite printing. (A) Schematics of (i) PETA grids printed on TPETA surface and (ii) *in vitro* reconstitution of actin filaments on patterned lipids. (B) FRAP experiment on membrane patches. Membranes with labelled lipids (DOPC : DOTAP 7 : 3 molar ratio doped with 5 mol% biotinylated lipid and 0.005 mol% Atto655-DOPE) were formed on square-patterned PETA patches, where an entire square (orange, top row) and a 2.5 μm diameter circular region (blue, bottom row) were subsequently bleached. Fluorescence intensity vs. time from these regions are plotted with: bleached square (orange), unbleached square (grey) and circular region (blue). (C) Confocal images of patterned lipids and actin filaments after incubation with streptavidin. Its associated intensity trace along the indicated line is plotted. Scale bar 10 μm .

only in the 10 μm squares with 10 μm spacing, indicating that membranes formed only on the PETA surface (Fig. 3).

To assess the mobility of the lipids on these membrane patches, we first bleached a single, entire square. This square did not recover in fluorescence in the timescale of our experiments (5 min), showing that the individual membrane patches are indeed disconnected (Fig. 3B). We also bleached a smaller circular region of 2.5 μm diameter within a membrane patch, and the

fluorescence recovered with a diffusion coefficient of $1.3 \pm 0.8 \mu\text{m}^2 \text{s}^{-1}$, which is similar to the values obtained on plane surfaces.

To demonstrate the utility of selective membrane deposition for targeting specific molecules onto the membranes, we used our previously developed minimal actin cortex.⁴⁴ In this setup, biotinylated lipids in the membrane are bound by streptavidin that in turn recruit stabilised and biotinylated actin filaments. We found that the streptavidin was selectively recruited to the lipid patches and that the actin filaments accumulated in this area (Fig. 3C). We also performed a control experiment, where the membranes were not incubated with streptavidin before the deposition of actin filaments (Fig. S6, ESI[†]). We observed that a significantly reduced number of actin filaments were localized on the membranous patches. We can still see a slightly increased intensity on the membrane, as compared to the surrounding regions, which can be attributed to the non-specific binding of actin filaments with positively charged lipids due to electrostatic forces.^{71,72}

Lastly, we performed a control on a planar PETA surface, where streptavidin was reconstituted with and without the formation of the lipid bilayer. As expected, we found that streptavidin was detected on the surface only with the presence of the lipids, excluding the possibility that they are simply adsorbing on the PETA surface (Fig. S7, ESI[†]), but are selectively recruited to the membranes by biotin-streptavidin coupling.

These results demonstrate that positive lipids can be patterned by composite printing of PETA and TPETA, which can further be employed to spatially pattern proteins.

2.5. Dynamic protein patterns on 3D microstructures

One of the major methodological advantages of 3D printing is that we can produce full 3D shapes that are not simply extrusions of 2D patterns. This added dimensionality gives us the opportunity to engineer and systematically vary the surface to volume ratio. This is a crucial parameter for reaction-diffusion processes that involve membranes for confinement and as catalytic surfaces, as peripheral membrane proteins attach to the lipid surface, and detach and diffuse in the bulk volume. In order to further explore this capability of our technique, we investigated the *E. coli* MinDE system, which has been shown *in vivo* to be a spatial regulator that positions the division ring to midcell,⁷³ and forms dynamic patterns when reconstituted on supported lipid membranes *in vitro*.^{63,74}

Pattern formation of the *E. coli* MinDE system involves two proteins: MinD and MinE. MinD forms a dimer in the presence of ATP, upon which it attaches cooperatively to the membrane (autocatalytic attachment). At higher local concentrations on the membrane, it recruits MinE, which stimulates MinD's ATPase activity that triggers its detachment from the membrane (catalytic detachment). This forms the basis for a reaction-diffusion mechanism, where the two proteins cycle between the bulk volume and the lipid surface, and is dynamically regulated by biochemical reactions between them. The patterns are therefore strongly dependent on geometry with different surface to volume ratios. On planar surfaces with (quasi-) infinite



Paper

bulk volume,⁶³ Min proteins form travelling waves; on patterned (finite) surfaces with infinite bulk volume they produce directional waves;³⁹ and in confined, cylindrical geometry, they perform pole-to-pole oscillations³ that are also seen *in vivo*.⁷³

In order to investigate MinDE's geometry sensitivity in more detail, we devised a selection of 3D lipid architectures. As MinDE require negatively charged membranes for self-organization,⁶⁵ we printed structures with Ormocomp and silanized them. A previous study on 2D patterned bilayers showed that MinDE waves switch from directional waves on long strips of membranes to more chaotic, spiral patterns when the strip width increased.³⁹ We wanted to observe whether MinDE patterns would respond in a similar fashion in 3D. Therefore, we first designed rod-like structures (Fig. 4B), and increased the width in the mid-section of the rod from 10 to 50 μm , thereby providing larger surface area for the available volume.

When we reconstituted the MinDE proteins *in vitro*, they formed traveling wave patterns on the structures with qualitatively different behaviours. For the 10 μm rod, waves travelled directionally along the axis, assimilating 1D waves. As we increased the width, we found that at 20 μm , the pattern resembled the spiral/chaotic patterns often seen on planar surface assays (Fig. 4C, D and Fig. S8, Movie 1, ESI[†]). The kymographs taken along the axis of the rods also reveal that the waves travel unidirectionally along the rod for narrow widths; whereas for the 20 μm case, the waves travel outwards from the centre of the spiral. Other wave properties are similar to previously reported experiments: the measured period (1–2 min) and wavelength

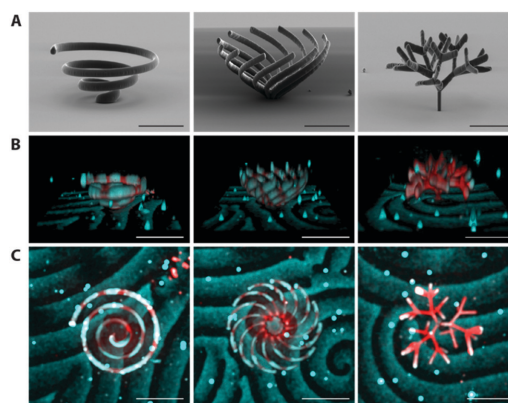


Fig. 5 Visualization of MinDE dynamic patterns on complex structures (Movie 2, ESI[†]). (A) SEM images of printed structures. (B) 3D view and (C) Top view of Min patterns on structures. Lipids are visualized in red, and MinD in cyan. The patterns were imaged as a 3D time lapse on a spinning disk confocal microscope, and processed using a custom written Fiji script. Scale bar 100 μm .

(~ 40 μm) compare well with previous studies on bilayers (period 0.6–2 min, wavelength 50–110 μm).⁷⁴ Since the width of the 10 μm rod is much smaller than the typical wavelength of the waves, the waves are spatially confined to travel along the long axis. This effect has previously been seen on 2D-patterned membranes,^{3,21,39} as well as *in vivo* by moulding bacteria into shapes.⁷⁵

In order to demonstrate the complexity of membrane morphology that could be obtained with this method, we designed a single spiral, a multi-spiral and a fractal tree that we coated with lipids. We then reconstituted MinDE proteins *in vitro* to show that the membranes retain functionality even at such complex shapes. To capture the full 4D information resulting from the Min dynamics on the 3D structures, we turned to spinning disk confocal microscopy. The fast frame rates (typically < 100 ms, compared to ~ 1 s for a confocal laser scanning microscope) allowed us to record 3D Z-stacks (50–60 slices at 2–3 μm intervals) at sufficient temporal resolution (10 s) (Fig. 5, Movie 2, ESI[†]). On both the single and the multi-spiral structures, the waves travel linearly on each of the rods, similarly to the horizontal rod. The waves on the fractal tree become more chaotic, due to the high density of branches that complexify the bulk-to-surface ratio, but an overall directionality of waves travelling from the central stem to the outside branches can still be visually confirmed.

With the toolbox developed here, we can now explore much more complex 3D geometries, which will allow us to investigate this behaviour in more detail. For example, MinDE do not only form traveling waves, but exhibits many more patterns such as quasi-stationary patterns⁷⁶ that so far have only been observed in quasi-infinite plane and bulk volume assays. Recent theoretical analysis of the MinDE system has reported that the pattern formation of MinDE heavily depends on the surface to volume coupling, suggestive of even richer and partly

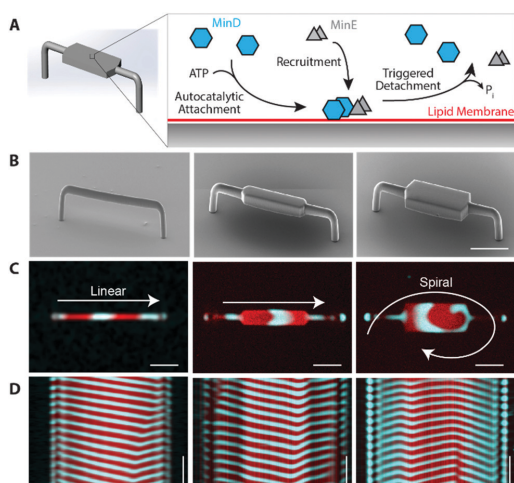


Fig. 4 MinDE dynamic self-organisation on 3D structures. (A) Schematic of MinDE molecular mechanism. (B) SEM images of printed structures. (C) Confocal images of dynamic patterns on the structures (from left to right, 10 μm , 20 μm , 50 μm widths), seen from the bottom of the structures. Images from the top and their 4D reconstructions are shown in Fig. S8 and Movie 1 (ESI[†]). (D) Kymograph of pattern taken along the axis of rods. Scale bar 20 μm horizontal, 4 min vertical.



unexplored MinDE pattern formation.^{77,78} In addition to their role as the spatial indicators of the *E. coli* midcell, MinDE waves have also been shown to position and transport biologically unrelated membrane-bound molecules by non-specific interactions.⁶⁷ The directionality of MinDE waves on rods demonstrated here could be exploited to specifically guide MinDE waves and thereby transport arbitrary molecules on membrane surfaces to a desired location. Taken together, this promises fascinating further developments in many directions: the practical toolbox introduced here, theoretical modelling of Min dynamics in three dimensions, as well as the computational tools that allow 4D image analysis,^{79–81} which are all required to investigate these questions further.

Together with the recent advances in cell-free protein reconstitution *in vitro*, the 3D printed structures demonstrated here can be used to template biological membranes and significantly expands the toolkit for bottom-up synthetic biology. Although self-assembly and self-organization of functional biomolecules have been shown to partly reproduce subcellular structures, the morphological complexity of cells and organelles can still be much more efficiently addressed by additionally employing cutting-edge microengineering technology. Membranous structures like the endoplasmic reticulum, or the invaginations in the mitochondria are systems where the membrane area per reaction volume is carefully and actively regulated, and such structures can be the target of a systematic investigation. Our work can be considered a starting point for the further 3D engineering of lipid–polymer interactions using multiple lipid types, materials with greater deformability and compositional complexity, and by miniaturisation of printed materials. Biochemical investigations in such biomimetic 3D geometries shed new insights into molecular mechanisms of proteins and open up new applications in bioengineering, with an added dimensionality to the conventional 2D fabrication techniques.

Conclusions

In this work, we have introduced a novel method to fabricate microenvironments for investigations of protein–lipid interactions modulated by geometry. In order to obtain structures at biologically relevant length scales, we employed 2-photon direct laser writing to 3D print micron-sized structures from PETA, TPETA and Ormocomp. We showed that supported lipid membranes can be formed on PETA and Ormocomp, whilst TPETA passivates. By utilising these properties and incorporating them as a composite structure, membranes as well as membrane-associated proteins can be spatially patterned. Engineering surface to volume ratios on the micrometer scale, our method enables fabrication of true 3D geometries to study the dependence of protein self-organization through reaction-diffusion, in particular the MinDE system from *E. coli*, on membrane morphology, as visualised through 4D image analysis. We recapitulate the striking transition from regular to more turbid wave fronts as soon as membrane dimensions exceed the scale of the wavelength in a particular direction,

indicating how tightly this protein system is adapted to a specific spatial setting within rod-like cells.

Conflicts of interest

There are no conflicts to declare.

Acknowledgements

We thank Enrico Lemma, Mark Hippler and Martin Bastmeyer (Karlsruhe Institute of Technology, Germany) for their helpful discussions on 2-photon photoresist optimization. We also thank Allen Liu (University of Michigan, USA) as well as Beatrice Ramm (Princeton University, USA) for insightful comments on the manuscript. We also thank the Biochemistry Core Facility of the Max Planck Institute of Biochemistry for assistance with protein purification, and the Imaging Core Facility of the same institution for assistance on the 4D image visualisation. The authors recognize financial support from Max Planck Bristol Centre for Minimal Biology and the Max Planck Society (MPG), as well as support from Center for Nanosciences, Munich.

References

- 1 S. Hussain, C. N. Wivagg, P. Szwedziak, F. Wong, K. Schaefer, T. Izoré, L. D. Renner, M. J. Holmes, Y. Sun, A. W. Bisson-Filho, S. Walker, A. Amir, J. Löwe and E. C. Garner, *eLife*, 2018, **7**, 1–45.
- 2 A. A. Bridges, M. S. Jentzsch, P. W. Oakes, P. Occhipinti and A. S. Gladfelter, *J. Cell Biol.*, 2016, **213**, 23–32.
- 3 K. Zieske and P. Schwille, *Angew. Chem., Int. Ed.*, 2013, **52**, 459–462.
- 4 F. Fanalista, A. Birnie, R. Maan, F. Burla, K. Charles, G. Pawlik, S. Deshpande, G. H. Koenderink, M. Dogterom and C. Dekker, *ACS Nano*, 2019, **13**, 5439–5450.
- 5 E. Sezgin, I. Levental, S. Mayor and C. Eggeling, *Nat. Rev. Mol. Cell Biol.*, 2017, **18**, 361–374.
- 6 E. Sezgin, I. Levental, M. Grzybek, G. Schwarzmann, V. Mueller, A. Honigsmann, V. N. Belov, C. Eggeling, Ü. Coskun, K. Simons and P. Schwille, *Biochim. Biophys. Acta, Biomembr.*, 2012, **1818**, 1777–1784.
- 7 M. Dezi, A. Di Cicco, P. Bassereau and D. Levy, *Proc. Natl. Acad. Sci. U. S. A.*, 2013, **110**, 7276–7281.
- 8 J. Korlach, C. Reichle, T. Müller, T. Schnelle and W. W. Webb, *Biophys. J.*, 2005, **89**, 554–562.
- 9 A. Yamada, S. Lee, P. Bassereau and C. N. Baroud, *Soft Matter*, 2014, **10**, 5878–5885.
- 10 S. Demarche, K. Sugihara, T. Zambelli, L. Tiefenauer and J. Vörös, *Analyst*, 2011, **136**, 1077–1089.
- 11 S. Kalsi, A. M. Powl, B. A. Wallace, H. Morgan and M. R. R. De Planque, *Biophys. J.*, 2014, **106**, 1650–1659.
- 12 T. Masters, W. Engl, Z. L. Weng, B. Arasi, N. Gauthier and V. Viasnoff, *PLoS One*, 2012, **7**(8), e44261.



- 13 R. Watanabe, N. Soga, D. Fujita, K. V. Tabata, L. Yamauchi, S. Hyeon Kim, D. Asanuma, M. Kamiya, Y. Urano, H. Suga and H. Noji, *Nat. Commun.*, 2014, **5**, ncomms5519.
- 14 F. J. Morera, G. Vargas, C. González, E. Rosenmann and R. Latorre, *Methods in Membrane Lipids*, 2007, vol. 400(1-2), pp. 571–585.
- 15 K. Zieske, J. Schweizer and P. Schwille, *FEBS Lett.*, 2014, **588**, 2545–2549.
- 16 S. D. Hansen, W. Y. C. Huang, Y. K. Lee, P. Bieling, S. M. Christensen and J. T. Groves, *Proc. Natl. Acad. Sci. U. S. A.*, 2019, **116**, 15013–15022.
- 17 J. T. Groves, N. Ulman, P. S. Cremer and S. G. Boxer, *Langmuir*, 1998, **14**, 3347–3350.
- 18 H. Nakashima, K. Furukawa, Y. Kashimura, K. Sumitomo, Y. Shinozaki and K. Torimitsu, *Langmuir*, 2010, **26**, 12716–12721.
- 19 P. Heo, S. Ramakrishnan, J. Coleman, J. E. Rothman, J. B. Fleury and F. Pincet, *Small*, 2019, **15**, 1–13.
- 20 H. Eto, N. Soga, H. G. Franquelim, P. Glock, A. Khmelinskaia, L. Kai, M. Heymann, H. Noji and P. Schwille, *ACS Appl. Mater. Interfaces*, 2019, **11**, 21372–21380.
- 21 Y. Caspi and C. Dekker, *eLife*, 2016, **5**, 1–27.
- 22 M. G. Guney and G. K. Fedder, *J. Micromech. Microeng.*, 2016, **26**(10), 105011.
- 23 M. Kadic, G. W. Milton, M. van Hecke and M. Wegener, *Nat. Rev. Phys.*, 2019, **1**, 198–210.
- 24 J. Knoška, L. Adriano, S. Awel, K. R. Beyerlein, O. Yefanov, D. Oberthuer, G. E. Peña Murillo, N. Roth, I. Sarrou, P. Villanueva-Perez, M. O. Wiedorn, F. Wilde, S. Bajt, H. N. Chapman and M. Heymann, *Nat. Commun.*, 2020, **11**, 1–12.
- 25 U. Bozuyuk, O. Yasa, I. C. Yasa, H. Ceylan, S. Kizilel and M. Sitti, *ACS Nano*, 2018, **12**(9), 9617–9625.
- 26 M. Hippler, E. Blasco, J. Qu, M. Tanaka, M. Wegener and M. Bastmeyer, *Nat. Commun.*, 2019, 1–8.
- 27 C. de Marco, C. C. J. Alcántara, S. Kim, F. Briatico, A. Kadioglu, G. de Bernardis, X. Chen, C. Marano, B. J. Nelson and S. Pané, *Adv. Mater. Technol.*, 2019, **4**, 1–7.
- 28 F. Klein, T. Striebel, J. Fischer, Z. Jiang, C. M. Franz, G. Von Freymann, M. Wegener and M. Bastmeyer, *Adv. Mater.*, 2010, **22**, 868–871.
- 29 B. Richter, T. Pauloehr, J. Kaschke, D. Fichtner, J. Fischer, A. M. Greiner, D. Wedlich, M. Wegener, G. Delaittre, C. Barner-Kowollik and M. Bastmeyer, *Adv. Mater.*, 2013, **25**, 6117–6122.
- 30 M. Hippler, E. D. Lemma, S. Bertels, E. Blasco, C. Barner-Kowollik, M. Wegener and M. Bastmeyer, *Adv. Mater.*, 2019, **31**(26), 1808110.
- 31 C. Barner-Kowollik, M. Bastmeyer, E. Blasco, G. Delaittre, P. Müller, B. Richter and M. Wegener, *Angew. Chem., Int. Ed.*, 2017, **56**, 15828–15845.
- 32 B. Richter, V. Hahn, S. Bertels, T. K. Claus, M. Wegener, G. Delaittre, C. Barner-Kowollik and M. Bastmeyer, *Adv. Mater.*, 2017, **29**(5), 1604342.
- 33 H. Ceylan, I. C. Yasa and M. Sitti, *Adv. Mater.*, 2017, **29**, 1605072.
- 34 F. Klein, B. Richter, T. Striebel, C. M. Franz, G. Von Freymann, M. Wegener and M. Bastmeyer, *Adv. Mater.*, 2011, **23**, 1341–1345.
- 35 O. Okay, *General Properties of Hydrogels*, Springer Berlin Heidelberg, Berlin, Heidelberg, 2010, vol. 6.
- 36 C. Schizas and D. Karalekas, *J. Mech. Behav. Biomed. Mater.*, 2011, **4**, 99–106.
- 37 M. Hippler, K. Weissenbruch, K. Richler, E. D. Lemma, M. Nakahata, B. Richter, C. Barner-kowollik, Y. Takashima, A. Harada, E. Blasco, M. Wegener, M. Tanaka and M. Bastmeyer.
- 38 F. R. Flohr, M. Shtil and R. Müller, Surface Functionalization Strategy for Bone Biomimetic Osteocyte Models, *Eur. Cells Mater.*, 2016, **32**(5), 76.
- 39 J. Schweizer, M. Loose, M. Bonny, K. Kruse, I. Monch and P. Schwille, *Proc. Natl. Acad. Sci. U. S. A.*, 2012, **109**, 15283–15288.
- 40 M. I. Angelova and D. S. Dimitrov, *Faraday Discuss. Chem. Soc.*, 1986, **81**, 303–311.
- 41 A. J. García-Sáez, D. C. Carrer and P. Schwille, in *Liposomes: Methods and Protocols: Biological Membrane Models*, ed. V. Weissig, Humana Press, Totowa, NJ, 2010, Volume 2, pp. 493–508.
- 42 J. Schindelin, I. Arganda-Carreras, E. Frise, V. Kaynig, M. Longair, T. Pietzsch, S. Preibisch, C. Rueden, S. Saalfeld, B. Schmid, J. Y. Tinevez, D. J. White, V. Hartenstein, K. Eliceiri, P. Tomancak and A. Cardona, *Nat. Methods*, 2012, **9**, 676–682.
- 43 D. Soumpasis, *Biophys. J.*, 1983, **41**, 95–97.
- 44 S. K. Vogel, 2016, pp. 213–223.
- 45 S. K. Vogel, F. Heinemann, G. Chwastek and P. Schwille, *Cytoskeleton*, 2013, **70**, 706–717.
- 46 B. Ramm, P. Glock and P. Schwille, *J. Vis. Exp.*, 2018, **137**, e58139.
- 47 D. Serien and S. Takeuchi, *Appl. Phys. Lett.*, 2015, **107**, 10–15.
- 48 E. Harnisch, M. Russew, J. Klein, N. König, H. Crailsheim and R. Schmitt, *Opt. Mater. Express*, 2015, **5**, 456.
- 49 A. Poursoroush, M. M. Sperotto and M. Laradji, *J. Chem. Phys.*, 2017, **146**, 1–10.
- 50 S. Moradi, A. Nowroozi and M. Shahlaei, *RSC Adv.*, 2019, **9**, 4644–4658.
- 51 K. Göpfrich, B. Haller, O. Staufer, Y. Dreher, U. Mersdorf, I. Platzman and J. P. Spatz, *ACS Synth. Biol.*, 2019, **8**, 937–947.
- 52 B. Seantier and B. Kasemo, *Langmuir*, 2009, **25**, 5767–5772.
- 53 M. Zhu, M. Lerum and W. Chen, *Langmuir*, 2012, **28**, 416–423.
- 54 S. Aura, V. Jokinen, M. Laitinen, T. Sajavaara and S. Franssila, *J. Micromech. Microeng.*, 2011, **21**(12), 125003.
- 55 C. L. Lay, Y. H. Lee, M. R. Lee, I. Y. Phang and X. Y. Ling, *ACS Appl. Mater. Interfaces*, 2016, **8**, 8145–8153.
- 56 H. Jia, T. Litschel, M. Heymann, H. Eto, H. G. Franquelim and P. Schwille, *Small*, 2020, **1906259**, 1–10.
- 57 D. Serien and S. Takeuchi, *ACS Biomater. Sci. Eng.*, 2017, **3**, 487–494.
- 58 A. Nakahara, Y. Shirasaki, K. Kawai, O. Ohara, J. Mizuno and S. Shoji, *Microelectron. Eng.*, 2011, **88**, 1817–1820.



- 59 C. Niederauer, P. Blumhardt, J. Mücksch, M. Heymann, A. Lambacher and P. Schwille, *Opt. Express*, 2018, **26**, 20492.
- 60 S. Chiantia, J. Ries, N. Kahya and P. Schwille, *ChemPhysChem*, 2006, **7**, 2409–2418.
- 61 L. K. Tamm and H. M. McConnell, *Biophys. J.*, 1985, **47**, 105–113.
- 62 A. Sonnleitner, G. J. Schuetz and T. Schmidt, *Biophys. J.*, 1999, **77**, 2638–2642.
- 63 M. Loose, E. Fischer-Friedrich, J. Ries, K. Kruse and P. Schwille, *Science*, 2008, **320**, 789–792.
- 64 S. J. Attwood, Y. Choi and Z. Leonenko, *Int. J. Mol. Sci.*, 2013, **14**, 3514–3539.
- 65 A. G. Vecchiarelli, M. Li, M. Mizuuchi and K. Mizuuchi, *Mol. Microbiol.*, 2014, **93**, 453–463.
- 66 K. Zieske and P. Schwille, *eLife*, 2014, **3**, 1–19.
- 67 B. Ramm, P. Glock, J. Mücksch, P. Blumhardt, D. A. García-Soriano, M. Heymann and P. Schwille, *Nat. Commun.*, 2018, **9**(1), 3942.
- 68 E. K. Sinner and W. Knoll, *Curr. Opin. Chem. Biol.*, 2001, **5**, 705–711.
- 69 J. Andersson and I. Köper, *Membranes*, 2016, **6**(2), 30.
- 70 H. Ceylan, I. C. Yasa and M. Sitti, *Adv. Mater.*, 2017, **29**(9), 1–7.
- 71 A. Laliberte and C. Gicquaud, *J. Cell Biol.*, 1988, **106**, 1221–1227.
- 72 C. F. E. Schroer, L. Baldauf, L. van Buren, T. A. Wassenaar, M. N. Melo, G. H. Koenderink and S. J. Marrink, *Proc. Natl. Acad. Sci. U. S. A.*, 2020, **117**, 5861–5872.
- 73 D. M. Raskin and P. A. J. de Boer, *Proc. Natl. Acad. Sci. U. S. A.*, 1999, **96**, 4971–4976.
- 74 B. Ramm, T. Heermann and P. Schwille, *Cell. Mol. Life Sci.*, 2019, **76**, 4245–4273.
- 75 F. Wu, B. G. C. Van Schie, J. E. Keymer and C. Dekker, *Nat. Nanotechnol.*, 2015, **10**(8), 719–726.
- 76 P. Glock, B. Ramm, T. Heermann, S. Kretschmer, J. Schweizer, J. Mu and P. Schwille, *ACS Synth. Biol.*, 2019, **8**(1), 148–157.
- 77 L. Wettmann, M. Bonny and K. Kruse, *PLoS One*, 2018, **13**, 1–20.
- 78 F. Brauns, G. Pawlik, J. Halatek, J. W. J. Kerssemakers, E. Frey and C. Dekker, *bioRxiv*, 2020, 2020.03.01.971952.
- 79 H. Peng, Z. Ruan, F. Long, J. H. Simpson and E. W. Myers, *Nat. Biotechnol.*, 2010, **28**, 348–353.
- 80 S. Daetwyler, U. Gunther, C. D. Modes, K. Harrington and J. Huisken, *Dev.*, 2019, **146**(6), DOI: 10.1242/dev.173757.
- 81 A. Spark, A. Kitching, D. Esteban-Ferrer, A. Handa, A. R. Carr, L. M. Needham, A. Ponjavic, A. M. Santos, J. McColl, C. Leterrier, S. J. Davis, R. Henriques and S. F. Lee, *Nat. Methods*, 2020, **17**, 1097–1099.



Supplementary Information

Membrane-coated 3D architectures for bottom-up synthetic biology

Hirumune Eto, Henri G. Franquelim, Michael Heymann & Petra. Schuille*

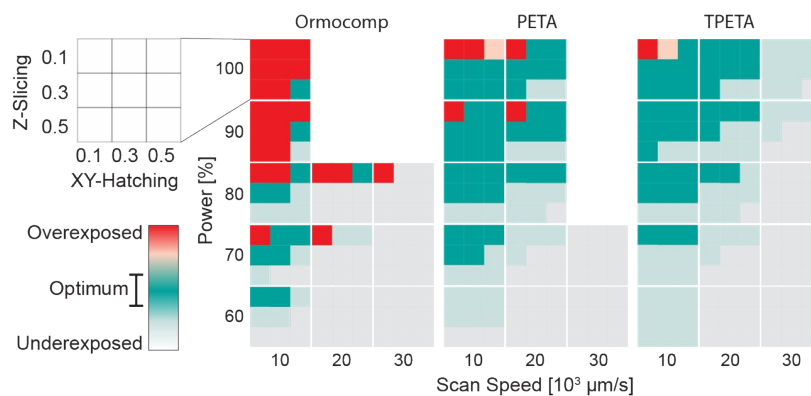


Figure S1. Sweep of writing parameters on rod-like structures. The photoresist was drop-cast onto a coverslip and the 3D microscaffolds were printed with Zeiss LCI "Plan-Neofluar" 25x/0.8 objective with an oil immersion. Optimum settings were: Ormocomp (power 80 % speed 10000 μm slicing 0.1 μm hatching 0.5 μm), PETA (power 80 % speed 10000 $\mu\text{m s}^{-1}$ slicing 0.3 μm hatching 0.1 μm) and TPETA (power 100 % speed 10000 $\mu\text{m s}^{-1}$ slicing 0.3 μm hatching 0.1 μm). SEM images at these conditions are shown in Figure 1.

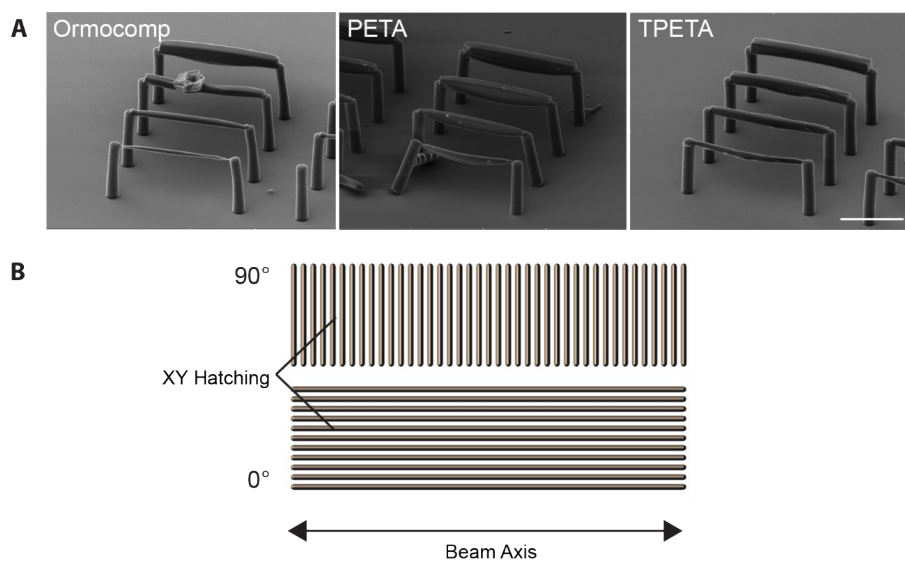


Figure 2. (A) Scanning electron microscopy images of rod-like structures with xy hatching at 0° (parallel) to beam axis. They were printed at the following settings: Ormocomp (power 80 % speed 10000 $\mu\text{m s}^{-1}$ slicing 0.1 μm hatching 0.3 μm), PETA (power 80 % speed 10000 $\mu\text{m s}^{-1}$ slicing 0.1 μm hatching 0.3 μm) and TPETA (power 90 % speed 10000 $\mu\text{m s}^{-1}$ slicing 0.1 μm hatching 0.3 μm). Scale bar 50 μm . (B) Schematic representing direction of xy hatching with respect to the beam axis.



Figure S3. (Left) FRAP measurement on PETA. SLB was formed in pH buffer with DOPC:DOTAP lipids doped with 0.005 mol % Atto655-DOPE. Fluorescence recovery confirms bilayer fluidity. (Right) TPETA surface after vesicle deposition, taken with the same laser settings (power 5%, pinhole 90 μm , gain 750, pixel dwell 1.58 μs). Absence of fluorescence indicates the lack of bilayer formation. Scale bar 5 μm .

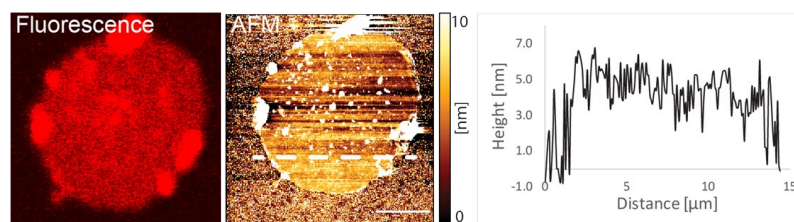


Figure S4. Bilayer verification on PETA. Membrane patches were prepared by fusing GUVs to the polymer surface. The membrane height ($4.7 \pm 0.9 \mu\text{m}$) was measured by atomic force microscopy. Scale bar $20 \mu\text{m}$, colour bar range 0-10 nm.

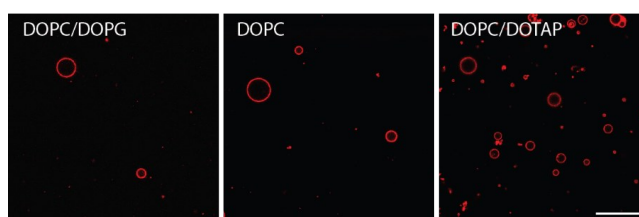


Figure S5. GUV deposition on plane TPETA. GUVs do not fuse upon contact with the surface. Instead, intact spherical GUVs can be observed nested on the surface, which were imaged at an equatorial cross section. Scale bar $40 \mu\text{m}$.

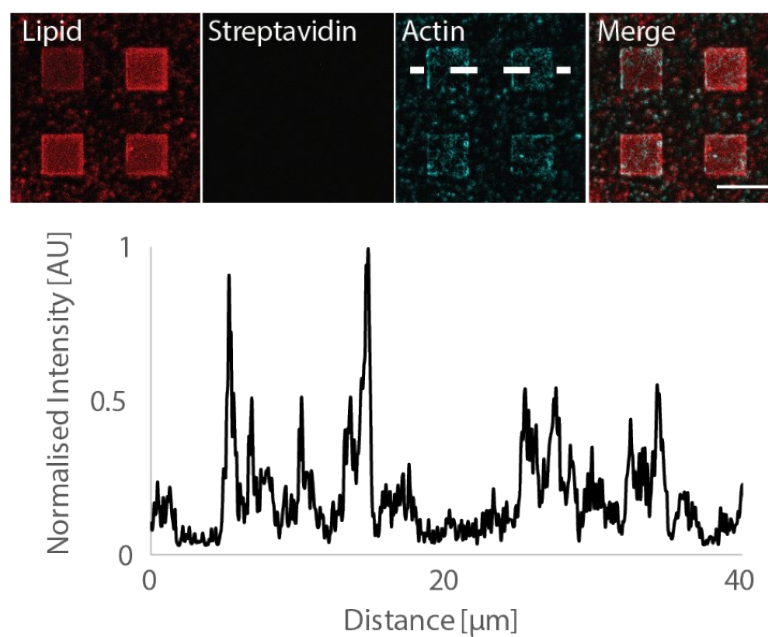


Figure S6. Fluorescence image of actin filaments on patterned lipids without streptavidin incubation, and its associated intensity trace. Actin filaments weakly localise on lipid patches due to weak electrostatic interaction of the filaments and the positively charged lipids. Scale bar 10 μm .

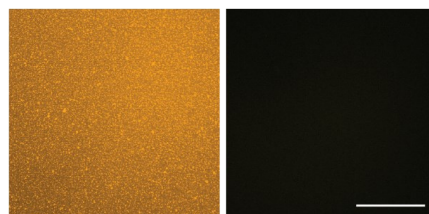


Figure S7. Dye-conjugated streptavidin on (left) PETA with biotin-doped membrane and (right) PETA without membrane, taken with the same laser settings (power 0.5%, pinhole 90 μm , gain 550, pixel dwell 1.58 μs). Lack of fluorescence on PETA without membrane indicates that the biotin-doped membrane is necessary for streptavidin recruitment onto the surface. Scale bar 10 μm .

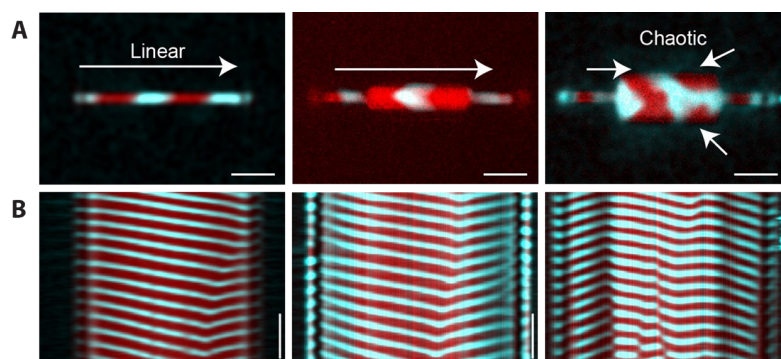


Figure S8. Confocal images of dynamic patterns on the structures (from left to right, 10 μm , 20 μm , 50 μm widths), seen from the top of the structures. (B) Kymograph of pattern taken along the axis of rods. Scale bar 20 μm horizontal, 4 min vertical.

Table S1. Mobile fraction obtained from FRAP experiments. Units are in %. Fluid bilayers are indicated in blue. Immobile bilayers are indicated in red. Errors are standard deviations calculated from 9 measurements (3 samples at 3 different locations on the membrane each).

Negative/neutral charged lipids

Material	Surface modifications	DOPC/DOPG	DOPC
Ormocomp	Plasma + APTES	98±2	97±3
	Plasma + pH buffer + Ca ²⁺ /Mg ²⁺	97±2	98±2
	Ph buffer + Ca/Mg	92±3	83±3
PETA	Ph buffer + Ca/Mg	39±5	51±5

Positive charged lipids

Material	Surface modifications	DOTAP
Ormocomp	Plasma + pH buffer	98±2
	pH Buffer	91±3
PETA	pH buffer	97±1

Movie 1. Confocal images of dynamic MinDE patterns on 10-50 μm rod structures, seen from top (top row), bottom (middle row) and 4D reconstructions (bottom row). Freeze-frames shown in Figure 4 and S8.

Movie 2. 4D reconstruction of MinDE dynamic patterns on (A) single spiral, (B) multi-spiral, (C) fractal tree. Lipids are visualized in red, MinD in cyan. Freeze-frames shown in Figure 5. Scale bar 100 μm .

6.4 Dendrimersome synthetic cells harbor the cell division machinery of bacteria

The fourth and final section of this chapter investigates how membranes themselves can be synthetically engineered so that more flexible and stable free-standing lipid bilayer systems can be created. Lipid vesicles are often employed as a model membrane system that suitably mimics cellular conditions *in vitro*, as they assimilate cells in their size, overall shape and their ability to encapsulate reaction volumes inside a lipid bilayer membrane [39]. However, they are notoriously unstable, and deformations away from their spherical geometry is a challenge that has not yet been conclusively solved [29].

Here, I turned to dendrimers, which is a class of synthetic molecules that mimic lipids in terms of their self-assembly into bilayers, as well as their membrane fluidity and thickness [103, 118]. They characteristically contain a benzene ring between the hydrophilic head and the fatty acid chains, which not only assists in their modularity during synthesis, but also promotes pi-pi stacking between adjacent dendrimer molecules, thus improving the stability of formed membranes. With the addition of a phosphate group and a further glycerol group, we synthesized dendrimers *de novo* that are negatively charged, and showed that dendrimer vesicles, or “dendrimersomes” are a suitable alternative to lipids for reconstituting membrane associating proteins, such as MinDE and FtsZ, *in vitro*. This paves the way for further investigations based on shape deformation as well as attempts towards the synthetic division of vesicles, which was previously impossible due to the low stability of lipid vesicles.

The section is the result of a collaboration between Anna Wagner, Anton Joseph, Mariia Vorobii and Cesar Rodriguez-Emmenegger (DWI-Leibniz Institute for Interactive Materials, Germany), as well as Shunshi Kohyama from the Schwille Lab. H.E., M.V., P.S. and C.R.E. conceived the project. H.E. and A.W. performed all Min protein *in vitro* reconstitution experiments. A.J. synthesized the dendrimers. H.E., A.W. and S.K. performed encapsulation experiments in droplets and vesicles and analysed the data.

6.4.1 Introduction

One of the ultimate goals of synthetic biology is to design and recreate a fully synthetic protocell from the bottom up. Such artificial cells should contain key aspects of biological behaviour, such as compartmentalisation, transport of molecules, metabolism, growth, and ideally, reproduction: cell division is one of the hallmark events of life, and is one of the most intriguing phenomena exhibited by a living cell.

The strategy to recapitulate such behaviours includes encapsulating components of the active cell machinery into synthetic cell-like compartments. The most prominent methods involve the use of liposomes, which are lipid bilayer compartments that mimic cells in their size as well as providing basic biochemical functionalities, as many proteins function at the lipid membrane interface [116]. In these systems, reconstitution of some of the minimal components of cell division has been demonstrated. A notable example of this is the *E. coli* Min system, which are the spatial indicators of the midcell of these bacteria [84]. They self-organise into dynamic patterns, whose behaviour is delicately governed by the interplay between the diffusion and kinetic rates of the molecules between the vesicle lumen and the lipid membrane. FtsZ proteins, which forms a protoring that is positioned by the Min system to recruit further proteins in

the divisome, also self-assemble into filaments when anchored onto the membrane. In this regard, liposomes are suitable model membrane systems to recapitulate protein behaviour in an *in vitro* setting.

However, liposomes are severely limited in their application for advanced functions for the following reasons. Lipids are chemically unstable, since many lipids contain unsaturated fatty acid chains that are prone to oxidation. They are also mechanically unstable, and any deformation away from their spherical, equilibrium shape has been a technically challenging [29]. This is a critical problem that limits further use of liposomes in the study of membrane deformations, including the division of a synthetic protocell.

We therefore turned to reengineering the membrane itself to improve the stability of these vesicles. Dendrimers have caught recent attention as a class of synthetic molecules that mimic lipids, not only in their basic chemical make up, since they have a hydrophilic head and a hydrophobic tail, but also in the fact that they self-assemble into fluid bilayer membranes [103, 118]. They typically contain a benzene ring within their hydrophobic region, which not only assists in the modularity of their functional components during synthesis, but also promotes pi-pi stacking between adjacent dendrimer molecules, thus improving the stability of formed membranes.

Protein-membrane interactions, however, can be complex. The association and dissociation of Min proteins from the membrane, as an example, is mediated by the insertion of their membrane targeting sequence [119, 120]. This often requires the correct functional groups present at the right quantities in order to trigger the normal behaviour of proteins. In order to create a suitable synthetic mimic of the lipid bilayer, its biophysical properties, such as membrane thickness and lateral mobility, as well as its biochemical functionalities must be finely tuned.

In this work, we synthesized dendrimer molecules *de novo*, first with a zwitterionic phosphoryl choline head group with a 12-carbon fatty acid chain length, and second with an additional glycerol group to add a net negative charge to the molecule (Fig 6.3). These new dendrimers co-assemble into bilayer membranes that mimic lipids in their bilayer height, fluidity and net negative charge, which is crucial for many bacterial proteins to function, including the Min and FtsZ proteins.

We rigorously tested the biomimicry of dendrimer membranes by forming a variety of model membrane systems: supported membranes, water-in-oil droplets and vesicles, and observed their interaction with the *E. coli* MinDE system. Not only did they form dynamic patterns, but they also showed remarkably similar behaviour to on lipid membranes. We also co-encapsulated Min and FtsZ proteins in dendrimer vesicles, where FtsZ filaments were spatially regulated by Min proteins. We therefore demonstrate that our dendrimer membrane is a functional analogy to the lipid bilayer, with a superior stability that make them suitable for future applications in studying membrane deformation.

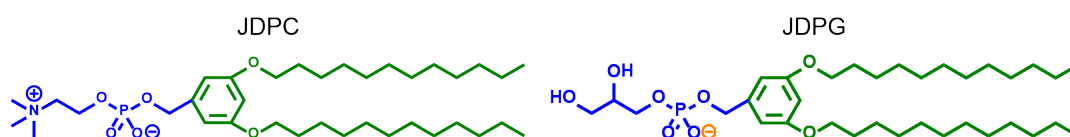


Figure 6.3. Chemical structures of JDPC and JDPG.

6.4.2 Methods

PREPARATION OF SUPPORTED BILAYER MEMBRANES

All lipids were purchased from Avanti Polar Lipids (Alabaster, AL, USA), unless otherwise stated. Dendrimers were synthesized and provided by A.J. To prepare SUVs, lipids were first dissolved in chloroform, with DOPC:DOPG:Atto655-DOPE (Atto-TEC GmbH, Siegen, Germany) in 7:3:0.005 molar ratio, whereas dendrimers were first dissolved in methanol with JDPC:JDPG:Atto655-DOPE (Atto-TEC GmbH, Siegen, Germany) in 7:3:0.005 molar ratio, unless otherwise stated. The solvent (chloroform/methanol) were dried under a nitrogen stream, and vials were placed in a desiccator to remove residual solvent for at least 2 h. Afterwards, lipids/dendrimers were rehydrated in Buffer M (25 mM Tris-HCl, 150 mM KCl, 5 mM MgCl₂, pH 7.5) to a concentration of 4 mgml⁻¹.

A chamber was constructed from a cut 0.5 ml eppendorf tube glued onto a glass coverslip (as in Fig 6.1b). The glass coverslips are best cleaned by rinsing with ethanol and water, before gluing on the eppendorf tube. These chambers were then plasma treated with oxygen at 50 % power, flow rate 0.3 sccm for 40 s (model Zepto, Diener Electronic). SUVs were added to the chamber, and after 3 min incubation at 37 °C on a heating block, the supported bilayer membrane was gently washed with a total of 2 ml buffer S (25 mM Tris-HCl, 150 mM KCl, pH 7.5) to remove excess vesicles.

FLUORESCENCE MICROSCOPY

All images were taken on a Zeiss LSM780 confocal laser scanning microscope using a Zeiss C-Apochromat x40/1.20 water-immersion objective (Carl Zeiss AG, Oberkochen, Germany), except for water-in-oil droplets, which were imaged with a x20 air objective. EGFP-MinD and mCherry-MinC was excited using a 488 nm argon laser, FtsZ-YFP-mts by the 561nm and Atto655-DOPE by the 633 nm HeNe laser. Obtained images were processed using Fiji [111].

FLUORESCENCE RECOVERY AFTER PHOTBLEACHING

On supported bilayer membranes, a circular spot of 5 μm diameter was illuminated with full laser power for 0.82s (50 iterations on the Zen Black software (Carl Zeiss AG, Oberkochen, Germany)), and the average fluorescence intensity was recorded every second for 100s. Measurements were taken at room temperature (23 °C). Intensity in a second area of the same dimensions was recorded in the same field of view, in order to correct for the intensity drift. The intensity trace was fit to the equation derived by Soumpasis [112].

$$f(t) = (I_0((\frac{2\tau_D}{t}) + I_1((\frac{2\tau_D}{t})))e^{-\frac{2\pi\tau_D}{t}}$$

Here, τ_D is the characteristic timescale for diffusion, and t is the time. $f(t)$ is the normalized fluorescence, and I_0 and I_1 are modified Bessel functions. The diffusion timescale for a bleached spot of radius r is $\tau_D = r^2/4D$ with D the diffusion coefficient. A custom script written in Python was used for curve fitting and data analysis.

SELF-ORGANISATION ON SUPPORTED BILAYER MEMBRANES

Self-organization assays were performed essentially as described in detail in [95]. In short, they were performed on preformed supported membranes in 200 μl of Buffer M (25 mM Tris-HCl pH 7.5, 150 mM KCl, 5 mM MgCl_2), with 2.5 mM Mg-ATP (stock: 100 mM ATP, in 100 mM MgCl_2 adjusted to pH 7.5) and at a constant room temperature of 23 °C. MinD was typically used at 1 μM (0.3 μM EGFP-MinD, 0.7 μM MinD) with 1 μM His-MinE, unless otherwise stated.

ENCAPSULATION INTO DROPLETS

To prepare the dendrimer-oil mixture, 10 mg/ml JDPC and JDPG are mixed in methanol at 7:3 ratio in a glass vial to a volume of 125 μl . The solvent is dried under nitrogen gas and then redissolved in 20 μl of n-decane while slowly shaking the glass vial. The resultant mixture is further mixed with 500 μl of Mineral oil (Carl Roth) (to 2.5 mg/ml of final dendrimer concentration). The dendrimer-oil mixture is subsequently vortexed for 1 min to homogenize the dendrimers in the mineral oil.

To encapsulate MinDE proteins inside droplets, 2 μl of the reaction mixture, consisting of 1 μM His-MinD (doped with 30 % His-EGFP-MinD), 0.5 μM His-MinE, 30 mg/ml BSA (Sigma-Aldrich) in reaction buffer (50 mM Tris-HCl pH 7.5, 150 mM GluK, and 5 mM GluMg), is added to 100 μl of dendrimer-oil mixture in a 0.6 ml tube. Subsequently, the mixture is emulsified by tapping the tube. An observation slide for microscopy is constructed by sticking an 18 x 18 mm glass coverslip (Menzel) on top of a 24 x 50 mm glass coverslip (Menzel) using thin strips of double-sided tape, which act as spacers. The droplet solution is injected into the thin space between the two coverslips, which fills up the space by capillary action.

ENCAPSULATION INTO VESICLES

The reaction mixture for vesicle encapsulation is composed of MinD, MinE, BSA, ATP at the same ratio as in droplet encapsulation, with additional 300 mM of sucrose to obtain higher density in the inner solution. In case of co-encapsulation with FtsZ, 0.5 μM mCherry-MinC, 2 μM FtsZ-YFP-mts, and 2.5 mM GTP are supplemented into the reaction mixture. In the outer solution, 330 mM glucose is added to the reaction buffer (same as droplets) to match the osmolarity of the inner solution.

500 μl of the outer solution is added to a 1.5 ml tube, and then topped up by 200 μl of the dendrimer-oil solution, which is gently dripped on top of the outer solution. In the meantime, 5 μl of the reaction mixture is added to 250 μl of dendrimer-oil mixture in a 1.5 ml tube and emulsified by tapping. 200 μl of this droplet solution is added to the dendrimer-oil phase of multi-layered solution.

Dendrimersomes are formed by centrifugation of the tube at 10,000 x g for 30 s, at room temperature. After centrifugation, the oil phase is discarded by pipetting and dendrimersomes are collected from the aqueous phase. The dendrimersome solution was transferred to 384-well glass bottom chamber. The glass surface of the chamber is passivated with 50 μl of 10 mg/mL BSA solution for 10 min and then washed with 100 μl of reaction buffer before usage.

6.4.3 Results

FORMATION OF SUPPORTED DENDRIMER BILAYER MEMBRANES

In order to systematically explore the robustness of interaction between Min system and fully synthetic dendrimer membranes, we turned to supported bilayer membranes. On this model membrane system, Min pattern formation has been extensively explored [88, 92, 93, 121], and serves an ideal platform to compare their behaviour to the lipid membrane.

Supported membranes on solid supports, such as glass, can be formed by vesicle fusion [122], whereby an attractive interaction between the headgroups of the amphiphilic molecule and the substrate surface promotes vesicles to rupture and spread on the surface. To do this, we generated small unilamellar vesicles at a high concentration (with the amount of membrane much greater than needed to completely cover all surfaces) and deposited them on a planar, plasma treated glass surface. Here, the plasma treatment exposes hydroxyl groups on the glass surface, making it hydrophilic with a net negative charge, and these charges can be bridged by the presence of divalent cations (such as Mg^{2+} or Ca^{2+}) in the buffer to promote the attractive electrostatic interaction between the surface and the dendrimer headgroups.

After the formation of supported bilayer membranes by vesicle deposition, we checked for homogeneous, fluid bilayers indicative of continuous membranes with no defects by Fluorescence recovery after photobleaching (FRAP) (Fig 6.4). Across the range of membrane compositions that we investigated (JDPG 0-40 %), the diffusion coefficient varied from 1.7 - 2.7 $\mu m^2 s^{-1}$, which is very similar to those measured for lipids (DOPG 0-40 %) that ranged from 1.0-2.7 $\mu m^2 s^{-1}$. This is also consistent with previously reported values of lipid membranes on glass [113, 114]. Their measured mobile fraction (0.97-1.02) is also high, indicative of a highly mobile membrane. Notably, the diffusion coefficient for lower PG content (ratio of JDPC:JDPG or DOPC:DOPG) tended to be higher than those for higher PG content. Here, the lack of net negative charge on the membrane results in a lower attraction to the substrate, and so the molecules can diffuse faster. Importantly, this trend is seen for both dendrimer and lipid membranes. Thus, our results indicate that we were able to form homogeneous, continuous bilayers with membrane fluidity analogous to those of lipid membranes.

MinDE PROTEINS FORM DYNAMIC SELF-ORGANISATION PATTERNS ON SUPPORTED DENDRIMER MEMBRANES

A crucial aspect of mimicking membranes is to provide the correct biochemical functionality, such as charge, and biophysical parameters, such as membrane thickness and fluidity, to allow proteins to interact. For reaction-diffusion processes that involve membranes as catalytic surfaces, their pattern formation depends critically on such parameters, since it is the rates at which they bind and unbind to/from the membrane, as well as their rates of diffusion on the membrane and in the bulk, that governs their self-organisation behaviour. In order to further interrogate the functional biomimicry of our dendrimer membranes, we employed the *E. coli* MinDE system, which has been shown *in vivo* to be a spatial regulator that positions the division ring to midcell [84], and forms dynamic patterns when reconstituted on supported lipid membranes

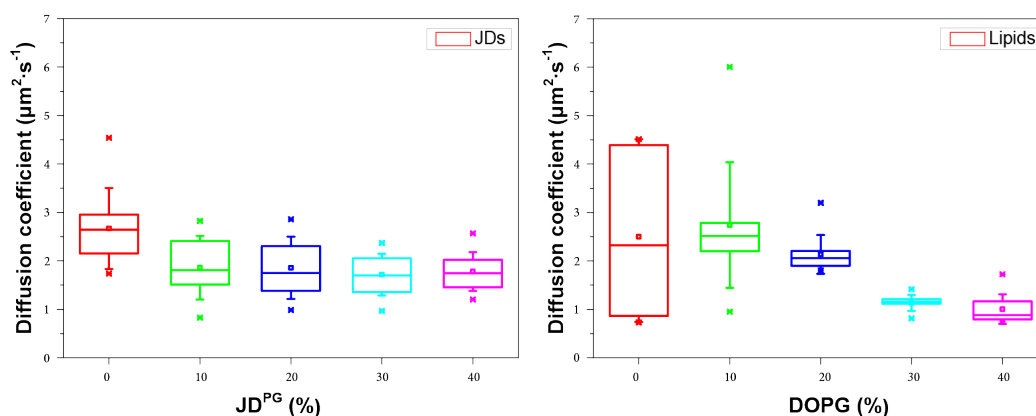


Figure 6.4. Fluidity of supported dendrimer and lipid membranes. Diffusion coefficients from FRAP experiments with varying JDPC:JDPC ratio (left) and DOPC:DOPG ratio (right).

in vitro.

Pattern formation of the *E. coli* MinDE system involves two proteins: MinD and MinE. MinD forms a dimer in the presence of ATP, upon which it attaches cooperatively to the membrane (autocatalytic attachment). At higher local concentrations on the membrane, it recruits MinE, which stimulates MinD's ATPase activity that triggers its detachment from the membrane (catalytic detachment). This forms the basis for a reaction-diffusion mechanism, where the two proteins cycle between the bulk volume and the lipid surface, and is dynamically regulated by biochemical reactions between them. Their patterns are therefore delicately governed by the interaction parameters between the protein and the membrane, and requires dendrimers to have a high level of biomimicry for Min proteins to function.

To see whether MinDE proteins form dynamic patterns, we reconstituted them in a range of protein conditions that typically form travelling wave patterns on supported lipid membranes. Keeping the MinD concentration at $1\ \mu\text{M}$, we swept through MinE concentrations from 0.5 to $5\ \mu\text{M}$. Remarkably, these proteins self-organised on our dendrimer membranes into dynamic travelling waves that not only qualitatively resembled patterns on lipid membranes, but also quantitatively (Fig 6.5). With increasing MinE concentration, the wave bandwidth decreased from around $100\ \mu\text{m}$ to $30\ \mu\text{m}$, which is expected, since a higher concentration of MinE triggers faster detachment of MinD from the membrane. Wave velocity also increased from $0.8\ \mu\text{m}/\text{s}$ to $1.9\ \mu\text{m}/\text{s}$ for dendrimers, which was a steeper trend than for lipid membranes that increased from $1.2\ \mu\text{m}/\text{s}$ to $2.6\ \mu\text{m}/\text{s}$. The overall trend, however, is still consistent with previously reported results [93].

Furthermore, in order to test whether the negatively charges are indeed necessary components of the membrane for MinDE pattern formation, we formed supported membranes with different fractions of JD^{PG} (0-40%). Here, we see from our fluorescence intensity that with increasing JD^{PG} fraction, there is increasing binding of MinD to the membrane, and below 10% JD^{PG}, there is no detectable pattern formation. MinD bandwidth as well as wave velocity also decreases with increasing JD^{PG} content, because of MinD's increasing affinity to the membrane. This is again consistent with our measurements on lipid membranes as well as with previously

reported results [93].

ENCAPSULATION OF MINDE PROTEINS IN DROPLETS AND VESICLES

In order to move closer to a synthetic cell, we then employed water-in-oil droplets as the simplest conceivable 3D mimic of cells, where we can compartmentalise Min protein oscillations in a membranous environment. In such confined systems, the surface to volume ratio of membrane to bulk reaction volume is drastically different to those on a supported bilayer membrane on a planar surface. This is known to give rise to different modes of oscillations, and reported patterns in lipid droplets include "pulsing", "travelling" and "pole-to-pole".

When we reconstituted MinDE proteins inside dendrimer droplets, we observed the modes of dynamic oscillations as expected for lipid droplets (Fig A.2). The oscillation periods are variable for the different modes of oscillations, ranging from 30 s in pulsing modes to 80 s in travelling modes. This range of periods is, however, also consistent with lipid droplets and can vary between the different modes of oscillation [99].

Next, we proceeded to encapsulate MinDE inside dendrimer vesicles, or dendrimersomes, which provides a bilayer interface that better resembles the biological cell. We formed these vesicles using an emulsion transfer method, and when we encapsulated the proteins inside these compartmentalised cellular mimics, they recapitulated the "pulsing", "travelling" and "pole-to-pole" modes of oscillation as expected for lipid vesicles (Fig 6.6). Again, the period ranged from 50 s in pulsing modes to 60 s in travelling modes, although the variation between the modes is less than compared to droplets. These values also fall within the range of previously demonstrated results in lipid vesicles [100].

CO-ENCAPSULATION OF MINCDE AND FtsZ PROTEINS IN DENDRIMERSOMES

To move closer to the construction of a synthetic protocell, we then co-encapsulated multiple components of the bacterial cell division machinery: FtsZ proteins that polymerise to form the Z-ring, as well as the MinCDE system, which includes the MinC protein as the negative regulator of FtsZ polymerisation in addition to the pattern forming MinDE system [82]. Here, we used the FtsZ-*mts* fusion protein, which localise on the membrane in the absence of additional anchoring proteins FtsA and ZipA [123]. When we reconstituted the protein systems inside dendrimersomes, FtsZ polymerised into bundles, while Min proteins formed oscillations as expected from independent reconstitution experiments [29, 100]. We also observed that the position of FtsZ bundles were anti-correlated with MinC/D maxima, thereby recapitulating MinC's negative regulation of FtsZ filament formation inside our encapsulated system (Fig 6.7).

These results suggest a high degree of similarity in biochemical functionality between dendrimersomes and lipid vesicles. Key behaviours of reconstituted systems were successfully recapitulated on dendrimer membranes. We therefore demonstrated that dendrimersomes can be considered a potential alternative model membrane system with a superior mechanical stability that can bring us closer to the synthetic division of a protocell.

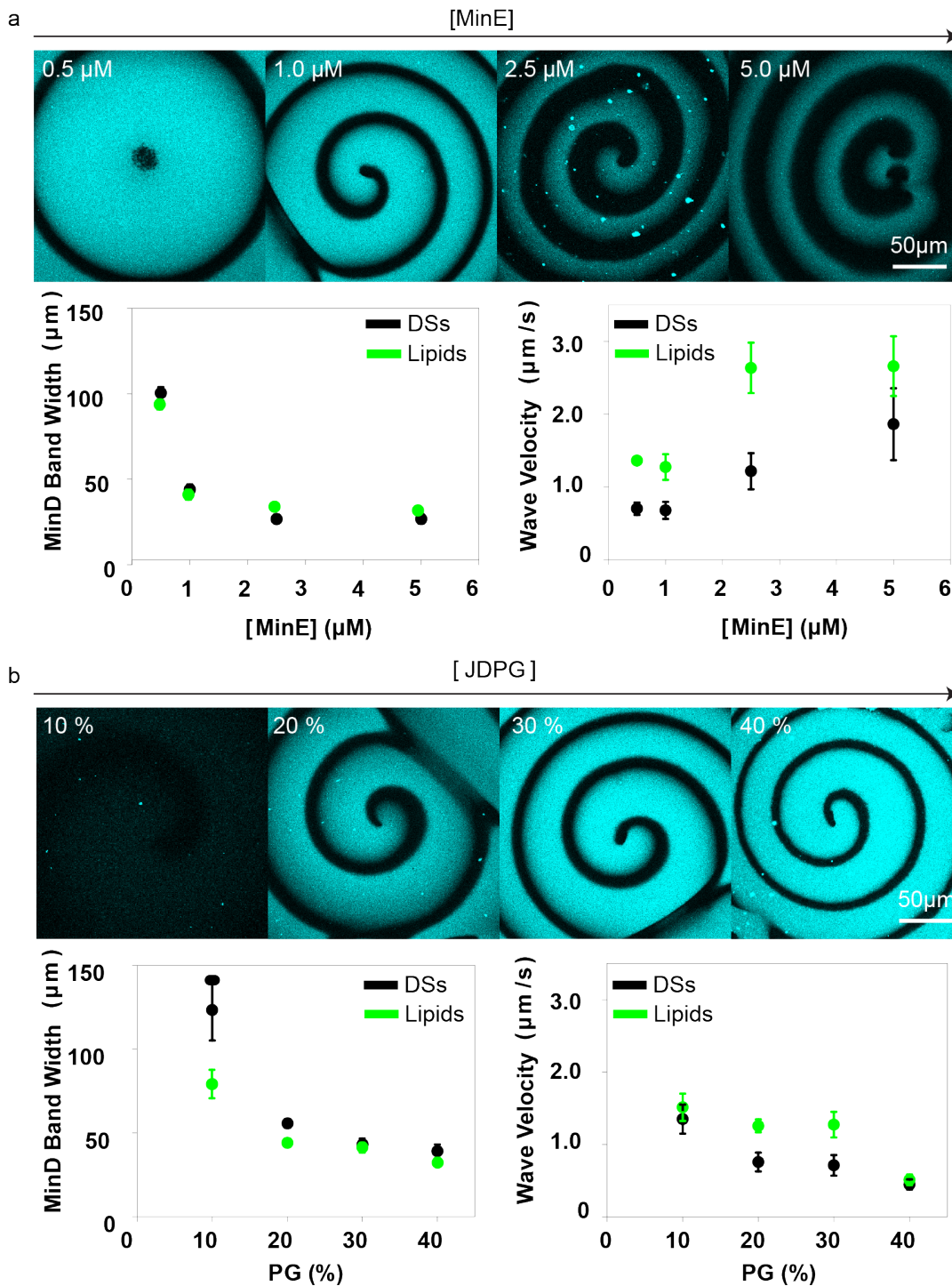


Figure 6.5. MinDE self-organisation patterns on supported dendrimer membranes. a) Patterns with increasing MinE concentration, MinD 1 μM . Graphs showing wave bandwidth (left) and wave velocity (right) against MinE concentration. b) Patterns with increasing PG content in the supported membranes, 1 μM MinD, 1 μM MinE. Graphs showing wave bandwidth (left) and wave velocity (right) against PG content in the membrane.

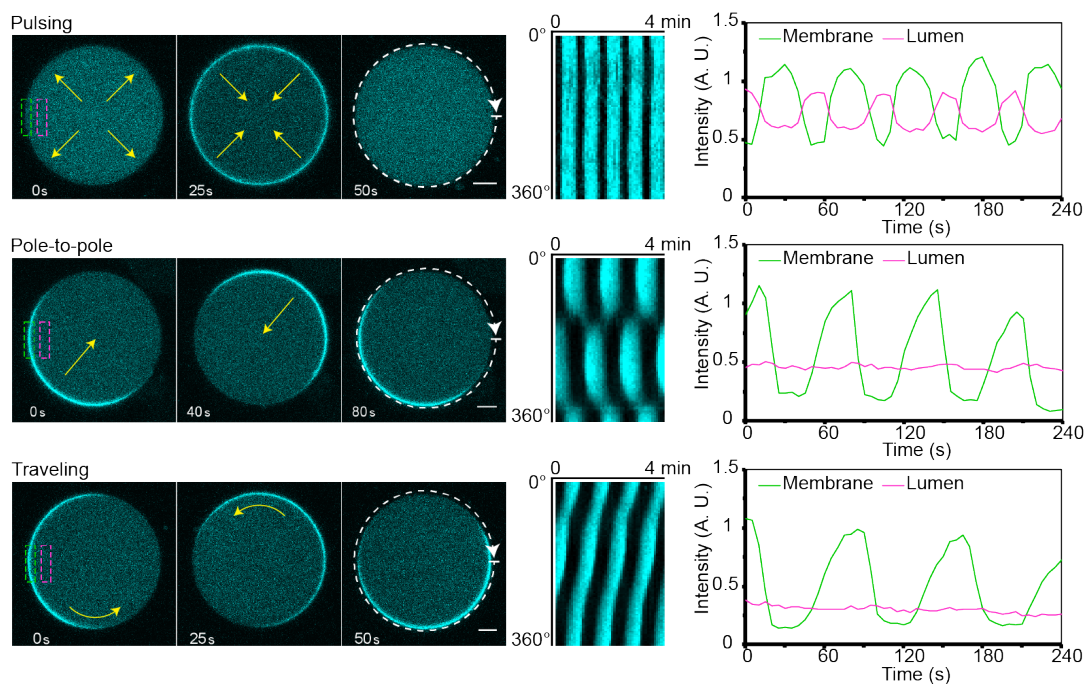


Figure 6.6. Encapsulation of MinDE inside dendrimersomes. MinDE displaying pulsing, pole-to-pole and travelling oscillations. Kymographs were taken along the indicated white dotted line, and intensity traces from the indicated ROI in the coloured boxes. MinD 1 μM (30 % EGFP-MinD), MinE 0.5 μM . Scale bar 5 μm .

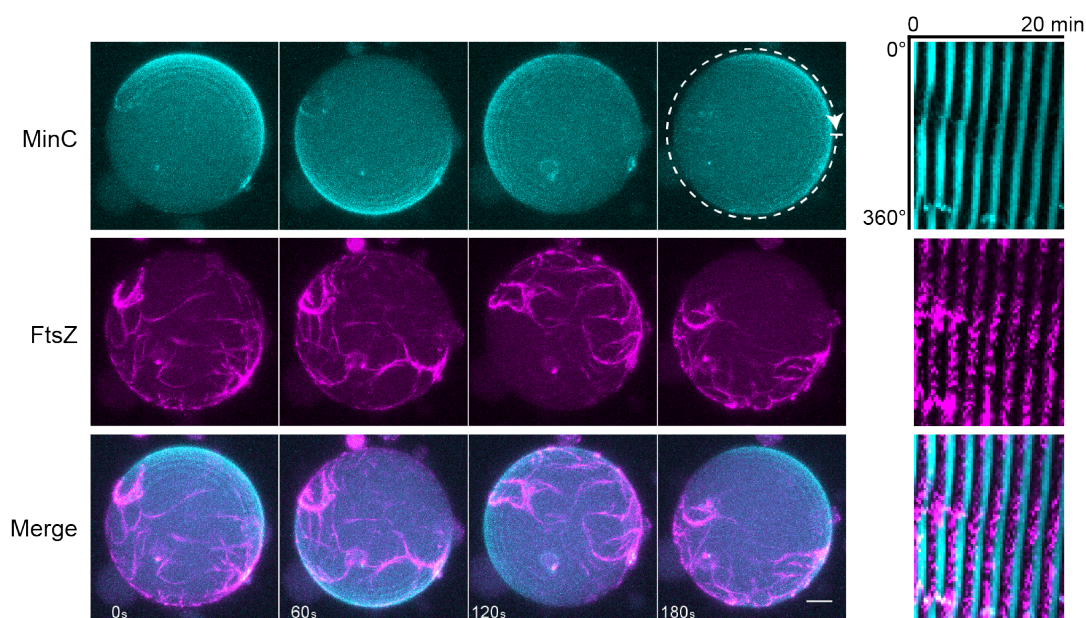


Figure 6.7. Co-encapsulation of MinCDE and FtsZ proteins in dendrimersomes. Maximum intensity projection of dendrimersomes with labelled MinC (cyan) and FtsZ (magenta). Timelapse images (left) and the kymograph (right) taken from the indicated white dotted line shows that FtsZ counter-oscillate with MinC. 0.5 μM mCherry-MinC, 2 μM FtsZ-YFP-mts, MinD 1 μM , MinE 0.5 μM . Scale bar 5 μm .

7

Development of protein-based hydrogels for 4D bioprinting

7.1 PUBLICATION P4: Shaping Giant Membrane Vesicles in 3D-Printed Protein Hydrogel Cages

The previous chapter demonstrated that microfabrication provides an effective strategy to mimic certain features of living entities, such as the sculpting of membranes into stable shapes and geometries relevant for protein function. Cellular as well as higher order structures, however, are highly dynamic, and are often actively regulated to perform mechanical work by transforming their shape. A prevalent challenge, therefore, is the construction of dynamic and controllable structures from biological materials as a platform technology to study related protein dynamics.

To tackle this challenge, I turned to 3D printing; in particular, two-photon based laser lithography of protein based hydrogels, since relevant biomolecules can be directly structured into soft, actuatable 3D shapes [62]. Their high spatial resolution also allows the printing of structures on the length scales of microns that are relevant to many biological processes. BSA based hydrogels are of particular interest, since they form stable, yet flexible 3D printed structures with Young's moduli in the physiological range (10 kPa - 2 MPa) [67]. Functionally modified BSA is also available, notably biotinylated BSA, which can be incorporated into the printed structures, and this allows further recruitment of biomolecules through biotin-streptavidin coupling, thus widening the scope of their applications [64].

In the associated publication P4, we applied this technology to selectively trap GUVs within a customized 3D printed BSA hydrogel structure. The lipid vesicle is a model membrane system already explored in Chapter 5, which constitute the basis for the engineering of advanced protocells and should ideally be subject to defined shape transformations. Since BSA-based hydrogels are known to swell at high pH [72], we used these shape-shifting structures to compress vesicles into different shapes upon pH stimuli. Through such reversible shape changes, we were also able to observe changes in the oscillation modes of MinDE self-organisation according to the shape that they were conformed into. Thus, we present 3D printing as an alternative method to externally trigger shape deformation of lipid vesicles to study their effects on encapsulated protein systems. This provides a platform technology that allows us to investigate how such synthetic cells react to and interact with external mechanical

deformations, and to probe the functionality of reconstituted cellular modules in bottom-up synthetic biology.

Shaping Giant Membrane Vesicles in 3D-Printed Protein Hydrogel Cages

Haiyang Jia, Thomas Litschel, Michael Heymann, Hiromune Eto, Henri G. Franquelim, and Petra Schwille

Author contributions:

H.J., M.H., and P.S. conceived the study. H.J. performed all experiments. H.E. and M.H. optimised the BSA printing and designed the structures. H.G.F. contributed to the experiments with phase separated vesicles. T.L. performed MinDE encapsulation in vesicles. All authors discussed and interpreted the results and revised the manuscript.

published in

Small (2020), 16, 27, 1906259

*Reprinted from [124] under the Creative Commons Attribution 4.0 International License
(see <https://creativecommons.org/licenses/by/4.0/>)*

Shaping Giant Membrane Vesicles in 3D-Printed Protein Hydrogel Cages

Haiyang Jia, Thomas Litschel, Michael Heymann, Hiromune Eto, Henri G. Franquelim, and Petra Schwille*

Giant unilamellar phospholipid vesicles are attractive starting points for constructing minimal living cells from the bottom-up. Their membranes are compatible with many physiologically functional modules and act as selective barriers, while retaining a high morphological flexibility. However, their spherical shape renders them rather inappropriate to study phenomena that are based on distinct cell shape and polarity, such as cell division. Here, a microscale device based on 3D printed protein hydrogel is introduced to induce pH-stimulated reversible shape changes in trapped vesicles without compromising their free-standing membranes. Deformations of spheres to at least twice their aspect ratio, but also toward unusual quadratic or triangular shapes can be accomplished. Mechanical force induced by the cages to phase-separated membrane vesicles can lead to spontaneous shape deformations, from the recurrent formation of dumbbells with curved necks between domains to full budding of membrane domains as separate vesicles. Moreover, shape-tunable vesicles are particularly desirable when reconstituting geometry-sensitive protein networks, such as reaction-diffusion systems. In particular, vesicle shape changes allow to switch between different modes of self-organized protein oscillations within, and thus, to influence reaction networks directly by external mechanical cues.

1. Introduction

Bottom-up reconstitution of well-characterized functional biomaterials, such as molecular entities, parts, and modules, with the final goal of constructing a synthetic cell, is a fascinating variant of Synthetic Biology.^[1] Although this goal may not easily be within reach in the next years and potentially decades, cell-free reconstitution of fundamental biological functions has interesting implications for research on the origin of life^[2] on one hand, and may open up new potential applications from medicine to technology

on the other hand.^[3] In order to accomplish large-scale biomimetic behavior and realize the vision of a fully functional synthetic cell, a large number of cutting-edge tools or technologies inspired by nanotechnology and material science have been developed and favorably employed.^[4] With regard to providing a maximally biocompatible and biomimetic compartment as a first step toward a cell-like reaction space, giant unilamellar vesicles (GUVs) composed of phospholipids have in the past years gained great attention.^[5] GUV membranes mimic cellular membranes in many relevant aspects, their lipid composition can be tuned over a wide range,^[6] they can be supported by a minimal cortex,^[7] and even large transmembrane proteins can be reconstituted into them.^[8] However, many advanced protein functionalities like cell division, differentiation, migration, and signaling require the establishment of spatial anisotropy, or in other words, polarization,^[9] which is hard to realize in spherical vesicles. In particular, reconstituted bacterial cell division machineries that are supposed

to ultimately induce controlled vesicle splitting have been shown to require elongated geometries with distinct symmetry axes.^[10]

Thus, developing ways for a controlled deformation of GUVs into desired shapes, resulting in an anisotropic membrane or a polar physical microenvironment, will greatly improve our toolbox for the bottom-up reconstitution of biological functionality toward a synthetic cell. So far, several methods to template membrane vesicles and induce anisotropic structure in vitro have been developed, like microfluidics,^[11] micropipette aspiration, optical tweezers, and dielectrophoretic field cages.^[12] However, most of them require sophisticated technology or are unable to dynamically control the membrane geometry in a well-defined, i.e., precise and programmable, manner. On the other hand, cell biology-derived tools like 2D micropatterning,^[13] hydrogels in 3D-printed microchannels,^[14] and 3D soft lithography of hydrogel^[15] have been successfully applied to control interfacial geometry in order to define the extracellular environment. Since the development of 3D printing technology, rationally designed 3D objects can be produced from various materials on different scales. In this context, stimuli-responsive hydrogels, which can cycle between expanded and condensed states in response to environmental triggers (e.g., pH, ionic strength), could constitute an attractive material for 3D or 4D Printing.^[16] In fact, pH-responsive Bovine serum albumin (BSA) hydrogels are already widely used to fabricate 3D

Dr. H. Jia, T. Litschel, Dr. M. Heymann, H. Eto, Dr. H. G. Franquelim, Prof. P. Schwille
Max Planck Institute of Biochemistry
Am Klopferspitz 18, D-82152 Martinsried, Germany
E-mail: schwille@biochem.mpg.de

 The ORCID identification number(s) for the author(s) of this article can be found under <https://doi.org/10.1002/smll.201906259>.

© 2020 The Authors. Published by WILEY-VCH Verlag GmbH & Co. KGaA, Weinheim. This is an open access article under the terms of the Creative Commons Attribution License, which permits use, distribution and reproduction in any medium, provided the original work is properly cited.

DOI: 10.1002/smll.201906259

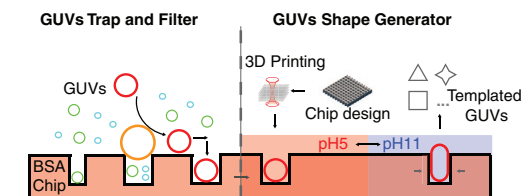


Figure 1. Concept of 3D-printed protein hydrogel trapping and templating giant vesicles (GUVs).

tissue scaffolds^[17] and generating smart 4D stimuli-responsive microactuators.^[16,18]

Here, we varied and expanded this technology toward the goal of selectively trapping GUVs within a customized 3D printed BSA hydrogel chip, and dynamically inducing structural anisotropy by applying external pH stimuli to the gel. The basic working principle is illustrated in **Figure 1**. 3D printed protein hydrogel can be designed as microchambers in appropriate sizes for capturing GUVs. The variable protein hydrogel structure acts as a geometrical cue to establish synthetic cell polarity in vitro by compressing vesicles into different shapes upon pH stimuli. This spatially well-defined microenvironment can mimic the dynamic native cell matrix, allowing us to investigate how synthetic cells react to and interact with external mechanical cues.

2. Results and Discussion

GUVs themselves can be generated either by electroformation, gentle hydration of dehydrated lipids, inverted emulsion transfer, or by microfluidic jetting. Procedures to handle these delicate objects are still not consummate.^[19] They encompass sedimentation with high-density fluids, immobilization on functionalized surfaces,^[20] manipulation by micropipette aspiration,^[21] or microfluidic systems.^[12,19] As an alternative, but still being compatible with these established protocols, our 3D BSA protein hydrogel GUVs traps were fabricated in a layer-by-layer procedure via two-photon polymerization process, using Rose bengal as the photoinitiator for BSA monomers (Scheme S1, Supporting Information). In contrast to other trapping approaches, surface functionalization for avoiding GUV-surface adhesion is not required for the 3D printed hydrogel chips. The electroformed GUVs filled with high-density solution, like sucrose, can spontaneously sink down into the hydrogel microchambers. Trapping in the chambers prevents GUVs from being flushed away and from being mechanically deformed by applied flow. To rationally design a trap that can be easily adapted to different sizes of GUVs, we chose a simple module consisting of a solid cube ($14 \times 14 \times 14 \mu\text{m}$) extruded-cut by half-cylinders (Diameter: $10 \mu\text{m}$) on both sides (Figure S3a, Supporting Information). These GUV traps were then arranged into a 10×10 -module array. By controlling the distance of rows and columns in the array, we can generate two different types of trap chips: individual traps, or group traps. With $1 \mu\text{m}$ distance for both rows and columns, the individual trap chip can be used to capture GUVs one by one within 81 separated cylinder wells (Figure 2a; and Figure S1a, Supporting

Information). The GUVs here utilized were obtained through electroformation,^[22] composed of DOPC(1,2-dioleoyl-sn-glycero-3-phosphocholine) and doped with 0.5 mol% Atto655-DOPE(1,2-dioleoyl-sn-glycero-3-phosphoethanolamine) for fluorescence detection. By extending the row distance to $15 \mu\text{m}$, groups of GUVs can be trapped between two full rows (Figure 2b; and Figure S1b, Supporting Information), in order to manipulate many vesicles at once, or to enforce their communications and interactions. The sizes of GUVs to be trapped depend on the diameters or distances, respectively (Figure 2c). GUVs with diameters larger than the gap distance are filtered out. The selective trapping of GUVs by the hydrogel chip, either as individuals or in groups, allows their size to be roughly controlled, as a first criterion toward establishing geometric anisotropy of vesicles.

In addition to allowing for a flexible size-filtering design, BSA hydrogel also shows great potential in generating smart pH stimuli-responsive microdevices that can be used to dynamically mimic the native cellular microenvironment in vitro. The isoelectric point of BSA is close to pH 5, where a protein has no net charge and fewer ion-dipole interactions. Therefore, the structures absorb less water than at higher pH and thus cover the smallest area at pH 5.^[18a,23] Due to the larger number of ionized amino acids in BSA, swelling of the structures can be induced at higher pH. However, precisely controlling pH can be difficult. To improve controllability, the swelling capability can be effectively tuned by fabrication parameters, such as slicing distance (layer distance), laser power, and laser scan speed, as shown in **Figure 3**; and Figure S2 (Supporting Information). The area swelling ratios of $14 \times 14 \times 15 \mu\text{m}$ cubes can be tuned from 1.1 to 1.7 (Figure 3b–d). A larger slicing distance results in lower crosslinking density and allows more water to enter inside the hydrogel, which in turn increases the swelling ability. Similarly, lower laser power also increases the swelling ratio to 1.7 (Figure 3c), but loses the spatial resolution of printing. Because of the lower crosslinking degree under low laser power, the structures printed at 30 mW laser power are $\approx 30\%$ larger than when printed at 50 mW (Figure S2d, Supporting Information). When varying the scan speed, structures at pH between 5 and 8 have weak swelling capability and the maximal swelling ratio at pH 11 can only reach a factor of 1.5 (Figure 3d).

The controllable swelling ratios of 3D printed hydrogel structures enable a programmable templating of GUV geometries with pH-stimuli responsive GUVs traps. Due to the swelling effect of the traps, the total structure occupies a larger volume, which should in turn shrink the free inner volume of the chambers. The swelling behavior of a square-frame trap was first investigated. It was designed by extruding cut $15 \times 15 \times 15 \mu\text{m}$ square wells in the center of $45 \times 45 \times 15 \mu\text{m}$ cuboid (Figure 3e). The hydrogel frame can swell 1.57 ± 0.15 fold (mean \pm s.d.) at pH 11 compared to pH 5; however, no shrinking of the inner area was observed. The potential reason is the increased surface tension at the inner side of the hydrogel frame, scaling inversely with radius. To improve the design toward a truly contractible and at the same time anisotropic trap, the structure was divided into eight separate small rectangular modules (Figure 3f). Allowing $2 \mu\text{m}$ distance between the modules in the relaxed state should support swelling in all directions. Because there exists no

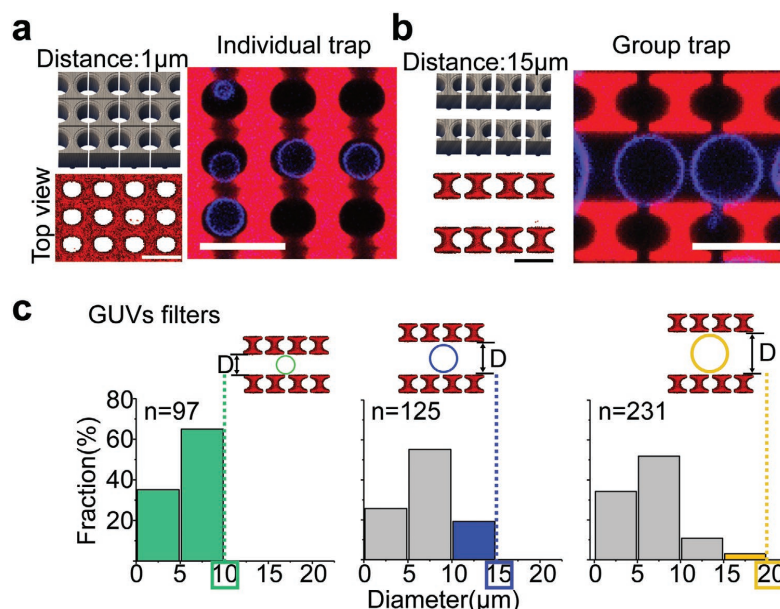


Figure 2. 3D-printed protein hydrogel chips filtering and trapping different-sized vesicles. a) Chip design for trapping individual GUVs, scale bar 20 μm. Left (top): All microchambers were integrated in one chip. Left (bottom): top view. Right: trapping individual GUVs in separated hydrogel chambers. b) Chip design for group trapping, scale bar 20 μm. Left (top): The chip was combined with separated units as barriers with certain distance. Left (bottom): top view. Right: trapping GUVs in between the hydrogel barriers. c) 3D printed hydrogel traps as GUV filters with different row distances. n: number of trapped GUV numbers. D: distance.

physical connection between the module surfaces as in the previous design, the section area of the inner free space could be decreased to 75% ($\pm 2.2\%$) in the swollen state when the pH was changed from 5 to 11 (Figure 3f, bottom right). Another advantage of the modular design is that the distance between the modules can be varied, in order to accommodate a larger growth regime and anisotropic compression. Small distances may lead to surface contact between the modules during swelling, which induces shape changes and restricts the overall compression effect (Figure S4, Supporting Information).

In order to evaluate the mechanical effects that can be obtained by vesicle compression, the pH stimuli-responsive hydrogel chambers were now applied to deform trapped membrane vesicles. The basic module of the group trap can swell in both x- and y- directions and thus occupies free space between modules after shifting pH from 5 to 11 (Figure 4a). In the rows, the distance between the modules was significantly reduced. Perpendicularly to this, two neighboring modules fused to yield a lens-shaped well, but with larger diameter than the half-cylinder at pH5. The channels between the individual barriers were also narrowed to about 50% (Figure 4a). In response to the pH stimuli, the hydrogel can process fast swelling within 1 min, supporting a dynamic mimicry of the cell microenvironment in vitro (Figure 4b; and Movie S1, Supporting Information). The trapped GUVs were now investigated by optical microscopy (Figure 4c). After shifting the pH to 11, the spherical vesicles were compressed by the closing

walls, flattening them and forcing them into nonspherical symmetry (Figure 4d,e). The distance between the two rows was $11.97 \pm 0.34 \mu\text{m}$ at pH 11, so that vesicles larger than $\approx 12 \mu\text{m}$ in diameter were compressed. With increasing confinement under swelling conditions over a time course of 6 min, the curvature became anisotropic, with flat areas facing the hydrogel and increased curvatures in the free zone (Figure 4d). At the same time, the membrane tension was increased, due to the loss of spherical symmetry and volume conservation, which imposes some constraints on the aspect ratio σ (length vs width) of the vesicles that can be reached by this procedure without compromising membrane integrity. An aspect ratio of up to about twofold (length vs width) could, however, be easily reached by this setup (Figure S5, Supporting Information). Importantly, the hydrogel swelling is reversible, and the vesicle shapes can thus be switched between spherical and elongated by alternating between the two pH values (Figure 4e).

Furthermore, different designs of the hydrogel structures allow us to induce unusual shapes of the GUVs, and thus, membrane geometries, by varying the contact zones between the hydrogel and the vesicles. The cylindrical chip was designed by extruding a cylinder (diameter, 15 μm) in the center of a cube ($20 \times 20 \times 20 \mu\text{m}$) (Figure 5a; and Figure S3d, Supporting Information). Then the cube with the cylindrical well was quartered. This chip was used to trap vesicles of $\approx 15 \mu\text{m}$ diameter. When the pH was increased from 5 to 11, the four separated modules swelled centripetally and compressed the captured membrane

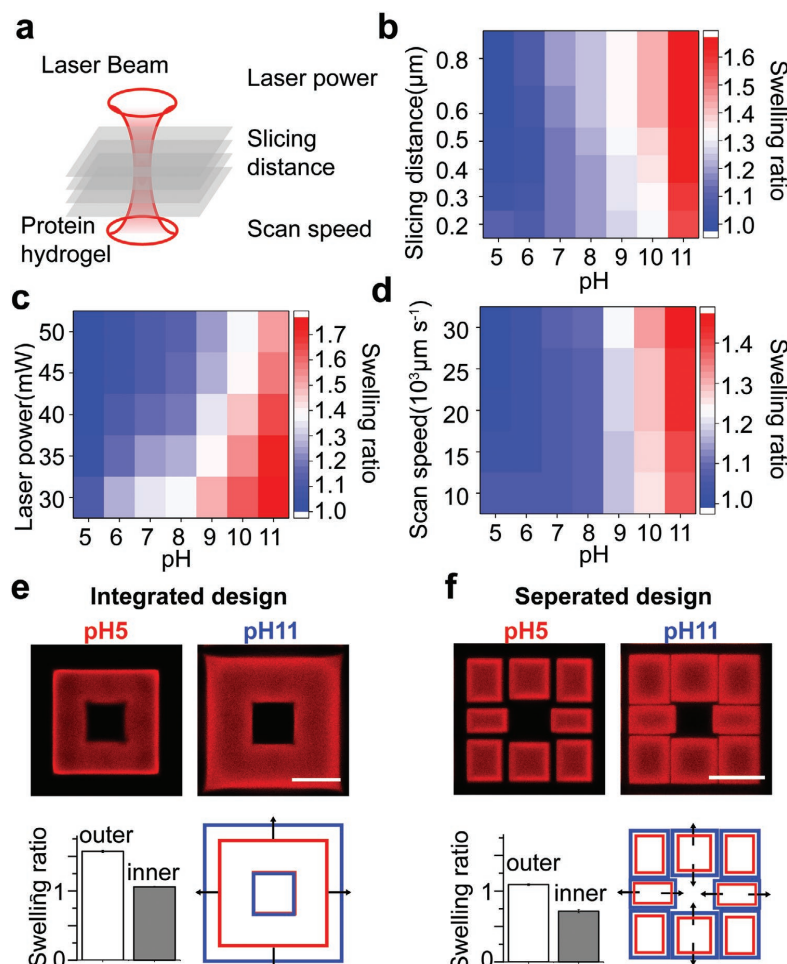


Figure 3. pH-stimuli responsive protein hydrogel. a) Laser fabrication of hydrogel layer by layer with two-photon excitation. b–d) Tuning pH-stimuli swelling ratio by varying slicing distance (b), laser power (c), and laser scan speed (d). Printing parameters: b) laser power: 50 mW, Scan speed: 30 000 $\mu\text{m s}^{-1}$; c) Slicing distance: 0.5 μm , Scan speed: 30 000 $\mu\text{m s}^{-1}$; d) Slicing distance: 0.5 μm ; laser power: 50 mW. e, f) pH-dependent swelling of integrated chip and the combined chip (Slicing distance: 0.5 μm ; laser power: 50 mW; Scan speed: 30 000 $\mu\text{m s}^{-1}$), scale bar 20 μm . Top: confocal imaging of the swelling effect under different pH. Bottom (left): swelling ratios of outer and inner area. Bottom (right): directional swelling. Area swelling ratio is defined as A/A_0 , where A_0 is the area of the structure at pH 5, printed under slicing distance: 0.5 μm , laser power: 50 mW, scan speed: 30 000 $\mu\text{m s}^{-1}$.

vesicle. The area of the cross-section was reduced, in turn the height was increased. Similarly, with alternative designs, GUVs can be deformed to other shapes like cross prisms, cubes, and triangular prisms (Figure 5b,c). Due to the surface tension of membrane vesicles, the templated cross-prismatic, cubic, and triangular prismatic vesicles all formed curved corners and spherical domes.

Having shown that GUVs can not only be reversibly compressed, but also molded into arbitrary nonspherical shapes by our laser-printed BSA pH-responsive hydrogel structures, we next aim to demonstrate how these mechanical constraints may

influence membrane structure and dynamics in the shaped vesicles. In particular, GUVs have long been used to elucidate the molecular details of lipid phase separation; however, their usually spherical symmetry and isotropic structure have significantly limited the comparability of these model membranes with biological ones. In physiological environments, cells acquire and maintain spatial and functional asymmetry of their plasma membrane^[24] in response to external mechanical cues. Similarly, in model membrane systems exhibiting visible lipid domains enriched in cholesterol and saturated lipids, strong correlations between membrane composition and 3D

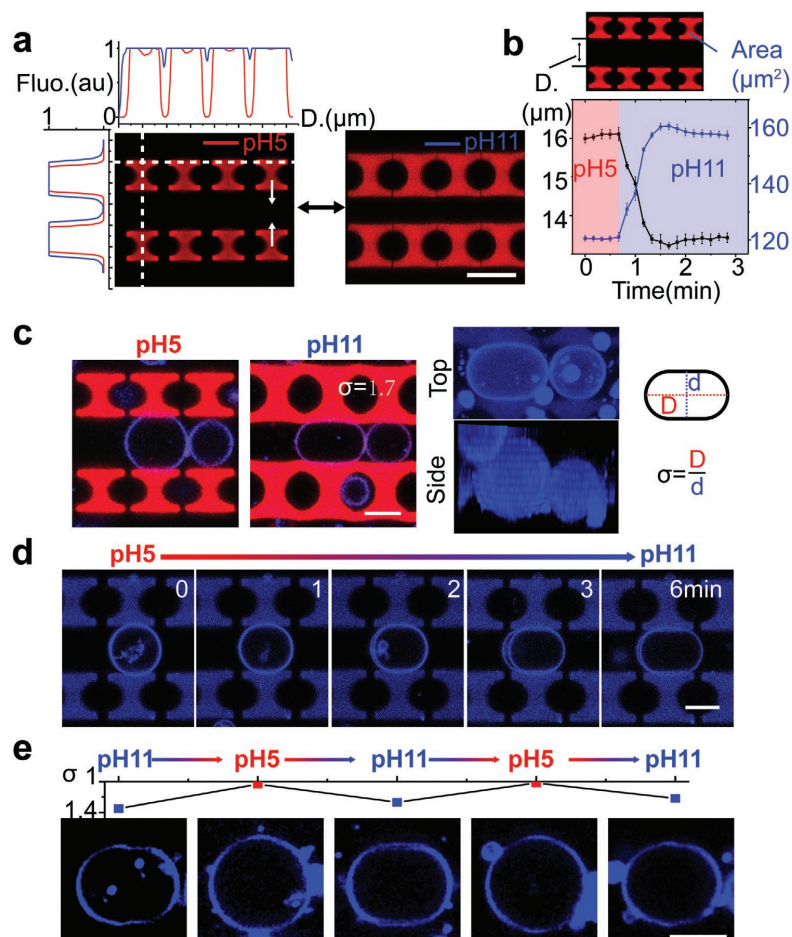


Figure 4. Reversibly deforming membrane vesicles by pH. a) Swelling effect of group trap at increased pH, scale bar 20 μm . The line plots demonstrate the swelling in both x- and y-axis, respectively. b) Response of geometry factors area and distance when transitioning to pH 11 solution. c) Swelling chip deforming DOPC GUV, scale bar 10 μm . Right: top and side view of deformed GUVs. d) Dynamic deformation of GUV by exchanging pH from 5 to 11, scale bar 10 μm . e) Reversibility of GUV aspect ratio (σ) by alternating pH, scale bar 10 μm .

vesicle shape could be observed, which suggest that, in turn, mechanical constraints will lead to significant membrane transformations.^[24,25]

The phase-separated GUVs we investigated in our stimuli-responsive hydrogel cages consisted of ternary lipid mixtures composed of cholesterol (Ch), sphingomyelin (SM), and the unsaturated phospholipid DOPC, with a molar ratio of 2:2:1 at room temperature.^[26] The mixture can separate into two coexisting membrane phases: a liquid-ordered phase (L_o) enriched in SM and Ch; and a liquid-disordered (L_d) phase consisting primarily of DOPC. To discriminate between the L_o and L_d phases by fluorescence microscopy, we used 0.3%NBD-DSPE and 0.2% Atto655-DOPE, respectively. The spherical phase-separated GUVs were trapped in the triangular prismatic hydrogel

chips (Figure S3c, Supporting Information). When the GUVs were compressed by the swelling hydrogel chamber under pH stimuli, the vesicles deformed to fit the diminished inner area, often accompanied by a large-scale reorganization and fusion of the domains on their membrane surface (Figure S6, Supporting Information). In several cases, particularly for vesicles with large domains, the spherical vesicle was transiently deformed upon compression into a dumbbell geometry, due to line tension between L_o - L_d domains,^[27] acquiring a clear curved neck at the domain boundary. Typically, the dumbbell-shaped phase-separated vesicle then rotated within the contracted hydrogel cavity, in order to adapt the space change and relax back into a spherical (yet compacted) energetically favorable shape (Figure 6b; and Figure S7, Movie S2 for top view of 3D

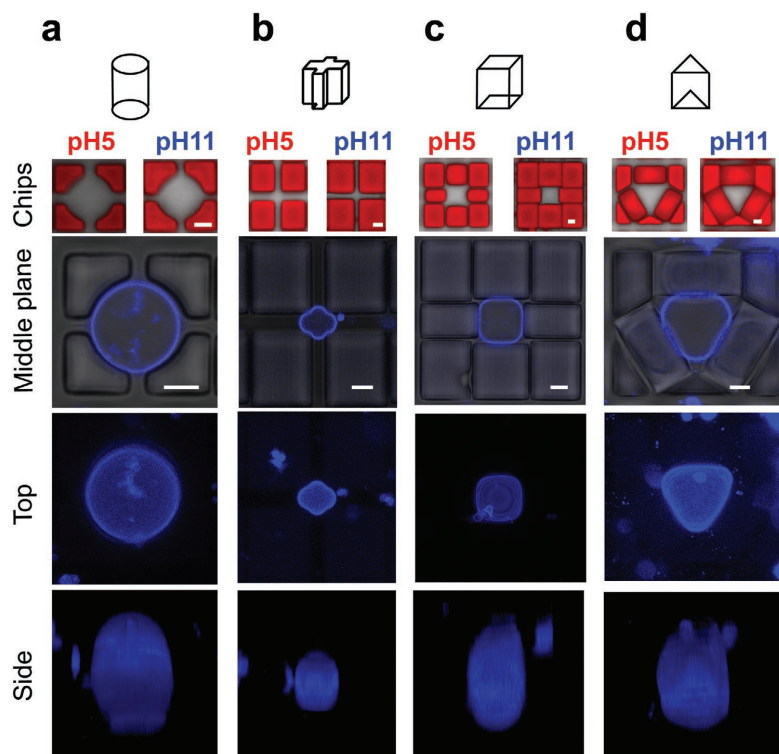


Figure 5. Various 3D hydrogel designs for templating DOPC vesicles into different shapes: a) cylinder, b) cross prism, c) cube, d) triangular prism. The schemes in the first row show the 3D geometries of trap wells. Below the schemes are the top views of the chips in response to different pH, scale bar 5 μm . Third row from top: confocal imaging of the middle cross-section of vesicles, scale bar 5 μm . The bottom two rows represent the 3D z-stack reconstitution of different geometrical vesicles.

imaging, and Movie S3 for orthogonal view, Supporting Information). Occasionally, however, the compression led to the fission of a Lo domain away from the trapped GUV membrane (i.e., budding as a way to overcome line tension,^[28] ultimately changing the overall membrane composition of the remaining “mother” vesicle (Figure 6c; and Movie S4, Supporting Information). In the control experiment without the swelling traps, no triggered deformation events were detected upon pH change from 5 to 11 (Figure S8, Supporting Information). Thus, the ability to exert gentle but significant mechanical pressure on GUVs in our custom-designed protein hydrogel cages opens up a new way of manipulating vesicle model systems, inducing features that could be of great relevance in the design of cellular mimics, such as shape and differential membrane curvature, respectively, tension.

The surface geometry that determines membrane dynamics also affects the spatiotemporal patterns and oscillations formed by reaction-diffusion systems.^[29] A striking example of a reaction-diffusion system is the Min protein system, consisting of the proteins MinC, MinD, and MinE, which oscillate between the cell poles and spatially position the bacterial cell division machinery in *Escherichia coli*.^[30] In vitro reconstitution of the

Min system on micropatterned surfaces or in microcompartments has shown that the geometry of the boundaries plays a pivotal role in its pattern formation and pace-making.^[10,31] Recently, the Min system has been encapsulated into 3D spherical compartments, motivated by the long-term goal of creating a self-reproducible synthetic cell.^[32] Unlike in vivo, this reconstituted reaction-diffusion system reveals several distinct oscillation modes, namely pulsing oscillations, pole-to-pole oscillations, and circling and trigger waves.^[32b] Causes for such diverse behaviors are differences in protein concentration, vesicle size, proteins ratio, or the isotropic geometry. Here, we used the 3D hydrogel shaped vesicles to demonstrate how the anisotropy of microenvironment influences the reaction-diffusion system.

We encapsulated the oscillating Min system (MinD (50% EGFP-MinD) & MinE) in negatively charged GUVs (DOPC:DOPG(1,2-dielaidoyl-sn-glycero-3-phospho-(1'-rac-glycerol); molar ratio, 4:1) with an inverted emulsion method (cDICE method^[33]). Subsequently, the vesicles were trapped within the hydrogel chips. Similar to what has been reported before,^[32b] the majority of the uncompressed vesicles was showing pulsing oscillations, for which all proteins simultaneously oscillate

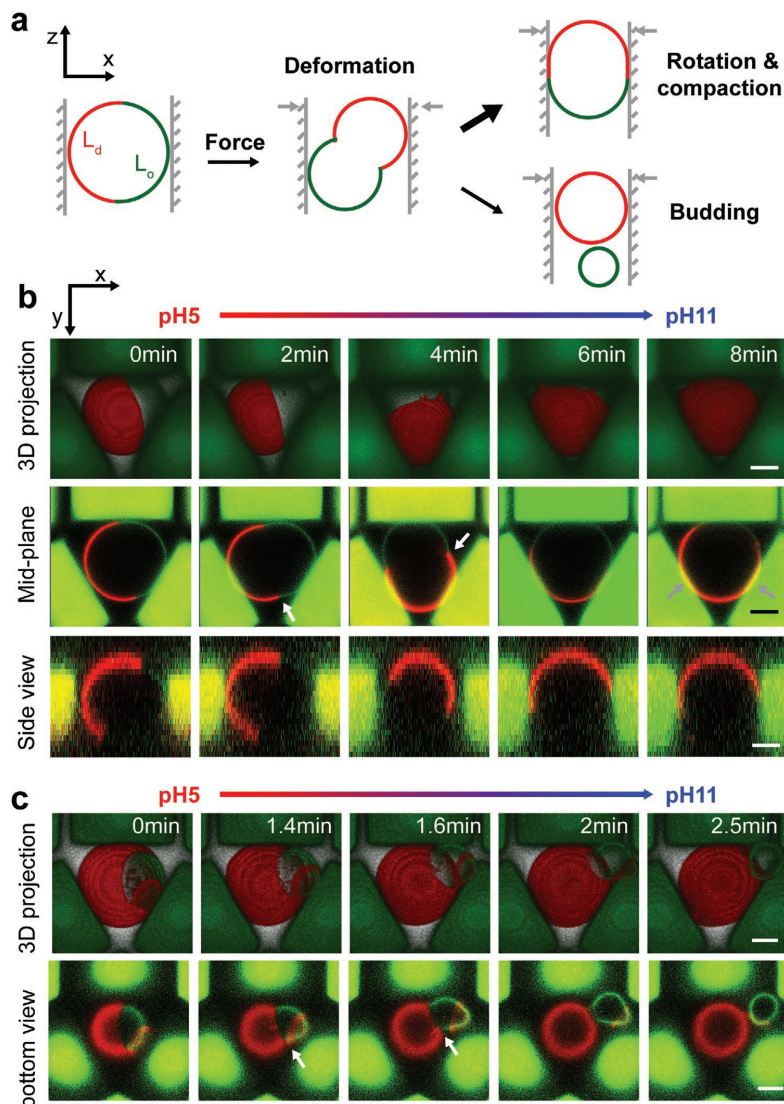


Figure 6. a) Scheme of dynamic lipid phase reorganization adapting to the space-induced membrane deformation. b) Dynamic membrane domain reorganization under pH-induced compression in the hydrogel chambers, scale bar 5 μm . c) Membrane budding driven by the compression of the hydrogel chambers, scale bar 5 μm . GUVs were produced from DOPC:SM:cholesterol (2:2:1) and labeled with NBD-DSPE (green) and Atto655-DOPE (red). The 3D projections of 3D images were compiled from Z-stack confocal images with ZEN software.

between the vesicle lumen and the inner membrane leaflet (Figure 7a). After the pH change from 5 to 11, vesicles that did not get deformed by the hydrogel structures, approximately maintained the oscillation frequency (Figure 7b,c). Since the electrical gradient across the vesicle membrane restricts proton transfer to the inside, intact vesicles showed minor and slow changes of the pH in the vesicle lumen.^[34] This minor change

can be buffered away by the chosen buffer system. However, for vesicles that were compressed due to the hydrogel swelling, we observed an increase in oscillation frequency compared to their uncompressed state (Figure 7d-f; and Movie S5, Supporting Information). We suspect a correlation to the resulting change in aspect ratio of the vesicles (Figure S9, Supporting Information). Larger aspect ratios result in shorter diffusion paths from

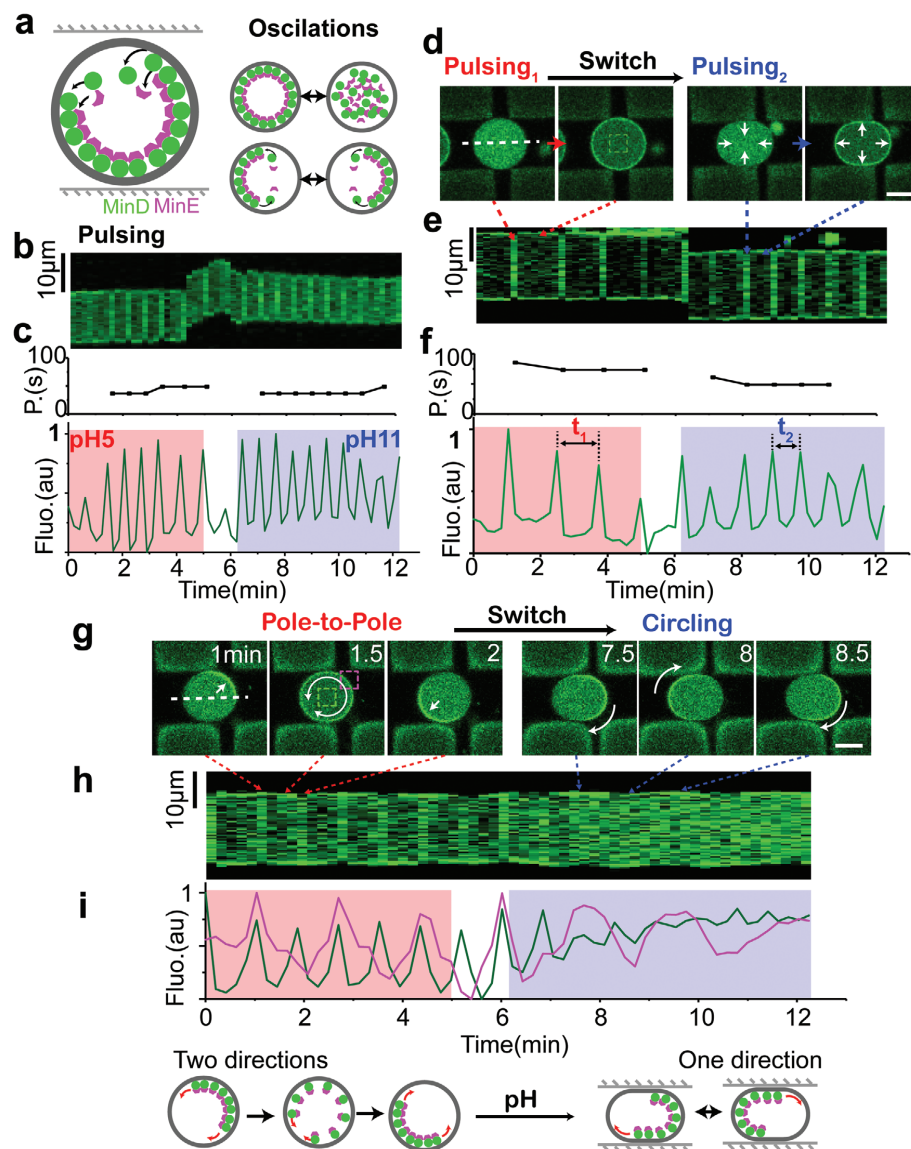


Figure 7. Protein oscillation modes transition in response to change in vesicle geometry. a) Schematic of Min protein oscillations in vesicles. b,c) Pulsing oscillation in a spherical vesicle under different pH conditions. d–f) Pulsing oscillation acceleration during vesicles compression. g–i) Min oscillation modes transition from pole-to-pole to circling. (d), (g), and (j) show imaging frames from the confocal time series of oscillation (1.5×10^{-6} M MinD, 1.5×10^{-6} M eGFP-MinD, 3×10^{-6} M MinE, 5×10^{-3} M ATP). Scale bar: 10 μ m. (b), (e), and (h) demonstrate the kymograph of the oscillation. The white dash lines on the vesicles indicate the position for the kymograph analysis. (c) and (f) (top) show the periods change inside vesicles. (c), (f) (bottom), and (i) either describe the fluorescence oscillation inside vesicles (green) or on the membrane (purple). The green and purple dash box shows the position for measuring the oscillation curves.

vesicle lumen to vesicle membrane and could explain a shorter period of oscillation. On the other hand, membrane vesicle compression leads to changes in membrane tension, which

could also affect the affinity of Min proteins to lipid bilayer and, consequently, alter the reaction diffusion rates. Indeed, *in vitro* reconstitution revealed that a reduced membrane affinity

of Min proteins results in faster traveling waves.^[35] As tense membranes resist the deformation, compressed vesicles would display an increasing membrane tension when compared to uncompressed spherical vesicles. Many studies have shown that protein–membrane interactions are strongly inhibited at high membrane tension.^[36] Thus, to evaluate this hypothesis, only MinD was encapsulated inside GUVs. Indeed, the compression of vesicles with the swelling hydrogel reduced the overall binding of MinD to the membranes (Figure S10a, Supporting Information). This result could be corroborated, as similar findings were observed in trapped vesicles under increased membrane tension undergoing a hypotonic shock (Figure S10b, Supporting Information).

Intriguingly, besides the changes in oscillation frequency, in some cases we observed that the oscillation mode transitioned into a different mode in response to the change in geometry. Figure 7g–i; and Movie S6 (Supporting Information) show a vesicle that initially exhibited pole-to-pole oscillations, in which the maximum protein concentration alternates between the two opposing membrane poles of the vesicle. Upon hydrogel swelling and thus vesicle compression, the protein oscillation switched to a different mode, which was previously described as circling waves:^[32,36b] the protein still is only bound to a small region on the membrane at a time, but now continuously revolves, i.e., “circles,” on the inside surface of the vesicle. Thus, we showed that dynamically regulating the anisotropy of spherical vesicles with pH-stimuli 3D hydrogel chip provides us with new mechanical cues for the investigation of reaction-diffusion systems in 3D artificial microenvironments.

3. Conclusion

We have developed a new toolbox for mechanical manipulation of GUVs—model membrane vesicles that constitute the basis for the engineering of advanced protocells and that should ideally be subject to defined shape transformations. This is particularly desirable when reconstituting membrane polarity- or shape-dependent protein systems, such as bacterial cell division machineries that request explicitly nonspherical geometries.^[10] Our hydrogel devices are based on custom-printed BSA protein that can be switched by pH, and are thus fully biocompatible. Their dimensions are limited only by the optical resolution of the two-photon laser used for printing. We demonstrated that the swelling ratio depends on the laser power used for printing, such that even more complex designs with differential volume expansion could in principle be realized. This opens up a fully new way of using GUVs as custom-made platforms to probe the functionality of reconstituted cellular modules in bottom-up synthetic biology. Our technique thus opens up exciting potential applications for synthetic cell and tissue engineering.

Supporting Information

Supporting Information is available from the Wiley Online Library or from the author.

Acknowledgements

H.J. was supported by the GRK2062, Molecular Principles of Synthetic Biology, funded by Deutsche Forschungsgemeinschaft (DFG). H.G.F. acknowledges financial support by the DFG within the SFB 863. This work is carried out in the context of the MaxSynBio consortium jointly funded by the Federal Ministry of Education and Research of Germany and the Max Planck Society.

Conflict of Interest

The authors declare no conflict of interest.

Keywords

3D printing, bottom-up synthetic biology, hydrogels, membranes, Min system

Received: October 30, 2019

Revised: January 30, 2020

Published online: February 27, 2020

- [1] H. Jia, P. Schwille, *Curr. Opin. Biotechnol.* **2019**, *60*, 179.
- [2] H. Jia, M. Heymann, F. Bernhard, P. Schwille, L. Kai, *New Biotechnol.* **2017**, *39*, 199.
- [3] C. Xu, S. Hu, X. Chen, *Mater. Today* **2016**, *19*, 516.
- [4] K. Göpfrich, I. Platzman, J. P. Spatz, *Trends Biotechnol.* **2018**, *36*, 938.
- [5] R. Dimova, M. Carlos *The Giant Vesicle Book*, CRC Press, Boca Raton, FL **2019**.
- [6] E. Sezgin, I. Levental, S. Mayor, C. Eggeling, *Nat. Rev. Mol. Cell Biol.* **2017**, *18*, 361.
- [7] S. K. Vogel, F. Greiss, A. Khmelinskaia, P. Schwille, *eLife* **2017**, *6*, e24350.
- [8] M. Dezi, A. Di Cicco, P. Bassereau, D. Lévy, *Proc. Natl. Acad. Sci. USA* **2013**, *110*, 7276.
- [9] C. Yeaman, K. K. Grindstaff, W. J. Nelson, *Physiol. Rev.* **1999**, *79*, 73.
- [10] K. Zieske, P. Schwille, *eLife* **2014**, *3*, e03949.
- [11] a) A. Yamada, S. Lee, P. Bassereau, C. N. Baroud, *Soft Matter* **2014**, *10*, 5878; b) F. Fanalista, A. Birnie, R. Maan, F. Burla, K. Charles, G. Pawlik, S. Deshpande, G. H. Koenderink, M. Dogterom, C. Dekker, *ACS Nano* **2019**, *13*, 5439; c) T. Robinson, P. S. Dittrich, *ChemBioChem* **2019**, *20*, 1701.
- [12] J. Koralach, C. Reichle, T. Müller, T. Schnelle, W. Webb, *Biophys. J.* **2005**, *89*, 554.
- [13] M. Théry, V. Racine, M. Piel, A. Pépin, A. Dimitrov, Y. Chen, J.-B. Sibarita, M. Bornens, *Proc. Natl. Acad. Sci. USA* **2006**, *103*, 19771.
- [14] Y. T. Kim, S. Bohjanen, N. Bhattacharjee, A. Folch, *Lab Chip* **2019**, *19*, 3086.
- [15] M. Bao, J. Xie, A. Piruska, W. T. Huck, *Nat. Commun.* **2017**, *8*, 1962.
- [16] B. Kaehr, J. B. Shear, *Proc. Natl. Acad. Sci. USA* **2008**, *105*, 8850.
- [17] P.-S. Li, I.-L. Lee, W.-L. Yu, J.-S. Sun, W.-N. Jane, H.-H. Shen, *Sci. Rep.* **2014**, *4*, 5600.
- [18] a) M. R. Lee, I. Y. Phang, Y. Cui, Y. H. Lee, X. Y. Ling, *Small* **2015**, *11*, 740; b) C. L. Lay, M. R. Lee, H. K. Lee, I. Y. Phang, X. Y. Ling, *ACS Nano* **2015**, *9*, 9708.
- [19] T. Robinson, P. Kuhn, K. Eyer, P. S. Dittrich, *Biomicrofluidics* **2013**, *7*, 044105.
- [20] D. Stamou, C. Duschl, E. Delamarque, H. Vogel, *Angew. Chem.* **2003**, *115*, 5738.

- [21] B. Sorre, A. Callan-Jones, J.-B. Manneville, P. Nassoy, J.-F. Joanny, J. Prost, B. Goud, P. Bassereau, *Proc. Natl. Acad. Sci. USA* **2009**, *106*, 5622.
- [22] A. Khmelinskaia, H. G. Franquelim, E. P. Petrov, P. Schwille, *J. Phys. D: Appl. Phys.* **2016**, *49*, 194001.
- [23] T. Peters Jr., *All About Albumin: Biochemistry, Genetics, and Medical Applications*, Academic Press, San Diego, CA **1995**.
- [24] D. Hoekstra, O. Maier, J. M. van der Wouden, T. A. Slimane, S. C. van IJzendoorn, *J. Lipid Res.* **2003**, *44*, 869.
- [25] K. Bacia, P. Schwille, T. Kurzchalia, *Proc. Natl. Acad. Sci. USA* **2005**, *102*, 3272.
- [26] S. L. Veatch, S. L. Keller, *Biophys. J.* **2003**, *85*, 3074.
- [27] A. J. García-Sáez, S. Chiantia, P. Schwille, *J. Biol. Chem.* **2007**, *282*, 33537.
- [28] F. Jülicher, R. Lipowsky, *Phys. Rev. Lett.* **1993**, *70*, 2964.
- [29] a) E. Frey, J. Halatek, S. Kretschmer, P. Schwille, *Physics of Biological Membranes*, Springer, Cham, Switzerland **2018**, p. 229; b) D. Thalmeier, J. Halatek, E. Frey, *Proc. Natl. Acad. Sci. USA* **2016**, *113*, 548.
- [30] M. Loose, E. Fischer-Friedrich, J. Ries, K. Kruse, P. Schwille, *Science* **2008**, *320*, 789.
- [31] a) J. Schweizer, M. Loose, M. Bonny, K. Kruse, I. Mönch, P. Schwille, *Proc. Natl. Acad. Sci. USA* **2012**, *109*, 15283; b) K. Zieske, P. Schwille, *Angew. Chem., Int. Ed.* **2013**, *52*, 459.
- [32] a) K. Zieske, G. Chwastek, P. Schwille, *Angew. Chem., Int. Ed.* **2016**, *55*, 13455; b) T. Litschel, B. Ramm, R. Maas, M. Heymann, P. Schwille, *Angew. Chem., Int. Ed.* **2018**, *57*, 16286.
- [33] M. Abkarian, E. Loiseau, G. Massiera, *Soft Matter* **2011**, *7*, 4610.
- [34] M. Megens, C. E. Korman, C. M. Ajo-Franklin, D. A. Horsley, *Biochim. Biophys. Acta* **2014**, *1838*, 2420.
- [35] B. Ramm, T. Heermann, P. Schwille, *Cell. Mol. Life Sci.* **2019**, *76*, 4245.
- [36] a) M. Saleem, S. Morlot, A. Hohendahl, J. Manzi, M. Lenz, A. Roux, *Nat. Commun.* **2015**, *6*, 6249; b) M. Simunovic, G. A. Voth, *Nat. Commun.* **2015**, *6*, 7219.

Copyright WILEY-VCH Verlag GmbH & Co. KGaA, 69469 Weinheim, Germany, 2020.

NANO MICRO
small

Supporting Information

for *Small*, DOI: 10.1002/smll.201906259

Shaping Giant Membrane Vesicles in 3D-Printed Protein Hydrogel Cages

*Haiyang Jia, Thomas Litschel, Michael Heymann, Hiromune Eto, Henri G. Franquelim, and Petra Schwille**

Supporting Information

Shaping giant membrane vesicles in 3D-printed protein hydrogel cages

Haiyang Jia, Thomas Litschel, Michael Heymann, Hiromune Eto, Henri G. Franquelim, Petra Schwille

Table of Contents

Experimental Procedures

Supplement scheme S1 and figure S1 to S10

Supplement Movie S1 to S6

References

Experimental Procedures

Preparation of BSA Solution

4.2g bovine serum albumin (BSA) (Lyophilized powder, A7030, Sigma Aldrich) and 1.62 mL of DMSO (18v/v%) were added to 20 mM HEPES buffer to make up a total volume of 9 mL solution. The mixture was centrifuged (20000g) for 15min to remove impurities and foam before use. 85mM rose bengal (Sigma Aldrich, 330000) was prepared separated. The BSA photoresist (420g L⁻¹) was prepared by mixing BSA resin and rose bengal at the ratio of 9:1v/v.

3D BSA Hydrogel printing

3D BSA hydrogel printing was processed with the Nanoscribe Photonic Professional (Nanoscribe GmbH). 3D structures were design with Solidwork. The parameters were defined with Describe. If without specifying, the following parameters were used, laser power: 50mW (100%), scan speed: 30000μm s⁻¹, slicing distance: 0.5μm, hatching distance: 0.2μm. All structures were printed with 63x NA1.4 objective in silicone isolator chamber (Thermo Fisher Scientific, 0717104) pasted on round glass coverslip (Diameter= 30mm, thickness #1.5).

During printing, the chambers were covered a small coverslip to avoid strong evaporation. After fabrication, structures were rinsed with Phosphate Buffered Saline (PBS) buffer (pH7) to remove the excess BSA resin and photoresist.

Swelling Studies

Five repeat free-form solid cuboids (14x14x15 μ m) with slicing distance 0.2–0.8 μ m were fabricated with different laser power (30mW-50mW) and scan speed (10000-30000 μ m s⁻¹). The swelling of structures were observed at different pHs (5-11) using confocal microscope. Structures swelling were studied from low pH to high pH. Structures were equilibrated in different pH solution for 10 minutes before they were transferred for imaging. Areas of the cubes were measure with Fiji (Analyze particles). Then the swelling ratios were calculation as A_{pH}/A_{pH5} , where A means area. Confocal imaging was performed on a commercial Zeiss LSM 780 laser scanning microscope, using a water immersion objective (C-Apochromat, 40 × /1.2W, Zeiss). Samples were excited with the 561 nm laser.

GUVs preparation

Giant unilamellar vesicles (GUVs) were produced by electroformation in PTFE chambers with Pt electrodes according to the published protocol^[20] with minor changes. Six microliter of lipid mixture (1mg/mL in chloroform) was spread onto two Pt wires and dried in a desiccator for 30 min. The chamber was filled with 350 μ L of an aqueous solution of sucrose (~ 300mOsm kg⁻¹). An AC electric field of 1.5 V (RMS) was applied at a frequency of 10Hz for 1.5h, followed by 2Hz for 0.25 h. Unless otherwise stated, vesicles composed of DOPC, containing additional 0.5mol% Atto655-DOPE, were electroformed in an aqueous solution of sucrose iso-osmolar compared to imaging buffer (~ 300mOsm kg⁻¹). For the phase separation, GUVs were prepared from mixtures of DOPC, SM (18:0), and cholesterol (2:2:1) plus 0.2mol% Atto655-DOPE and 0.3mol%NBD-DSPE.

GUVs trapping and shaping

3D structures were exchanged into pH5 PBS buffer (~294mOsm kg⁻¹) for 10min. Then, 20 μ L or more of the GUV suspension (without-diluted) were added on top of the printed structures in the imaging chambers. Samples were incubated for at least 0.5 h at room temperature. After GUVs sinking down and diffusing inside the traps, samples were transferred for imaging. Then, samples were gently equilibrated into pH11 PBS buffer for 10min to reach the maximal swelling. The deformation of the trapped GUVs were imaged with confocal microscopy. To

avoid bursting the GUVs during deformation, the osmolality of pH11 PBS buffer ($\sim 307\text{mOsm kg}^{-1}$) was slightly higher than sucrose solution inside GUVs.

Min oscillation in vesicles

1. Proteins

The plasmids for the expression of His-MinD^[28], His-EGFP-MinD^[32] and His-MinE^[28] have been described previously. His-MinD, His-EGFP-MinD and His-MinE were purified according to the published protocols. In brief, proteins were expressed in *E. coli BL21* (DE3) pLysS and further were purified via Ni-NTA affinity purification. Then proteins were further purified using gel filtration chromatography in storage buffer (50mM HEPES, pH 7.25, 150mM KCl, 10% Glycerol, 0.1mM EDTA). Proteins were quick-frozen and stored in aliquots at -80°C until further use.

2. Proteins Encapsulation in vesicles

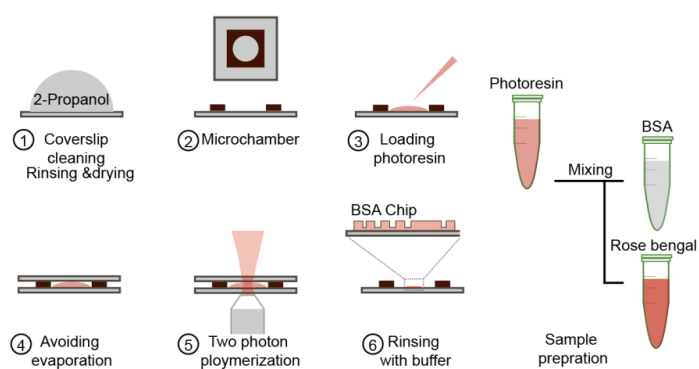
Min system was encapsulated in vesicles by emulsion transfer (the cDICE method^[31]) according to the published protocol^[30b]. Briefly, both inner and outer solution contain Min protein buffer (25mM tris-HCl (pH 7.5), 150mMKCl and 5mM MgCl₂). In addition, the solution encapsulated in the GUVs contained 1.5 μM MinD, 1.5 μM eGFP-MinD, 3 μM MinE, 5mM ATP, v/v 15% iodixanol (from OptiPrepTM, Sigma Aldrich) and an oxygen scavenger system (3.7U ml⁻¹ pyranose oxidase, 90U/ml catalase, 0.8% glucose. Osmolarity of encapsulated solution was about 560mOsm kg⁻¹, measured with Fiske[®] Micro-Osmometer Model 210). As the GUV-surrounding solution, Min protein reaction buffer and 200 mM glucose were used to match the osmolarity of the inner solution.

The lipid we used is DOPC (1,2-Dioleoyl-sn-glycero-3-phosphocholine, Avanti Polar Lipids, Inc.) and DOPG (1,2-Dioleoyl-sn-glycero-3-phosphoglycerol, Avanti Polar Lipids, Inc.) (Both 25mg ml⁻¹ in chloroform) in a ratio of 4:1. The lipids were mixed in a silicon oil (5 cST) and mineral oil (sigma-aldrich. M5904) mixture (ratio, 4:1).

Then the inner solution was loaded into a 1 mL syringe, which was then placed into a syringe pump system (neMESYS base 120 with neMESYS 290N) and connected through tubing to a glass capillary (100 μm inner diameter). 700 μl of outer solution was pipetted into a spinning cDICE chamber, followed by approximately 5ml of the lipid-in-oil mixture. The capillary tip

was then immersed in the oil phase and the inner phase injected at a flow rate of $50\mu\text{l h}^{-1}$ for 15 minutes. The vesicles were withdrawn from the cDICE chamber with a micropipette.

Supplement figures



Scheme S1. Schematics of 3D printing BSA hydrogel

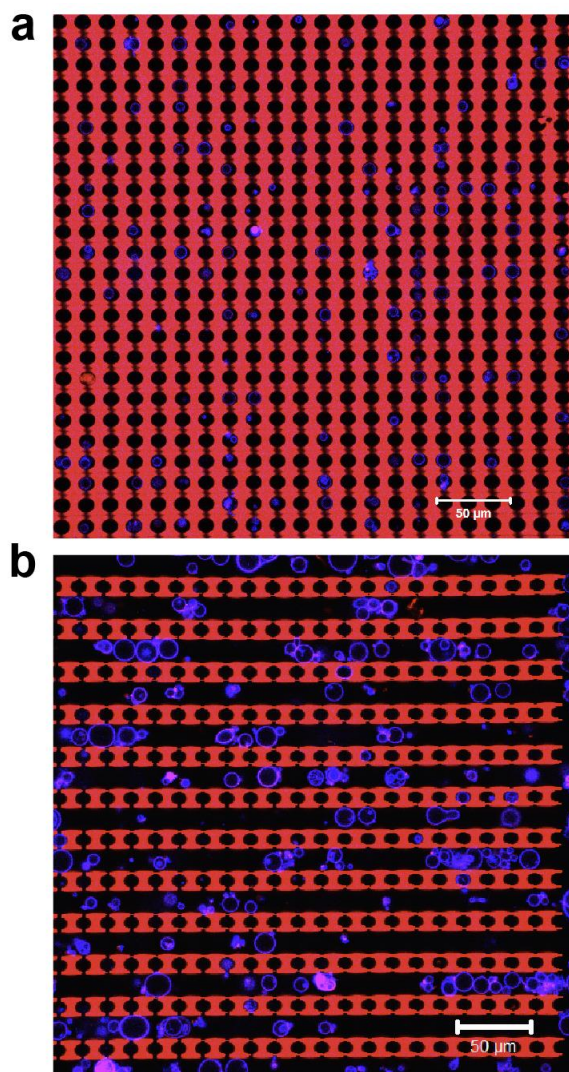


Figure S1. Overviews of the GUVs trapped in a.) The individual trap chip (22x 25 array) and b.) The group trap chip (11 channels), scale bar 50μm. GUVs were produced with DOPC and labelled with 0.5mol% Atto655-DOPE.

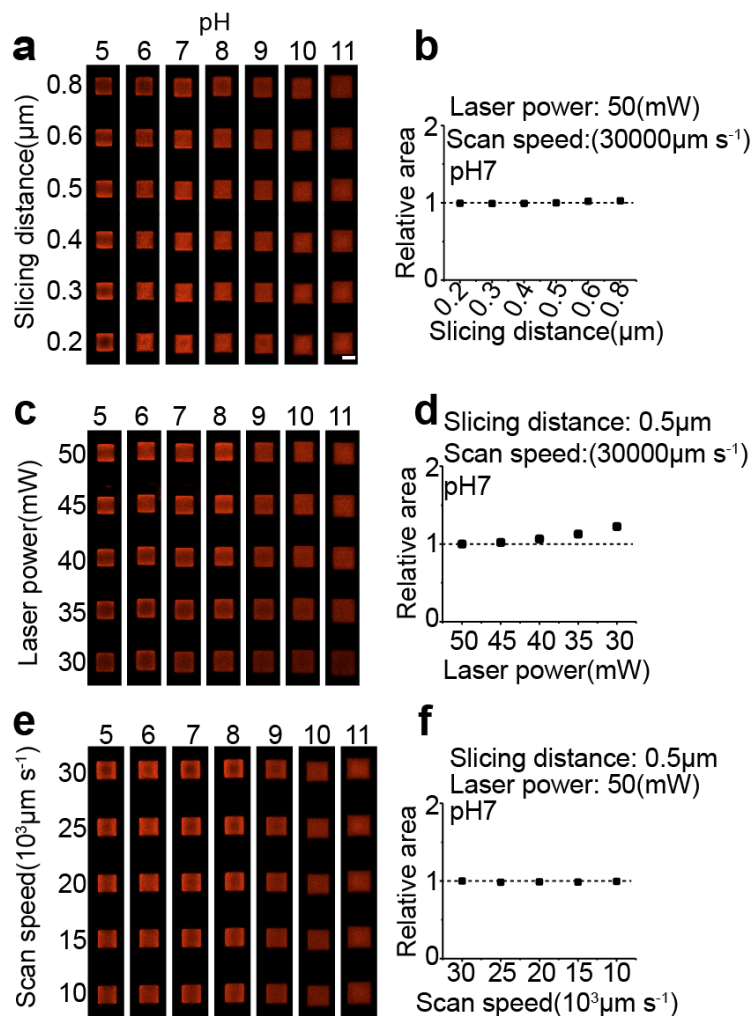


Figure S2. pH-dependent swelling of 3D printed cubic hydrogels fabricated with different fabrication parameters a.) pH responsive swelling of hydrogel cube with different slicing distances from 0.2 to 0.8 μm (Laser power: 50mW, Scan speed: 30000 $\mu\text{m s}^{-1}$), scale bar 10 μm . b.) relative area of structures printed with different slicing distance at pH7. The slicing distance will not influence printing size of the structures. c.) pH responsive swelling of hydrogel cube with different laser power from 30 to 50mW (Slicing distance: 0.5 μm , Scan speed: 30000 $\mu\text{m s}^{-1}$). d.) Relative area of structures printed with different laser power at pH7. Printing with laser power lower than 40mW increased structure size. e.) pH responsive

swelling of hydrogel cube with different laser scan speed from 10000 to 30000 $\mu\text{m s}^{-1}$ (Slicing distance: 0.5 μm ; laser power: 50mW). f.) Relative area of structures printed with different scan speed at pH7. The relative area calculated with A/A_0 , where A_0 means the area of structure printed with fabrication parameters (Slicing distance: 0.5 μm , Laser power: 50mW, Scan speed: 30000 $\mu\text{m s}^{-1}$).

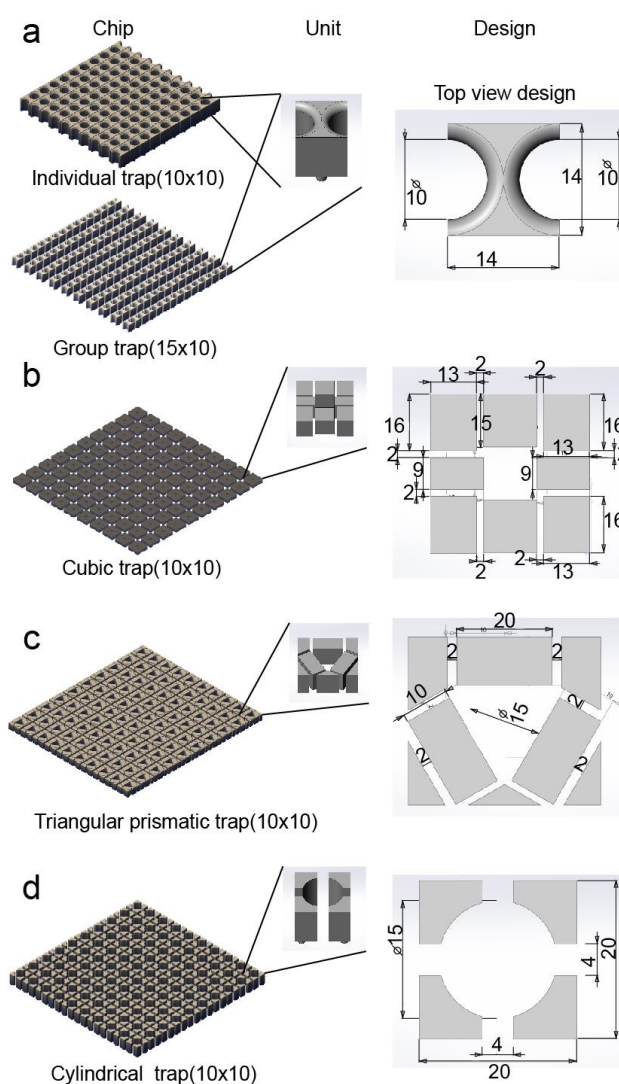


Figure S3. Schematic designs and dimensions of 3D protein hydrogel traps a.) Individual traps with 10x10 array in Fig. 1a. and group traps in Fig. 1b ,c, Fig.3 . b. and Fig.6.) Cubic traps with a 10x10 array in Fig.2f and Fig. 4. c.) Triangular prismatic traps with a 10x10 array in Fig. 4 and Fig. 5. d.) 10x10 cylindrical traps array in Fig. 4. If without specifying, all the structures used in this research are freestanding designs with pillars as supports (Diameters 2 μm , Height 2 μm)

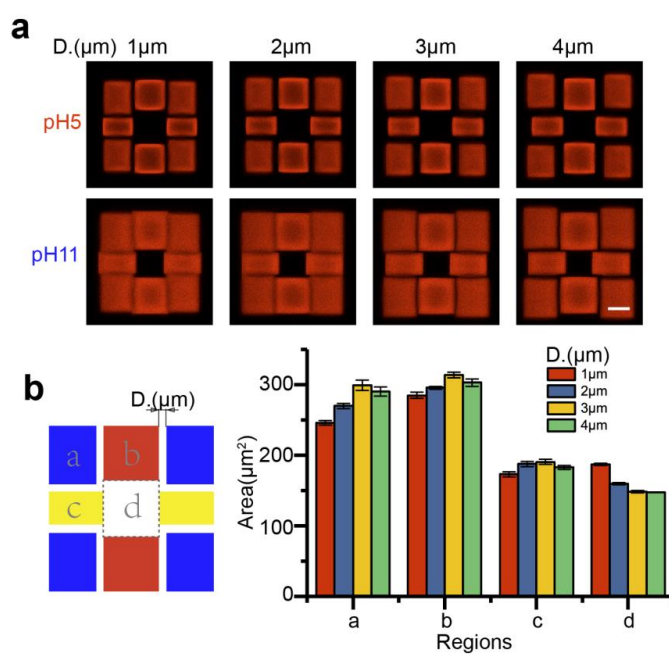


Figure S4. Distances between modules influence structure swelling capability. a.) pH responsive swelling of cubic traps with different distances between modules, scale bar, 10 μ m. b.) Area swelling of different regions in the cubic trap with different distances, when pH was changed from 5 to 11. Module b and c are freestanding structures with pillar supports. Module a were cuboid without pillar supports.

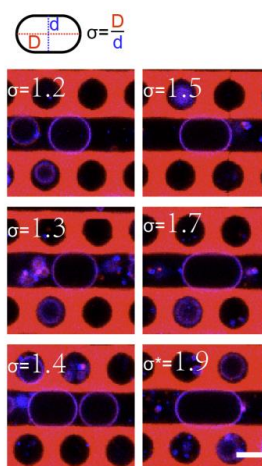


Figure S5. Swelling hydrogel compressing GUVs with different aspect ratios σ (width compared to length), scale bar 10 μ m. The deformation of GUVs were processed in the group trap chip. Due to the size difference, GUVs with different aspect ratio can be obtained from the swelling compression. * GUV (Diameter>15 μ m) trapped in the chip had been compressed at pH5.

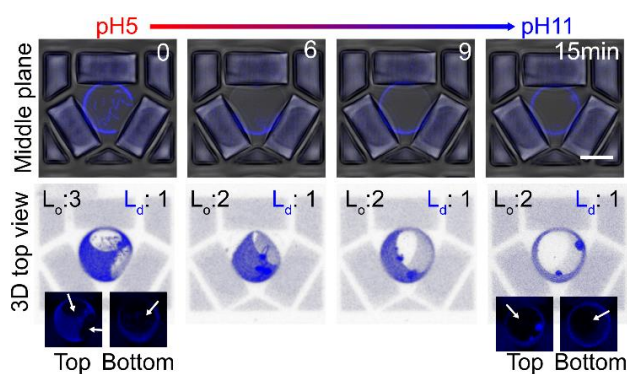
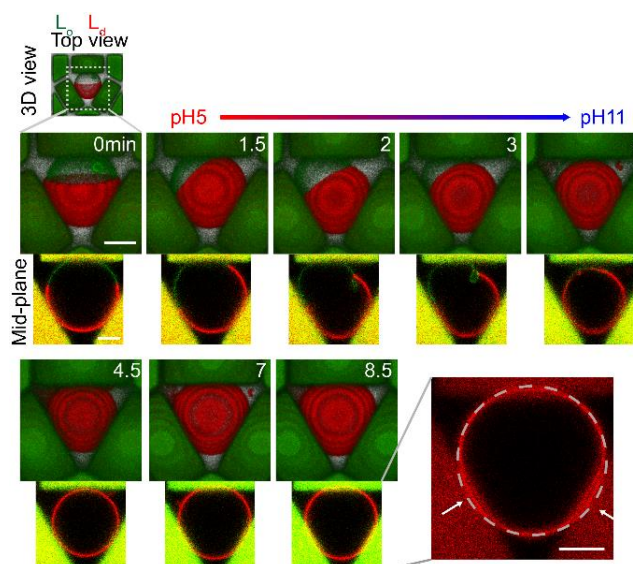


Figure S6. Dynamic lipid domain fusion and reorganization adapting to the space-induced membrane deformation, Scale bar, 10 μ m. Top: confocal images of middle plane of the vesicle. Bottom: top view of the 3D z-stack reconstitution. The numbers show the domain numbers of L_o and L_d phase. GUVs were produced from DOPC:SM:cholesterol (2:2:1). GUV



in the images was labelled with Atto655-DOPE (blue).

Figure S7. Dynamic membrane domain reorganization under pH-induced compression in the hydrogel chambers, scale bar 5 μ m. GUVs were produced from DOPC:SM:cholesterol (2:2:1) and labelled with NBD-DSPE(green) and Atto655-DOPE (red). The top views of 3D images were compiled from Z-stack confocal images with ZEN software.

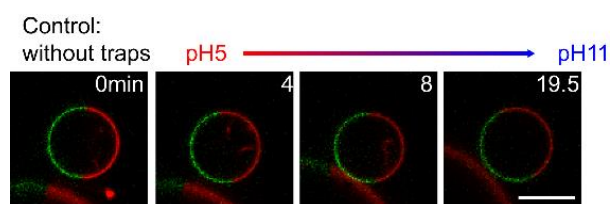


Figure S8. Free standing phase-separated GUVs upon pH stimuli, scale bar, 10 μ m. GUV in the images was labelled NBD-DSPE (green) and Atto655-DOPE (red).

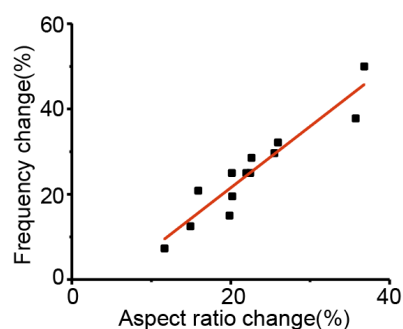


Figure S9. Pulsing oscillation acceleration during vesicles compression ($1.5\mu\text{M}$ MinD, $1.5\mu\text{M}$ eGFP-MinD, $3\mu\text{M}$ MinE, 5mM ATP). Pulsing frequency change versus aspect ratio (W/H) change of vesicles that were before- and after- compressed.

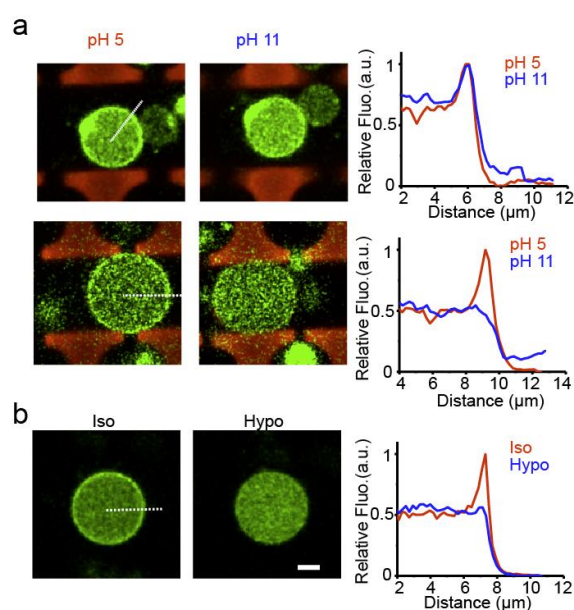


Figure S10. a.) Vesicle compression could oppose Min protein binding ($1.5\mu\text{M}$ MinD). b.) MinD-membrane interaction under hypotonic and isotonic condition. To generate the hypotonic shock, the outer solution osmolality was increased about 20mOsm by adding water in the surrounding buffer. Scale bar, $5\mu\text{m}$. The white dash lines show the position for radial plot profiles.

Supplement Movies

Supplement Movie S1. pH responsive swelling of group trap, when pH was shift from 5 to 11.

Supplement Movie S2. Dynamic membrane phase separation and reorganization in pH-stimuli 3D hydrogel chamber (top view)

Supplement Movie S3. Dynamic membrane phase separation and reorganization in pH-stimuli 3D hydrogel chamber (orthogonal view)

Supplement Movie S4. Membrane budding driven by the space compression of the pH-stimuli 3D hydrogel chambers (top view)

Supplement Movie S5. Pulsing oscillation acceleration during vesicles compression

Supplement Movie S6. Min oscillation modes transition from pole-to-pole to circling.

References

- [1] A. Khmelinskaia, H. G. Franquelim, E. P. Petrov, P. Schwille, *J. Phys. D* **2016**, 49, 194001.
- [2] M. Loose, E. Fischer-Friedrich, J. Ries, K. Kruse, P. Schwille, *Science* **2008**, 320, 789.
- [3] K. Zieske, J. Schweizer, P. Schwille, *FEBS letters* **2014**, 588, 2545.
- [4] M. Abkarian, E. Loiseau, G. Massiera, *Soft Matter* **2011**, 7, 4610.
- [5] T. Litschel, B. Ramm, R. Maas, M. Heymann, P. Schwille, *Angew Chem. Int. Ed. Engl.* **2018**, 57, 16286.

8

Other applications of microfabrication

8.1 Microwells for upright imaging of bacteria

In this section, I applied microfabrication techniques to aid the super-resolution imaging of the divisome in *Bacillus subtilis*. In particular, I employed two-photon laser lithography as an alternative to standard 2D photolithography to fabricate a master template for downstream soft lithography. Here, two-photon direct laser writing (2PP-DLW) proved a useful tool for fabricating objects with high aspect ratios with easy preparation methods, without the need for the pre- or post-baking of photoresists. High resolutions, with features sizes of down to a micron, can be achieved [125], which is necessary for making structures relevant to bacteria with typical dimensions of 1 μm in width 3 μm in length. Using these 3D printed structures as a template, I employed soft lithography to make microwells in PDMS, which were used to "house" bacteria in their upright positions for super-resolution imaging. With increased resolution in the xy-plane as opposed to the z-direction, features that lie perpendicular to the axis of these cylindrical cells, such as the Z-ring, can be imaged at higher spatial resolution, and therefore greatly improves imaging quality.

The results of this section is a collaboration between Kimberley Cramer and Ralf Jungmann (Max Planck Institute of Biochemistry). **H.E.** fabricated the microwells. **K.C.** prepared the cells for imaging. **H.E.** and **K.C.** trapped cells in microwells and imaged the cells.

8.1.1 Introduction

Bacterial cell division is an essential cellular process, and is also a remarkable feat of molecular self-assembly where a nanoscale divisome machine builds on a pre-positioned FtsZ ring, eventually constructing a micron-scale wall (septum) at mid-cell [126, 127]. The divisome consists of a complex protein network extending from the cytoplasm to all three layers of the cell envelope [128–130]. This includes scaffold proteins, peptidoglycan synthases and hydrolases that remodel the peptidoglycan network, as well as proteins that coordinate cell division and chromosome segregation [126]. However, the exact hierarchical assembly of proteins is not yet understood [127].

One of the main problems that limit progress in this research is the size of bacteria: they typically grow to a cylindrical shape of around 1 μm in diameter and 3 μm in length [131]. Being so close to the diffraction limit, these organisms are difficult to

analyse by standard microscopy. An effective solution to gain higher resolution is through the use of microfabrication [132, 133], where bacteria can be trapped vertically inside custom-shaped microwells. This makes use of the asymmetrical distribution of the point-spread function, which can be 3-4 fold smaller in xy compared to the z direction [134]. Thus, by positioning the division ring in the xy plane, higher resolution can be gained without any change in optical instrumentation.

In this project, we make use of microfabrication to image components of the divisome by DNA-paint super-resolution imaging [135]. I employed two-photon laser lithography to make a lithography template, from which microwells can be made as PDMS replicas. The microwells were designed to fit a single bacteria in its upright position, making sure that the division ring is placed in the xy plane. The development of this technique allows us to investigate the hierarchical assembly of the divisome by super-resolution imaging.

8.1.2 Methods

FABRICATION OF MICROWELLS

To enhance the adhesion of the micropillars to the substrate, a silicon wafer (4 inches) was initially immersed in 3-(trimethoxysilyl)propyl methacrylate (Sigma-Aldrich) (0.1 mL in 20 mL ethanol) for 15 min, rinsed in water, and dried with nitrogen.

For 3D printing, scaffold geometries were designed in Solidworks (Dassault Systèmes, France), and print parameters then specified in Describe (Nanoscribe GmbH, Germany) and fabricated on a commercial DLW system (Photonic Professional, Nanoscribe GmbH, Germany) with a Zeiss Plan-Apochromat 63x/1.4 Oil DIC objective. The IP-S photoresist (Photonic Professional, Nanoscribe GmbH, Germany) was drop-cast onto the coverslip and printed in dip-in mode. Laser power of 70% and scan speed 10000 μm was used. After exposure, the structures were developed and rinsed with isopropyl alcohol and dried with a stream of nitrogen.

To apply a release agent, we dropcast CYTOP 109AE onto the fabricated silicon wafer and spincoated at 500 rpm for 30 s, and then gently cured on a hotplate at 50 °C over 20 min, until full solvent evaporation.

To fabricate the microwells, PDMS was first mixed with a cross linker in 10:1 weight ratio and then cast on the master template. A clean glass coverslip was placed on top and gently weighed down. PDMS was cured in an oven at 75 °C over 2 h. The PDMS/coverslip was then carefully peeled off using a scalpel.

SCANNING ELECTRON MICROSCOPY

Samples were first sputter-coated with platinum/palladium on a high-resolution automatic sputter coater (Cressington 208HR) at 20 mA and 0.1 mbar Argon for 3 \times 20 s. The thickness of the applied coatings was measured with a built-in thickness controller to be 2.0 nm. They were then imaged using TESCAN MIRA3 FESEM operating at an accelerating voltage of 10 kV in SE mode.

PREPARATION OF CELLS

WT *Bacillus subtilis* [131] were plated on LB agar plates and grown overnight in LB at 30 °C. For vegetative cells, cells were diluted 1:1000 and grown at 30 °C in SMG

media (15 mM $(\text{NH}_4)_2\text{SO}_4$, 61 mM K_2HPO_4 , 44 mM KH_2PO_4 , 3.4 mM sodium citrate $2\times\text{H}_2\text{O}$, 1.7 mM MgSO_4 , 5.9 mM glutamate and 27 mM glucose supplemented with 1.0 mM tryptophan) until $\text{OD}_{600} = 0.15$ then fixed as previously described [136]. Cells were concentrated to $\text{OD}_{600} = 0.5$ before fixation, and after washed 3x with PBS. To visualize DNA, samples were incubated with 60 ng/ml DAPI, for 10 min at RT. PDMS wells were stained with 500 pM Nile Red dye for 5 min at RT.

Before addition of cells, the PDMS chambers were plasma treated with oxygen at 50 % power, flow rate 0.3 sccm for 15 s (model Zepto, Diener Electronic). We then constructed a chamber to load the cells and for imaging, assembled from a silicone isolator chamber (Thermo Fisher Scientific, 0717104) pressed on to the PDMS/coverslip. 15 μL of cell suspension was then added to the area directly over the PDMS wells and centrifuged for 10 min at $3,700 \times g$ in a swinging bucket centrifuge with homemade adapters.

IMAGING

The widefield imaging was performed in Imaging Facility of the Max Planck Institute of Biochemistry (MPIB-IF) on a GE DeltaVision Elite system based on an OLYMPUS IX-71 inverted microscope, an UPLSAPO 60xW objective and a PCO sCMOS 5.5 camera.

8.1.3 Results

The schematics of the fabrication is given in Fig 8.1. To fabricate the microwells, I first designed the master template. Micropillars were printed at 1 μm diameter and 5 μm height, so that the ultimate microwells dimensions can accommodate a single cell of bacteria that sit fully upright, and these were arranged in a 15×15 grid with 10 μm spacing. After sweeping the printing parameters, I found that stable structures could be printed at 70 % laser power and 10000 $\mu\text{m}/\text{s}$ scan speed.

For these micropillars, the z-slicing parameter was set to 0.3 μm . This is a commonly used setting (recommended by Nanoscribe) for printing in IP-S photoresist with the 63x objective, since it usually gives a good balance between the printing speed and print quality. However, when observed on the Scanning Electron Microscopy (SEM), individual layers of printing was clearly visible, and the surfaces of the micropillars appeared rough, which can make the subsequent release of PDMS difficult. Therefore, I coated the micropillars with CYTOP - which I used in section 5.2 as a refractive index-matched polymer alternative to PDMS, but it also has a very low surface energy that is commonly used as a release layer in soft lithography. The SEM images of the pillars after CYTOP coating reveal that the roughness from the printing was smoothed out by the additional polymer coating. This physical modification, as well as the ultra-hydrophobic surface treatment, aids in the efficient release of PDMS from the master mold.

I then formed the microwells by soft lithography. From fluorescence images, we see that the chamber dimensions are faithful copies of the micropillars, which are 1 μm in diameter and 5 μm in height. Before loading the chambers with cells, a gentle plasma treatment is necessary to render the surfaces hydrophilic, which allows water to fill up the wells. After loading the cells with gentle centrifugation, we could

observe that the cells indeed localise in their upright positions in our microfabricated wells.

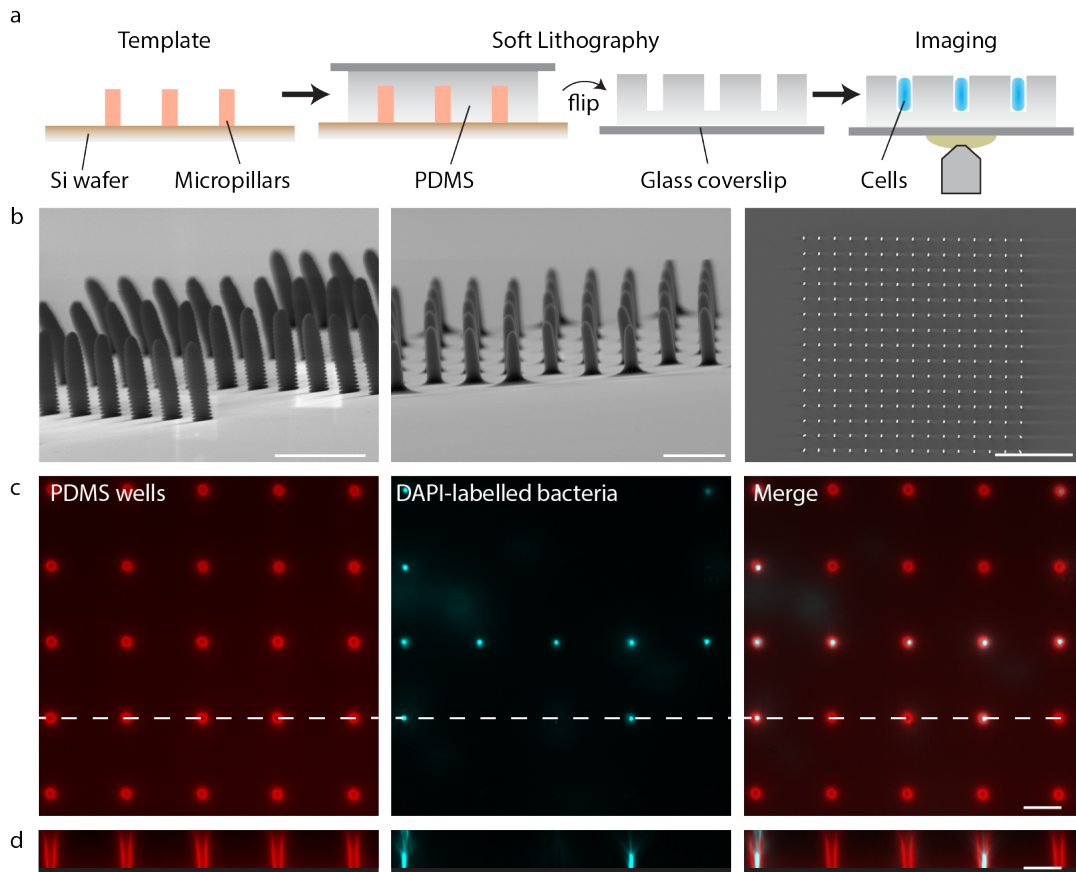


Figure 8.1. Microfabrication of wells for upright imaging of bacteria. a) Schematic of workflow. b) 3D printed micropillars as template before (left) and after (middle) CYTOP treatment, scale bar 5 μm . Zoomed out overview (right), scale bar 50 μm . c) Fluorescent images of PDMS wells, stained with Nile Red, and bacteria stained in DAPI, with d.) their cross section along the indicated dotted line. Scale bar 5 μm .

9

Discussion and Future Perspectives

In this thesis, I set out to advance methods that recreate relevant cell-like geometries for bottom-up synthetic biology. Through the use of a diverse array of microfabrication methods, I developed ways to pattern stable membranes on rigid supports, in dimensions ranging from planar 2D substrates, embossed 2.5D compartments, and fully 3D structures. The fabrication of dynamic, shape-shifting 4D structures made of protein-based hydrogels demonstrated an alternative strategy to deform lipid vesicles, and I investigated the reengineering of more stable free-standing membrane systems from synthesized dendrimer molecules that permit more strenuous shape transformations. Finally, I applied 3D printing to enable the upright imaging of bacteria, facilitating the imaging of the divisome by super-resolution techniques. In this discussion, I examine these developments in turn and evaluate their effectiveness for the challenges that lie ahead.

MULTIDIMENSIONAL PATTERNING OF SUPPORTED LIPID BILAYERS

Microfabrication is an effective way to create custom-designed structures from patternable materials, and in this thesis, I used this as the substrate onto which I formed supported lipid bilayers. The SLB is a widely employed model membrane system, whose patterning has contributed to many *in vitro* investigations in the past [39]. Thus, the expansion of SLB patterning onto fully 3D structures represents a significant step towards more faithfully recreating the morphological complexity of cells and organelles. Subcellular membranous structures such as the endoplasmic reticulum, or invaginations in the mitochondria are systems where the membrane area per reaction volume is carefully and actively regulated, and such structures can surely become the target of a systematic investigation using 3D patterning strategies.

The limitations faced by SLBs in general, however, also apply to the methods developed in this thesis. Firstly, they are incapable of incorporating transmembrane proteins [39], thus restricting the range of biochemical systems that can be reconstituted in this membrane. Secondly, their membrane properties are influenced by the underlying substrate, resulting in reduced membrane fluidity or even alterations in their biophysical or biochemical behaviour [137]. Thirdly, they are formed on rigid supports, and therefore the membrane shapes themselves cannot be dynamically transformed.

Many of these problems have been partly or even fully addressed in many SLB systems. For example, instead of forming SLBs directly on the substrate, polymer

cushions or spacers could be used, which increases the hydration layer between the membrane and the substrate [39, 41]. This extra space allows transmembrane proteins to be reconstituted in the membrane. Such strategies also effectively decouple the membrane from the substrate, and the fluidity and as well as other membrane properties, such as phase separation, more closely resemble those of free-standing membrane systems [137].

The mechanical inflexibility of SLBs, however, which is inherent to the rigidity of the underlying substrate, is an issue that cannot be easily solved. We can speculate that, by using soft, deformable materials to support membrane formation, SLBs can also be dynamically actuated. In fact, hydrogels, synthetic or protein based, have a wealth of chemically functional components available that we would potentially allow us to prepare the substrate for membrane deposition. This includes negatively charged (-COOH), biotinylated or acrylate-terminated polyethylene glycol (PEG), with also the possibility to 3D print them [138]. There are also shape-shifting hydrogels and pH-responsive BSA-based structures, as demonstrated in the associated publication P4, that provide the interesting prospect of fabricating SLB-coated structures that transform in shape. This has, however, never been demonstrated, and instead, free-standing membrane systems, such as lipid vesicles, are still the preferred choice as the mechanically flexible model membrane system.

We can probe further into material innovation in order to increase the effectiveness of these SLB systems. In this thesis, I explored Ormocomp, pentaerythritol triacrylate (PETA) and trimethylolpropane ethoxylate triacrylate (TPETA) as examples of readily available 3D printable materials for SLB formation. They have high chemical and physical stability, with little swelling or dissolution, while also having the chemical functionality that I could tune to optimise the lipid-substrate interaction for membrane deposition. Glass is another material that is commonly used for SLB formation, and has also been recently 3D printed even on the microscale [139]. These materials, however, are not refractive index matched to the surrounding medium (commonly water, $n=1.33$), and therefore cause severe optical distortions that can obscure fluorescence imaging.

In this regard, I explored materials like CYTOP, which are refractive index matched [140], and have ideal optical properties for use in microscopy-based *in vitro* reconstitution assays. Fabrication methods that use these materials, however, are still less well explored, and the associated publication P2 was a contribution that demonstrated an alternative method - negative molding - to pattern them. Another promising candidate is MyPolymer: a commercially available refractive index matched polymer, which can be UV light-patterned based on acrylate groups present in their monomers [141]. Further developments in this direction would drastically improve imaging qualities, not only for standard microscopy methods, but also for super-resolution imaging, and would signify a considerable step up in the tools available for biological research in general.

GEOMETRY SENSITIVITY OF MINDE SELF-ORGANISATION

Despite these challenges, the developments made in this thesis in membrane patterning prepare us well for further investigation into the geometry sensitivity of the *E. coli* MinDE system. First of all, the photolithography-patterned metal deposition technique

allowed us to define membrane patches that are diffusively uncoupled from one another. In this setup, lateral diffusion of molecules on the membrane is restricted within a pre-disposed boundary, whereas the molecules are free to diffuse in an unrestricted bulk volume. The boundary conditions imposed by this geometry, where the chromium barriers serve as diffusively reflective edges but only on the surface, enforces Min proteins to self-organise in waves that travel along the longest axis of the membrane. This was a demonstration of how geometry sensing is central to Min self-organisation, and we were able to use this property to facilitate the investigation behind the non-specific transport of membrane bound proteins by Min waves (associated publication P1).

The membrane morphology offered by these slides are also a good starting point to elucidate how self-organisation patterns on adjacent membrane patches are coupled by the diffusion through the bulk solution [46]. As the Min waves pass through, the wave maxima has a locally increased concentration of proteins on the membrane, and consequently, in the bulk just above this membrane before the proteins rapidly diffuse away. This concentrated "cloud" of proteins can couple through the volume onto the adjacent membrane patch, thus correlating the patterns. However, the bulk here is completely unconstrained, and a way to restrict diffusion in the bulk volume, much analogous to the defined membrane patches on the planar surface, is still desirable.

The compartmentalised, 2.5D structures developed in this thesis, made from negative molding in CYTOP, were built on previous attempts to fabricate such relevant geometries [96]. The cylindrical geometry, resembling those of *E. coli* themselves, presents membrane coverage around an encapsulated bulk volume, thus confining protein diffusion. Patterning membranes in this geometry lead to the recapitulation of pole-to-pole oscillations *in vitro*, which was a defining demonstration that engineering the surface:volume ratio give rise to qualitatively different pattern formation, which, in this case, closely resembled *in vivo* behaviours [96]. However, the limitations of using negative molding to fabricate microstructures, used in associated publication P2 as well as in previously developed systems [23, 96], is that the shapes are restricted to extrusions of 2D designs, since a template must be by pressed down into a mold and then peeled off to reveal embossed structures. This limits the complexity of geometries that can be fabricated by such methods, and is insufficient for a comprehensive exploration of how Min dynamics are dependent on 3D geometry.

The development of membrane-coated 3D structures in this thesis, based on 3D printing, is therefore a major methodological step towards addressing this question. With this additional degree of spatial freedom, we can engineer the surface to volume ratio so that diffusion in the bulk, as well as the surface, can be systematically regulated. With this tool at our disposal, we can now also tune the biochemistry to further explore pattern formation of the MinDE system.

Recent studies have shown that the attachment of the His-tag to MinE, which is necessary for protein purification, to the C-terminus confers ATPase-stimulating activity closer to the WT protein than the more conventionally used N-terminus attachment [95]. These constructs then displayed a variety of Turing-like, "stationary" patterns on quasi-infinite plane and bulk volume assays. This is suggestive of even richer and partly unexplored MinDE pattern formation on geometry engineered substrates. In fact, our preliminary results, together with Maria Reverte (Schwille lab), suggest that geometry can entrain pattern formation (Fig 9.1). When we printed

micropillars and varied their height, diameter and inter-pillar distance to vary the available surface to volume ratio, we found that the Min patterns that are normally "labyrinth" on planar surfaces conform into spots which regularly fill the spaces between the pillars. This calls for further experimental and theoretical investigation into how stationary patterns are affected by geometrical designs.

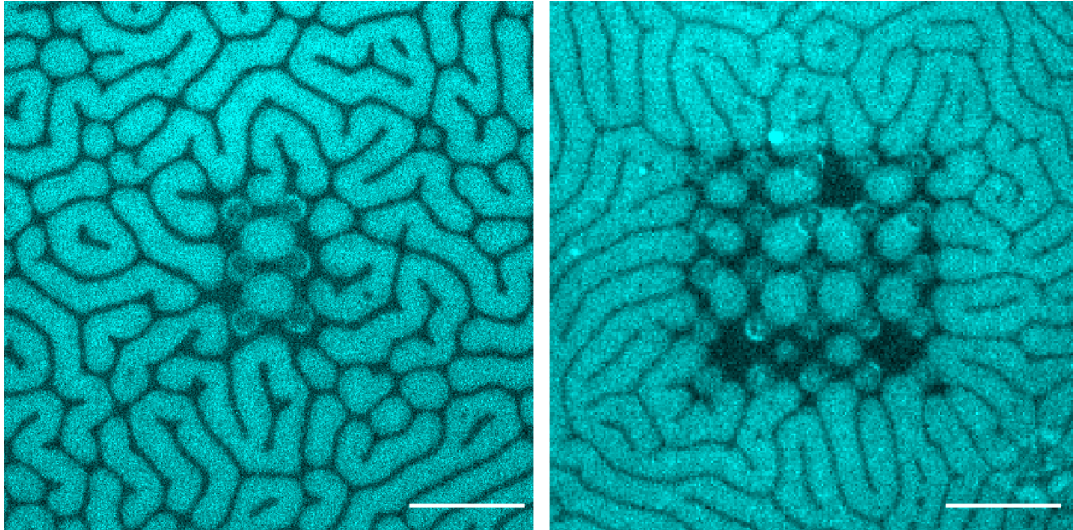


Figure 9.1. MinDE stationary patterns on geometry patterned substrates. Min patterns appear to conform in between micropillars, diameter 10 μm , height 50 μm , inter-pillar distance 10 μm . Scale bar 20 μm .sof

Additional biomolecular investigations include a closer attention on MinE proteins, which undergo conformational change from their latent to reactive state as they stimulate MinD's ATPase activity on the membrane [92]. As ATP is hydrolysed and Min proteins unbind from the membrane, MinE switches back into its latent state, and traverses the majority of the bulk in their unreactive conformation. An intriguing construct is the I24N mutant, which lacks this conformational switch. Macromolecular crowding can also be used in conjunction, which limit the diffusion of molecules in the bulk volume, and also affect the distribution of Min proteins through space by excluded volume effect [46, 89, 90]. Both these tools modulate how, and in what state, Min proteins travel through volume, thereby affecting pattern formation.

In a different application of this technology, we can think of the patterned surfaces on 2D, as well as on 3D rods as demonstrated in this thesis, as Min "waveguides". This then allows us to observe their interference, as waves that propagate along two distinct paths are eventually brought together at a junction. By adjusting the design of the structures, we can regulate path lengths, as well as using modules such as rods with concentric circles that appear to slow down the wave propagation in our preliminary data (Fig A.3). Studying interference of waves underlined by a reaction-diffusion mechanism draws fascinating comparisons to classical wave interference, and has only been studied in a number of cases where wave propagation can be well-controlled.

In addition to their role as the spatial indicators of the *E. coli* midcell, MinDE patterns position, transport and also sort biologically unrelated membrane-bound molecules by non-specific interactions (associated publication P1). The control that we have over the direction of the waves allows us to potentially guide arbitrary molecules

to a desired location in 3D space, offering an intriguing nanotechnological prospect. External cues, such as light-controlled switching of Min pattern formation [142], as well as specific recruitment of further biomolecules, e.g., by Deoxyribonucleic acid (DNA) origami, can then further enhance the applicability of such a novel, molecular-powered transport system.

DYNAMIC DEFORMATION OF MEMBRANE STRUCTURES

In this thesis, I also explored the possibility of using synthetic dendrimer molecules to form more stable vesicles, which would be better suited for membrane deformation studies. The chemical synthesis of amphiphilic molecules has yielded extremely stable bilayer membranes in the past, however, the functional analogy to the lipid bilayer, in terms of providing the right biological platform, required careful evaluation, and had so far been only partly demonstrated [143–145].

The recapitulation of Min protein patterns on these membranes can therefore be considered a major leap in how we can view the dendrimer membranes: as an appropriate model membrane system for *in vitro* reconstitution experiments. The formation of intricate reaction-diffusion patterns, which requires the combinatorial tuning of reaction kinetics of proteins diffusion rates between the membrane and the bulk volume, signified a remarkable level of biomimicry. Co-encapsulation of Min and FtsZ into dendrimersomes also demonstrated that key components of the cell division machinery can function similarly inside dendrimersomes, thereby advocating the use of these molecules for the construction of artificial cells in the future.

The question of whether these molecules can be used completely interchangeably with lipids, however, cannot yet be conclusively answered. A series of thorough investigations that examine protein-membrane interactions on a wide range of species is surely required. Min proteins, for example, only insert their amphiphilic membrane targeting sequences between the headgroups and the hydrophobic tails, and thus only loosely interacting with the top leaflet of the membrane. More complex transmembrane proteins, or protein complexes that require higher-level organisation within the membrane itself, would set interesting benchmarks for the suitability of dendrimer membranes for reconstitution experiments.

In this regard, dendrimersomes present a unique opportunity for synthetic biology - in particular for inducing cell division in artificial protocells. Vesicle division or deformation has already been demonstrated in a variety of ways, for example, through binding curvature-inducing species to the membrane [146], controlled phase separation of lipid species [147], or asymmetrical binding of proteins on the inner and outer leaflets of the bilayer [Litschel2019, 148]. The majority of these methods modulate the intrinsic curvature of the membrane, leading to a shift in the equilibrium membrane morphology, thus membrane deformation. In a recent study, dendrimersomes have also demonstrated spectacular shape transformations, stemming from the incorporation of photocleavable groups that spontaneously change the local membrane curvature [143]. If the positioning of such species could be regulated, for example, through non-specific transport by Min proteins [105], we have the possibility to induce shape transformation at a desired location, which is a fascinating prospect.

DYNAMIC ACTUATION OF PROTEIN-BASED HYDROGELS

In contrast to deforming vesicles by regulating the intrinsic curvature of membranes, the actuation of BSA-based hydrogels developed in this thesis provides an external cue to mechanically squeeze vesicles out of their spherical shape. The use of 3D printing enables the deformation of GUVs into shapes that are unachievable by previous microfabrication methods. For example, vesicle traps using soft lithography (and therefore, 2.5D structures) could squeeze vesicles horizontally but not vertically, resulting in a rather flat ellipsoid shape than the cylindrical shapes desired to mimic bacterial geometry [29]. The pH provides an easy, reversible cue to trigger actuation. Our work can therefore be considered as an effective demonstration of how shape-shifting, 3D printed materials can be applied to synthetic biology.

Using such triggers that cause drastic changes in biochemical conditions, however, often limit the range of applicable biochemical systems. The protein system encapsulated inside vesicles, in this case the Min system, was evidently unaffected by the pH change occurring outside. However, the addition of further biomolecular components becomes challenging, and any crosstalk occurring between the inside and outside of the vesicle must be carefully monitored. Any use of transmembrane proteins, for example, can therefore be immediately excluded. These changes are also global, and thus restrict the capacity for local and specific shape transformations that are required to build downstream complexity.

To address these issues, we embarked on creating a fully biomolecular system that relies on a contractile minimal actomyosin cortex to controllably deform these 3D printed microstructures (which is outlined in a submitted manuscript, not included in this thesis). By incorporating biotinylated BSA into the protein-based photoresin, we were able to specifically target the assembly of stabilised actin networks on 3D printed structures. Here, the actuation was triggered by activating myosin, and we were able to deform not only simple structures such as pillars or hinged V-units, but also complex structures such as a robotic arm and a hand that could make hand signals. We thereby recapitulated a cellular motor system with the capacity to integrate other biological or biomimetic modules [149, 150], such as molecular sensors, signaling factors, feedback regulators, as well as other protein motors. We therefore present a novel platform on which to develop future miniature soft robotics, and we can anticipate wider applications of these techniques in general, particularly to recapitulate shape transformations from bioengineered materials, which is one of the central goals of synthetic biology.

Part III
Appendix

Supplementary Information: A diffusiophoretic mechanism for ATP-driven transport without motor proteins

Beatrice Ramm, Andriy Goychuk, Alena Khmelinskaia, Philipp Blumhardt,
Hiromune Eto, Kristina A. Ganzinger, Erwin Frey and Petra Schwille

Author contributions:

B.R., A.G., E.F. and P.S. conceived the study. B.R. performed all experiments. H.E. and B.R. fabricated chromium-patterned slides. A.G. and E.F. designed the theoretical analysis. A.G. conducted the theoretical analysis. B.R., A.K. and P.B. designed experiments. A.K. designed DNA origami. A.K. and B.R. prepared origami. K.A.G. developed single-particle tracking code. B.R., A.G., P.B. and K.A.G. analysed data. B.R., A.G., E.F. and P.S. wrote the manuscript. All authors discussed and interpreted the results and revised the manuscript

published in

Nature Physics (2021)

Reprinted from [115] under the Creative Commons Attribution 4.0 International License
(see <https://creativecommons.org/licenses/by/4.0/>)

Supplementary information

A diffusiophoretic mechanism for ATP-driven transport without motor proteins

In the format provided by the authors and unedited

Supplementary Information

A diffusiophoretic mechanism for ATP-driven transport without motor proteins

Beatrice Ramm^{1,2,#}, Andriy Goychuk^{3,#}, Alena Khmelinskaia^{1,4}, Philipp Blumhardt¹, Hiromune Eto¹, Kristina A. Ganzinger⁵, Erwin Frey^{3,*} & Petra Schwille^{1,*}

¹Max Planck Institute of Biochemistry, Am Klopferspitz 18, 82152 Martinsried, Germany.

²Present affiliation: Department of Physics, Princeton University, 08544 Princeton, NJ, USA

³Arnold-Sommerfeld-Center for Theoretical Physics and Center for NanoScience, Ludwig-Maximilians-Universität München, D-80333 München, Germany

⁴Present affiliation: University of Washington, Institute for Protein Design, 98195 Seattle, WA, USA

⁵Living Matter Program, AMOLF, 1098 XG Amsterdam, The Netherlands

#These authors contributed equally: Beatrice Ramm and Andriy Goychuk

*Correspondence to: frey@lmu.de, schwille@biochem.mpg.de

Contents

Supplementary Theoretical Description.....	3
I. Chemical potential gradients induce flows, which couple by an out-of-equilibrium diffusiophoretic mechanism.....	3
1. Large particle density in MinD-rich regions and large mean particle density	3
2. Cargo density is limited by abundance of streptavidin and origami	4
3. Flory-Huggins theory of mixing: an equilibrium picture	7
4. Phenomenological coupling between diffusive fluxes: an out-of-equilibrium picture	15
5. Analytic solution and fitting of reduced model	18
6. Diffusion coefficient of cargo molecules	20
7. Determining the spatial distribution of multiple cargo species.....	22
II. Discussion of alternative thermodynamic transport mechanisms	23
1. Depletion attraction cannot explain cargo transport	23
2. Static volume exclusion cannot explain cargo transport	23
3. Flory-Huggins mixing in the limit of small densities	24
4. Significant impact of cargo on MinDE reaction kinetics is unlikely	27
III. Discussion of related non-equilibrium transport mechanisms	29
1. Illustrative derivation of the diffusiophoretic drift velocity in 3D solutions.....	29
2. Diffusiophoretic drift requires solute fluxes	34
3. Relation to our phenomenological approach to diffusiophoresis	36
Supplementary Figures.....	39
Supplementary Tables	44
Supplementary Methods.....	46
Supplementary Notes.....	48
Supplementary References	54

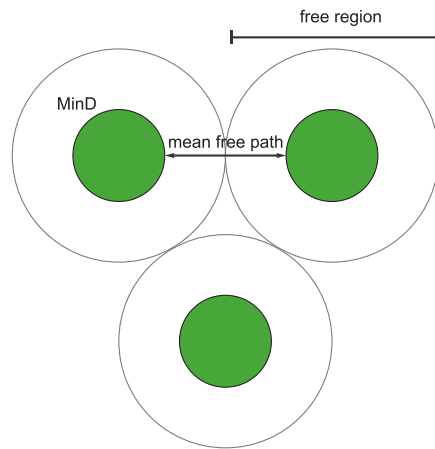
Supplementary Theoretical Description

I. Chemical potential gradients induce flows, which couple by an out-of-equilibrium diffusiophoretic mechanism

Elaborating the brief description in the main text, we here explain our theory in full detail. First, we estimate the abundance of membrane-bound molecules, which provides important information for the correct formulation of our theory (sections I.1 “Large particle density in MinD-rich regions and large mean particle density” and I.2 “Cargo density is limited by abundance of streptavidin and origami”). Then, to formulate a theoretical model, we treat the population of membrane-bound molecules as a lattice gas. Specifically, we use the Flory-Huggins theory of mixing to calculate the local chemical potential of each molecular species (section I.3 “Flory-Huggins theory of mixing: an equilibrium picture”). Finally, we consider chemical-potential-induced particle flows, and their coupling via an effective inter-particle friction (referred to as Maxwell-Stefan-like phenomenological approach, cf. section I.4 “Phenomenological coupling between diffusive fluxes: an out-of-equilibrium picture”). In section I.5 “Analytic solution and fitting of reduced model”, we then reduce our model to find an analytic solution and to fit it to our experimental data. Based on our fitting parameters, we predict the diffusion coefficient of cargo in the presence of MinD from its measured value in the dilute limit (section I.6 “Diffusion coefficient of cargo molecules”). Section I.7 “Determining the spatial distribution of multiple cargo species” then serves as a brief outline on how our theory can be extended by additional cargo species.

1. Large particle density in MinD-rich regions and large mean particle density

The MinD monomer density in the MinD maxima reaches a value of about $13\,200\ \mu\text{m}^{-2}$ ^{1,2}, which corresponds to a MinD dimer density of $6\,600\ \mu\text{m}^{-2}$. Since a single MinD dimer occupies approximately $25\ \text{nm}^2$ on the membrane, this gives an estimated maximal surface coverage of 16.5%. Assuming a circular packing of the free areas around different MinD dimers (cf. illustration “Estimation of the mean free path between MinD dimers”), the mean free path between two MinD dimers is then estimated to be 2.7 MinD dimer radii, which corresponds to $67\ \text{Å}$.



Estimation of the mean free path between MinD dimers. We represent MinD dimers (or streptavidin molecules) by disks with radii $R_p \approx 2.5$ nm, and assume that around these disks there are circular “free regions” with radii R_{free} which are devoid of other membrane-bound particles. These “free regions” can cover at most $\pi/(2\sqrt{3}) \sim 91\%$ of the membrane. This estimate yields an average mean free path between membrane-bound particles of 46 Å (67 Å for the average distance between MinD dimers in the MinD maxima). Treating the MinD dimers (or streptavidin molecules) as square plates of size 5×5 nm² instead of circular disks yields a very similar estimate for the average mean free path between membrane-bound particles of 51 Å (73 Å for the average distance between MinD dimers in the MinD maxima).

For an assumed sinusoidal MinD profile, we estimate that on average 8.25% of the membrane is covered by MinD^a. Furthermore, on average another 16.5% of the membrane is covered by streptavidin molecules, as measured by Fluorescence Correlation Spectroscopy-based image calibration². A single streptavidin molecule occupies 25 nm² on the membrane, like a MinD dimer. Thus, the mean free path between two arbitrary membrane-bound particles (MinD dimer or streptavidin) is 46 Å. To conclude, the above estimates show that the mean free path between any two membrane-bound particles is comparable to the particle size itself, which suggests that there are significant interactions between particles.

2. Cargo density is limited by abundance of streptavidin and origami

Each cargo molecule is a composite object consisting of a DNA origami scaffold and multiple streptavidin building blocks, which also serve as membrane tethers for the DNA origami

^a We base this estimate on the known value for the maximum MinD surface coverage and assume that the spatial distribution of MinD is a perfect sinusoidal curve. Computing the mean MinD coverage from the mean intensity can yield a slightly higher value of approximately 10% but does not significantly affect our results.

scaffolds (cf. Fig. 1a in the main text). A DNA origami scaffold can only bind to the membrane by binding to streptavidin molecules via their biotinylated oligonucleotide handles. The streptavidin molecules in turn are coupled to biotinylated lipids in the SLB. Hence, the total number of membrane-bound cargo (N_g) should be limited by the abundance of both the number of DNA origami (N_{o+}) in the assay and the available membrane-bound streptavidin (N_s). In the following, we will estimate how many DNA origami are bound to the membrane via streptavidin (i.e. the abundance of cargo) as well as the abundance of free streptavidin molecules (i.e. those that are not linked to DNA origami).

The amount of biotinylated lipids in the membrane determines the number of membrane-bound streptavidin. The tetrameric streptavidin binds two to three biotinylated lipids simultaneously and as the streptavidin-biotin interaction is very strong the streptavidin off-rate is negligible on the time-scales of our experiments³. Since we incubate the membrane with surplus streptavidin before we wash away any unbound streptavidin, we assume that all biotinylated lipids are bound to streptavidin. Hence, one can estimate the (average) streptavidin density from the molar fraction of biotinylated lipids (here 1%), their density and the streptavidin/biotinylated lipid binding valency (here 2.5)³ to be about $\bar{c}_s \approx 6.6 \times 10^3 \mu\text{m}^{-2}$. We previously also confirmed this density estimate using Fluorescence Correlation Spectroscopy-based image calibration². For a membrane of size A , this yields a total of $N_s = A \bar{c}_s$ streptavidin molecules that are bound to the membrane.

The number of membrane-bound streptavidin molecules (N_s) and the number of available DNA origami scaffolds (N_{o+}) are constant for all experiments. Each DNA origami scaffold has n biotinylated oligonucleotide handles that can attach to membrane-bound streptavidin. Because of the strong binding between biotin and streptavidin we expect that all biotin-streptavidin bonds are saturated (if there are sufficient DNA origami, each with n biotinylated oligonucleotide handles, in the system) and that a membrane-bound streptavidin only binds to one biotinylated oligonucleotide at a time^b. If all DNA origami were to bind to the membrane, then this would correspond to an average density of $\bar{c}_{o+} = N_{o+}/A$. This would

^b Under the conditions used in our experiments, each membrane-bound streptavidin has a residual biotin binding valency of 1.5³. This low residual valency, and also the spacing of individual biotinylated oligonucleotide handles, should prevent binding of multiple handles to one streptavidin. However, binding of multiple biotinylated oligonucleotide handles to one streptavidin cannot be entirely excluded for cargo with many handles and consequently smaller handle spacing, i.e. cargo-15, cargo-28 and cargo-42.

leave $N_s - n N_{o+}$ freely diffusing (i.e. not linked to DNA origami scaffolds) streptavidin molecules on the membrane. In contrast, for large numbers of biotinylated oligonucleotide handles per origami ($n > N_s/N_{o+}$), all streptavidin molecules would bind to DNA origami scaffolds. Then, the DNA origami scaffolds would compete for the available membrane-bound streptavidin molecules, due to volume exclusion effects between different DNA origami^c and a strong entropic penalty for binding DNA origami to the membrane. This competition would effectively result in only $N_g = N_s/n$ membrane-bound DNA origami (corresponding to an average membrane-bound cargo density of $\bar{c}_g = N_g/A$), while leaving $N_{o+} - N_g$ DNA origami scaffolds unbound. Thus, we expect that the number of biotinylated oligonucleotide handles on the DNA origami (n) determines the number (n) of cross-linked streptavidin building blocks per DNA origami (cf. Figs. 1d and 2a in the main text), as this corresponds to the minimal amount of membrane-bound DNA origami that at the same time maximizes the number of biotin-streptavidin bonds. To summarize, the abundance (average concentration) of membrane-bound cargo is given by $\bar{c}_g = \min(\bar{c}_{o+}, \bar{c}_s/n)$.

With the given amount of streptavidin on the membrane and origami in the assay (Supplementary Table 1), we expect that all streptavidin molecules are bound to the biotinylated oligonucleotide handles on the DNA origami scaffolds for a number of handles $n \geq \bar{c}_s/\bar{c}_{o+} \approx 21$. Consequently, for origami with a larger number of biotinylated oligonucleotide handles such as $n = 28$ or $n = 42$ in our experiments (which is equivalent to a larger number of cross-linked streptavidin molecules), not all origami can bind to membrane-bound streptavidin. Thus, we would expect a decrease of the surface density of DNA origami for $n > 21$, and that in this case there are no free streptavidin molecules left on the membrane. In good agreement with these arguments, the average fluorescence intensity of DNA origami scaffolds in our experiments indicates that the average density of membrane-bound streptavidin molecules is the limiting factor for the binding of DNA origami to the membrane for $n \geq 15$ (Extended Data Fig. 2c). Conversely, this means that for $n < 15$ the limiting factor for the binding of DNA origami to the membrane is the abundance of DNA origami themselves. Then, all of the available DNA origami will bind to the membrane via

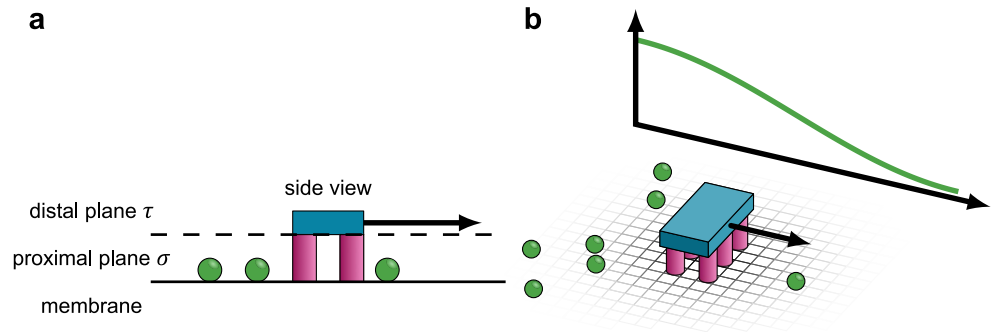
^c In our experiments, we observe that membrane-bound DNA origami scaffolds cover up to 55% of the membrane (based on the total amount of DNA origami scaffolds in the experimental assay).

streptavidin, resulting in an average coverage of 55%. As discussed above, at these densities one should expect significant volume exclusion effects.

3. Flory-Huggins theory of mixing: an equilibrium picture

In order to describe the thermodynamics of the free streptavidin molecules and the artificial cargo (i.e. streptavidin molecules that are crosslinked into an effective polymer) on the membrane, we formulated a Flory-Huggins theory⁴⁻⁶. To that end, we assumed that any (infinitesimally small) region on the membrane can (on the molecular scale) be described as a well-mixed lattice gas. On the mesoscopic scale, we then considered particle density gradients on the membrane surface. Then, we specifically asked: given a (externally imposed) heterogeneous distribution of active particles (i.e., we assume that there are stationary MinD protein density gradients on the membrane), what is the ensuing thermal equilibrium distribution of passive particles (cargo and free streptavidin molecules)? To answer this question, we determined the corresponding chemical potentials μ_i for each species as discussed next.

In order to formulate a theoretical model, it is instructive to consider the architecture of the cargo molecules used in the experiments (see illustration “[Conceptualized model geometry](#)”). Each cargo molecule is a composite object, which consists of a DNA origami scaffold and multiple streptavidin building blocks. The lower facet of the rod-shaped DNA origami is located between 5 and 11 nm above the membrane (see [Supplementary Note 1](#)). The streptavidin building blocks also serve as membrane tethers with a height of roughly 5 nm. Furthermore, MinD proteins bind to the membrane and form a monomolecular layer about 5 nm high⁷. These geometric properties of the system imply that cargo transport is dominated by interactions between MinD and streptavidin. As a consequence of the architecture of our cargo molecules, there are two distinct interaction layers (see illustration “[Conceptualized model geometry](#)”): (σ) the *proximal plane* refers to the thin layer near the membrane, which has a height of 11 nm, and (τ) the *distal plane* refers to the thin layer above the proximal plane, which has a height of 8 nm. In our theoretical analysis, we considered these two layers, the proximal plane and the distal plane, as two distinct lattice gases that are strictly coupled



Conceptualized model geometry (cf. Fig. 2a in the main text). **a**, Side view of the artificial cargo and MinD on the membrane. **b**, Isometric view of the artificial cargo and MinD on the membrane. Cargo molecules are composite objects which consist of a DNA origami scaffold (blue) and multiple streptavidin building blocks (magenta). The lower facet of the rod-shaped DNA origami is located between 5 and 11 nm above the membrane, from where the DNA origami body extends a further 8 nm (see Supplementary Note 1). The streptavidin building blocks also serve as membrane tethers. Furthermore, MinD proteins (green spheres) bind to the membrane in a monomolecular layer of about 5 nm height⁷. Therefore, we expect that cargo transport is dominated by interactions between MinD and streptavidin. This setup signifies two distinct interaction layers of the cargo with the proteins, which we indicate with the following labels: (σ) In the *proximal plane*, each DNA origami crosslinks multiple streptavidin blocks into a polymer-like object g , which intersperses with MinD proteins p , free streptavidin molecules s , and solvent. (τ) In the *distal plane*, we assume that only solvent surrounds the bulky DNA origami body o . We describe both interaction layers as lattice gases (indicated by the black grid), but with different lattice constants in the proximal and in the distal plane. MinDE protein density gradients introduce a bias to the diffusion of the cargo molecule (black arrow).

through the cargo molecules (which are present in *both* layers with a common local density c_g but distinct effective sizes a_g and a_o). Here and in the following, we use the term “size” to refer to the 2D projected area of the different particles on the membrane (i.e. membrane footprint). We choose the lattice constants of the proximal plane ($\ell_\sigma = 5$ nm, corresponds to the diameter of a typical MinD dimer or streptavidin molecule) and the distal plane ($\ell_\tau = 16$ nm, corresponds to the short side of the DNA origami) to match the typical length of the associated particles, respectively.

Directly above the membrane (*proximal plane* σ), each DNA origami scaffold crosslinks multiple streptavidin blocks into a polymer-like object g , which intersperses with MinD proteins^d p , free streptavidin molecules s , and solvent. Because streptavidin molecules and MinD dimers have a diameter of roughly 5 nm, we choose the lattice constant of the proximal

^d In the following, we neglect the distribution of MinE proteins. MinE proteins are recruited to the membrane by MinD proteins and therefore typically localize to the edge of MinD patterns. Therefore, we assume that MinD is a good proxy for the total distribution of MinDE proteins.

plane accordingly: $\ell_\sigma = 5$ nm. Then, each individual MinD dimer, free streptavidin molecule, and patch of solute occupies one lattice site of size (area) $a_\sigma = \ell_\sigma^2$. Cargo molecules with n streptavidin building blocks occupy n lattice sites and therefore have an effective size of $a_g = n a_\sigma$ on the membrane. We assume that these four species of molecules form a lattice gas with a free energy density f^σ , which is described by the Flory-Huggins theory of mixing⁴⁻⁶

$$\frac{f^\sigma}{k_B T} = \sum_i c_i \ln \theta_i + \sum_{i,j} c_i \theta_j \chi_{ij}. \quad (\text{S1})$$

Here, c_i and θ_i refer to the surface density and surface coverage of each species (cargo g , free streptavidin s , MinD proteins p and solvent q), respectively, while the Flory-Huggins parameters χ_{ij} are a measure for the interaction energy between different molecular species. At this point, we assume that there is no direct attraction or repulsion between the different species (e.g. due to electrostatic interactions); thus, all of the interaction parameters between the different species must vanish: $\chi_{ij} = 0$. On the membrane, each lattice site is either occupied by cargo g , free streptavidin s , MinD proteins p , or solvent q . Specifically, cargo molecules occupy a local surface fraction $\theta_g(\mathbf{x}) = n a_\sigma c_g(\mathbf{x})$ at a surface density of $c_g(\mathbf{x})$, free streptavidin molecules occupy a local surface fraction $\theta_s(\mathbf{x}) = a_\sigma c_s(\mathbf{x})$ at a surface density of $c_s(\mathbf{x})$, and MinD proteins occupy a local surface fraction $\theta_p(\mathbf{x}) = a_\sigma c_p(\mathbf{x})$ at a surface density of $c_p(\mathbf{x})$. Then, the solvent occupies the remainder of the surface at a local surface fraction $\theta_q(\mathbf{x}) = 1 - \theta_g(\mathbf{x}) - \theta_s(\mathbf{x}) - \theta_p(\mathbf{x})$, which corresponds to a local surface density of $c_q(\mathbf{x}) = \theta_q(\mathbf{x})/a_\sigma$. By taking the derivative of the free energy density, Eq. (S1), with respect to the surface density of cargo molecules, one obtains the contribution of the *proximal plane* σ (near the membrane) to the total chemical potential of a cargo molecule:

$$\frac{\mu_g^\sigma(\mathbf{x})}{k_B T} = \frac{\partial f^\sigma}{\partial c_g} \frac{1}{k_B T} = \ln[\theta_g(\mathbf{x})] - n \ln[1 - \theta_g(\mathbf{x}) - \theta_s(\mathbf{x}) - \theta_p(\mathbf{x})] + (1 - n). \quad (\text{S2a})$$

Here, $\theta_g(\mathbf{x}) = n a_\sigma c_g(\mathbf{x})$ indicates the local surface fraction occupied by cargo molecules, $\theta_s(\mathbf{x}) = a_\sigma c_s(\mathbf{x})$ indicates the local surface fraction occupied by free streptavidin molecules, and $\theta_p(\mathbf{x}) = a_\sigma c_p(\mathbf{x})$ indicates the local surface fraction occupied by MinD proteins. The second term of Eq. (S2a) corresponds to a *volume exclusion* effect, where a local increase of cargo density will lead to a local depletion of solvent. The size ratio between cargo and the solvent patches is given by $(n a_\sigma) / (a_\sigma)$, and contributes to this volume exclusion effect. The third term of Eq. (S2a) is a constant and thus drops out when one calculates the gradients of the chemical potential. Analogously, the chemical potential of a free streptavidin molecule is

given by

$$\frac{\mu_s^\sigma(\mathbf{x})}{k_B T} = \frac{\partial f^\sigma}{\partial c_s k_B T} = \ln[\theta_s(\mathbf{x})] - \ln[1 - \theta_g(\mathbf{x}) - \theta_s(\mathbf{x}) - \theta_p(\mathbf{x})]. \quad (\text{S2b})$$

The second term of Eq. (S2b) corresponds to a *volume exclusion* effect, where a local increase of streptavidin density will lead to a local depletion of solvent. The streptavidin molecules have the same size as the solute patches (a_σ), and thus there is no pre-factor before the volume exclusion term. Finally, the chemical potential of a membrane-bound MinD protein is given by

$$\frac{\mu_p^\sigma(\mathbf{x})}{k_B T} = \frac{\partial f^\sigma}{\partial c_p k_B T} = \ln[\theta_p(\mathbf{x})] - \ln[1 - \theta_g(\mathbf{x}) - \theta_s(\mathbf{x}) - \theta_p(\mathbf{x})]. \quad (\text{S2c})$$

The second term of Eq. (S2c) corresponds to a *volume exclusion* effect, where a local increase of MinD dimer density will lead to a local depletion of solvent. The MinD dimers have the same size as the solute patches (a_σ), and thus there is no pre-factor before the volume exclusion term.

At an altitude of 11 nm above the membrane, the *distal plane* τ contains only DNA origami scaffolds and solvent. Because each DNA origami scaffold is 16 nm wide and 110 nm long, we choose the lattice constant of the proximal plane accordingly: $\ell_\tau = 16$ nm. Then, each DNA origami scaffold occupies roughly seven lattice sites with a total size of $a_o = 7 a_\tau$ (yielding a width of 16 nm and a length of 112 nm), while each patch of solute has an effective size of $a_\tau = \ell_\tau^2$. Specifically, the DNA origami scaffolds occupy a local surface fraction $\theta_o(\mathbf{x}) = 7 a_\tau c_g(\mathbf{x})$, at a local surface density of $c_o(\mathbf{x}) = c_g(\mathbf{x})$. Then, the solvent occupies the remainder of the distal plane at a local surface fraction $\theta_\rho(\mathbf{x}) = 1 - \theta_o(\mathbf{x})$, which corresponds to a local surface density of $c_\rho(\mathbf{x}) = \theta_\rho(\mathbf{x})/a_\tau$. Analogously to Eq. (S1), we assume that these two species of molecules form a lattice gas with a free energy density f^τ , which is described by the Flory-Huggins theory of mixing⁴⁻⁶:

$$\frac{f^\tau}{k_B T} = \sum_i c_i \ln \theta_i + \sum_{i,j} c_i \theta_j \chi_{ij}. \quad (\text{S3})$$

Here, c_i and θ_i refer to the surface density and surface coverage of each species (DNA origami o and solvent ρ), respectively, while $\chi_{o\rho}$ is a measure for the interaction energy between the two species. As before, we assume that there is no direct interaction between the different species in the distal layer (e.g. due to electrostatic interactions); thus, the corresponding interaction parameter vanishes: $\chi_{o\rho} = 0$. Then, by taking the derivative of the free energy

10

density, Eq. (S3), with respect to the surface density of cargo molecules, we find the contribution of the *distal plane* τ (11 nm above the membrane) to the total chemical potential of a cargo molecule^e:

$$\frac{\mu_g^\tau(\mathbf{x})}{k_B T} = \frac{\partial f^\tau}{\partial c_g k_B T} = \ln[\theta_o(\mathbf{x})] - 7 \ln[1 - \theta_o(\mathbf{x})] - 6. \quad (\text{S4})$$

Here, $\theta_o(\mathbf{x}) = 7 a_\tau c_g(\mathbf{x})$ refers to the surface fraction occupied by the bulky DNA origami scaffolds.

The total chemical potential of a cargo molecule has a contribution from the proximal plane σ , Eq. (S2a), and a contribution from the distal plane τ , Eq. (S4). To find an expression for this chemical potential, we integrated out the two interaction layers near the membrane. Specifically, we again started from the Flory-Huggins theory of mixing⁴⁻⁶, but now expressed the free energy density *per volume* in terms of the surface particle densities (in comparison, Eqs. (S1) and (S3) describe the free energy density *per area*). The proximal interaction layer has a thickness of $d^\sigma = 11$ nm and the distal layer has a thickness of $d^\tau = 8$ nm. We neglected variations in the cross-sectional area of the different molecular species within the proximal and distal layers, respectively. We assumed that the local volumetric density of cargo is given by $c_g/(d^\sigma + d^\tau)$ in both layers, while the volume fraction that is locally occupied by cargo is given by the surface coverage in the corresponding interaction layer (θ_g in the proximal layer, θ_o in the distal layer). We also applied these arguments for the MinD proteins (only present in the proximal layer at a volumetric density c_p/d^σ and volume fraction θ_p), free streptavidin molecules (only present in the proximal layer at a volumetric density c_s/d^σ and volume fraction θ_s) and the solvent patches in both interaction layers. Then, we integrated the free energy density per volume across both interaction layers to arrive at the free energy density per area. By taking the derivative of the resulting free energy density per area with respect to the surface density of cargo molecules, we found the following expression for the total chemical potential of a cargo molecule:

^e Here, we have approximated the DNA origami as a polymer with 7 segments. Alternatively, one could also treat the distal layer as an ideal solution (i.e. set the “polymer factor” to 1). This alternative choice does not affect our general results which will be discussed in more detail at the end of this section. Specifically, due to the resulting entropic repulsion between different DNA origami, entropic volume exclusion effects are not sufficient to explain the strong cargo gradients that we observed in our experiments (reaching near-saturation values in DNA origami coverage $\theta_o \rightarrow 1$ where the second term in Eq. (S4) and the equivalent third term in Eq. (S5) diverge logarithmically).

$$\frac{\mu_g(\mathbf{x})}{k_B T} = \ln[\theta_g(\mathbf{x})] - n \ln[1 - \theta_g(\mathbf{x}) - \theta_s(\mathbf{x}) - \theta_p(\mathbf{x})] - 7 \ln[1 - \theta_o(\mathbf{x})], \quad (\text{S5})$$

where we have used $d^\sigma / (d^\sigma + d^\tau) \ln[\theta_g(\mathbf{x})] + d^\tau / (d^\sigma + d^\tau) \ln[\theta_o(\mathbf{x})] = \ln[\theta_g(\mathbf{x})] + cst$, and omitted all constant terms. Note that Eq. (S5) contains *both* a saturation term in the proximal layer (second term) as well as in the distal layer (third term). The chemical potentials of the streptavidin molecules, Eq. (S2b), and of the MinD proteins, Eq. (S2c), remain the same as calculated earlier, i.e. $\mu_s(\mathbf{x}) \equiv \mu_s^\sigma(\mathbf{x})$ and $\mu_p(\mathbf{x}) \equiv \mu_p^\sigma(\mathbf{x})$.

In our experimental assay, ATP-consuming reactions continuously drive the MinDE protein distribution out of equilibrium and maintain a non-equilibrium, spatially non-uniform steady state that exhibits protein gradients (and fluxes)^{8–11}. In stark contrast to the Min proteins, the cargo molecules and the free streptavidin molecules show only thermal Brownian diffusion while being bound to the membrane; they can be considered permanently bound to the membrane as they have a negligible detachment rate due to their strong membrane anchoring³. As a consequence, both the cargo molecules and free streptavidin molecules adopt a thermal equilibrium state, which is lacking any gradients in the chemical potentials ($\nabla\mu_g = \nabla\mu_s = 0$). In other words, the (passive) Brownian particles in different regions of the membrane have identical chemical potentials in an adiabatic response to the externally imposed distribution of active particles, the MinD proteins: $\nabla\mu_p \equiv \nabla\mu_p^\sigma \neq 0$. Given these constraints regarding the spatial profile of the chemical potential, we then determined the distribution of all passive particles as follows.

The constraint that the cargo molecules are in local thermal equilibrium, $\nabla\mu_g = 0$, yields the following partial differential equation by taking the gradient of Eq. (S5) and using the chain rule for multivariable functions,

$$\left[\frac{\partial\mu_g}{\partial\theta_g} \frac{\partial\theta_g}{\partial\theta_o} + \frac{\partial\mu_g}{\partial\theta_o} \right] \nabla\theta_o + \frac{\partial\mu_g}{\partial\theta_s} \nabla\theta_s + \frac{\partial\mu_g}{\partial\theta_p} \nabla\theta_p = 0, \quad (\text{S6a})$$

while the constraint $\nabla\mu_s \equiv \nabla\mu_s^\sigma = 0$ directly implies, by using the chain rule for multivariable functions,

$$\frac{\partial\mu_s^\sigma}{\partial\theta_g} \frac{\partial\theta_g}{\partial\theta_o} \nabla\theta_o + \frac{\partial\mu_s^\sigma}{\partial\theta_s} \nabla\theta_s + \frac{\partial\mu_s^\sigma}{\partial\theta_p} \nabla\theta_p = 0. \quad (\text{S6b})$$

The ratio $\partial\theta_g/\partial\theta_o = a_g/a_o = (n a_\sigma)/(7 a_\tau) \approx n/70$ is fully determined by the number n of streptavidin blocks per cargo. Since a heterogeneous spatial distribution of proteins (Min pattern), i.e. $\nabla\theta_p$, is externally maintained, Eqs. (S6a) and (S6b) form a closed set of partial

differential equations^f in the variables θ_o and θ_s (together with the additional constraint that the average density of the different molecular species is conserved).

Finally, we will now impose a (externally maintained) spatial distribution of MinDE proteins and solve Eqs. (S6a) and (S6b) with the constraint that the average density of the different molecular species is conserved (mass conservation). Note that neither the precise functional form of the MinDE protein coverage distribution θ_p nor the dimension of the geometry are important: In general, the equilibrium distribution of the cargo coverage will be determined by the distribution of MinD proteins and the abundance of all molecules in the assay, and therefore have the form $\theta_o(\theta_p, \bar{\theta}_p, \bar{\theta}_o, \bar{\theta}_s, n)$. Similarly, the equilibrium distribution of the streptavidin coverage has the form $\theta_s(\theta_p, \bar{\theta}_p, \bar{\theta}_o, \bar{\theta}_s, n)$. Thus, by using the (multivariable) chain rule of differentiation, one could fully eliminate all gradients from Eqs. (S6a) and (S6b):

$$\left[\frac{n a_\sigma}{7 a_\tau} \frac{\partial \mu_g}{\partial \theta_g} + \frac{\partial \mu_g}{\partial \theta_o} \right] \frac{\partial \theta_o}{\partial \theta_p} + \frac{\partial \mu_g}{\partial \theta_s} \frac{\partial \theta_s}{\partial \theta_p} + \frac{\partial \mu_g}{\partial \theta_p} = 0, \quad (\text{S6a}^*)$$

$$\frac{n a_\sigma}{7 a_\tau} \frac{\partial \mu_s^\sigma}{\partial \theta_g} \frac{\partial \theta_o}{\partial \theta_p} + \frac{\partial \mu_s^\sigma}{\partial \theta_s} \frac{\partial \theta_s}{\partial \theta_p} + \frac{\partial \mu_s^\sigma}{\partial \theta_p} = 0, \quad (\text{S6b}^*)$$

and directly solve for the coverage of passive particles as a function of the protein coverage. Note that Eqs. (S6a^{*}) and (S6b^{*}) can also be obtained by directly setting $\mu_g = cst$ and $\mu_s = cst$, and expanding the resulting equations to first order in the protein coverage θ_p . Alternatively, one can also obtain Eqs. (S6a^{*}) and (S6b^{*}) by integrating Eqs. (S6a) and (S6b) over an arbitrary infinitesimal line segment ds , and perform a change of variables $ds \cdot \nabla \theta = d\theta$. Since we were also interested in the spatial distribution of passive molecules, however, we translated Eqs. (S6a) and (S6b) into a boundary value problem, in a 1D geometry of length $L \equiv 1$. Specifically, this boundary value problem enforces the constraint that the average density of the different molecular species is conserved. We introduced two fields for the *cumulative coverage* (this corresponds to the *cumulative mass* for density fields) of DNA origami $\Theta_o = \frac{1}{L} \int_0^x dy \theta_o(y)$ and streptavidin molecules $\Theta_s = \frac{1}{L} \int_0^x dy \theta_s(y)$, resulting in the additional two differential equations

$$\theta_o = L \nabla \Theta_o, \quad (\text{S6c})$$

$$\theta_s = L \nabla \Theta_s. \quad (\text{S6d})$$

^f To keep the equations concise, we have chosen not to insert the partial derivatives of the chemical potentials with respect to particle coverage, $\partial \mu_i / \partial \theta_j$. These partial derivatives are easily obtained from Eqs. (S2b) and (S5).

Thus, in summary, we have four partial differential equations (S6a), (S6b), (S6c) and (S6d) with the four boundary conditions $\Theta_s(0) = 0$, $\Theta_s(L) = \bar{\theta}_s(n)$, $\Theta_o(0) = 0$, and $\Theta_o(L) = \bar{\theta}_o(n)$. As we have discussed in section 1.2 “Cargo density is limited by abundance of streptavidin and origami”, the average coverage of free streptavidin molecules and cargo (equivalent to their density or abundance) depend on the number of streptavidin blocks per cargo molecule. Then, we imposed the following coverage distribution of proteins⁸:

$$\theta_p = \bar{\theta}_p 2 \cos\left(\frac{\pi x}{2L}\right)^2, \quad (\text{S7})$$

and numerically solved the closed set of partial differential equations (S6a), (S6b), (S6c) and (S6d), as shown in Fig. 2b,c in the main text and Extended Data Fig. 3a. These results show that entropic mixing effects can in principle lead to transport of passive particles in a gradient of active particles (Fig. 2b,c in the main text and Extended Data Fig. 3a). However, this disagrees with our experiments where we observed a far stronger redistribution of the passive cargo molecules than entropic mixing would predict (Fig. 2b in the main text and Extended Data Fig. 3a). This observation can be explained as follows. The weak entropic sorting of the cargo’s small streptavidin blocks in a fixed gradient of MinD proteins originates from the second term in the proximal chemical potential of cargo, Eq. (S2a), and the equivalent second term in the total chemical potential of cargo, Eq. (S5), which corresponds to a volume exclusion term (free streptavidin molecules experience analogous entropic sorting according to Eq. (S2b)). Specifically, the fixed distribution of active MinD proteins constrains the local mixture of cargo, streptavidin molecules and MinD proteins. In response, the passive cargo and streptavidin molecules will distribute in such a way that maximizes the local area fraction that is occupied by solvent (mixing). However, just as there is volume exclusion between particles in the proximal layer σ , there is also volume exclusion between particles in the distal layer τ which accommodates the DNA origami scaffolds (cf. illustration “Conceptualized model geometry”). Furthermore, the particles in the distal layer are much larger than the particles in the proximal layer. Thus, agglomeration of cargo is prevented by the second term in the distal chemical potential of cargo, Eq. (S4), and the equivalent third term in the total chemical

⁸ This specific choice serves to (roughly) approximate the spatial profile of MinD in the assay that contains cargo-15, cargo-28 or cargo-42 (cf. Fig. 1d in the main text). There, roughly 30-50% of the raw image pixels can be classified as MinD-minima (Fig. 1g in the main text), which suggests an almost symmetric MinD profile. The spatial profile of MinD becomes increasingly asymmetric for cargo with decreasing number of streptavidin n . However, the precise form of the MinD profile should not be relevant, as the spatial dimension x can be fully eliminated from Eqs. (S6a) and (S6b), cf. resulting Eqs. (S6a*) and (S6b*).

potential of cargo, Eq. (S5), which diverges logarithmically as the area fraction θ_o that is covered by DNA origami scaffolds approaches saturation, $\theta_o \rightarrow 1$. As the volume exclusion term in the distal chemical potential of cargo, Eq. (S4), that prevents cargo agglomeration (cf. the equivalent third term in the total chemical potential of cargo, Eq. (S5)) has a greater weight than the volume exclusion term in the proximal chemical potential of cargo, Eq. (S2a), which creates cargo gradients in response to the imposed distribution of MinD proteins (cf. the equivalent second term in the total chemical potential of cargo, Eq. (S5)), we conclude that mixing effects alone may *never* be sufficient to reach near-saturation densities (cf. section I.2 “Cargo density is limited by abundance of streptavidin and origami”) like in our experiments.

4. Phenomenological coupling between diffusive fluxes: an out-of-equilibrium picture

As described in the main text, we next relaxed our previous assumption of fixed external chemical potential gradients and considered their dynamics. According to Onsager’s theory of nonequilibrium thermodynamics¹², gradients in a chemical potential $\nabla\mu_i$ imply particle fluxes \mathbf{j}_i . In the present context, a possible candidate for a non-equilibrium process in a crowded environment is the coupling of particle fluxes through (mesoscopic) friction caused by non-specific interactions between proteins and cargo molecules on the membrane. This phenomenological friction may originate from hydrodynamic interactions, or also from collisions given that the mean free path between membrane-bound particles is only about 50 Å (see section I.1 “Large particle density in MinD-rich regions and large mean particle density”). In fluids, a frictional coupling between the diffusive fluxes of dilute solutes is mediated by hydrodynamic interactions (and a two-particle interaction potential) and has been predicted by Derjaguin¹³ (cf. section “Discussion of related non-equilibrium transport mechanisms”). In gases, a phenomenologically similar (but mechanistically distinct) coupling between diffusive fluxes originates from a direct momentum transfer due to binary collisions and has been predicted by the Maxwell-Stefan theory of diffusion^{14,15}, as well as experimentally observed for three-component gas mixtures^{16,17}. Since there are different microscopic mechanisms that can lead to a coupling between diffusive fluxes, we formulated a phenomenological theory where each species on the membrane obeys a Maxwell-Stefan-

like effective force-balance equation^{14,15,h,i}:

$$\nabla\mu_i + \xi_i \frac{\mathbf{j}_i}{c_i} + \sum_k c_k \zeta_{ik} \left(\frac{\mathbf{j}_i}{c_i} - \frac{\mathbf{j}_k}{c_k} \right) = 0. \quad \left(\begin{array}{c} \text{S8,} \\ \text{1 in main text} \end{array} \right)$$

Here, the index $i \in \{p, g, s\}$ refers to MinD proteins, cargo molecules with bound streptavidin, and free streptavidin molecules, respectively. Conceptually, the thermodynamic driving forces, caused by chemical potential gradients, are balanced by friction forces between the different macromolecules and lipid molecules (with friction coefficients ξ_i) as well as among the different macromolecules themselves (with coupling constants ζ_{ik}). Note that, according to Onsager's reciprocal relations¹², the matrix of coupling constants must be symmetric: $\zeta_{ik} = \zeta_{ki}$. Then, by summing the effective force balance equations for each particle species weighted with the respective particle concentration, one can verify that all friction forces due to particle-particle interactions cancel out. The underlying physical reason for these cancellations is the conservation law for the global momentum (i.e. global force balance). The last term in Eq. (S8) corresponds to a momentum transfer between any two particle species. On average, these momentum transfers must cancel out to satisfy momentum conservation. The second term in Eq. (S8) dissipates momentum into the membrane, and the first term in Eq. (S8) is a potential force which in our case originates from the free energy of mixing^j.

Since our experiments showed a nonequilibrium steady state, $\partial_t c_i = 0$, we continued to analyse the steady state of the model. While cargo and streptavidin molecules exhibit Brownian motion and relax to a thermal equilibrium state with vanishing fluxes $\mathbf{j}_g = \mathbf{j}_s = 0$, the MinD protein patterns are kept in a non-equilibrium steady state maintained by off-equilibrium chemical reactions (ATPase activity). Because the fluxes of passive cargo and streptavidin molecules vanish, there is no need to consider a coupling ζ_{sg} between them. Furthermore, Eq. (S8) shows that the self-coupling coefficients ζ_{ii} are irrelevant for the mean field dynamics. For single molecules, however, such a self-coupling should lead to a density-dependent self-diffusion coefficient, as has been observed for MinD by Loose et al.¹ using

^h The last term in Eq. (S8) corresponds to an effective friction (i.e. momentum transfer) that is proportional to the velocity difference between the fluxes of different particle species. Note that one would use analogous terms to couple different fluids in dense multi-component liquids.

ⁱ The validity of the phenomenological theory that is presented here is independent of the detailed microscopic mechanism, because it relies on very general Onsager-like arguments. Calculating the coupling coefficients from a microscopic picture is an interesting problem on its own, which is hinted at in section III.1 "Illustrative derivation of the diffusiophoretic drift velocity in 3D solutions".

^j In general, the potential force can also contain contributions from electrostatic or other interactions between particles.

single-particle tracking and for membrane-bound DNA origami using Fluorescence Correlation Spectroscopy¹⁸.

Since the fluxes of the passive particles, cargo and streptavidin molecules, vanish ($\mathbf{j}_g = \mathbf{j}_s = 0$), the fluxes of the MinD proteins are given by

$$\mathbf{j}_p = -\frac{c_p \nabla \mu_p}{\xi_p + c_g \zeta_{pg} + c_s \zeta_{ps}}, \quad (\text{S9})$$

where the chemical potential gradient of the MinD proteins is given by Eq. (S2c). After inserting Eq. (S9) back into the force balance equation, Eq. (S8), one obtains the following relations between the externally maintained chemical potential gradients of the active particles (MinD proteins) and the induced chemical potential gradients of the passive particles (streptavidin and cargo molecules), respectively:

$$\nabla \mu_g = \zeta_{pg} \mathbf{j}_p = -\frac{c_p \zeta_{pg}}{\xi_p + c_g \zeta_{pg} + c_s \zeta_{ps}} \nabla \mu_p, \quad (\text{S10a})$$

$$\nabla \mu_s = \zeta_{ps} \mathbf{j}_p = -\frac{c_p \zeta_{ps}}{\xi_p + c_g \zeta_{pg} + c_s \zeta_{ps}} \nabla \mu_p. \quad (\text{S10b})$$

Here, the chemical potential gradient of the cargo molecules is given by Eq. (S5), the chemical potential gradient of streptavidin molecules is given by Eq. (S2b), and the chemical potential gradient of the MinD proteins is given by Eq. (S2c). Analogous to our numerical solution of the Flory-Huggins model (see section 1.3 “[Flory-Huggins theory of mixing: an equilibrium picture](#)”), we formulated Eqs. (S10a) and (S10b) as a 1D boundary-value problem in a domain of size $L \equiv 1$, by introducing the two additional fields $\Theta_o = \frac{1}{L} \int_0^x dy \theta_o(y)$ and $\Theta_s = \frac{1}{L} \int_0^x dy \theta_s(y)$ and their respective boundary conditions $\Theta_s(0) = 0$, $\Theta_s(L) = \bar{\theta}_s(n)$, $\Theta_o(0) = 0$, and $\Theta_o(L) = \bar{\theta}_o(n)$. As before, we imposed the distribution of MinD proteins (externally maintained by a reaction-diffusion system) as given by Eq. (S7).

In the absence of mutual friction between the macromolecules ($\zeta_{ik} = 0$), Eq. (S8) reduces to the Flory-Huggins model ($\nabla \mu_g = \nabla \mu_s = 0$) which implies weak cargo redistribution in a stationary gradient of active proteins. In contrast, in the presence of (frictional) coupling ($\zeta_{ik} \neq 0$) between cargo molecules and MinD protein fluxes ($\mathbf{j}_p \neq 0$), the cargo molecules are not only redistributed due to entropic demixing effects, but in addition they are transported along protein gradients by these nonequilibrium protein fluxes. As consequence of this additional bias, cargo redistribution is significantly stronger than by equilibrium thermodynamic forces alone, which quantitatively explains our experimental data (Fig. 2b,c in

the main text and Extended Data Fig. 3a). We expect that individual streptavidin molecules experience a coupling ζ_{ps} to MinD fluxes, which arises from a mesoscopic friction. Consequently, we also expect that the coupling constant ζ_{pg} between MinD and a specific cargo has a contribution from the origami scaffold as well as from each of its n streptavidin molecules:

$$\zeta_{pg} = \zeta_{po} + n \zeta_{ps}. \quad (\text{S11})$$

This implies that the extent of cargo redistribution should increase with the number of streptavidin integrated into the cargo, as indeed observed in our experiments (Fig. 1e in the main text). This suggests that diffusiophoresis is not limited to the transport of large cargo, but can also explain the transport of small molecules (with similar size as MinD proteins), such as individual membrane-bound streptavidin molecules as reported in this study (Fig. 1d in the main text) and previous ones^{2,19}.

5. Analytic solution and fitting of reduced model

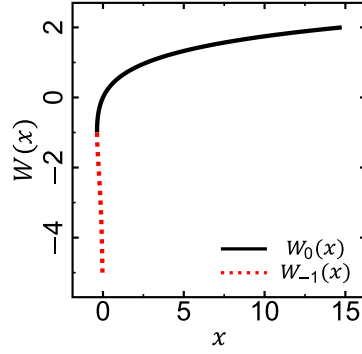
To further elucidate the mechanism underlying MinDE-induced transport, we simplified our theoretical model. Specifically, we neglected membrane saturation effects (i.e. the second terms in Eqs. (S2a), (S2b), (S2c), (S4) and thus both the second and third terms in Eq. (S5)), so that the chemical potential of a particle with size a_i reduces to $\mu_i \approx k_B T \ln(a_i c_i)$. Then, the effective force-balance equation, Eq. (S8), takes the form of a generalized Fick's law for the MinD protein fluxes in the non-equilibrium steady state with a density-dependent diffusion coefficient $D_p(c_g, c_s)$:

$$\mathbf{j}_p \approx -\frac{k_B T}{\xi_p + c_g \zeta_{pg} + c_s \zeta_{ps}} \nabla c_p \equiv -D_p(c_g, c_s) \nabla c_p. \quad \left(\begin{array}{l} \text{S12,} \\ \text{2 in main text} \end{array} \right)$$

Because the number of free streptavidin is typically small (see section 1.2 “Cargo density is limited by abundance of streptavidin and origami”), we assumed that free streptavidin molecules do not significantly contribute to the dynamics, $c_s \zeta_{ps} \ll c_g \zeta_{pg}$. After inserting Eq. (S12) back into the force balance equation, Eq. (S8), one obtains the following relation between cargo molecule and MinD protein gradients:

$$\nabla c_g = -\frac{c_g}{c_x + c_g} \nabla c_p, \quad (\text{S13})$$

with typical *interaction density* $c_x = \xi_p / \zeta_{pg}$. In the equilibrium state, where the fluxes of cargo molecules vanish $\mathbf{j}_g = 0$, the distribution of the cargo molecules will be determined by the distribution of MinD proteins, the abundance of molecules in the assay, and the



Lambert W-function. The Lambert W-function is defined as the inverse function of $f(x) = x e^x$ and has two real branches, W_0 and W_{-1} .

interaction density c_x . Therefore, the local cargo density will have the form $c_g(c_p, c_x, \bar{c}_g, \bar{c}_p)$. Thus, by using the chain rule of differentiation, one can fully eliminate all gradients from Eq. (S13) to obtain the following ordinary differential equation:

$$\frac{\partial c_g}{\partial c_p} = -\frac{c_g}{c_x + c_g}. \quad (\text{S14})$$

Alternatively, one can also obtain the ordinary differential equation (S14) by integrating Eq. (S13) over an arbitrary infinitesimal line segment ds , and performing a change of variables $ds \cdot \nabla c = dc$. Eq. (S14) can be solved by integration, and yields the following relationship between the cargo molecule density and the MinD protein density:

$$c_g(c_p) = c_x W_0 \left[\frac{c_g(0)}{c_x} \exp \left(\frac{c_g(0) - c_p}{c_x} \right) \right]. \quad \left(\begin{array}{l} \text{S15,} \\ \text{3 in main text} \end{array} \right)$$

Here, W_0 refers to the principal branch of the Lambert W-function, which is defined as the inverse function of $f(x) = x e^x$ (cf. illustration “Lambert W-function”). In terms of fluorescence intensities, $I_g = \alpha_g c_g$ and $I_p = \alpha_p c_p$, Eq. (S15) can be rewritten as

$$I_g(I_p) = r I_x W_0 \left[\frac{I_g(0)}{r I_x} \exp \left(\frac{I_g(0)}{r I_x} - \frac{I_p}{I_x} \right) \right], \quad (\text{S16})$$

where we have defined the fluorescence ratio $r = \alpha_g/\alpha_p$ and the typical MinD intensity corresponding to the interaction density $I_x = \alpha_p c_x$. In our experiments, we controlled the abundance of all fluorescent molecules.

Our experimental data were collected over a set of experiments performed on different days. Each set of samples (that were measured on a particular day) contains at least one

measurement that was performed with cargo-1. Thus, as reference values for each day, we used the mean fluorescence intensities of the different channels in the cargo-1 samples. Then, we normalised all fluorescence channels to their respective reference values. Since the normalised average fluorescence intensity of the DNA origami is 1.0 for the cargo-1 samples and their average density is $313 \mu\text{m}^{-2}$ (assuming that all DNA origami bind to the membrane), we estimated the (normalised) fluorescence yield of a DNA origami/cargo molecule as $\alpha_g \approx 3.2 \times 10^{-3} \mu\text{m}^2$. The MinD monomer density in the MinD maxima reaches a value of about $13\,200 \mu\text{m}^{-2}$ ^{1,2}. Thus, by measuring the normalised fluorescence intensity in the MinD maxima (1.47, normalised to the average MinD fluorescence), we estimated the fluorescence yield of a MinD dimer as $\alpha_p \approx 2.2 \times 10^{-4} \mu\text{m}^2$. This results in the following fluorescence ratio: $r \approx 14.5$. Having estimated the fluorescence ratio r from our experiments, we then fitted Eq. (S16) to the experimental data, with I_x as fit parameter (Fig. 3a in the main text and Extended Data Fig. 3b). Then, we determined the interaction parameter, $\theta_x^{-1} = (a_p c_x)^{-1} = I_x^{-1} (\alpha_p / a_p) \propto \zeta_{pg}$; here, α_p refers to the MinD fluorescence yield and a_p refers to the size of a MinD dimer. Our fitting procedure confirmed our initial expectation $\zeta_{pg} = \zeta_{po} + n \zeta_{ps}$, as can be seen from Fig. 3b in the main text and Extended Data Fig. 5h^k.

6. Diffusion coefficient of cargo molecules

Our theory suggests that increasing the surface density of membrane-bound molecules (MinD, streptavidin, or cargo) will also increase the friction that each molecule experiences; specifically, Eq. (S8) states that each molecule not only transfers momentum to the membrane, but also to surrounding molecules. Thus, we expect that the diffusion coefficient of all molecules depends on the local density of membrane-bound molecules, as we have demonstrated with Eq. (S12) for the expected diffusion coefficient of MinD. To further validate our model, we determined the (mesoscopic) diffusion coefficient of the cargo molecules from our theory, and then compared these predictions with experimental data on the (microscopic) diffusion coefficient of cargo molecules that we obtained from single particle tracking.

^k The absolute value of the fitted interaction parameter is smaller than the value that we have estimated for our full model (cf. Supplementary Table 1), because we have neglected saturation effects in deriving our fit curve, Eq. (S16). As discussed in section I.5 “Flory-Huggins theory of mixing: an equilibrium picture”, saturation effects strongly counteract the buildup of cargo gradients and thus require a stronger coupling parameter ζ_{pg} to generate significant cargo gradients.

To obtain theoretical predictions, we neglected membrane saturation effects analogously to section I.5 “Analytic solution and fitting of reduced model”, so that the chemical potential of a particle with size a_i reduces to $\mu_i \approx k_B T \ln(a_i c_i)$. Furthermore, because the number of free streptavidin molecules is typically small (see section I.2 “Cargo density is limited by abundance of streptavidin and origami”¹), we neglected the density of free streptavidin molecules ($c_s \approx 0$). Then, the effective force-balance equation, Eq. (S8), takes the form of a generalized Fick’s law for the cargo fluxes, where gradients in the cargo molecule density (∇c_g) relax with a density-dependent diffusion coefficient $D_g(c_p)$:

$$\mathbf{j}_g \approx -\frac{k_B T}{\xi_g + c_p \zeta_{pg}} \nabla c_g \equiv -D_g(c_p) \nabla c_g. \quad (\text{S17})$$

By substituting the typical interaction density $c_x = \xi_p / \zeta_{pg}$, the diffusion coefficient of cargo molecules in the dilute limit $D_g^0 = k_B T / \xi_g$, and the diffusion coefficient of MinD proteins in the dilute limit $D_p^0 = k_B T / \xi_p$, one obtains:

$$D_g(c_p) \approx \frac{D_g^0}{1 + (D_g^0 / D_p^0)(c_p / c_x)}. \quad (\text{S18})$$

We measured the diffusion coefficient of cargo-2 and of cargo-42, D_g^0 , in the dilute limit (Fig. 3c in the main text). The diffusion coefficient of membrane-bound MinD proteins in the dilute limit was assumed to be $D_p^0 \approx 0.425 \mu\text{m}^2\text{s}^{-1}$, based on single particle tracking data from Loose et al¹. Using these data and the interaction parameters that we obtained by fitting the reduced model, Eq. (S16), to the experimental data (cf. Fig. 3a in the main text and Extended Data Fig. 3b for examples of the fits as well as Fig. 3b in the main text and Extended Data Fig. 5h for the fitted interaction parameters), we then predicted how the diffusion coefficient of a cargo molecule should change in the presence of MinD, in reference to its diffusion coefficient in the dilute limit. Comparing our prediction of the diffusion coefficient with experimental measurements, we found good agreement (Fig. 3c in the main text and Extended Data Fig. 5a). Specifically, we also found that cargo with more streptavidin blocks is affected *less* by the

¹ The assumptions made in section I.2 “Cargo density is limited by abundance of streptavidin and origami” should remain valid for the single particle tracking experiments even though the overall densities are about 100 times lower, as the ratio between membrane-bound streptavidin (biotinylated lipids) and DNA origami is kept similar: We use 100 times less biotinylated lipids (0.01%) and 100-1000 times less DNA origami than in the other experiments.

presence of MinD, because the base value of its diffusion coefficient (in the dilute limit) is much smaller (Fig. 3c in the main text and Extended Data Fig. 5a).

7. Determining the spatial distribution of multiple cargo species

The numerical computation of the cargo distributions in response to an imposed spatial profile of MinD, when multiple cargo species are present in the assay, were performed analogously to the numerical computations for only one cargo species by determining the corresponding boundary value problem. Specifically, note that in deriving our Flory-Huggins and phenomenological Maxwell-Stefan type models, we have *already* considered two passive species (cargo and streptavidin molecules). Adding one more cargo species does not introduce new physical concepts. Thus, it is straightforward to extend these equations by one additional chemical potential for the second cargo species (cf. Eqs. (S2a), (S2b), (S2c), (S4) and (S5)) and one additional equation for the flux of the second cargo species (i.e. so that there are three passive species), just by following the calculations that we have already presented for two passive species^m. These calculations then yield an additional partial differential equation that determines the distribution of the third passive species in response to the spatial profile of MinD proteins (cf. Eqs. (S6a) and (S6b) for the Flory-Huggins type model and Eqs. (S10a) and (S10b) for the phenomenological Maxwell-Stefan type model). Similarly, this procedure also yields an additional partial differential equation for the cumulative coverage of the third species, cf. Eqs. (S6c) and (S6d), which enforces the mass conservation of the additional density field. Furthermore, for the sake of simplicity, we assumed equal abundance of all different cargo species on the membraneⁿ; analogously, in our experimental assays we also provided an equal abundance of different DNA origami (i.e. with different numbers of biotinylated oligonucleotide handles).

^m As the number of species increases, these equations become increasingly complicated. Thus, we used a symbolic math package (SymPy for Python)⁶⁹ to determine the constitutive equations and translate them into matrix form.

ⁿ In principle, it is possible that different cargo molecules (i.e. cargo molecules with different numbers of biotinylated oligonucleotide handles on the DNA origami) are present at different surface densities even though they have the same abundance in the assay. Specifically, DNA origami with more biotinylated oligonucleotide handles have a stronger binding to the membrane, while all DNA origami experience an entropic penalty for binding due to volume exclusion effects. Here, however, we have not considered a detailed theory of such a competitive binding as it mostly affects the time frame before the beginning of the actual experiments.

II. Discussion of alternative thermodynamic transport mechanisms

In the following, we will first elaborate that neither depletion attraction (section II.1 “Depletion attraction cannot explain cargo transport”) nor a volume exclusion by immobile MinD proteins (section II.2 “Static volume exclusion cannot explain cargo transport”) can explain the cargo transport phenomenon that we observed in our experiments. Then, we revisit our previous Flory-Huggins and phenomenological Maxwell-Stefan type theories, and ask how they behave in the limit of small densities (section II.3 “Flory-Huggins mixing in the limit of small densities”), i.e. when steric repulsion between different cargo molecules can be neglected on a mesoscopic scale. Finally, we discuss that we do not expect a significant impact of cargo on the MinDE reaction kinetics (section II.4 “Significant impact of cargo on MinDE reaction kinetics is unlikely”).

1. Depletion attraction cannot explain cargo transport

Depletion attraction arises from a classical entropic effect, where finite-sized molecules (like MinD) can access a larger spatial region if larger molecules (like DNA-Origami) “clump” together²⁰; see Fig. 6 in the main text for an illustration. This results in effective (Asakura-Oosawa) depletion forces²⁰ that act on the larger molecules and which are proportional to the concentration of the smaller molecules, c_p . Phenomenologically, one can represent this depletion attraction as a *negative pressure*, $p \propto -c_p$. If the concentration of the smaller molecule, c_p , is spatially heterogeneous, then this will result in effective pressure gradients, $-\nabla p \propto \nabla c_p$. Consequently, one would expect depletion attraction to lead to an accumulation of cargo molecules in MinD-rich regions. Because this expectation contradicted our experiments, we concluded that depletion attraction plays no significant role for cargo transport. Furthermore, we did not observe depletion-force-induced aggregation of cargo molecules when MinD was homogeneously distributed (Extended Data Fig. 1).

2. Static volume exclusion cannot explain cargo transport

To simplify our experimental setup as much as possible, suppose that membrane-bound MinD proteins act as static obstacles of size a_p and surface density c_p . Then, such obstacles locally occupy a fraction $\theta_p = a_p c_p$ of the surface, thereby reducing the space accessible by the cargo molecules. In thermal equilibrium, cargo molecules spread uniformly across the accessible space, which implies $c_g \propto \theta_{\text{free}} = (1 - \theta_p)$ for the cargo molecule density. Formally, one way

that this expectation can be seen^o is by solving for the steady-state solution of cargo diffusing in a porous medium:

$$\partial_t c_g = \nabla [D_g \theta_{\text{free}} \nabla (c_g / \theta_{\text{free}})]. \quad (\text{S19})$$

A porous medium is best explained by comparing it to a sponge. Let us suppose that the pores in this sponge contain a solution. A concentration difference across nearby pores corresponds to an osmotic pressure and leads to solute fluxes between these pores. In the end, all pores will contain the same concentration of solute ($c_g / \theta_{\text{free}}$). Here, an onlooker that doesn't know about the existence of these pores (e.g. if one were to only image radioactively labelled solute particles) will observe a local concentration of c_g , which will in general not be homogeneous. Eq. (S19) corresponds to the continuum limit of such a porous medium. In our case, MinD takes up space on the membrane, and thus the MinD-free areas can be interpreted as "pores". Eq. (S19) then corresponds to Darcy's law²¹, with a local osmotic pressure that is proportional to the local particle density $c_g / \theta_{\text{free}}$ in each "pore". This relation shows that protein gradients may induce cargo gradients solely by locally reducing the accessible space. However, it also implies that the resulting distribution of cargo molecules does not depend on any intrinsic features of the cargo molecules, contradicting our experimental observations (Fig. 1d-g in the main text). We conclude that MinD proteins do not act as static obstacles for the cargo molecules.

3. Flory-Huggins mixing in the limit of small densities

We have seen in section I.3 "Flory-Huggins theory of mixing: an equilibrium picture" that, in principle, entropic mixing effects may lead to a gradient of passive particles (cargo or streptavidin molecules) in response to a gradient of active particles (MinD proteins). This phenomenon originates from volume exclusion effects (cf. second term in the proximal chemical potential of cargo, Eq. (S2a), and the equivalent second term in the total chemical potential of cargo, Eq. (S5)) and the corresponding steric repulsion between diffusing cargo and diffusing MinD proteins. However, there must also be a steric repulsion between the bulky DNA-origami scaffolds of the cargo molecules (cf. second term in the distal chemical potential

^o Another way to see this expectation is by writing down the Flory-Huggins mixing entropy (cf. section I.3 "Flory-Huggins theory of mixing: an equilibrium picture") and the resulting equilibrium condition, but with the distinct difference that the MinD proteins *may not move at all* and thus reduce the accessible volume: $f / (k_B T) = \theta_{\text{free}} \sum_i (c_i / \theta_{\text{free}}) \ln(\theta_i / \theta_{\text{free}})$. This constrains the possible distribution of particles more strongly than only an imposed spatial profile of MinD, as we have done in section I.3 "Flory-Huggins theory of mixing: an equilibrium picture".

of cargo, Eq. (S4), and the equivalent third term in the total chemical potential of cargo, Eq. (S5), which diverges logarithmically as the local cargo density approaches saturating values by covering the whole locally available membrane area), which counteracts the buildup of cargo gradients. Thus, as we have seen, at the particle densities in our experiments, mixing effects alone cannot account for the strong density gradients of passive particles.

Yet, one may ask: what if the cargo density is much smaller than in our setup, so that mesoscopic volume exclusion effects between different DNA-origami scaffolds may be neglected? Then, we can drop the second term of Eq. (S4), which would diverge logarithmically at high densities and which is equivalent to the third term of Eq. (S5), so that the total chemical potential of membrane-bound cargo in our Flory-Huggins model is given by:

$$\frac{\mu_g(\mathbf{x})}{k_B T} = \ln[\theta_g(\mathbf{x})] - n \ln[1 - \theta_g(\mathbf{x}) - \theta_s(\mathbf{x}) - \theta_p(\mathbf{x})], \quad (\text{S20a})$$

where we have neglected constant contributions. The fraction of the area covered by the DNA origami scaffolds, $\theta_o(\mathbf{x})$, is related to the area fraction covered by the cargo's streptavidin blocks, $\theta_g(\mathbf{x})$, as follows: $\theta_o(\mathbf{x}) = \theta_g(\mathbf{x}) (7 a_\tau)/(n a_\sigma)$. Furthermore, the chemical potential of free streptavidin molecules is given by (cf. Eq. (S2b)):

$$\frac{\mu_s(\mathbf{x})}{k_B T} = \ln[\theta_s(\mathbf{x})] - \ln[1 - \theta_g(\mathbf{x}) - \theta_s(\mathbf{x}) - \theta_p(\mathbf{x})]. \quad (\text{S20b})$$

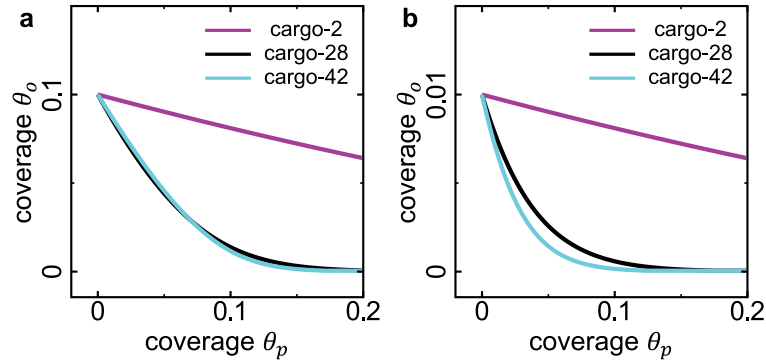
We assume that the passive cargo molecules and the free streptavidin molecules reach an equilibrium state in an adiabatic response to the distribution of active MinD proteins, so that gradients in the chemical potential vanish, $\nabla\mu_g(\mathbf{x}) = 0$ and $\nabla\mu_s(\mathbf{x}) = 0$. Note that this equilibrium condition is equivalent to $\mu_g(\mathbf{x}) = cst$ and $\mu_s(\mathbf{x}) = cst$. Then, we solve the equation $\mu_s(\mathbf{x}) = cst$ for θ_s and set the (general) boundary values $\theta_s(0)$ and $\theta_g(0)$ to obtain the following equation for the local amount of free streptavidin molecules:

$$\theta_s = \frac{\theta_s(0)}{1 - \theta_g(0)} [1 - \theta_g - \theta_p]. \quad (\text{S21a})$$

By inserting Eq. (S21a) into Eq. (S20a), solving the equation $\mu_g(\mathbf{x}) = cst$ for θ_p and setting the (general) boundary value $\theta_g(0)$, this yields the following implicit equation for the local amount of cargo molecules:

$$\theta_p = 1 - \theta_g(\theta_p) - [1 - \theta_g(0)] \left[\frac{\theta_g(\theta_p)}{\theta_g(0)} \right]^{\frac{1}{n}}. \quad (\text{S21b})$$

25

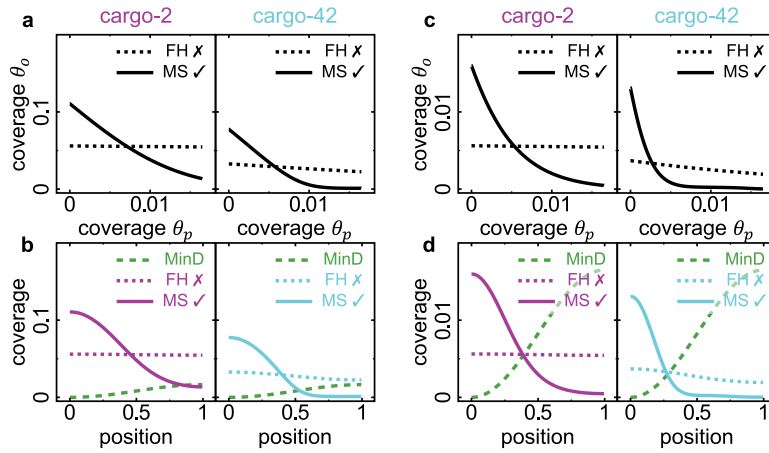


Cross-correlation between cargo coverage and MinD coverage at very low cargo densities. To obtain this graph, we have used Eq. (S21b) and the relation $\theta_o(x) = \theta_g(x) (7 a_\tau) / (n a_\sigma) \approx \theta_g(x) (70/n)$. Furthermore, we have assumed that the cargo molecules do not exceed (a) a coverage of 0.1, which is 1 order of magnitude smaller than the typical values in our experiments, or (b) a coverage of 0.01, which is 2 orders of magnitude smaller than the typical values in our experiments.

As the illustration “Cross-correlation between cargo coverage and MinD coverage at very low cargo densities” shows, at large densities of MinD proteins (similar to our experiments) it would be possible to generate a gradient in the cargo molecules even without a diffusiophoretic mechanism if the density of cargo molecules is sufficiently small (one or two orders of magnitude smaller than in our experiments).

In a cell, the density of MinD proteins is expected to be smaller than in our experimental setup. Thus, we have also tested in our model whether one would still expect a pattern in the passive cargo if the density of MinD was one order of magnitude smaller, and if the density of passive molecules was one or two orders of magnitude smaller than in our experiments. As the illustration “Low MinD and low cargo density” shows, a diffusiophoretic mechanism leads to much stronger gradients in the cargo molecules than entropic sorting effects.

Our theoretical analysis in this section thus shows: if the cargo density is much smaller than in our experimental assay, then mixing effects can readily build up cargo gradients as long as the MinD density remains high (cf. illustration “Cross-correlation between cargo coverage and MinD coverage at very low cargo densities”). If the MinD density is also reduced compared to our experiments, then a diffusiophoretic mechanism is mandatory to create significant cargo gradients (cf. illustration “Low MinD and low cargo density”).



Low MinD and low cargo density. We tested our model in a regime where the MinD density is one order of magnitude smaller than in our experiments. **a,b** Cargo coverage one order of magnitude smaller than in our experiments. Model parameters: (cargo-2) average coverages $\bar{\theta}_p = 0.00825$, $\bar{\theta}_s = 0.0149$ and $\bar{\theta}_o = 0.055$; interaction parameter (in terms of MinD coverage) $\theta_x^{-1} = 220$; (cargo-42) average coverages $\bar{\theta}_p = 0.00825$, $\bar{\theta}_s = 0$ and $\bar{\theta}_o = 0.028$; interaction parameter (in terms of MinD coverage) $\theta_x^{-1} = 620$. Surface coverages $\theta = a c$ and surface densities c are related via the particle size a . **c,d** Cargo coverage two orders of magnitude smaller than in our experiments. Model parameters: (cargo-2) average coverages $\bar{\theta}_p = 0.00825$, $\bar{\theta}_s = 0.00149$ and $\bar{\theta}_o = 0.0055$; interaction parameter (in terms of MinD coverage) $\theta_x^{-1} = 220$; (cargo-42) average coverages $\bar{\theta}_p = 0.00825$, $\bar{\theta}_s = 0$ and $\bar{\theta}_o = 0.0028$; interaction parameter (in terms of MinD coverage) $\theta_x^{-1} = 620$. Surface coverages $\theta = a c$ and surface densities c are related via the particle size a .

4. Significant impact of cargo on MinDE reaction kinetics is unlikely

As the MinDE distribution was influenced by the presence of cargo, we wondered whether cargo may change the kinetic (un)binding rates of MinDE. To answer this question, we analysed the average fluorescence intensity of the patterns, i.e. the membrane density of the molecules. While we found that the density of streptavidin and MinD were relatively similar for all conditions, the density of membrane-bound DNA origami decreased by roughly 44% when we increased the number of streptavidin building blocks from 1 to 42 (Extended Data Fig. 2c-e). The latter suggested that the average density of membrane-bound streptavidin, which remained unaffected, is the limiting factor for binding of DNA origami to the membrane (see section 1.2 “Cargo density is limited by abundance of streptavidin and origami” for details). As the presence of cargo did not change the average membrane density of MinD (Extended Data Fig. 2d), it is unlikely to significantly affect their (un)binding rates. Furthermore, cargo always accumulated in regions where both the MinD density and thus

protein recruitment to the membrane are already low, and is thus unlikely to significantly hinder protein (un)binding.

Cargo and streptavidin molecules have a strong membrane affinity and negligible detachment rates³. Therefore, MinD-induced detachment of cargo or streptavidin from the membrane is highly unlikely.

III. Discussion of related non-equilibrium transport mechanisms

In the following, we will relate our Maxwell-Stefan-like phenomenological approach to diffusiophoresis to a commonly employed hydrodynamic theory for 3D solutions^{22–35} which was pioneered by Derjaguin¹³. In particular, we will follow the reasoning and calculations by Marbach & Bocquet³¹, as well as by Golestanian³² to derive a phoretic drift velocity for uncharged particles. We will place special emphasis on the assumptions underlying these calculations and discuss their validity for our experimental system. Taken together, the analysis below will show that diffusive fluxes are essential to obtain a finite diffusiophoretic drift velocity.

1. Illustrative derivation of the diffusiophoretic drift velocity in 3D solutions

We assume that the passive cargo molecules are much larger than the MinD proteins. This approximation should be appropriate for the DNA origami scaffold of the cargo molecules since we use DNA-Origami with a size of 110×16 nm and a MinD dimer has a size of 5×5 nm (although this size difference creates only a weak length scale separation along the DNA-Origami's long axis). However, this assumption may not be strictly valid for streptavidin molecules^p, which have roughly the same size as a membrane-bound MinD dimer (5×5 nm). Although the following calculations have limited applicability to our experimental setup with only weak length scale separation between cargo and solute (while being perfectly valid for colloidal systems), they will conceptually illustrate how diffusiophoretic transport may emerge from microscopic interactions.

The approximation that the length scales of cargo and of the MinD dimer separate allows one to consider the MinD proteins as a solute field with density c_p , whose temporal evolution is given by the Smoluchowski equation,

$$\partial_t c_p = \nabla \cdot \left[D_p \nabla c_p + c_p \frac{D_p}{k_B T} \nabla \Psi - c_p \mathbf{v} \right] \equiv -\nabla \cdot \mathbf{j}_p. \quad (\text{S22})$$

Here, Ψ denotes the interaction potential between the MinD proteins and the cargo, and \mathbf{v} refers to the local advection velocity due to flow in the surrounding fluid. As we will show below, the interactions Ψ between MinD proteins and the cargo will induce a slip flow \mathbf{v} in

^p A more general treatment would require describing the hydrodynamic interactions between solute molecules with the Rotne-Prager tensor. Here, we will not carry out such a calculation, especially since additional caveats (discussed below in more detail) like the coupling between 2D fluid membrane and 3D aqueous solution apply.

the surrounding fluid. Furthermore, we put ourselves in the (moving) reference frame of a cargo molecule, and consider the cargo molecule as a rigid one-dimensional wall placed at position $z = 0$. Since all particles involved in the process are small, we assume that the fluid dynamics is described by a stationary Stokes flow at low Reynolds number,

$$\eta \Delta \mathbf{v} - \nabla P - c_p \nabla \Psi = 0, \quad (\text{S23a})$$

$$\nabla \cdot \mathbf{v} = 0. \quad (\text{S23b})$$

Here, the field P denotes the local pressure in the fluid. The velocity field \mathbf{v} also advects the MinD proteins, cf. Eq. (S22). In the third term of Eq. (S23a), the body force acting on each MinD protein due to its interaction with the cargo molecule is transferred to the fluid, which drives the fluid flow \mathbf{v} .

There are several important reservations one might have with regard to the above approach: (i) First, the typical mean free path between two membrane-bound particles in our experimental system is only 46 \AA , which amounts to roughly 15 water molecules. Continuum hydrodynamic approaches are typically valid down to a molecular scale of 10 \AA , below which the microscopic properties of water (i.e. viscosity) begin to significantly deviate from its bulk properties³⁶. Thus, if any two MinD dimers or streptavidin molecules come closer than 10 \AA (which may happen fairly regularly given that their average distance is only 46 \AA), then a continuum hydrodynamic theory loses its validity at such small scales and one needs a particle-based kinetic analysis. (ii) Second, the above theoretical approach (more specifically, Eq. (S23a)) is based on the assumption that the Reynolds number is small ($Re \ll 1$). With the Reynolds number given by $Re = \frac{vL}{\eta}$, where L is the typical length scale of the fluid flow, this requires a relatively small fluid flow velocity. To estimate whether this assumption is valid for our experimental setup, we have to investigate the typical velocity of the particles at the molecular scale. The typical length scale of the corresponding hydrodynamic problem is $L = 46 \text{ \AA}$ and the kinematic viscosity of water at 20°C is given by³⁷ $\eta = 1 \times 10^{-6} \text{ m}^2 \text{ s}^{-1}$. The typical velocity of the fluid between two membrane-bound particles should be in the range between the thermal velocity of these particles and the thermal velocity of water molecules. In the following, we will estimate the typical thermal velocity of a particle as the root mean square velocity:

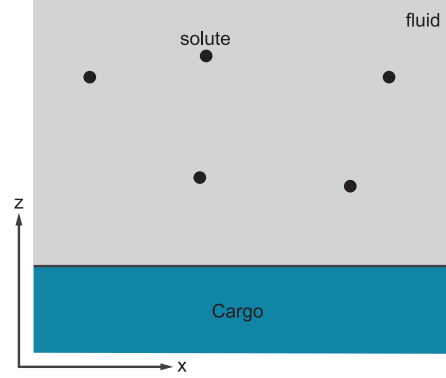
$$\sqrt{\langle v^2 \rangle} = \sqrt{\frac{f k_B T}{m}}, \quad (\text{S24})$$

where f refers to the number of translational degrees of freedom ($f = 2$ for 2D motion and $f = 3$ for 3D motion). MinD dimers have a molecular weight of 66 kDa, while streptavidin molecules (tetramers) have a molecular weight of 53 kDa. These membrane-bound molecules are confined to planar 2D motion and thus (at 20°C) move with a thermal velocity of 8.6 ms^{-1} and 9.6 ms^{-1} for MinD dimers and streptavidin, respectively. Water has a molecular weight of 18 Da and may move in the whole 3D solution, thus with a thermal velocity of 637 ms^{-1} . Consequently, the Reynolds number will typically be in a range between $Re \sim 0.04$ (if the fluid moves at the thermal velocity of a MinD protein) and $Re \sim 2.9$ (if the fluid moves at the thermal velocity of a water molecule)^q. These estimates suggest that at the given length scales one might have to take into account the momentum terms of the Navier-Stokes equations, thus possibly invalidating Eq. (S23a). (iii) Third, the Knudsen number for the membrane-bound particles, which relates the molecular free path to the molecular scale (5 nm for a MinD dimer or a streptavidin molecule), is only $Kn \sim 0.92$. At such small length scales, any gas (which can also mean a gas of solutes) will begin to show hydrodynamic properties like viscosity. In the case of MinD proteins, this is suggested by the density-dependence of their diffusion constant, which decreases as the surface density of MinD increases¹. For a gas, it is possible to derive these hydrodynamic properties from the Boltzmann equation with the Chapman-Enskog theory^{38,r}. (iv) Fourth and finally, in the above approach one considers a single fluid only, while actually in our experimental setup there are two fluids with different viscosities: a 3D half-space of water and a 2D lipid bilayer that contains membrane-bound molecules.

With these reservations in mind, we will in the following explore the consequences of the above approach to our experimental system. Despite the possible limitations in applicability, it will provide important conceptual insights into the mechanisms underlying diffusiophoresis. Thus, we will now turn to analyse the continuum approach for a cargo particle that is much

^q The lipid bilayer membrane is a fluid whose kinematic viscosity should be significantly larger than that of water. Specific values are 0.06 Pa s for the dynamic viscosity of a 5 nm thick membrane of DOPC⁷⁰. Assuming a close packing of the phospholipids where each phospholipid takes up 10 \AA^2 , and taking the typical mass of a DOPC molecule⁷¹ as 786 Da, this results in a kinematic viscosity of $23 \times 10^{-6} \text{ m}^2 \text{ s}^{-1}$. Thus, any flow in the liquid upper leaflet of the supported lipid bilayer will be associated with smaller Reynolds numbers.

^r Here, a careful theoretical treatment would be needed. The Chapman-Enskog theory is typically applied to gases, where particles only interact via collisions. In our case, particles may also interact via hydrodynamic interactions.



Simplified geometry of a cargo which is surrounded by solute molecules and fluid. We approximate the cargo molecule as a rigid wall by assuming that there is a length scale separation between cargo and solute.

larger than the MinD proteins. Due to the separation of length scales, we consider the surface of the cargo molecule as a solid wall (cf. illustration “Simplified geometry of a cargo which is surrounded by solute molecules and fluid”). The interaction potential, $\Psi(z)$, should only depend on the relative distance between a MinD protein and the wall. We assume that the cargo is rigid and thus that the wall is impermeable, so that the flow velocity and the particle fluxes along the normal axis (z -axis) vanish: $v_z = 0$ and $j_{p,z} = 0$. Then, in the stationary case, Eq. (S22) reduces to a balance between a diffusive flux and an advective flux due to the interaction potential $\Psi(z)$:

$$D_p \partial_z c_p + \frac{c_p D_p}{k_B T} \partial_z \Psi(z) = 0. \quad (\text{S25})$$

By integrating this expression over z , one obtains a Boltzmann-like protein profile,

$$c_p(z) = c_\infty \exp\left[-\frac{\Psi(z)}{k_B T}\right], \quad (\text{S26})$$

where c_∞ corresponds to the far-field concentration of the MinD proteins. Similarly, by using $v_z = 0$, the z -component (perpendicular to the interface defined by the cargo molecule) of the Stokes equations, Eq. (S23a), yields the following force balance equation between the pressure gradient and the potential force $\partial_z \Psi$:

$$\partial_z P = -c_p \partial_z \Psi. \quad (\text{S27})$$

Again, integrating once over z yields an expression for the hydrodynamic pressure field:

$$P_\infty - P(z) = -c_\infty \int_\infty^z dz' \partial_z \Psi(z') \exp\left[-\frac{\Psi(z')}{k_B T}\right] = -c_\infty \int_{\Psi_\infty}^\Psi d\Psi \exp\left[-\frac{\Psi}{k_B T}\right]. \quad (\text{S28})$$

Next, we require that the interaction potential vanishes in the far field, $\lim_{z \rightarrow \infty} \Psi(z) = \Psi_\infty = 0$, and thus obtain the following expression for the hydrodynamic pressure field

$$P(z) = P_\infty + k_B T c_\infty \left[\exp\left(-\frac{\Psi(z)}{k_B T}\right) - 1 \right] = P_\infty + k_B T (c_p - c_\infty). \quad (\text{S29})$$

Here, P_∞ refers to the hydrostatic pressure in the far field, where the ambient fluid is at rest. In Eq. (S29), the term $c_p k_B T$ can be identified as a local osmotic pressure that is induced by interactions between MinD proteins and the cargo wall. As there is a density gradient of solutes in the far field, $\partial_x c_\infty$, the resulting pressure gradient drives fluid flow parallel to the cargo surface, i.e. along the x -axis. Furthermore, since our simplified geometry consists of an infinite wall as the cargo surface, we assume that the fluid flow is translation invariant along the x -axis, $\partial_x v_x \equiv 0$ and therefore $\partial_x^2 v_x \equiv 0$ (i.e. we assume that variations along the x -axis are significantly smaller than variations along the z -axis because of the separation of length scales). Then, we obtain the following equation for the x -component of the velocity field:

$$\eta \partial_z^2 v_x = \partial_x P = k_B T \left[\exp\left(-\frac{\Psi(z)}{k_B T}\right) - 1 \right] \partial_x c_\infty. \quad (\text{S30})$$

This relation can be integrated using no shear stress boundary conditions in the far field, $\partial_z v_x|_{z \rightarrow \infty} = 0$. One obtains:

$$\int_0^\infty dz z \partial_z^2 v_x = [z \partial_z v_x]_0^\infty - \int_0^\infty dz \partial_z v_x = -v_x|_{z \rightarrow \infty} + v_x(0). \quad (\text{S31})$$

Finally, we use no-slip boundary conditions at the cargo surface, $v_x(0) = 0$, to obtain the far-field fluid slip velocity:

$$v_x|_{z \rightarrow \infty} = -\frac{k_B T}{\eta} \int_0^\infty dz z \left[\exp\left(-\frac{\Psi(z)}{k_B T}\right) - 1 \right] \partial_x c_\infty. \quad (\text{S32})$$

Returning to the lab frame, the cargo slip velocity is given by⁵:

$$v_g = +\frac{k_B T}{\eta} \int_0^\infty dz z \left[\exp\left(-\frac{\Psi(z)}{k_B T}\right) - 1 \right] \partial_x c_\infty. \quad (\text{S33})$$

⁵ This is equivalent to assuming that the fluid is at rest in the far field, $v_x|_{z \rightarrow \infty} = 0$, and computing the corresponding boundary velocity $v_x(0)$.

For purely steric hard-sphere interactions between MinD and the cargo molecules,

$$\Psi(z) = \begin{cases} \infty, & z \leq R_p \\ 0, & z > R_p \end{cases} \quad (\text{S34})$$

we can explicitly perform the integral in Eq. (S33). Then, the diffusiophoretic slip is given by

$$\mathbf{v}_g = -\frac{k_B T R_p^2}{\eta} \frac{1}{2} \nabla c_p. \quad (\text{S35})$$

Thus, we have recapitulated the conceptual calculations by Marbach & Bocquet³¹, as well as by Golestanian³² to show how a density gradient of proteins can induce a diffusiophoretic drift (advection) via hydrodynamic interactions and an interaction potential. In the next section, we will discuss these results in depth.

2. Diffusiophoretic drift requires solute fluxes

At first glance, Eq. (S35) could be interpreted as a diffusiophoretic drift which is driven by a density gradient of solute molecules (in our case the MinD proteins). However, such an interpretation overlooks the fact that according to Fick's laws, particle density gradients and fluxes are closely related. Using the Stokes-Einstein relation for the diffusion coefficient of the solute molecules (MinD, assuming spherical particles in 3D solution), $D_p = k_B T / (6\pi\eta R_p)$, and Fick's first law, $\mathbf{j}_p = -D_p \nabla c_p$, Eq. (S35) can be rewritten as

$$\mathbf{v}_g = -3\pi R_p^3 D_p \nabla c_p = 3\pi R_p^3 \mathbf{j}_p. \quad (\text{S36})$$

In this form, the equation for the diffusiophoretic slip velocity reveals that the diffusiophoretic drift of a cargo molecule (in 3D and at low densities) is directly related to the diffusive flux \mathbf{j}_p of the solute molecules (MinD). Consequently, while from Eq. (S35) one could conclude that a finite gradient ∇c_p of solute molecules (MinD) is sufficient to observe a diffusiophoretic effect, Eq. (S36) shows that actually finite solute fluxes \mathbf{j}_p are required. To further elucidate this point, let us suppose that there are no fluxes of solute molecules in the laboratory frame, and that instead their spatial distribution is fully determined by some stationary trapping potential V^t . Then the total flux of solute molecules in the laboratory frame becomes:

$$D_p \partial_x c_p + \frac{c_p D_p}{k_B T} \partial_x V \equiv 0. \quad (\text{S37})$$

[†] Such a trapping potential could be realized via an electrostatic field that selectively acts on charged solutes but does not affect the electrically neutral cargo. Typically, such an electrostatic field will lead to an electrophoretic current of the charged solutes. In a closed container, this electrophoretic current will eventually be balanced by a diffusive flux, yielding a steady state with a vanishing net flux of the charged solutes.

Inserting Eq. (S37) (flux-free steady state condition of the Smoluchowski equation in the laboratory frame) into Eq. (S22) (Smoluchowski equation in the co-moving frame of the cargo, in steady state and in addition also considering the trapping potential V), and using translation invariance of the interaction potential Ψ along the x -axis, this yields the following balance equation for the x -component of the flux of solute molecules in the co-moving frame of the cargo molecule:

$$-j_{p,x} = D_p \partial_x c_p + \frac{c_p D_p}{k_B T} \partial_x V - c_p v_x = -c_p v_x. \quad (\text{S38})$$

Thus, if the advective fluxes that arise from some potential V and the diffusive fluxes balance in the laboratory frame, then the net flux in the co-moving frame will be determined solely by the velocity v_x of the co-moving frame and the local density c_p . In addition, as before, we assume that the cargo is rigid and thus that the cargo wall is impermeable, so that the fluid flow velocity and the particle fluxes along the normal axis (z -axis) vanish, $v_z = 0$ and $j_{p,z} = 0$. Together with the steady-state condition, $\partial_t c_p = -\nabla \cdot \mathbf{j}_p = 0$, and the incompressibility of the fluid, $\nabla \cdot \mathbf{v} = \partial_x v_x + \partial_z v_z = \partial_x v_x = 0$ (equivalent to the translation invariance that we have assumed before), this gives:

$$\nabla \cdot \mathbf{j}_p = v_x \partial_x c_p = 0. \quad (\text{S39})$$

Thus, there is no diffusiophoretic slip velocity ($v_x = 0$) and the diffusiophoretic cross-mobility vanishes if there are no solute particle fluxes^u. In that case, the distribution of cargo particles in response to the solute particles reduces to an equilibrium problem, which has been discussed in sections I.3 “Flory-Huggins theory of mixing: an equilibrium picture” and II.2 “Static volume exclusion cannot explain cargo transport”. In summary, the main insight gained in this paragraph is that a diffusiophoretic slip of the cargo molecule can only occur if there are solute (MinD) fluxes. In contrast, in the absence of particle fluxes, the spatial distribution of all particles is determined solely by a free energy functional, i.e. by the laws of equilibrium thermodynamics.

^u Another way to see this is by starting with the hydrodynamic pressure field, Eq. (S29), but with a position-dependent hydrostatic pressure in the far field: $P(x, z) = P_\infty(x) + k_B T (c_p - c_\infty)$. Assuming that the fluid is at rest in the far field, where the interaction potential vanishes, the x -component of the Stokes equations, cf. Eq. (S23a), in the far field is then given by $\partial_x P_\infty + c_\infty \partial_x V = 0$. If the distribution of solutes in the far field is determined by the potential V , cf. Eq. (S37), then the total driving force of the fluid vanishes, $\partial_x P(x, z) + c_p \partial_x V = 0$, which implies a vanishing diffusiophoretic slip velocity (i.e. the boundary velocity $v_x(0)$ vanishes).

3. Relation to our phenomenological approach to diffusiophoresis

The hydrodynamic approach discussed in sections III.1 “Illustrative derivation of the diffusiophoretic drift velocity in 3D solutions” and III.2 “Diffusiophoretic drift requires solute fluxes” relies on the assumption that particle densities are small. In the following, we will compare these results to the corresponding results of our Maxwell-Stefan-like phenomenological theory in the limit of small densities. We will indicate analogous terms in square brackets. The hydrodynamic approach, Eq. (S35), yields the following relation for the net flux of cargo molecules:

$$\mathbf{j}_g = -D_g \nabla c_g - c_g [3\pi R_p^3] [D_p \nabla c_p]. \quad (\text{S40})$$

The corresponding current for the cargo molecules obtained from the Maxwell-Stefan-like phenomenological theory, Eq. (S8), in the limit of small densities (where self-diffusion is density-independent) and for two interacting particle species reads:

$$\mathbf{j}_g = -\frac{k_B T}{\xi_g} \nabla c_g - c_g \left[\frac{\zeta_{pg}}{\xi_g} \right] \left[\frac{k_B T}{\xi_p} \nabla c_p \right]. \quad (\text{S41})$$

In our experiments, the resulting patterns are in a steady state (cf. Fig. 1b in the main text). The solute (MinD) molecules are in a nonequilibrium steady state with a finite flux $\mathbf{j}_p \neq 0$, due to their ATP-driven membrane (un)binding dynamics. In contrast, the *passive* cargo molecules (which are permanently bound to the planar membrane) can only relax towards a thermal equilibrium state with vanishing fluxes $\mathbf{j}_g = 0$.

Solving Eq. (S40) in the flux-free steady state, one finds that the distribution of cargo molecules in response to a gradient of proteins in a 3D solution is given by:

$$c_g(c_p) = c_g(0) \exp[-3\pi R_p^2 R_g c_p]. \quad (\text{S42})$$

We can rewrite this equation, Eq. (S42), in terms of the volume fraction that is occupied by solute, $\theta_p = \frac{4}{3}\pi R_p^3 c_p$, and obtain:

$$c_g(\theta_p) = c_g(0) \exp\left[-\frac{9 R_g}{4 R_p} \theta_p\right]. \quad (\text{S43})$$

Analogously, Eq. (S41) yields

$$c_g(c_p) = c_g(0) \exp\left[-\frac{\zeta_{pg}}{\xi_p} c_p\right] = c_g(0) \exp\left[-\frac{c_p}{c_x}\right], \quad (\text{S44})$$

where we have defined the typical interaction parameter in the same way as in the main text $c_x^{-1} = \zeta_{pg}/\xi_p$. In the main text, we have then expressed the interaction parameter in terms of the solute size (2D projected area), $\theta_x^{-1} = 1/(a_p c_x)$, where the surface fraction occupied by solute is given by $\theta_p = a_p c_p$.

We note that the stationary distributions that result from the 3D hydrodynamic theory, Eq. (S43), and from our Maxwell-Stefan-like phenomenological approach to particle diffusion on a 2D membrane, Eq. (S44), have identical mathematical form in the low-density limit. Furthermore, the corresponding transport equations that describe the dynamics before the onset of the steady state, Eqs. (S40) and (S41), are also formally equivalent. Keeping in mind all of our reservations concerning the applicability of the 3D hydrodynamic theory to our experimental setup (cf. section III.1 “[Illustrative derivation of the diffusiophoretic drift velocity in 3D solutions](#)”), we make a leap of faith and assume that Eqs. (S43) and (S44) are identical. Then, the interaction parameter θ_x^{-1} would be given by

$$\theta_x^{-1} = \frac{9 R_g}{4 R_p}, \quad (\text{S45})$$

where R_g is the radius of a cargo particle and R_p is the radius of a solute molecule (MinD dimer). For cargo molecules that are 22 times larger in diameter than the solute molecules (naively approximating the rod-like cargo as a sphere of radius 110 nm and the MinD dimer as a sphere of radius 5 nm), this yields a value of $\theta_x^{-1} \sim 50$. In comparison, our fitting procedure of the reduced model (cf. Fig. 3b in the main text and Extended Data Fig. 5h) yielded typical values around $\theta_x^{-1} \sim 10^y$, while in our full model we used typical values around $\theta_x^{-1} \sim 300^w$. While this comparison between the interaction parameters that one would expect from a 3D hydrodynamic theory and our 2D interaction parameters neglects many important details like the geometry of the problem, it illustrates conceptually that hydrodynamic interactions between different particles might actually be sufficient to drive a diffusiophoretic drift in our experiments. Given the relevance of 2D surfaces (membranes) and membrane-bound proteins

^y To obtain our fit curves, we neglected entropic repulsion between different cargo molecules that arises due to volume exclusion. In doing so, our fitted parameters are likely smaller than the “true” interaction parameters.

^w As discussed in section I.3 “[Flory-Huggins theory of mixing: an equilibrium picture](#)”, for our full model we used a strong entropic repulsion term for the DNA origamis that originates from Flory-Huggins theory. Assuming an ideal solution instead yields a weaker repulsion and thus requires weaker interaction parameters.

for all forms of life, we believe that it might be interesting to generalize the current framework of diffusiophoresis^{31,32} to a 2D+3D hydrodynamic setting.

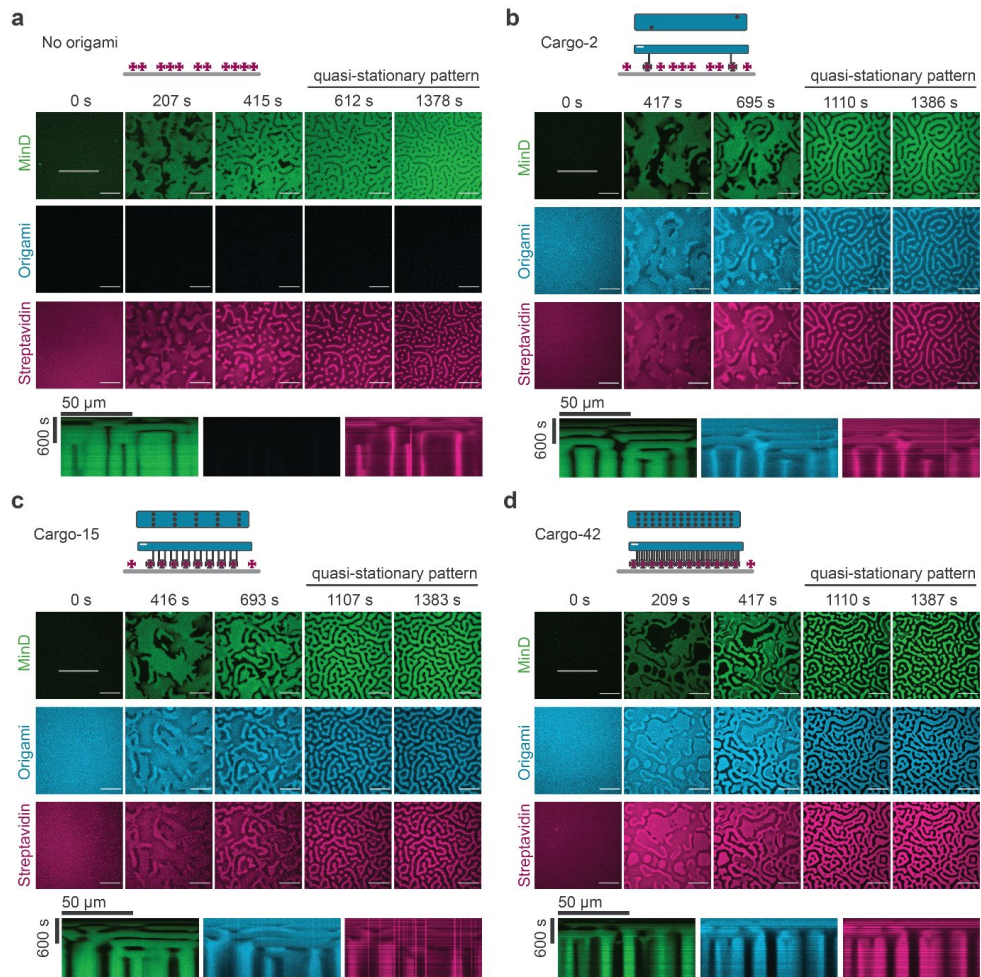
In closing we would like to note that there may also be a second mechanism for the coupling of different particle fluxes, namely kinetic interactions. Specifically, our simple estimates of the Reynolds number suggest that inertial effects may be significant. This is further underlined by the small mean free path between the involved membrane-bound particles of only 46 Å. For example, in the case of an ideally elastic frontal collision, the momentum transfer during a single collision event is given by

$$\Delta p = -2\Delta v \frac{m_1 m_2}{m_1 + m_2}. \quad (\text{S46})$$

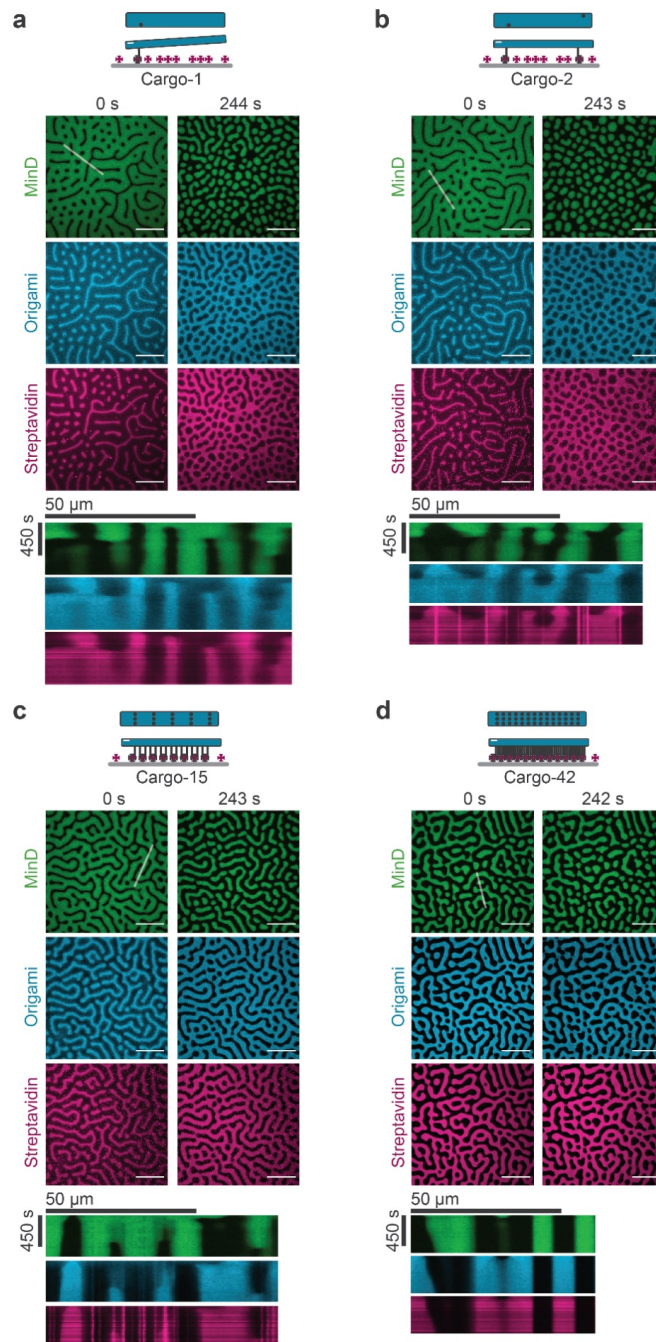
Such a momentum transfer via particle collisions directly yields the coupling term in Eq. (S8).

To summarize, in this section we have discussed that the phenomenological coupling between particle fluxes in the Maxwell-Stefan-like phenomenological theory may originate from hydrodynamic interactions or from momentum transfer via direct interactions, yielding two microscopic mechanisms that can lead to a mesoscopic friction between different molecular species.

Supplementary Figures

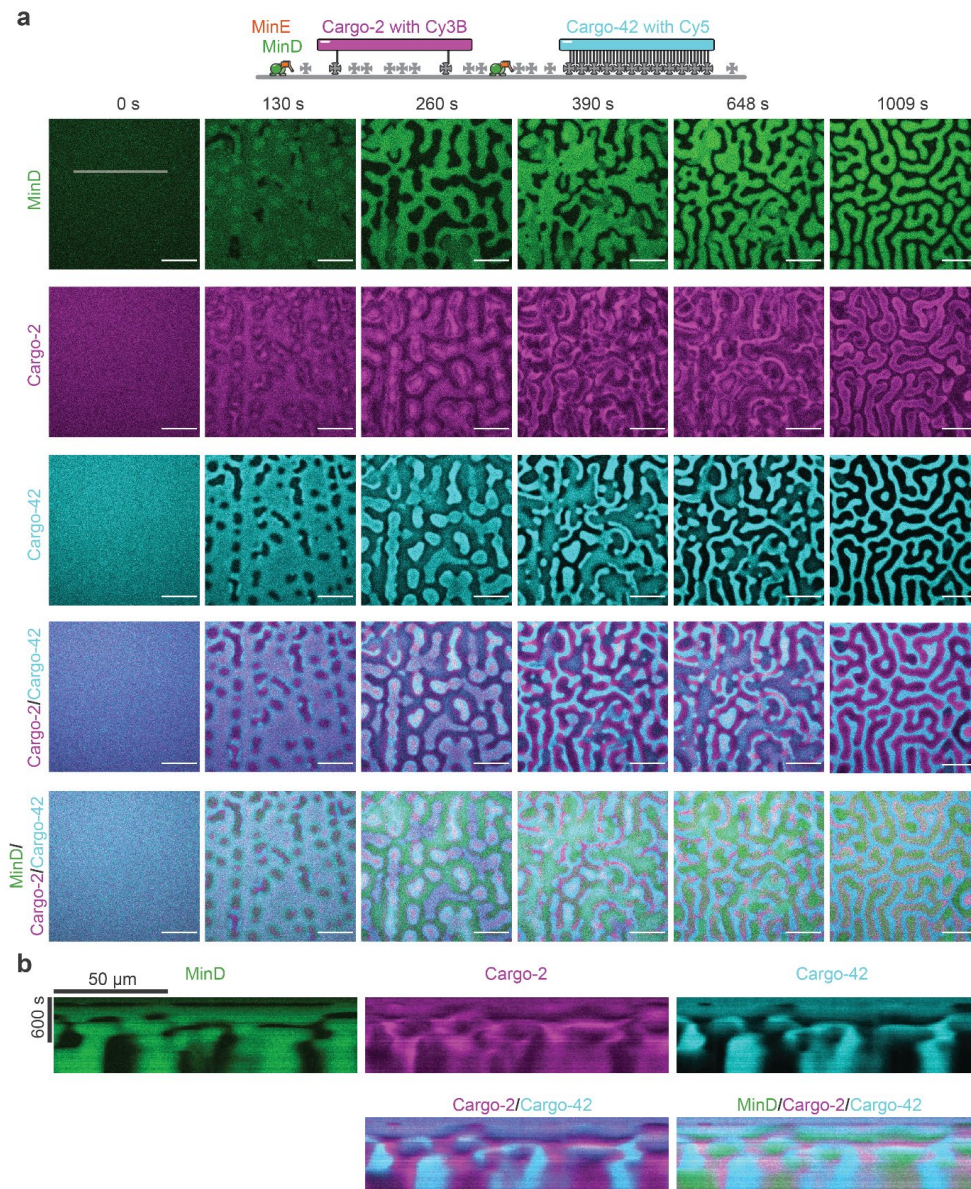


Supplementary Figure S1: MinDE induces pattern formation of cargo from an initially homogenous state. Representative time-series and kymograph (along line selection) of MinDE self-organization, which induces patterns of DNA origami and streptavidin when **a**, no origami, **b**, cargo-2, **c**, cargo-15 and **d**, cargo-42 is present (1 μM MinD (30% EGFP-MinD), 1.5 μM MinE-His, in absence or presence of 0.1 nM origami-Cy5 with 2, 15 or 42 biotinylated oligonucleotides, Alexa568-streptavidin). Panel b is identical to Figure 1b,c. Scale bars: 50 μm

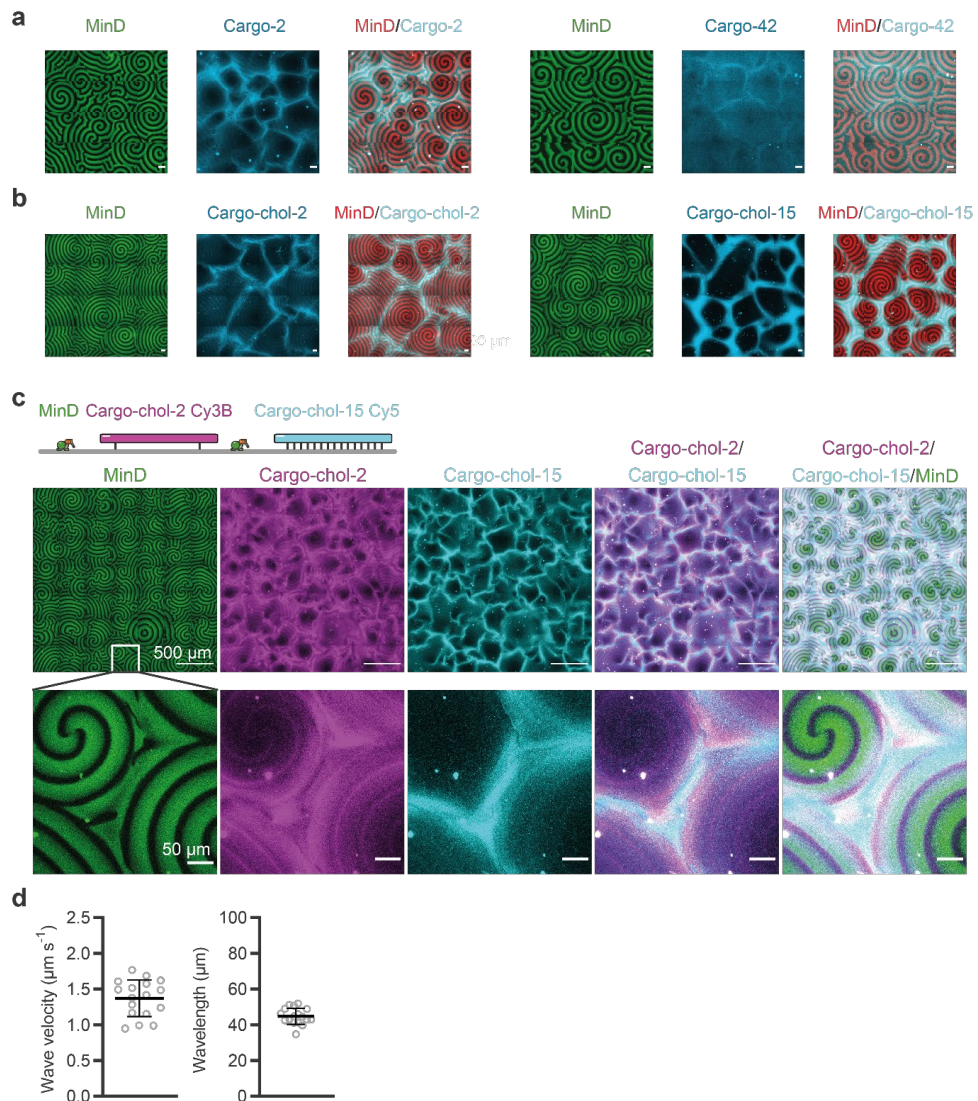


Supplementary Figure S2: Changes in the MinDE patterns are mimicked by cargo. Representative time-series and kymograph showing changes in MinD and cargo molecule patterns in presence of **a**, cargo-1, **b**, cargo-2, **c**, cargo-15 and **d**, cargo-42 (1 μM MinD (30% EGFP-MinD), 1.5 μM MinE-His, origami-Cy5 with 1, 2, 15 or 42 biotinylated oligonucleotides, Alexa568-streptavidin) upon addition of more MinE (addition of 1.5 μM MinE-His). MinE addition directly before $t = 0$ s. Scale bars: 50 μm

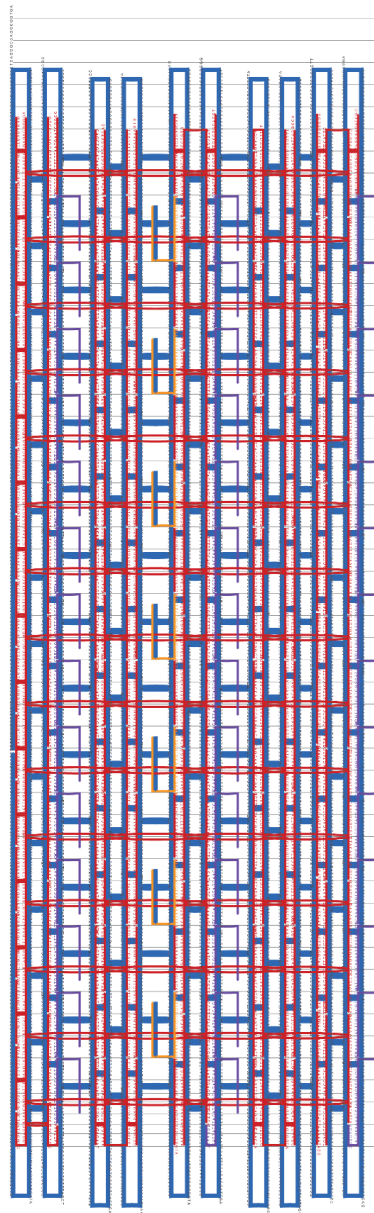
40



Supplementary Figure S3: MinDE induces pattern formation of two distinct cargoes, cargo-2 and cargo-42, from an initially homogenous state. **a**, Representative time-series of MinD, cargo-2 and cargo-42 pattern formation. ATP is added to start self-organization directly before $t=0$ s (1 μ M MinD (30% EGFP-MinD), 1.5 μ M MinE-His, 50 pM origami-Cy3B with 2 biotinylated oligonucleotides, 50 pM origami-Cy5 with 42 biotinylated oligonucleotides, non-labelled streptavidin). Scale bars: 50 μ m **b**, Kymographs of the line selection shown in **a**.



Supplementary Figure S4: Dynamic MinDE waves transport and sort cargo, establishing large-scale gradients. Representative images of large scale gradients originating from transport of **a**, cargo-2 and cargo-42 and **b**, cargo-Chol-2 and cargo-chol-15 (1 μM MinD, 5 μM His-MinE, with **a**, 0.1 nM origami-Cy5 with 2 or 42 biotinylated oligonucleotides, non-labeled streptavidin or **b**, 0.1 nM origami-Cy3b with 2 or 15 hybridizing oligonucleotides, 10 nM TEG-cholesteryl oligonucleotide) Scale bars: 50 μm . Overlaid images are identical to Figure 5c. **c**, Representative images of individual and overlaid channels of sorting of cargo-chol-2 and cargo-chol-15 by MinDE waves (1 μM MinD (30% EGFP-MinD), 5 μM His-MinE with 50 pM origami-Cy3b with 2 and 50 pM origami-Cy5 with 15 hybridizing oligonucleotides, 10 nM TEG-cholesteryl oligonucleotide). Scale bars: top, 500 μm ; bottom, 50 μm . **d**, Wave velocity and wavelength of MinDE waves on unconstrained bilayers in presence of cargo-2, cargo-chol-2 or cargo-chol-15 with N=17 analysed time-series.



Supplementary Figure S5. Design of the elongated 20-helix bundle DNA origami with 42 handle positions. The dye-modified and connector oligonucleotides required for fluorescence detection are highlighted in orange, the 42 possible positions for incorporation of biotinylated oligonucleotide handles for binding to streptavidin in purple, core staples in black and the M13 p7249 scaffold is coloured in blue.

Supplementary Tables

Supplementary Table 1: Model Parameters and variables. Overview of the parameters and all dependent variables used in the Flory-Huggins type and phenomenological Maxwell-Stefan type theories.

Parameter	Value	Explanation
θ_x^o	200	Interaction parameter between origami scaffold and MinD, in terms of MinD coverage
θ_x^s	10	Interaction parameter between streptavidin and MinD, in terms of MinD coverage
n	1–42	Number of streptavidin attached to origami

Estimated from experiments:

$\overline{\theta}_p$	0.0825	Average MinD surface coverage. Derived from measured densities ^{1,2} .
$\overline{\theta}_{o+}$	0.55	Average origami surface coverage (distal), if all available DNA origami in the assay (0.1 nM) were to bind to the available streptavidin molecules.
$\overline{\theta}_{s+}$	0.165	Average surface coverage of available streptavidin molecules (free + bound). Derived from measured densities ² .

Dependent variables:

$\overline{\theta}_o$	$\min(\overline{\theta}_{o+}, \overline{\theta}_{s+} a_o/a_c)$	Average origami surface coverage (distal), which is limited by the density of available streptavidin molecules.
$\overline{\theta}_s$	$\overline{\theta}_{s+} - \overline{\theta}_o a_c/a_o$	Average surface coverage of free streptavidin molecules.

Supplementary Table 2. List of plasmids used in this study.

Plasmid name	Source
pET28a-His-MinD_MinE	³⁹ (Addgene # 133621)
pET28a-His-EGFP-MinD	⁴⁰ (Addgene # 133622)
pET28a-His-MinE	³⁹
pET28a-MinE-His	⁴¹ (Addgene # 133623)
pREP41X	Susan Forsburg ⁴²
pREP42X	Susan Forsburg ⁴²
pMBL-sfGFP-MinDMinE	⁴¹
pET28a-mCherry-2xEcMTS	² (Addgene # 133624)
pET28a-mCherry-GGBSMTS	²
pREP41X-sfGFP-MinD	This study
pREP42X-MinE	This study
pREP41X_coex_sfGFP-MinD_MinE	This study
pREP42X-mCherry-BsMTS	This study
pREP42X-mCherry	This study
pREP42X-mCherry-BsMTS	This study

Supplementary Table 3. List of primers used in this study.

Name	Sequence 5' to 3'
BR64	CTTGACAGCTCGTCCATGCC
BR223	GTAAATCATACCTCGAGGGATCCACCATGAGCAAAGGAGAAGAACTTTTCAC
BR224	GACATTCCTTTTACCCGGGGATCCTTATCCTCCGAACAAGCGTTTGAG
BR225	GTAAATCATACCTCGAGGGATCCACCATGGCATTACTCGATTTCTTCTCTCG
BR226	GACATTCCTTTTACCCGGGGATCCTTATTTAGCTCTTCTGCTCCGGTAAG
BR227	GTAAATCATACCTCGAGGGATCCACCATGGTGAGCAAGGGCGAG
BR228	GACATTCCTTTTACCCGGGGATCCTTAAGAACAACACCGAAGAAAGATTTG
BR229	GATAATAATGGTTTCTTAGACGTGTCGATCGACTCTAGAGGATCAGAAAATTATC
BR230	GAAAAGTGCCACCTGACGTGCATTACTAATAGAAAGGATTATTTCACTTCTAATTACACAAATCCG
KN_294	CAGAAACGCTGGTAAAAGTAAAA
KN_312	TTTTACTTTTACCAGCGTTTCTG
KN_644	GCATGGACGAGCTGTACAAGTAAGGATCCCCGGGTAAAAGGAATGTC
KN_645	TTCCTTTTACCCGGGGATCCCCGAAGCTTTTATCCTCCGAACA
KN_646	GGATCCCCGGGTAAAAGGAATGTC
KN_647	GATCCCTCGAGGTATGATTTAAC

Supplementary Methods

Generation of plasmids

DNA fragments and vector backbones were amplified by PCR or obtained by restriction enzyme digestion so that they contained 15-20 bp overlaps between adjacent fragments that were combined using the GeneArt Seamless Cloning and Assembly Enzyme Mix (Thermo Fisher Scientific, Waltham, USA). pREP41X-sfGFP-MinD encodes the *E. coli* MinD with an N-terminal fusion of sfGFP, where the sfGFP-MinD coding region was amplified from pMBL-sfGFP-MinDMinE⁴¹ (primer BR223/BR224) and the backbone was obtained by digesting pREP41X with BamHI. pREP42X-MinE encodes the *E. coli* MinE, where the MinE coding region was amplified from pMBL-sfGFP-MinDMinE⁴¹ (primer BR225/BR226) and the backbone was obtained by digesting pREP42X with BamHI. pREP41X_coex_sfGFP-MinD_MinE encodes sfGFP-MinD and MinE under the same promoter that is duplicated on the plasmid. It was generated by amplifying the backbone from pREP41X-sfGFP-MinD (primer KN_646/KN_647) and the MinE fragment from pREP42X-MinE (primer R229/BR230). pREP42X-mCherry-BsMTS encodes the C-terminal fusion of the *B. subtilis* MinD membrane targeting sequence (MTS) (GSGKGMMMAKIKSFFGVRS; AA 254-268) to mCherry, where the mCherry- BsMTS coding region was amplified from plasmid pET28a-mCherry-GGBSMTS² (primer BR227/BR228) and the backbone was obtained by digesting pREP42X with BamHI. pREP42X-mCherry encodes mCherry and was obtained by amplifying two regions from pREP42X-mCherry-BsMTS (primer KN_294/BR64, KN_312/KN_644). pREP42X-mCherry-2xEcMTS encodes the C-terminal fusion of two copies of the *E. coli* MinD MTS (GSGIEEEKKGLKRLFGGGGSIEEEKKGLKRLFGG; AA 256–270) to mCherry and was obtained by amplifying two regions from pREP42X-mCherry-BsMTS (primer KN_294/KN_647, KN_312/KN_646) and the insert was amplified from pET28a-mCherry-2xEcMTS² (primer KN_645/BR227).

S. pombe culture and transformation

YES media was prepared from yeast extract (5 g/l), glucose (30 g/l) and adenine, histidine, leucine, uracil and lysine (each 225 mg/l). Selective medium was prepared from EMM broth (Formedium, Norfolk, Great Britain) supplemented with adenine, histidine, leucine, uracil and lysine (each 225 mg/l) from which either leucine, uracil or both were omitted for selection of *S. pombe* carrying pREP41X, pREP42X or both plasmids, respectively. Solid medium was prepared with 2% Difco Bacto Agar.

For transformation a 5 ml YES media pre-culture was inoculated with FY61 and grown at 30 °C, 220 rpm for 16 h. A 50 ml YES culture was inoculated 1:200 from the pre-culture and grown at 30 °C, 220 rpm for 30-48 h until an OD600 of 0.5. Cells were pelleted by centrifugation (4 °C, 4000 g, 10 min) and washed once with 25 ml 1x TE buffer (10 mM Tris-HCl pH 7.5, 1 mM EDTA). After another centrifugation step, cells were resuspended in 1 ml LiAc/1xTE buffer (10 mM Tris-HCl pH 7.5, 1 mM EDTA, 100 mM Lithium Acetate pH 7.5) and incubated for 30 min at 30 °C. 200 µl of the suspension was transferred into a new tube and mixed with 20 µl of sonicated salmon sperm DNA (10 mg/ml, Agilent Technologies, Santa Clara, USA) as carrier and 1 µg plasmid, and subsequently incubated at room temperature for 10 min. Afterwards 1.2 ml of PEG/LiAc/TE buffer was added (40% PEG4000, 10 mM Tris-HCl pH 7.5, 1 mM EDTA, 100 mM Lithium Acetate pH 7.5) and the mixture was incubated for 3 min at 30 °C, 250 rpm. DMSO was added to a final concentration of 5%, before heatshock for 15 min at 42 °C. Cells were pelleted at 7000 g for 30 s, resuspended with 300 µl 1xTE buffer and spread on plates with the respective selective medium. After 3-5 days of incubation at 30 °C colonies were picked and restriking. Individual clones were picked and grown in selective medium to generate glycerol stocks (50% glycerol).

Supplementary Notes

Supplementary Note 1:

The lower facet of the 8 nm high DNA origami rod is located about 5-11 nm above the membrane, as it is bound to the membrane via several spacers: the dsDNA oligonucleotide linker, a TEG-biotin moiety and the streptavidin molecule. The length of the dsDNA linker can be estimated to about 6.1 nm taking into account the rise per basepair (bp) of 0.34 nm of B-DNA⁴³. The oligonucleotide is connected to the anchoring biotin moiety via TEG with a length of about 1.4 nm¹⁸. Thus, the total linker length can be estimated to be about 7 nm. As the persistence length of dsDNA is about 50 nm⁴³⁻⁴⁵, the dsDNA linker is rigid. However, the connection to the DNA origami is only single stranded giving the dsDNA linkers freedom for bending⁴⁶. The height of membrane-bound streptavidin was measured to be ~4 nm⁴⁷ in good agreement with measurements from EM/crystal structures^{48,49}.

Supplementary Note 2:

To verify that it is indeed the effective cargo size (membrane footprint) rather than the number of membrane attachment sites (streptavidin building blocks), i.e. the membrane diffusion (Fig. 3c in the main text), that determines the extent of the cargo transport, we employed an alternative anchoring strategy for the DNA origami structures. The resulting cargo (cargo-chol) only consists of the DNA origami scaffold, in which we incorporated oligonucleotides at the bottom positions that could hybridize with oligonucleotides modified with a TEG-cholesteryl moiety that directly inserts into the lipid bilayer (Extended Data Fig. 4). As in the case for the composite cargo (consisting of a DNA origami scaffold and streptavidin building blocks) the total length of the linker is about 7 nm (6.1 nm dsDNA, 1.4 nm TEG moiety) and the connection of the linker to the DNA origami is single-stranded giving it freedom for bending. Hence, in this case the lower facet of the origami scaffold is located at an altitude of at most 7 nm above the membrane and thus the origami body can presumably directly interact with MinDE on the membrane. Increasing the number of attachment sites on cargo-chol from 2 to 15 (cargo-chol-2 and cargo-chol-15) slowed diffusion in absence of MinDE similar to our observations for the composite cargo (Extended Data Fig. 5a) and in line with previous studies on membrane diffusion of DNA origami nanostructures^{18,46,50,51}. Cargo-chol-2 and cargo-chol-15 diffused slightly faster than the respective composite cargoes cargo-2 and cargo-42, which can presumably be explained by streptavidin binding 2-3 biotinylated lipids³. In the presence

48

of 1 μM MinD, both cargo-chol-2 and cargo-chol-15 are slowed similar to the composite cargoes, which indicates that they experience an additional friction due to the presence of MinD (Extended Data Fig. 5a). In contrast to the composite cargo, increasing the number of attachment sites on cargo-chol also strongly increased their ability to bind to the membrane (Extended Data Fig. 5e) as previously observed for cholesteryl-bound DNA origami nanostructures^{46,50}. To account for these different membrane densities, we analysed the redistribution of cargo-chol-2 and cargo-chol-15 by MinDE at three different concentrations, determining the contrast of the resulting images and the interaction parameter (Extended Data Figs. 4b, 5b-d,h). While increasing membrane densities of cargo-chol-2 and cargo-chol-15 were accompanied by increasing contrast, it is clear that even at the lowest densities of cargo-chol-2 the contrast is higher than that of cargo-2 which diffuses similarly fast as cargo-chol2 (Extended Data Fig. 5g). At the highest membrane densities, the contrast of cargo-chol-2 and cargo-chol-15 rather resembles that of cargo-42. By fitting the 2D histograms of the images, we determined the interaction parameters of cargo-chol-2 and cargo-chol-15 (Extended Data Fig. 5h). The interaction parameter of cargo-chol-15 is slightly larger than that of cargo-chol-2, but both are on the same order of magnitude as that of cargo-42. When we let MinDE self-organize in the presence of differently labelled cargo-chol-2 and cargo-chol-15, we found that MinDE also induced sorting of these two cargo molecules. Similar to the composite cargoes, we found that the cargo with the higher interaction parameter, cargo-chol-15 was localized to MinD-free regions and was framed by cargo-chol-2 (Extended Data Fig. 5i). Importantly, that cargo-chol-2, which diffuses similar or even slightly faster than cargo-2 and one order of magnitude faster than cargo-42, interacts with MinD to a similar extent as cargo-42 shows that indeed the effective size of the cargo molecules determines the extent of the transport: the membrane footprint and thus the effective size of cargo-chol-2 is larger because presumably the entire origami scaffold with a membrane footprint of 1760 nm^2 ($110\text{ nm} \times 16\text{ nm}$) interacts with MinD, whereas in the case of cargo-2 and cargo-42 mostly the streptavidin building blocks (membrane footprint of a single streptavidin: 25 nm^2) interact with MinD (total membrane footprint of cargo-2: 50 nm^2 , cargo-42: 1050 nm^2).

Supplementary Note 3:

Since we have demonstrated MinDE-induced cargo transport with experiment and theory, we wondered whether it is possible to directly observe biased cargo motion on a single cargo level

using single particle tracking. To this end we tracked single cargo molecules under conditions where regular unidirectional MinDE waves had formed (Extended Data Fig. 8). As in our simplified single-particle tracking setup (i.e. with a homogeneous density of MinD, Fig. 3c in the main text, Extended Data Fig. 5a), we found that particles seemed to diffuse faster when located inside the MinD minima, i.e. in regions with low MinD density, and slower in the MinD maxima. However, we could not detect any directed motion. To confirm these experimental results, we made a simple theoretical estimate whether it would be possible to discern diffusion from advection in a system such as ours.

In the following, we specifically refer to our experimental realization where MinDE form traveling waves, because a stationary state with vanishing fluxes (while having the advantage of simplifying our analysis) only allows to reliably measure the stationary distribution of particles. In our experiments we have a true single particle tracking situation, i.e. a very low density of DNA origami molecules that do not interact with each other. In a situation with traveling waves, the MinDE gradients have a typical length scale of 40 μm (Supplementary Fig. S4). The waves themselves travel at a velocity of 1.4 $\mu\text{m s}^{-1}$ and consist of both a forward-pointing and a backward-pointing gradient. Therefore, each cargo molecule is subjected to a forward-pointing MinD gradient over a typical time scale of $\Delta t = 30$ s per wave period, alternated with a backward-pointing gradient.

For single particles, the mean squared displacement due to diffusion in 2D is given by $2D_g\Delta t$, and due to advection is given by $(v_g\Delta t)^2$. The typical diffusion constant of cargo-42 in our experiments is $D_{g-42} = 0.06 \mu\text{m}^2\text{s}^{-1}$, while the typical diffusion constant of cargo-2 is $D_{g-2} = 0.65 \mu\text{m}^2\text{s}^{-1}$. Next, we will estimate the advection velocity v_g . Starting from Eq. (7) in the main text,

$$\partial_t c_g = -\nabla \cdot \mathbf{j}_g = \nabla \cdot \left[D_g \frac{(1 + c_g/c_x) \nabla c_g + (c_g/c_x) \nabla c_p}{1 + c_g/c_x + (D_g/D_p)(c_p/c_x)} \right], \quad \left(\begin{array}{l} \text{S47} \\ \text{7 in main text} \end{array} \right)$$

we invoke the low-density limit (true single particle tracking situation). With this simplification, we obtain the following equation for the cargo flux:

$$\mathbf{j}_g = -D_g \nabla c_g - c_g D_g c_x^{-1} \nabla c_p \equiv -D_g \nabla c_g + c_g v_g, \quad (\text{S48})$$

where the *interaction density* is given by $c_x = \xi_p/\zeta_{pg}$. The first term of Eq. (S48) corresponds to diffusion and the second term corresponds to advection with an advection velocity of $v_g =$

50

$-D_g c_x^{-1} \nabla c_p$. By expressing surface densities in terms of coverage, $\theta_p = a_p c_p$ and $\theta_x = a_p c_x$, we may thus write the advection velocity as:

$$v_g = -D_g \theta_x^{-1} \nabla \theta_g. \quad (\text{S49})$$

The typical effective interaction parameter is $\theta_{x-2}^{-1} \sim 5.6$ for cargo-2 and $\theta_{x-42}^{-1} \sim 21.4$ for cargo-42, as obtained from our fits (Fig. 3b in the main text). Overall, the MinD coverage is between 16.5% in the MinD maxima and 0% in the MinD minima. Thus, we may estimate the typical gradient of MinD coverage as $\|\nabla \theta_p\| \approx 0.165/(20\mu\text{m}) = 0.00825 \mu\text{m}^{-1}$. Taken together, these estimates yield a typical advection velocity of $v_{g-2} \approx 0.030 \mu\text{m s}^{-1}$ for cargo-2 and $v_{g-42} \approx 0.011 \mu\text{m s}^{-1}$ for cargo-42. Then, the dimensionless number

$$\frac{v_g \Delta t}{(2D_g \Delta t)^{1/2}} \approx 0.14 \text{ for cargo-2, } 0.17 \text{ for cargo-42}$$

informs us that diffusive transport is stronger than advective transport on the scale of a single molecule. We can also make analogous estimates for cargo-cho1-2 ($D_{g-c2} = 0.89 \mu\text{m}^2\text{s}^{-1}$, $\theta_{x-c2}^{-1} = 21.7$) and cargo-cho1-5 ($D_{g-c15} = 0.24 \mu\text{m}^2\text{s}^{-1}$, $\theta_{x-c15}^{-1} = 24.7$), yielding dimensionless numbers of 0.65 and 0.39, respectively.

Consequently, it is difficult to discern advection from diffusion on the single molecule level. Even if we assume that the true interaction parameter is one order of magnitude larger (because we typically underfit the interaction parameters due to neglecting large particle densities), this still only yields a dimensionless factor of order unity. Combined with the back-and-forth motion of cargo due to the periodic nature of the MinDE waves, this would still make a distinction between advection and diffusion difficult.

Supplementary Note 4:

MinDE self-organization *in vitro* generally reproduces all features of their behaviour *in vivo*⁵², except that the patterns *in vitro* occur on an about 10 times larger length scale than those *in vivo*^{1,39,52-55}. This difference is thought to arise from differences in the physico-chemical properties of the reaction environment. For example, crowding in solution has been shown to reduce the wavelength *in vitro*^{39,56,57}. Similarly, we have shown here (Fig. 1g in the main text) and previously² that crowding on the membrane reduces the length scale of the patterns *in vitro*. In order to test whether the difference in wavelength between *in vitro* and *in vivo* is

indeed caused by differences in the reaction environment, and whether MinDE patterns with a short wavelength would be able to regulate other proteins by diffusiophoresis under these more physiologically relevant conditions, we expressed MinDE as well as model peripheral membrane proteins² heterologously in the fission yeast *S. pombe*. In the, from *E. coli* evolutionary distant, fission yeast, other proteins can be seen as close to inert in regard to *E. coli* MinDE and the larger size and higher protein levels in *S. pombe* facilitate detection of protein dynamics by fluorescence microscopy.

Adapting a co-expression from Terbush *et al.*⁵⁸ we first designed a plasmid for co-expression of *E. coli* sfGFP-MinD and MinE under the same, duplicated promoter (Extended Data Fig. 9a). *S. pombe* cells harbouring this plasmid displayed bright foci that were dynamic. Closer inspection revealed that MinD seemed to preferentially bind to intracellular membranes over the plasma membrane. The round vesicular structures stained by MinD most likely represent vacuoles⁵⁹. Most cells displayed traveling wave dynamics (Extended Data Fig. 9b), but also more complex dynamics and pole-to-pole oscillations could be observed (Extended Data Fig. 9c,d). In contrast, in regular sized *E. coli* MinDE usually perform pole-to-pole oscillations^{54,60}, in elongated *E. coli* they exhibit multi-node standing waves⁵⁴ and only in very rare cases traveling waves can be observed⁶¹. This deviation can be explained with the well-described geometry sensitivity of MinDE^{56,62-65} and the larger dimensions of an *S. pombe* cell compared to *E. coli* (*S. pombe*: 3.5 μm x 8-14 μm ⁶⁶; *E. coli*: 0.7-1 μm x 2.6-4.0 μm ⁶⁷): in *E. coli* cells whose shape was greatly altered by mutations or custom shaping in microstructures, traveling waves and complex dynamics can also be observed⁶³⁻⁶⁵. Analysis of cells exhibiting traveling wave dynamics, allowed us to obtain an estimate of the wavelength and velocity of the MinDE dynamics in *S. pombe*. Intriguingly, the wavelength of MinDE dynamics in *S. pombe* of (8.3 \pm 1.7) μm (Extended Data Fig. 9e) was similar to the wavelength that has been reported for MinDE dynamics in *E. coli* of about 8-11 μm ^{52,54,55} and thus much smaller than the wavelength of MinDE self-organization *in vitro*^{1,2,39}. The obtained velocity of (0.06 \pm 0.02) $\mu\text{m s}^{-1}$ (Extended Data Fig. 9f) is lower than the values that have been reported for wave propagation on SLBs *in vitro* of about 0.1-0.6 $\mu\text{m s}^{-1}$ ^{1,2,39,53}. The estimated oscillation period obtained from these values is about 140 s and thus slightly larger than the one reported for the dynamics in *E. coli* of about 40-120 s^{52,54,63,68} which could be caused by differences in temperature, protein levels, density of anionic lipids, which are all factors reported to influence the velocity of wave propagation *in vivo* or *in vitro*⁵².

As a control that the observed dynamics were indeed ascribable to MinDE self-organization, we expressed sfGFP-MinD in the absence of MinE in *S. pombe* (Extended Data Fig. 9g). As expected, sfGFP-MinD seemed to localize to the same intracellular membranes, but the overall distribution was far more homogenous and showed no obvious dynamics. Thus, MinDE self-organization can be reconstituted in the fission yeast *S. pombe*. Having shown that MinDE self-organize in *S. pombe* at a similar length scale as in their native host *E. coli*, we set out to show that MinDE can also regulate other proteins via diffusiophoresis under these physiologically more relevant conditions. To this end we constructed a second expression plasmid, that could be maintained in *S. pombe* next to the co-expression plasmid for sfGFP-MinD/MinE. For simplicity, we employed model peripheral proteins as cargo. We have previously shown that these proteins are also regulated by MinDE *in vitro*²: whenever MinD density was high, the density of the model peripheral membrane proteins was low. While these proteins have a much shorter membrane dwell time than the DNA origami nanostructures and thus are not subject to a net transport by MinDE², we believe that they also experience diffusiophoretic transport resulting in their redistribution. For expression in *S. pombe*, we generated plasmids encoding one of three different mCherry versions analogous to the ones used for the *in vitro* study²: soluble mCherry (mCh), mCherry fused to the membrane targeting sequence (MTS) of the *B. subtilis* MinD (mCh-MTS(BsD)) and mCherry fused to a tandem repeat of the MTS of the *E. coli* MinD itself (mCh-MTS(2xMinD)) (Extended Data Fig. 10a). When expressed in *S. pombe* in the absence of MinDE, mCh-MTS(BsD) and mCh-MTS(2xMinD) homogeneously bound to cellular membranes (Extended Data Fig. 10c,d) and the soluble mCh exhibited a homogenous cytoplasmic localization (Extended Data Fig. 10b). When co-expressed with sfGFP-MinDE, the overall localization of all constructs was similar. Intriguingly, however, we found that wherever fluorescence intensity of MinDE was high, the intensity of mCh-MTS(BsD) and mCh-MTS(2xMinD) was reduced and vice versa (Extended Data Fig. 10f,g). In contrast, when MinDE was co-expressed with the soluble control protein mCh, no such changes in fluorescence intensity were observed (Extended Data Fig. 10e). Hence, MinDE-dependent transport of proteins by diffusiophoresis also occurs, when MinDE dynamics are reconstituted in *S. pombe*.

Supplementary References

1. Loose, M., Fischer-Friedrich, E., Herold, C., Kruse, K. & Schwille, P. Min protein patterns emerge from rapid rebinding and membrane interaction of MinE. *Nat. Struct. Mol. Biol.* **18**, 577–583 (2011).
2. Ramm, B. *et al.* The MinDE system is a generic spatial cue for membrane protein distribution in vitro. *Nat. Commun.* **9**, 3942 (2018).
3. Dubacheva, G. V. *et al.* Controlling Multivalent Binding through Surface Chemistry: Model Study on Streptavidin. *J. Am. Chem. Soc.* **139**, 4157–4167 (2017).
4. Flory, P. J. Thermodynamics of High Polymer Solutions. *J. Chem. Phys.* **10**, 51–61 (1942).
5. Huggins, M. L. Solutions of Long Chain Compounds. *J. Chem. Phys.* **9**, 440 (1941).
6. de Gennes, P.-G. *Scaling concepts in polymer physics*. (Cornell University Press, 1979).
7. Miyagi, A., Ramm, B., Schwille, P. & Scheuring, S. High-speed AFM reveals the inner workings of the MinDE protein oscillator. *Nano Lett.* **18**, 288–296 (2018).
8. Halatek, J. & Frey, E. Highly Canalized MinD Transfer and MinE Sequestration Explain the Origin of Robust MinCDE-Protein Dynamics. *Cell Rep.* **1**, 741–752 (2012).
9. Halatek, J. & Frey, E. Rethinking pattern formation in reaction-diffusion systems. *Nat. Phys.* **14**, 507–514 (2018).
10. Halatek, J., Brauns, F. & Frey, E. Self-organization principles of intracellular pattern formation. *Philos. Trans. R. Soc. B Biol. Sci.* **373**, 20170107 (2018).
11. Brauns, F., Halatek, J. & Frey, E. Phase-space geometry of reaction-diffusion dynamics. *arXiv* 1812.08684v1 <http://arxiv.org/abs/1812.08684> (2018).
12. Balian, R. *From Microphysics to Macrophysics*. (Springer, Berlin, Heidelberg, 2007). doi:10.1007/978-3-540-45480-9.
13. Derjaguin, B. V., Sidorenkov, G. P., Zubashchenko, E. A. & Kiseleva, E. V. Kinetic phenomena in boundary films of liquids. *Kolloidn. Zh* **9**, 335–347 (1947).
14. Maxwell, J. C. IV. On the dynamical theory of gases. *Philos. Trans. R. Soc. London* **157**, 49–88 (1866).

-
15. Stefan, J. Über das Gleichgewicht und die Bewegung, insbesondere die Diffusion von Gasgemengen. *Sitzber. Akad. Wiss. Wien* **63**, 63–124 (1871).
 16. Duncan, J. B. & Toor, H. L. An experimental study of three component gas diffusion. *AIChE J.* **8**, 38–41 (1962).
 17. Krishna, R. & Wesselingh, J. A. The Maxwell-Stefan approach to mass transfer. *Chem. Eng. Sci.* **52**, 861–911 (1997).
 18. Czogalla, A., Kauert, D. J., Seidel, R., Schwille, P. & Petrov, E. P. DNA origami nanoneedles on freestanding lipid membranes as a tool to observe isotropic-nematic transition in two dimensions. *Nano Lett.* **15**, 649–655 (2015).
 19. Shih, Y.-L. *et al.* Active Transport of Membrane Components by Self-Organization of the Min Proteins. *Biophys. J.* **116**, 1469–1482 (2019).
 20. Asakura, S. & Oosawa, F. On interaction between two bodies immersed in a solution of macromolecules. *J. Chem. Phys.* **22**, 1255–1256 (1954).
 21. Sahimi, M. *Applications of percolation theory*. (Taylor & Francis, London, 1995).
 22. Anderson, J. L., Lowell, M. E. & Prieve, D. C. Motion of a particle generated by chemical gradients Part 1. Non-electrolytes. *J. Fluid Mech.* **117**, 107–121 (1982).
 23. Prieve, D. C., Anderson, J. L. & Lowell, M. E. Motion of a particle generated by chemical gradients Part 2. Electrolytes. *J. Fluid Mech.* **148**, 247–269 (1984).
 24. Sear, R. P. Diffusiophoresis in Cells: A General Nonequilibrium, Nonmotor Mechanism for the Metabolism-Dependent Transport of Particles in Cells. *Phys. Rev. Lett.* **122**, 128101 (2019).
 25. Shi, N., Nery-Azevedo, R., Abdel-Fattah, A. I. & Squires, T. M. Diffusiophoretic Focusing of Suspended Colloids. *Phys. Rev. Lett.* **117**, 258001 (2016).
 26. Shin, S. *et al.* Size-dependent control of colloid transport via solute gradients in dead-end channels. *Proc. Natl. Acad. Sci. U. S. A.* **113**, 257–261 (2016).
 27. Nasouri, B. & Golestanian, R. Exact Phoretic Interaction of Two Chemically Active Particles. *Phys. Rev. Lett.* **124**, 168003 (2020).

-
28. Illien, P., Golestanian, R. & Sen, A. 'Fuelled' motion: Phoretic motility and collective behaviour of active colloids. *Chem. Soc. Rev.* **46**, 5508–5518 (2017).
 29. Abécassis, B., Cottin-Bizonne, C., Ybert, C., Ajdari, A. & Bocquet, L. Boosting migration of large particles by solute contrasts. *Nat. Mater.* **7**, 785–789 (2008).
 30. Palacci, J., Abécassis, B., Cottin-Bizonne, C., Ybert, C. & Bocquet, L. Colloidal motility and pattern formation under rectified diffusiophoresis. *Phys. Rev. Lett.* **104**, 138302 (2010).
 31. Marbach, S. & Bocquet, L. Osmosis, from molecular insights to large-scale applications. *Chem. Soc. Rev.* **48**, 3102–3144 (2019).
 32. Golestanian, R. Phoretic Active Matter. *arXiv* 1909.03747v3 <http://arxiv.org/abs/1909.03747> (2019).
 33. Agudo-Canalejo, J., Illien, P. & Golestanian, R. Phoresis and Enhanced Diffusion Compete in Enzyme Chemotaxis. *Nano Lett.* **18**, 2711–2717 (2018).
 34. Paustian, J. S. *et al.* Direct measurements of colloidal solvophoresis under imposed solvent and solute gradients. *Langmuir* **31**, 4402–4410 (2015).
 35. Prieve, D. C., Malone, S. M., Khair, A. S., Stout, R. F. & Kanj, M. Y. Diffusiophoresis of charged colloidal particles in the limit of very high salinity. *Proc. Natl. Acad. Sci. U. S. A.* **116**, 18257–18262 (2019).
 36. Bocquet, L. & Charlaix, E. Nanofluidics, from bulk to interfaces. *Chem. Soc. Rev.* **39**, 1073–1095 (2010).
 37. Kestin, J., Sokolov, M. & Wakeham, W. A. Viscosity of Liquid Water in the Range -8 °C to 150 °C. *J. Phys. Chem. Ref. Data* **7**, 941–948 (1978).
 38. Brilliantov, N. V. & Poeschel, T. *Kinetic Theory of Granular Gases*. (Oxford University Press, 2004).
 39. Loose, M., Fischer-Friedrich, E., Ries, J., Kruse, K. & Schwille, P. Spatial regulators for bacterial cell division self-organize into surface waves in vitro. *Science* **320**, 789–792 (2008).
 40. Zieske, K., Schweizer, J. & Schwille, P. Surface topology assisted alignment of Min protein waves. *FEBS Lett.* **588**, 2545–2549 (2014).

-
41. Glock, P. *et al.* Stationary patterns in a two-protein reaction-diffusion system. *ACS Synth. Biol.* **8**, 148–157 (2019).
 42. Forsburg, S. L. Comparison of *Schizosaccharomyces pombe* expression systems. *Nucleic Acids Res.* **21**, 2955–2956 (1993).
 43. Bloomfield, V. A., Crothers, D. M. & Tinoco, J. I. *Nucleic Acids: Structures, Properties, and Functions*. University Science Books (2000). doi:10.1007/s00897000456a.
 44. Rivetti, C., Guthold, M. & Bustamante, C. Scanning force microscopy of DNA deposited onto mica: Equilibration versus kinetic trapping studied by statistical polymer chain analysis. *J. Mol. Biol.* **264**, 919–932 (1996).
 45. Smith, S. B., Cui, Y. & Bustamante, C. Overstretching B-DNA: The elastic response of individual double-stranded and single-stranded DNA molecules. *Science* **271**, 795–799 (1996).
 46. Khmelinskaia, A., Mücksch, J., Petrov, E. P., Franquelim, H. G. & Schwille, P. Control of Membrane Binding and Diffusion of Cholesteryl-Modified DNA Origami Nanostructures by DNA Spacers. *Langmuir* **34**, 14921–14931 (2018).
 47. Scheuring, S., Müller, D. J., Ringler, P., Heymann, J. B. & Engel, A. Imaging streptavidin 2D crystals on biotinylated lipid monolayers at high resolution with the atomic force microscope. *J. Microsc.* **193**, 28–35 (1999).
 48. Weber, P. C., Ohlendorf, D. H., Wendoloski, J. J. & Salemme, F. R. Structural Origins of High-Affinity Biotin Binding. *Science* **243**, 85–88 (1989).
 49. Fan, X. *et al.* Single particle cryo-EM reconstruction of 52 kDa streptavidin at 3.2 Angstrom resolution. *Nat. Commun.* **10**, 2386 (2019).
 50. Khmelinskaia, A., Franquelim, H. G., Petrov, E. P. & Schwille, P. Effect of anchor positioning on binding and diffusion of elongated 3D DNA nanostructures on lipid membranes. *J. Phys. D: Appl. Phys.* **49**, 194001 (2016).
 51. Kocabey, S. *et al.* Membrane-Assisted Growth of DNA Origami Nanostructure Arrays. *ACS Nano* **9**, 3530–3539 (2015).
 52. Ramm, B., Heermann, T. & Schwille, P. The *E. coli* MinCDE system in the regulation of

-
- protein patterns and gradients. *Cell. Mol. Life Sci.* **76**, 4245–4273 (2019).
53. Vecchiarelli, A. G., Li, M., Mizuuchi, M. & Mizuuchi, K. Differential affinities of MinD and MinE to anionic phospholipid influence Min patterning dynamics in vitro. *Mol. Microbiol.* **93**, 453–463 (2014).
 54. Raskin, D. M. & de Boer, P. A. J. Rapid pole-to-pole oscillation of a protein required for directing division to the middle of Escherichia coli. *Proc. Natl. Acad. Sci. U. S. A.* **96**, 4971–4976 (1999).
 55. Touhami, A., Jericho, M. & Rutenberg, A. D. Temperature dependence of minD oscillation in Escherichia coli: Running hot and fast. *J. Bacteriol.* **188**, 7661–7667 (2006).
 56. Schweizer, J. *et al.* Geometry sensing by self-organized protein patterns. *Proc. Natl. Acad. Sci. U. S. A.* **109**, 15283–15288 (2012).
 57. Martos, A. *et al.* FtsZ Polymers Tethered to the Membrane by ZipA Are Susceptible to Spatial Regulation by Min Waves. *Biophys. J.* **108**, 2371–2383 (2015).
 58. Terbush, A. D., Porzondek, C. A. & Osteryoung, K. W. Functional analysis of the chloroplast division complex using schizosaccharomyces pombe as a heterologous expression system. *Microsc. Microanal.* **22**, 275–289 (2016).
 59. Takegawa, K. *et al.* Vesicle-mediated protein transport pathways to the vacuole in Schizosaccharomyces pombe. *Cell Struct. Funct.* **28**, 399–417 (2003).
 60. Hu, Z. & Lutkenhaus, J. Topological regulation of cell division in Escherichia coli involves rapid pole to pole oscillation of the division inhibitor MinC under the control of MinD and MinE. *Mol. Microbiol.* **34**, 82–90 (1999).
 61. Bonny, M., Fischer-Friedrich, E., Loose, M., Schwille, P. & Kruse, K. Membrane Binding of MinE Allows for a Comprehensive Description of Min-Protein Pattern Formation. *PLoS Comput. Biol.* **9**, e1003347 (2013).
 62. Zieske, K. & Schwille, P. Reconstitution of pole-to-pole oscillations of min proteins in microengineered polydimethylsiloxane compartments. *Angew. Chemie Int. Ed.* **52**, 459–462 (2013).
 63. Wu, F., van Schie, B. G. C., Keymer, J. E. & Dekker, C. Symmetry and scale orient Min

-
- protein patterns in shaped bacterial sculptures. *Nat. Nanotechnol.* **10**, 719–726 (2015).
64. Corbin, B. D., Yu, X. & Margolin, W. Exploring intracellular space: function of the Min system in round-shaped *Escherichia coli*. *Embo J.* **21**, 1198–2008 (2008).
65. Männik, J. *et al.* Robustness and accuracy of cell division in *Escherichia coli* in diverse cell shapes. *Proc. Natl. Acad. Sci.* **109**, 6957–6962 (2012).
66. Fantes, P. A. Control of cell size and cycle time in *Schizosaccharomyces pombe*. *J. Cell Sci.* **24**, 51–67 (1977).
67. Zaritsky, A. & Woldringh, C. L. Chromosome replication rate and cell shape in *Escherichia coli*: Lack of coupling. *J. Bacteriol.* **135**, 581–587 (1978).
68. Raskin, D. M. & De Boer, P. A. J. MinDE-Dependent Pole-to-Pole Oscillation of Division Inhibitor MinC in *Escherichia coli*. *J. Bacteriol.* **181**, 6419–6424 (1999).
69. Meurer, A. *et al.* SymPy: symbolic computing in Python. *PeerJ Comput. Sci.* **3**, e103 (2017).
70. Block, S. Brownian Motion at Lipid Membranes: A Comparison of Hydrodynamic Models Describing and Experiments Quantifying Diffusion within Lipid Bilayers. *Biomolecules* **8**, 30 (2018).
71. National Center for Biotechnology Information. PubChem Database. CID=10350317, https://pubchem.ncbi.nlm.nih.gov/compound/1_2-Dioleoyl-sn-Glycero-3-Phosphocholine (accessed on July 22, 2020).

A.2 Appendix to Section 6.4

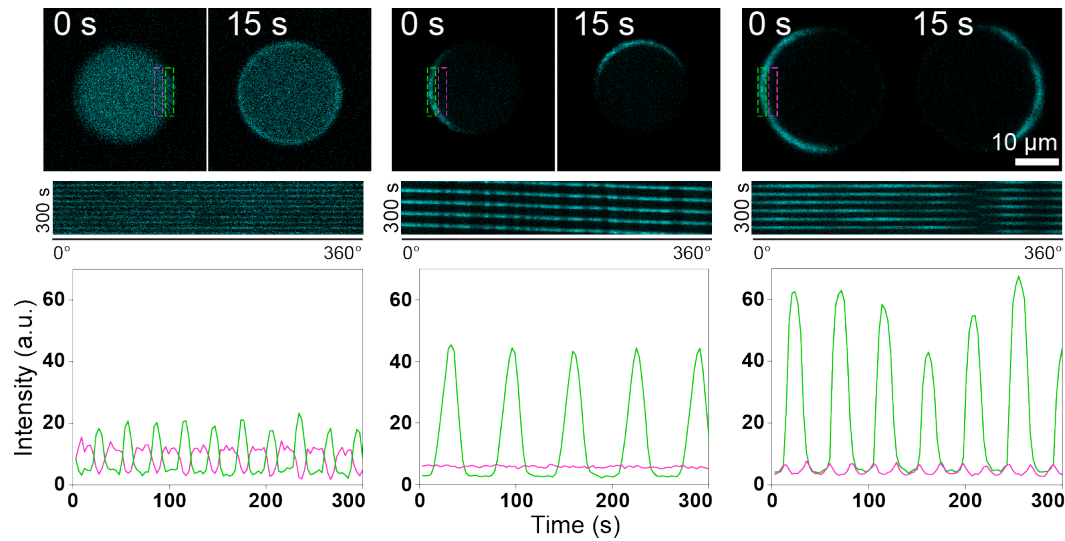


Figure A.2. Encapsulation of MinDE inside droplets. MinDE displayed pulsing, pole-to-pole and travelling oscillations. Kymographs were taken along the droplet perimeter, and intensity traces from the indicated ROI in the coloured boxes. MinD 1 μM (30 % EGFP-MinD), MinE 0.5 μM .

A.3 Appendix to Chapter 9

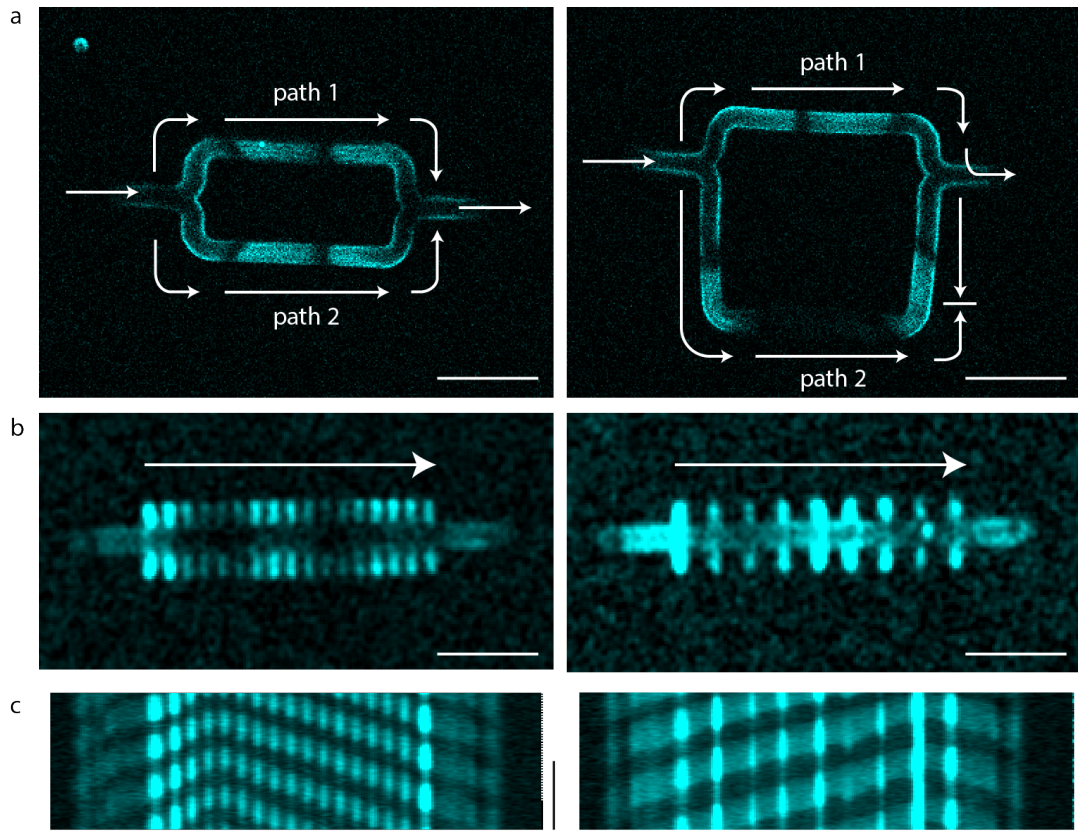


Figure A.3. MinDE waves on 3D waveguides. a) Min waves travelling on rods that bifurcate into 2 different paths. Waves travelling on 2 paths with the same path length join back up in phase (left). Waves travelling on different path lengths annihilate at a point where 2 path lengths are the same. b) Rods with a row of concentric discs and c) their associated kymographs. MinD 1 μM , His-MinE 1 μM , ATP 2.5 mM.

A.4 General contribution to the public

I insert an article written by Violet van Houwelingen based on an interview conducted by her on my views on recent developments in 3D bioprinting. This was published on the Synthetic Cell Initiative website (syntheticcell.eu) for the readership of the general public.

[syntheticcell.eu](https://www.syntheticcell.eu)

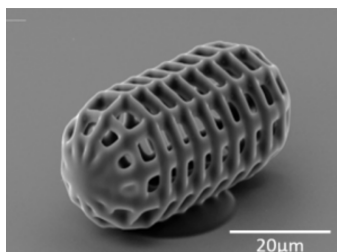
Designing minimal cells with 3D bioprinting - Synthetic Cell

4-5 minutes

The ability of three dimensional printers of biomaterials – 3D bioprinters – to mimic cells on the microscale makes this technique an attractive starting point for constructing minimal cells from the bottom-up. Hiromune Eto makes use of a two-photon laser printer to create hydrogel protein structures. Since these bio-printed materials are proteins themselves, a specific 3D shape can trigger or enhance responses from the cell's own proteins. Mr. Eto tells us more about his work with bioprinting, which was published in the journal [Small](#):

How does 3D-bioprinting work?

“By applying 3D-bioprinting to synthetic biology, we can print much more complex structures than has been possible before. Up until now researchers have shaped biological material using two-dimensional fabrication methods, which limits what we can create. We could merely “pull up” 2D shapes, such as a circle or a square, and produce an “extruded” shape like a cylinder or a cuboid. Now, with 3D-printing, our team can better mimic cellular features that are relevant to the proteins we study. This means we can influence different functions in the cell, like metabolism and the transport of materials.”

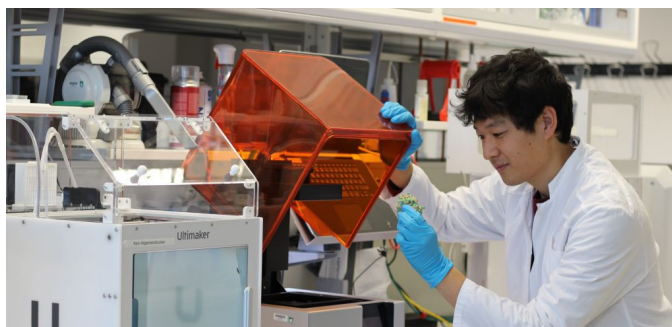


“We print structures or shapes in three dimensions on a microscopic scale or smaller, similar to the size of a cell. For this we use a protein mixture of bovine serum albumin. We also work with polymer materials, which have many relevant and desirable biochemical properties. Biology, including cells and proteins, can interact with these 3D-printed biological materials in many ways. At the Schuille lab we study two of those possibilities.”

How do the printed materials mimic cell functions?

“We can create different kinds of surface topographies through 3D printing that resemble cellular structures, for one. These geometrical features can in turn influence protein behavior. Our ability to build structures with a 3D printer is so precise, we can now for example print a protein in a shape that makes it bind more strongly to another protein, triggering a different reaction inside the cell. This means we are able to link specific reactions inside a cell to a certain geometry, which give us clues as to why cells or organelles are shaped the way they are.”

“The second technique has to do with directly 3D printing proteins in the form of hydrogel. The proteins react to the light from the laser: they crosslink to each other to form polymer networks or gels. We now have an exciting opportunity to 3D print micron-sized protein robots, with specific biochemical functionality. This is particularly cool, because the things we print can directly interact with the cells that we study. They can also dynamically change shape – through changes in pH or through interactions with other proteins.”



What kind of applications are possible with 3D bioprinting?

“The big advantage of 3D bioprinting is not that we can mass produce structures with one specific design, but rather that we can do rapid prototyping, where we can make many different designs relatively quickly. Micro-printing is particularly useful for working out what type of design is effective. It has already had a big impact on academic research as well as product development. Once we can confirm that a certain shape works, we can hand our proof of concept over to an industry partner who can place this design on the market.”

“The worldwide interest in the potential of 3D bio-printing is growing. Aside from our lab at the MPI, there are clusters in Japan, Singapore, United States and Germany applying 3D printing to cells. A cluster of researchers in Switzerland for example is working on cell-made carriers – micro-swimmers – that can deliver drugs such as vaccines to specific parts of the body. Several groups in Heidelberg and Karlsruhe in Germany are also investigating how 3D printing can improve regeneration of tissues. Researchers are even 3D printing artificial meat, meaning lab-grown meat, to revolutionize how food can be brought to our table.”

3D bioprinter at work: making the “cell” from BSA photoresin – image of the resulting printed cell can be found in the article text above:

More information:

- [Schwille Group at Max Planck Research Network in Synthetic Biology](#)
- [Synthetic cell researchers working on 3D bioprinting](#)

Lab images and video: Hiromune Eto

List of Figures

1.1	Commonly used microfabrication techniques	4
1.2	Positive and negative tone photoresists	5
1.3	Applications of soft lithography	8
1.4	Working principles of two-photon direct laser writing	10
2.1	Commonly used model membrane systems	12
3.1	3D printing of protein-based hydrogels	17
4.1	Overview of the <i>E. coli</i> MinDE system	20
6.1	Fabrication of patterned SLBs by chromium deposition	34
6.2	MinDE self-organisation on arbitrary shaped membranes	35
6.3	Chemical structures of JDPC and JDPG	105
6.4	Fluidity of supported dendrimer and lipid membranes	109
6.5	MinDE self-organisation patterns on supported dendrimer membranes	111
6.6	Encapsulation of MinDE in dendrimersomes	112
6.7	Co-encapsulation of MinCDE and FtsZ proteins in dendrimersomes . .	112
8.1	Microfabrication of wells for upright imaging of bacteria	144
9.1	MinDE stationary patterns on geometry patterned substrates	148
A.2	Encapsulation of MinDE in droplets	215
A.3	MinDE waves on 3D waveguides	216

LIST OF FIGURES

List of Abbreviations

2PP-DLW	two-photon direct laser writing
<i>E. coli</i>	<i>Escherichia coli</i>
BPD	benzophenone derivative
BSA	bovine serum albumin
DNA	Deoxyribonucleic acid
DOPC	1,2-dioleoyl-sn-glycero-3-phosphocholine
DOPG	1,2-dioleoyl-sn-glycero-3-phospho-(1'-rac-glycerol
FAD	Flavin Adenine Dinucleotide
FMN	Flavin Mononucleotide
FRAP	Fluorescence recovery after photobleaching
GUV	giant unilamellar vesicles
HDMS	Bis(trimethylsilyl)amine
ITO	indium tin oxide
LUV	large unilamellar vesicles
MTS	membrane targeting sequence
PDMS	polydimethylsiloxane
PEG	polyethylene glycol
PETA	pentaerythritol triacrylate
RB	Rose Bengal
SEM	Scanning Electron Microscopy
SLB	supported lipid bilayer
SUV	small unilamellar vesicles
TPETA	trimethylolpropane ethoxylate triacrylate

Bibliography

1. Weibel, D. B., DiLuzio, W. R. & Whitesides, G. M. Microfabrication meets microbiology. *Nature Reviews Microbiology* **5**, 209–218. doi:10.1038/nrmicro1616 (Mar. 2007) (cit. on pp. 3, 6).
2. Duncombe, T. A., Tentori, A. M. & Herr, A. E. Microfluidics: reframing biological enquiry. *Nature reviews. Molecular cell biology* **16**, 554–567. doi:10.1038/nrm4041 (2015) (cit. on p. 3).
3. Rusconi, R., Garren, M. & Stocker, R. Microfluidics expanding the frontiers of microbial ecology. *Annual Review of Biophysics* **43**, 65–91. doi:10.1146/annurev-biophys-051013-022916 (2014) (cit. on p. 3).
4. Bhushan, B. *Encyclopedia of Nanotechnology* (ed Bhushan, B.) 1–9. doi:10.1007/978-90-481-9751-4 (Springer Netherlands, Dordrecht, 2012) (cit. on p. 3).
5. Qin, D., Xia, Y. & Whitesides, G. M. Soft lithography for micro- and nanoscale patterning. *Nature Protocols* **5**, 491–502. doi:10.1038/nprot.2009.234 (2010) (cit. on pp. 3, 7, 23).
6. Bártolo, P. J. *Stereolithographic Processes* 1–36. doi:10.1007/978-0-387-92904-0_1 (2011) (cit. on pp. 3, 7, 9).
7. Voldman, J., Gray, M. L. & Schmidt, M. A. Microfabrication in biology and medicine. *Annual Review of Biomedical Engineering*, 401–425. doi:10.1146/annurev.bioeng.1.1.401 (1999) (cit. on p. 3).
8. Wu, F. & Dekker, C. Nanofabricated structures and microfluidic devices for bacteria: From techniques to biology. *Chemical Society Reviews* **45**, 268–280. doi:10.1039/c5cs00514k (2016) (cit. on p. 3).
9. Bennett, M. R. & Hastay, J. Microfluidic devices for measuring gene network dynamics in single cells. *Nature Reviews Genetics* **10**, 628–638. doi:10.1038/nrg2625 (2009) (cit. on p. 3).
10. Unger, M. A., Chou, H. P., Thorsen, T., Scherer, A. & Quake, S. R. Monolithic microfabricated valves and pumps by multilayer soft lithography. *Science* **288**, 113–116. doi:10.1126/science.288.5463.113 (2000) (cit. on pp. 3, 4, 7).
11. Thorsen, T., Maerkl, S. J. & Quake, S. R. Microfluidic large-scale integration. *Science* **298**, 580–584. doi:10.1126/science.1076996 (Oct. 2002) (cit. on p. 3).
12. Madou, M. & Wang, C. *Photolithography, Encyclopedia of Nanotechnology* (ed Bhushan, B.) doi:10.1007/978-90-481-9751-4 (Springer Netherlands, Dordrecht, 2012) (cit. on pp. 3, 5, 6).
13. Théry, M., Racine, V., Piel, M., Pépin, A., Dimitrov, A., Chen, Y., Sibarita, J. B. & Bornens, M. Anisotropy of cell adhesive microenvironment governs cell internal organization and orientation of polarity. *Proceedings of the National Academy of Sciences of the United States of America* **103**, 19771–19776. doi:10.1073/pnas.0609267103 (2006) (cit. on pp. 3, 6).

14. Reymann, A.-c., Martiel, J.-l., Cambier, T., Blanchoin, L., Boujemaa-paterski, R. & Théry, M. Nucleation geometry governs ordered actin networks structures. *Nature Materials* **9**, 827–832. doi:10.1038/nmat2855 (2010) (cit. on pp. 3, 6).
15. Microchem. *SU-8 2000 Permanent Epoxy Negative Photoresist* tech. rep. (2015). doi:10.1146/annurev.matsci.28.1.153 (cit. on p. 5).
16. Groves, J. T., Ulman, N. & Boxer, S. G. Micropatterning Fluid Lipid Bilayers on Solid Supports. *Science* **275**, 651–654. doi:10.1126/science.275.5300.651 (1997) (cit. on pp. 5, 13, 31, 33).
17. Groves, J. T., Ulman, N., Cremer, P. S. & Boxer, S. G. Substrate-membrane interactions: Mechanisms for imposing patterns on a fluid bilayer membrane. *Langmuir* **14**, 3347–3350. doi:10.1021/la9711701 (1998) (cit. on pp. 5, 13, 31, 35).
18. Hansen, S. D., Huang, W. Y., Lee, Y. K., Bieling, P., Christensen, S. M. & Groves, J. T. Stochastic geometry sensing and polarization in a lipid kinase–phosphatase competitive reaction. *Proceedings of the National Academy of Sciences of the United States of America* **116**, 15013–15022. doi:10.1073/pnas.1901744116 (2019) (cit. on pp. 5, 13).
19. Tayar, A. M., Karzbrun, E., Noireaux, V. & Bar-Ziv, R. H. Synchrony and pattern formation of coupled genetic oscillators on a chip of artificial cells. *Proceedings of the National Academy of Sciences* **114**, 11609–11614. doi:10.1073/pnas.1710620114 (Oct. 2017) (cit. on p. 6).
20. Watanabe, R., Soga, N., Fujita, D., Tabata, K. V., Yamauchi, L., Hyeon Kim, S., Asanuma, D., Kamiya, M., Urano, Y., Suga, H. & Noji, H. Arrayed lipid bilayer chambers allow single-molecule analysis of membrane transporter activity. *Nature Communications* **5**, ncomms5519. doi:10.1038/ncomms5519 (July 2014) (cit. on p. 6).
21. Lehnert, D., Wehrle-Haller, B., David, C., Weiland, U., Ballestrem, C., Imhof, B. A. & Bastmeyer, M. Cell behaviour on micropatterned substrata: Limits of extracellular matrix geometry for spreading and adhesion. *Journal of Cell Science* **117**, 41–52. doi:10.1242/jcs.00836 (2004) (cit. on p. 6).
22. Yang, Y., Kulangara, K., Sia, J., Wang, L. & Leong, K. W. Engineering of a microfluidic cell culture platform embedded with nanoscale features. *Lab on a Chip* **11**, 1638–1646. doi:10.1039/c0lc00736f (2011) (cit. on p. 6).
23. Wu, F., Van Schie, B. G., Keymer, J. E. & Dekker, C. Symmetry and scale orient Min protein patterns in shaped bacterial sculptures. *Nature Nanotechnology* **10**, 1–8. doi:10.1038/nnano.2015.126 (2015) (cit. on pp. 6, 22, 29, 147).
24. Quist, A. P., Pavlovic, E. & Oscarsson, S. Recent advances in microcontact printing. *Analytical and Bioanalytical Chemistry* **381**, 591–600. doi:10.1007/s00216-004-2847-z (2005) (cit. on p. 6).
25. Venkatesan, S., Jerald, J., Asokan, P. & Prabakaran, R. *A Comprehensive Review on Microfluidics Technology and its Applications in Recent Advances in Mechanical Engineering* (eds Kumar, H. & Jain, P. K.) (Springer Singapore, Singapore, 2020), 235–245 (cit. on p. 6).

-
26. Robinson, T., Kuhn, P., Eyer, K. & Dittrich, P. S. Microfluidic trapping of giant unilamellar vesicles to study transport through a membrane pore. *Biomicrofluidics* **7**, 1–8. doi:10.1063/1.4816712 (2013) (cit. on p. 7).
 27. Yandrapalli, N. & Robinson, T. Ultra-high capacity microfluidic trapping of giant vesicles for high-throughput membrane studies. *Lab on a Chip* **19**, 626–633. doi:10.1039/C8LC01275J (2019) (cit. on p. 7).
 28. Yamada, A., Lee, S., Bassereau, P. & Baroud, C. N. Trapping and release of giant unilamellar vesicles in microfluidic wells. *Soft Matter* **10**, 5878. doi:10.1039/C4SM00065J (June 2014) (cit. on p. 7).
 29. Ganzinger, K. A., Merino-Salomón, A., García-Soriano, D. A., Butterfield, A. N., Litschel, T., Siedler, F. & Schwille, P. FtsZ Reorganization Facilitates Deformation of Giant Vesicles in Microfluidic Traps**. *Angewandte Chemie International Edition* **59**, 21372–21376. doi:10.1002/anie.202001928 (Nov. 2020) (cit. on pp. 7, 14, 23, 65, 104, 105, 110, 150).
 30. Fanalista, F., Birnie, A., Maan, R., Burla, F., Charles, K., Pawlik, G., Deshpande, S., Koenderink, G. H., Dogterom, M. & Dekker, C. Shape and Size Control of Artificial Cells for Bottom-Up Biology. *ACS Nano* **13**, 5439–5450. doi:10.1021/acsnano.9b00220 (2019) (cit. on pp. 7, 14, 23).
 31. Aghvami, S. A., Opathalage, A., Zhang, Z. K., Ludwig, M., Heymann, M., Norton, M., Wilkins, N. & Fraden, S. Rapid prototyping of cyclic olefin copolymer (COC) microfluidic devices. *Sensors and Actuators, B: Chemical* **247**, 940–949. doi:10.1016/j.snb.2017.03.023 (2017) (cit. on p. 7).
 32. Pati, F., Jang, J., Lee, J. W. & Cho, D. W. *Extrusion bioprinting* **5**, 123–152. doi:10.1016/B978-0-12-800972-7.00007-4 (Elsevier Inc., 2015) (cit. on p. 7).
 33. Derakhshanfar, S., Mbeleck, R., Xu, K., Zhang, X., Zhong, W. & Xing, M. 3D bioprinting for biomedical devices and tissue engineering: A review of recent trends and advances. *Bioactive Materials* **3**, 144–156. doi:10.1016/j.bioactmat.2017.11.008 (2018) (cit. on p. 7).
 34. Raman, R. & Bashir, R. *Stereolithographic 3D bioprinting for biomedical applications* 89–121. doi:10.1016/B978-0-12-800972-7.00006-2 (Elsevier Inc., 2015) (cit. on p. 7).
 35. Barner-Kowollik, C., Bastmeyer, M., Blasco, E., Delaittre, G., Müller, P., Richter, B. & Wegener, M. 3D Laser Micro- and Nanoprinting: Challenges for Chemistry. *Angewandte Chemie - International Edition* **56**, 15828–15845. doi:10.1002/anie.201704695 (2017) (cit. on pp. 7, 9).
 36. Klein, F., Striebel, T., Fischer, J., Jiang, Z., Franz, C. M., Von Freymann, G., Wegener, M. & Bastmeyer, M. Elastic fully three-dimensional microstructure scaffolds for cell force measurements. *Advanced Materials* **22**, 868–871. doi:10.1002/adma.200902515 (2010) (cit. on p. 9).
 37. Blasco, E., Wegener, M. & Barner-Kowollik, C. Photochemically Driven Polymeric Network Formation: Synthesis and Applications. *Advanced Materials* **29**. doi:10.1002/adma.201604005 (2017) (cit. on p. 9).
-

38. Yeagle, P. L. in *The Membranes of Cells (Third Edition)* (ed Yeagle, P. L.) Third Edit, 27–56 (Academic Press, Boston, 2016). doi:<https://doi.org/10.1016/B978-0-12-800047-2.00002-4> (cit. on p. 11).
39. Czogalla, A., Grzybek, M., Jones, W. & Coskun, Ü. Validity and applicability of membrane model systems for studying interactions of peripheral membrane proteins with lipids. *Biochimica et Biophysica Acta - Molecular and Cell Biology of Lipids* **1841**, 1049–1059. doi:[10.1016/j.bbalip.2013.12.012](https://doi.org/10.1016/j.bbalip.2013.12.012) (2014) (cit. on pp. 11, 14, 65, 104, 145, 146).
40. Lagny, T. J. & Bassereau, P. Bioinspired membrane-based systems for a physical approach of cell organization and dynamics: Usefulness and limitations. *Interface Focus* **5**. doi:[10.1098/rsfs.2015.0038](https://doi.org/10.1098/rsfs.2015.0038) (2015) (cit. on pp. 11, 14).
41. Bunea, A. I., Harloff-Helleberg, S., Taboryski, R. & Nielsen, H. M. Membrane interactions in drug delivery: Model cell membranes and orthogonal techniques. *Advances in Colloid and Interface Science* **281**, 102177. doi:[10.1016/j.cis.2020.102177](https://doi.org/10.1016/j.cis.2020.102177) (2020) (cit. on pp. 11, 14, 146).
42. Richter, R. P., Bérat, R. & Brisson, A. R. Formation of Solid-Supported Lipid Bilayers: An Integrated View. *Langmuir* **22**, 3497–3505. doi:[10.1021/la052687c](https://doi.org/10.1021/la052687c) (Apr. 2006) (cit. on p. 11).
43. Lipowsky, R. & Seifert, U. Adhesion of Vesicles and Membranes. *Molecular Crystals and Liquid Crystals* **202**, 17–25. doi:[10.1080/00268949108035656](https://doi.org/10.1080/00268949108035656) (1991) (cit. on p. 13).
44. Seantier, B. & Kasemo, B. Influence of mono- and divalent ions on the formation of supported phospholipid bilayers via vesicle adsorption. *Langmuir* **25**, 5767–5772. doi:[10.1021/la804172f](https://doi.org/10.1021/la804172f) (2009) (cit. on p. 13).
45. Zan, G. H., Tan, C., Deserno, M., Lanni, F. & Lösche, M. Hemifusion of giant unilamellar vesicles with planar hydrophobic surfaces: A fluorescence microscopy study. *Soft Matter* **8**, 10877–10886. doi:[10.1039/c2sm25702e](https://doi.org/10.1039/c2sm25702e) (2012) (cit. on p. 13).
46. Schweizer, J., Loose, M., Bonny, M., Kruse, K., Monch, I. & Schwille, P. Geometry sensing by self-organized protein patterns. *Proceedings of the National Academy of Sciences* **109**, 15283–15288. doi:[10.1073/pnas.1206953109](https://doi.org/10.1073/pnas.1206953109) (2012) (cit. on pp. 13, 21, 22, 29, 31, 147, 148).
47. Bayerl, T. M. & Bloom, M. Physical properties of single phospholipid bilayers adsorbed to micro glass beads. *Biophysical Journal* **58**, 357–362 (1990) (cit. on p. 13).
48. Brausemann, A., Gerhardt, S., Schott, A. K., Einsle, O., Große-Berkenbusch, A., Johnsson, N. & Gronemeyer, T. Crystal structure of Cdc11, a septin subunit from *Saccharomyces cerevisiae*. *Journal of Structural Biology* **193**, 157–161. doi:[10.1016/j.jsb.2016.01.004](https://doi.org/10.1016/j.jsb.2016.01.004) (2016) (cit. on p. 13).
49. Griffiths, A. D. & Tawfik, D. S. Man-made cell-like compartments for molecular evolution. *Nature Biotechnology* **16**, 652–656 (1998) (cit. on p. 13).

-
50. Courtois, F., Olguin, L. F., Whyte, G., Bratton, D., Huck, W. T., Abell, C. & Hollfelder, F. An integrated device for monitoring time-dependent in vitro expression from single genes in picolitre droplets. *ChemBioChem* **9**, 439–446. doi:10.1002/cbic.200700536 (2008) (cit. on p. 13).
 51. Dittrich, P. S., Jahnz, M. & Schwille, P. A new embedded process for compartmentalized cell-free protein expression and on-line detection in microfluidic devices. *ChemBioChem* **6**, 811–814. doi:10.1002/cbic.200400321 (2005) (cit. on p. 13).
 52. Nisisako, T. & Torii, T. Microfluidic large-scale integration on a chip for mass production of monodisperse droplets and particles. *Lab on a Chip* **8**, 287–293. doi:10.1039/b713141k (2008) (cit. on p. 14).
 53. Heida, T., Neubauer, J. W., Seuss, M., Hauck, N., Thiele, J. & Fery, A. Mechanically Defined Microgels by Droplet Microfluidics. *Macromolecular Chemistry and Physics* **218**, 1–19. doi:10.1002/macp.201600418 (2017) (cit. on p. 14).
 54. Vogel, S. K., Wölfer, C., Ramirez-Diaz, D. A., Flassig, R. J., Sundmacher, K. & Schwille, P. Symmetry Breaking and Emergence of Directional Flows in Minimal Actomyosin Cortices. *Cells* **9**, 8–10. doi:10.3390/cells9061432 (2020) (cit. on p. 14).
 55. Stauer, O., Schröter, M., Platzman, I. & Spatz, J. P. Bottom-Up Assembly of Functional Intracellular Synthetic Organelles by Droplet-Based Microfluidics. *Small* **16**. doi:10.1002/smll.201906424 (2020) (cit. on p. 14).
 56. Bridges, A. A., Jentsch, M. S., Oakes, P. W., Occhipinti, P. & Gladfelter, A. S. Micron-scale plasma membrane curvature is recognized by the septin cytoskeleton. *Journal of Cell Biology* **213**, 23–32. doi:10.1083/jcb.201512029 (2016) (cit. on p. 14).
 57. Walde, P., Cosentino, K., Engel, H. & Stano, P. Giant Vesicles: Preparations and Applications. *ChemBioChem* **11**, 848–865. doi:10.1002/cbic.201000010 (2010) (cit. on p. 14).
 58. Blosser, M. C., Horst, B. G. & Keller, S. L. cDICE method produces giant lipid vesicles under physiological conditions of charged lipids and ionic solutions. *Soft Matter* **12**, 7364–7371. doi:10.1039/C6SM00868B (2016) (cit. on pp. 14, 23).
 59. Braunschweig, A. B., Huo, F. & Mirkin, C. A. Molecular printing. *Nature Chemistry* **1**, 353–358. doi:10.1038/nchem.258 (2009) (cit. on p. 15).
 60. Strale, P. O., Azioune, A., Bugnicourt, G., Lecomte, Y., Chahid, M. & Studer, V. Multiprotein Printing by Light-Induced Molecular Adsorption. *Advanced Materials* **28**, 2024–2029. doi:10.1002/adma.201504154 (2016) (cit. on p. 15).
 61. Jia, H., Kai, L., Heymann, M., García-Soriano, D. A., Härtel, T. & Schwille, P. Light-Induced Printing of Protein Structures on Membranes in Vitro. *Nano Letters* **18**, 7133–7140. doi:10.1021/acs.nanolett.8b03187 (2018) (cit. on p. 15).
 62. Serien, D. & Sugioka, K. Fabrication of three-dimensional proteinaceous micro- and nano-structures by femtosecond laser cross-linking. *Opto-Electronic Advances* **1**, 18000801–18000818. doi:10.29026/oea.2018.180008 (2018) (cit. on pp. 15, 16, 113).
-

63. Spikes, J. D., Shen, H. R., Kopecková, P. & Kopecek, J. Photodynamic crosslinking of proteins. III. Kinetics of the FMN- and rose bengal-sensitized photooxidation and intermolecular crosslinking of model tyrosine-containing N-(2-hydroxypropyl)methacrylamide copolymers. *Photochemistry and photobiology* **70**, 130–7. arXiv: j . 1751-1097 . 1999 . tb07980 . x [10 . 1111] (Aug. 1999) (cit. on p. 15).
64. Seidlits, S. K., Schmidt, C. E. & Shear, J. B. High-resolution patterning of hydrogels in three dimensions using direct-write photofabrication for cell guidance. *Advanced Functional Materials* **19**, 3543–3551. doi:10 . 1002 / adfm . 200901115 (2009) (cit. on pp. 15, 113).
65. Allen, R., Nielson, R., Wise, D. D. & Shear, J. B. Catalytic three-dimensional protein architectures. *Analytical Chemistry* **77**, 5089–5095. doi:10 . 1021/ac0507892 (2005) (cit. on p. 15).
66. Qin, X. H., Ovsianikov, A., Stampfl, J. & Liska, R. Additive manufacturing of photosensitive Hydrogels for tissue engineering applications. *BioNanoMaterials* **15**, 49–70. doi:10 . 1515/bnm-2014-0008 (2014) (cit. on p. 16).
67. Lay, C. L., Lee, Y. H., Lee, M. R., Phang, I. Y. & Ling, X. Y. Formulating an Ideal Protein Photoresist for Fabricating Dynamic Microstructures with High Aspect Ratios and Uniform Responsiveness. *ACS Applied Materials & Interfaces* **8**, 8145–8153. doi:10 . 1021/acsami . 6b02306 (Mar. 2016) (cit. on pp. 16, 113).
68. Lafferty, J. W., Strande, J. R., Kerns, P. M., Fox, N. A. & Basu, S. The interaction of photoactivators with proteins during microfabrication. *Journal of Photochemistry and Photobiology A: Chemistry* **275**, 81–88. doi:10 . 1016/j . jphotochem . 2013 . 10 . 017 (2014) (cit. on p. 16).
69. Basu, S., Cunningham, L. P., Pins, G. D., Bush, K. A., Taboada, R., Howell, A. R., Wang, J. & Campagnola, P. J. Multiphoton excited fabrication of collagen matrixes cross-linked by a modified benzophenone dimer: Bioactivity and enzymatic degradation. *Biomacromolecules* **6**, 1465–1474. doi:10 . 1021/bm049258y (2005) (cit. on p. 16).
70. Serien, D. & Takeuchi, S. Multi-Component Microscaffold with 3D Spatially Defined Proteinaceous Environment. *ACS Biomaterials Science and Engineering* **3**, 487–494. doi:10 . 1021/acsbiomaterials . 6b00695 (2017) (cit. on p. 16).
71. Erben, A., Hörning, M., Hartmann, B., Becke, T., Eisler, S. A., Southan, A., Cranz, S., Hayden, O., Kneidinger, N., Königshoff, M., Lindner, M., Tovar, G. E., Burgstaller, G., Clausen-Schaumann, H., Sudhop, S. & Heymann, M. Precision 3D-Printed Cell Scaffolds Mimicking Native Tissue Composition and Mechanics. *Advanced Healthcare Materials* **9**, 1–15. doi:10 . 1002/adhm . 202000918 (2020) (cit. on p. 16).
72. Kaehr, B. & Shear, J. B. Multiphoton fabrication of chemically responsive protein hydrogels for microactuation. *Proceedings of the National Academy of Sciences of the United States of America* **105**, 8850–8854. doi:10 . 1073/pnas . 0709571105 (2008) (cit. on pp. 16, 26, 113).

-
73. Lee, M. R., Phang, I. Y., Cui, Y., Lee, Y. H. & Ling, X. Y. Shape-shifting 3D protein microstructures with programmable directionality via quantitative nanoscale stiffness modulation. *Small* **11**, 740–748. doi:10.1002/smll.201401343 (2015) (cit. on p. 16).
 74. Khripin, C. Y., Brinker, C. J. & Kaehr, B. Mechanically tunable multiphoton fabricated protein hydrogels investigated using atomic force microscopy. *Soft Matter* **6**, 2842–2848. doi:10.1039/c001193b (2010) (cit. on p. 16).
 75. Connell, J. L., Ritschdorff, E. T. & Shear, J. B. Three-dimensional printing of photoresponsive biomaterials for control of bacterial microenvironments. *Analytical Chemistry* **88**, 12264–12271. doi:10.1021/acs.analchem.6b03440 (2016) (cit. on p. 16).
 76. Noji, H., Yasuda, R., Yoshida, M. & Kinoshita, K. Direct observation of the rotation of F1-ATPase. *Nature* **386**, 299–302. doi:10.1038/386299a0 (Mar. 1997) (cit. on p. 19).
 77. Kai, L., Roos, C., Haberstock, S., Proverbio, D., Ma, Y., Junge, F., Karbyshev, M., Dötsch, V. & Bernhard, F. in *Chemical Genomics and Proteomics: Reviews and Protocols* (ed Zanders, E. D.) 201–225 (Humana Press, Totowa, NJ, 2012). doi:10.1007/978-1-61779-349-3_14 (cit. on p. 19).
 78. Kuruma, Y. & Ueda, T. The PURE system for the cell-free synthesis of membrane proteins. *Nature Protocols* **10**, 1328–1344. doi:10.1038/nprot.2015.082 (2015) (cit. on p. 19).
 79. Shin, J. & Noireaux, V. An E. coli cell-free expression toolbox: Application to synthetic gene circuits and artificial cells. *ACS Synthetic Biology* **1**, 29–41. doi:10.1021/sb200016s (2012) (cit. on p. 19).
 80. Sachse, R., Wüstenhagen, D., Šamalíková, M., Gerrits, M., Bier, F. F. & Kubick, S. Synthesis of membrane proteins in eukaryotic cell-free systems. *Engineering in Life Sciences* **13**, 39–48. doi:10.1002/elsc.201100235 (2013) (cit. on p. 19).
 81. Schwille, P., Spatz, J., Landfester, K., Bodenschatz, E., Herminghaus, S., Sourjik, V., Erb, T. J., Bastiaens, P., Lipowsky, R., Hyman, A., Dabrock, P., Baret, J. C., Vidakovic-Koch, T., Bieling, P., Dimova, R., Mutschler, H., Robinson, T., Tang, T. Y., Wegner, S. & Sundmacher, K. MaxSynBio: Avenues Towards Creating Cells from the Bottom Up. *Angewandte Chemie - International Edition* **57**, 13382–13392. doi:10.1002/anie.201802288 (2018) (cit. on p. 19).
 82. Ramm, B., Heermann, T. & Schwille, P. The E. coli MinCDE system in the regulation of protein patterns and gradients. *Cellular and Molecular Life Sciences* **76**, 4245–4273. doi:10.1007/s00018-019-03218-x (2019) (cit. on pp. 19, 21, 22, 25, 30, 110).
 83. Adler, H. I., Fisher, W. D., Cohen, A. & Hardigree, A. A. MINIATURE escherichia coli CELLS DEFICIENT IN DNA. *Proceedings of the National Academy of Sciences* **57**, 321–326. doi:10.1073/pnas.57.2.321 (Feb. 1967) (cit. on p. 19).
 84. Raskin, D. M. & de Boer, P. A. J. Rapid pole-to-pole oscillation of a protein required for directing division to the middle of Escherichia coli. *Proceedings of the National Academy of Sciences* **96**, 4971–4976. doi:10.1073/pnas.96.9.4971 (1999) (cit. on pp. 19, 104, 108).
-

85. Adams, D. W. & Errington, J. Bacterial cell division: Assembly, maintenance and disassembly of the Z ring. *Nature Reviews Microbiology* **7**, 642–653. doi:10.1038/nrmicro2198 (2009) (cit. on p. 21).
86. Vicente, M. & Rico, A. I. The order of the ring: Assembly of Escherichia coli cell division components. *Molecular Microbiology* **61**, 5–8. doi:10.1111/j.1365-2958.2006.05233.x (2006) (cit. on p. 21).
87. Lutkenhaus, J., Pichoff, S. & Du, S. Bacterial cytokinesis: From Z ring to divisome. *Cytoskeleton* **69**, 778–790. doi:10.1002/cm.21054 (2012) (cit. on p. 21).
88. Loose, M., Fischer-Friedrich, E., Ries, J., Kruse, K. & Schwille, P. Spatial Regulators for Bacterial Cell Division Self-Organize into Surface Waves in Vitro. *Science* **320**, 789–792. doi:10.1126/science.1154413 (2008) (cit. on pp. 21, 108).
89. Martos, A., Petrasek, Z. & Schwille, P. Propagation of MinCDE waves on free-standing membranes. *Environmental Microbiology* **15**, 3319–3326. doi:10.1111/1462-2920.12295 (Dec. 2013) (cit. on pp. 21, 148).
90. Caspi, Y. & Dekker, C. Mapping out Min protein patterns in fully confined fluidic chambers. *eLife* **5**, 1–27. doi:10.7554/eLife.19271 (2016) (cit. on pp. 21, 22, 148).
91. Miyagi, A., Ramm, B., Schwille, P. & Scheuring, S. High-Speed Atomic Force Microscopy Reveals the Inner Workings of the MinDE Protein Oscillator. *Nano Letters* **18**, 288–296. doi:10.1021/acs.nanolett.7b04128 (2018) (cit. on p. 21).
92. Denk, J., Kretschmer, S., Halatek, J., Hartl, C., Schwille, P. & Frey, E. MinE conformational switching confers robustness on self-organized Min protein patterns. *Proceedings of the National Academy of Sciences of the United States of America* **115**, 4553–4558. doi:10.1073/pnas.1719801115 (2018) (cit. on pp. 21, 22, 108, 148).
93. Vecchiarelli, A. G., Li, M., Mizuuchi, M. & Mizuuchi, K. Differential affinities of MinD and MinE to anionic phospholipid influence Min patterning dynamics in vitro. *Molecular Microbiology* **93**, 453–463. doi:10.1111/mmi.12669 (2014) (cit. on pp. 21, 108–110).
94. Shih, Y. L., Huang, K. F., Lai, H. M., Liao, J. H., Lee, C. S., Chang, C. M., Mak, H. M., Hsieh, C. W. & Lin, C. C. The N-terminal Amphipathic Helix of the topological specificity factor mine is associated with shaping membrane curvature. *PLoS ONE* **6**. doi:10.1371/journal.pone.0021425 (2011) (cit. on p. 21).
95. Glock, P., Ramm, B., Heermann, T., Kretschmer, S., Schweizer, J., Mu, J. & Schwille, P. Stationary Patterns in a Two-Protein Reaction-Diffusion System. doi:10.1021/acssynbio.8b00415 (2019) (cit. on pp. 22, 23, 25, 107, 147).
96. Zieske, K. & Schwille, P. Reconstitution of self-organizing protein gradients as spatial cues in cell-free systems. *eLife* **3**, 1–19. doi:10.7554/eLife.03949 (2014) (cit. on pp. 22, 29, 65, 147).

-
97. Vecchiarelli, A. G., Li, M., Mizuuchi, M., Hwang, L. C., Seol, Y., Neuman, K. C. & Mizuuchi, K. Membrane-bound MinDE complex acts as a toggle switch that drives Min oscillation coupled to cytoplasmic depletion of MinD. *Proceedings of the National Academy of Sciences* **113**, E1479–E1488. doi:10.1073/pnas.1600644113 (Mar. 2016) (cit. on p. 22).
 98. Litschel, T., Ramm, B., Maas, R., Heymann, M., Schwille, P., Zieske, K., Chwastek, G. & Schwille, P. Protein Patterns and Oscillations on Lipid Monolayers and in Microdroplets. *Angewandte Chemie - International Edition* **55**, 13455–13459. doi:10.1002/anie.201606069 (2016) (cit. on p. 23).
 99. Kohyama, S., Yoshinaga, N., Yanagisawa, M., Fujiwara, K. & Doi, N. Cell-sized confinement controls generation and stability of a protein wave for spatiotemporal regulation in cells. *eLife* **8**, 1–30. doi:10.7554/eLife.44591 (July 2019) (cit. on pp. 23, 110).
 100. Litschel, T., Ramm, B., Maas, R., Heymann, M. & Schwille, P. Beating Vesicles: Encapsulated Protein Oscillations Cause Dynamic Membrane Deformations. *Angewandte Chemie - International Edition* **57**, 16286–16290. doi:10.1002/anie.201808750 (2018) (cit. on pp. 23, 110).
 101. Wettmann, L., Bonny, M. & Kruse, K. Effects of geometry and topography on Min-protein dynamics. *PLoS ONE* **13**, 1–20. doi:10.1371/journal.pone.0203050 (2018) (cit. on pp. 23, 25, 29).
 102. Brauns, F., Pawlik, G., Halatek, J., Kerssemakers, J. W., Frey, E. & Dekker, C. Bulk-surface coupling reconciles Min-protein pattern formation in vitro and in vivo. *bioRxiv*, 2020.03.01.971952. doi:10.1101/2020.03.01.971952 (2020) (cit. on pp. 23, 25).
 103. Percec, V., Wilson, D. A., Leowanawat, P., Wilson, C. J., Hughes, A. D., Kaucher, M. S., Hammer, D. A., Levine, D. H., Kim, A. J., Bates, F. S., Davis, K. P., Lodge, T. P., Klein, M. L., Devane, R. H., Aqad, E., Rosen, B. M., Argintaru, A. O., Sienkowska, M. J., Rissanen, K., Nummelin, S. & Ropponen, J. Self-Assembly of Janus Dendrimers into Uniform Dendrimersomes and Other Complex Architectures. *Science* **328**, 1009–1015. doi:10.1126/science.1185547 (2010) (cit. on pp. 25, 104, 105).
 104. Thalmeier, D., Halatek, J. & Frey, E. Geometry-induced protein pattern formation. *Proceedings of the National Academy of Sciences* **113**, 548–553. doi:10.1073/pnas.1515191113 (2016) (cit. on p. 29).
 105. Ramm, B., Glock, P. & Schwille, P. In Vitro Reconstitution of Self-Organizing Protein Patterns on Supported Lipid Bilayers. *Journal of Visualized Experiments* **137**, e58139. doi:10.3791/58139 (2018) (cit. on pp. 30, 32, 149).
 106. Vale, R. D. The molecular motor toolbox for intracellular transport. *Cell* **112**, 467–480. doi:10.1016/S0092-8674(03)00111-9 (2003) (cit. on p. 30).
 107. Theriot, J. A. The polymerization motor. *Traffic* **1**, 19–28. doi:10.1034/j.1600-0854.2000.010104.x (2000) (cit. on p. 30).
-

BIBLIOGRAPHY

108. Almonacid, M., Ahmed, W. W., Bussonnier, M., Maily, P., Betz, T., Voituriez, R., Gov, N. S. & Verlhac, M. H. Active diffusion positions the nucleus in mouse oocytes. *Nature Cell Biology* **17**, 470–479. doi:10.1038/ncb3131 (2015) (cit. on p. 30).
109. Colin, A., Letort, G., Razin, N., Almonacid, M., Ahmed, W., Betz, T., Terret, M. E., Gov, N. S., Voituriez, R., Gueroui, Z. & Verlhac, M. H. Active diffusion in oocytes nonspecifically centers large objects during prophase I and meiosis I. *Journal of Cell Biology* **219**. doi:10.1083/jcb.201908195 (2020) (cit. on p. 30).
110. Goehring, N. W., Trong, P. K., Bois, J. S., Chowdhury, D., Nicola, E. M., Hyman, A. A. & Grill, S. W. Polarization of PAR Proteins by Advective Triggering of a Pattern-Forming System. *Science* **334**, 1137–1141. doi:10.1126/science.1208619 (Nov. 2011) (cit. on p. 30).
111. Schindelin, J., Arganda-Carreras, I., Frise, E., Kaynig, V., Longair, M., Pietzsch, T., Preibisch, S., Rueden, C., Saalfeld, S., Schmid, B., Tinevez, J. Y., White, D. J., Hartenstein, V., Eliceiri, K., Tomancak, P. & Cardona, A. Fiji: An open-source platform for biological-image analysis. *Nature Methods* **9**, 676–682. doi:10.1038/nmeth.2019. arXiv: 1081-8693 (2012) (cit. on pp. 32, 106).
112. Soumpasis, D. Theoretical Analysis of Fluorescence Photobleaching Recovery Experiments. *Biophysical journal* **41**, 95–97. doi:10.1016/S0006-3495(83)84410-5 (1983) (cit. on pp. 32, 106).
113. Chiantia, S., Ries, J., Kahya, N. & Schwille, P. Combined AFM and Two-Focus SFCS Study of Raft-Exhibiting Model Membranes. *ChemPhysChem* **7**, 2409–2418. doi:10.1002/cphc.200600464 (2006) (cit. on pp. 35, 108).
114. Tamm, L. K. & McConnell, H. M. Supported phospholipid bilayers. *Biophysical Journal* **47**, 105–113. doi:10.1016/S0006-3495(85)83882-0 (1985) (cit. on pp. 35, 108).
115. Ramm, B., Goychuk, A., Khmelinskaia, A., Blumhardt, P., Eto, H., Ganzinger, K. A., Frey, E. & Schwille, P. A diffusiophoretic mechanism for ATP-driven transport without motor proteins. *Nature Physics*. doi:10.1038/s41567-021-01213-3 (Apr. 2021) (cit. on pp. 37, 153).
116. Yeagle, P. L. in *The Membranes of Cells (Third Edition)* (ed Yeagle, P. L.) Third Edit, 291–334 (Academic Press, Boston, 2016). doi:https://doi.org/10.1016/B978-0-12-800047-2.00012-7 (cit. on pp. 65, 104).
117. Eto, H., Soga, N., Franquelim, H. G., Glock, P., Khmelinskaia, A., Kai, L., Heymann, M., Noji, H. & Schwille, P. Design of Sealable Custom-Shaped Cell Mimicries Based on Self-Assembled Monolayers on CYTOP Polymer. *ACS Applied Materials & Interfaces* **11**, 21372–21380. doi:10.1021/acsami.9b05073 (June 2019) (cit. on p. 66).
118. Rodriguez-Emmenegger, C., Xiao, Q., Kostina, N. Y., Sherman, S. E., Rahimi, K., Partridge, B. E., Li, S., Sahoo, D., Reveron Perez, A. M., Buzzacchera, I., Han, H., Kerzner, M., Malhotra, I., Möller, M., Wilson, C. J., Good, M. C., Goulian, M., Baumgart, T., Klein, M. L. & Percec, V. Encoding biological recognition in a bicomponent cell-membrane mimic. *Proceedings of the National Academy of Sciences of the United States of America* **116**, 5376–5382. doi:10.1073/pnas.1821924116 (2019) (cit. on pp. 104, 105).

-
119. Szeto, T. H., Rowland, S. L., Rothfield, L. I. & King, G. F. Membrane localization of MinD is mediated by a C-terminal motif that is conserved across eubacteria, archaea, and chloroplasts. *Proceedings of the National Academy of Sciences of the United States of America* **99**, 15693–15698. doi:10.1073/pnas.232590599 (2002) (cit. on p. 105).
 120. Hu, Z. & Lutkenhaus, J. A conserved sequence at the C-terminus of MinD is required for binding to the membrane and targeting MinC to the septum. *Molecular Microbiology* **47**, 345–355. doi:10.1046/j.1365-2958.2003.03321.x (2003) (cit. on p. 105).
 121. Heermann, T., Ramm, B., Glaser, S. & Schwille, P. Local Self-Enhancement of MinD Membrane Binding in Min Protein Pattern Formation. *Journal of Molecular Biology* **432**, 3191–3204. doi:10.1016/j.jmb.2020.03.012 (2020) (cit. on p. 108).
 122. Ramm, B., Glock, P., Mücksch, J., Blumhardt, P., García-Soriano, D. A., Heymann, M. & Schwille, P. The MinDE system is a generic spatial cue for membrane protein distribution in vitro. *Nature Communications* **9**, 3942. doi:10.1038/s41467-018-06310-1 (Dec. 2018) (cit. on p. 108).
 123. Ramirez-Diaz, D. A., García-Soriano, D. A., Raso, A., Mücksch, J., Feingold, M., Rivas, G. & Schwille, P. Treadmilling analysis reveals new insights into dynamic FtsZ ring architecture. *PLoS Biology* **16**, 1–20. doi:10.1371/journal.pbio.2004845 (2018) (cit. on p. 110).
 124. Jia, H., Litschel, T., Heymann, M., Eto, H., Franquelim, H. G. & Schwille, P. Shaping Giant Membrane Vesicles in 3D-Printed Protein Hydrogel Cages. *Small* **16**, 1906259. doi:10.1002/smll.201906259 (July 2020) (cit. on p. 115).
 125. Guney, M. G. & Fedder, G. K. Estimation of line dimensions in 3D direct laser writing lithography. *Journal of Micromechanics and Microengineering* **26**, 105011. doi:10.1088/0960-1317/26/10/105011 (Oct. 2016) (cit. on p. 141).
 126. Du, S. & Lutkenhaus, J. Assembly and activation of the Escherichia coli divisome. *Molecular Microbiology* **105**, 177–187. doi:10.1111/mmi.13696 (2017) (cit. on p. 141).
 127. Gamba, P., Veening, J. W., Saunders, N. J., Hamoen, L. W. & Daniel, R. A. Two-step assembly dynamics of the Bacillus subtilis divisome. *Journal of Bacteriology* **191**, 4186–4194. doi:10.1128/JB.01758-08 (2009) (cit. on p. 141).
 128. De Boer, P. A. J. Advances in understanding *E. coli* cell fission. *Current opinion in microbiology* **13**, 730–737. doi:10.1016/j.mib.2010.09.015. Advances (2010) (cit. on p. 141).
 129. Lutkenhaus, J., Pichoff, S. & Du, S. Bacterial cytokinesis: From Z ring to divisome. *Cytoskeleton* **69**, 778–790. doi:10.1002/cm.21054 (2012) (cit. on p. 141).
 130. Tsang, M. J. & Bernhardt, T. G. Guiding divisome assembly and controlling its activity. *Current Opinion in Microbiology* **24**, 60–65. doi:10.1016/j.mib.2015.01.002 (2015) (cit. on p. 141).
 131. Burkholder, P. R. & Giles, N. H. Induced Biochemical Mutations in Bacillus Subtilis. *American Journal of Botany* **34**, 345–348. doi:10.1002/j.1537-2197.1947.tb12999.x (1947) (cit. on pp. 141, 142).
-

132. Bisson-Filho, A. W., Hsu, Y. P., Squyres, G. R., Kuru, E., Wu, F., Jukes, C., Sun, Y., Dekker, C., Holden, S., VanNieuwenhze, M. S., Brun, Y. V. & Garner, E. C. Treadmilling by FtsZ filaments drives peptidoglycan synthesis and bacterial cell division. *Science* **355**, 739–743. doi:10.1126/science.aak9973 (2017) (cit. on p. 142).
133. Whitley, K. D., Jukes, C., Tregidgo, N., Karinou, E., Almada, P., Cesbron, Y., Henriques, R., Dekker, C. & Holden, S. FtsZ treadmilling is essential for Z-ring condensation and septal constriction initiation in *Bacillus subtilis* cell division. *Nature Communications* **12**, 2448. doi:10.1038/s41467-021-22526-0 (Dec. 2021) (cit. on p. 142).
134. Hartmann, R., Carregal-Romero, S., Parak, W. J. & Rivera_Gil, P. in *Frontiers of Nanoscience* **1**, 181–196 (2012). doi:10.1016/B978-0-12-415769-9.00007-8 (cit. on p. 142).
135. Jungmann, R., Avendaño, M. S., Woehrstein, J. B., Dai, M., Shih, W. M. & Yin, P. Multiplexed 3D cellular super-resolution imaging with DNA-PAINT and Exchange-PAINT. *Nature Methods* **11**, 313–318. doi:10.1038/nmeth.2835 (Mar. 2014) (cit. on p. 142).
136. Cramer, K., Bolender, A. L., Stockmar, I., Jungmann, R., Kasper, R. & Shin, J. Y. Visualization of bacterial protein complexes labeled with fluorescent proteins and nanobody binders for STED microscopy. *International Journal of Molecular Sciences* **20**. doi:10.3390/ijms20143376 (2019) (cit. on p. 143).
137. Parthasarathy, R., Yu, C. H. & Groves, J. T. Curvature-modulated phase separation in lipid bilayer membranes. *Langmuir* **22**, 5095–5099. doi:10.1021/la060390o (2006) (cit. on pp. 145, 146).
138. Selimis, A., Mironov, V. & Farsari, M. Direct laser writing: Principles and materials for scaffold 3D printing. *Microelectronic Engineering* **132**, 83–89. doi:10.1016/j.mee.2014.10.001 (2014) (cit. on p. 146).
139. Kotz, F., Quick, A. S., Risch, P., Martin, T., Hoose, T., Thiel, M., Helmer, D. & Rapp, B. E. Two-Photon Polymerization of Nanocomposites for the Fabrication of Transparent Fused Silica Glass Microstructures. *Advanced Materials* **33**. doi:10.1002/adma.202006341 (2021) (cit. on p. 146).
140. Asahi Glass Co. Ltd., J. *Cytop Technical Report* tech. rep. (Asahi Glass Co. Ltd., Japan), 1–5 (cit. on p. 146).
141. Niederauer, C., Blumhardt, P., Mücksch, J., Heymann, M., Lambacher, A. & Schwille, P. Direct characterization of the evanescent field in objective-type total internal reflection fluorescence microscopy. *Optics Express* **26**, 20492. doi:10.1364/oe.26.020492 (2018) (cit. on p. 146).
142. Glock, P., Brauns, F., Halatek, J., Frey, E. & Schwille, P. Design of biochemical pattern forming systems from minimal motifs. *eLife* **8**, 1–17. doi:10.7554/eLife.48646 (2019) (cit. on p. 149).
143. Kostina, N. Y., Wagner, A. M., Haraszti, T., Rahimi, K., Xiao, Q., Klein, M. L., Percec, V. & Rodriguez-Emmenegger, C. Unraveling topology-induced shape transformations in dendrimersomes. *Soft Matter* **17**, 254–267. doi:10.1039/d0sm01097a (2021) (cit. on p. 149).

-
144. Xiao, Q., Yadavalli, S. S., Zhang, S., Sherman, S. E., Fiorin, E., Da Silva, L., Wilson, D. A., Hammer, D. A., André, S., Gabius, H. J., Klein, M. L., Goulian, M. & Percec, V. Bioactive cell-like hybrids coassembled from (glyco)dendrimerosomes with bacterial membranes. *Proceedings of the National Academy of Sciences of the United States of America* **113**, E1134–E1141. doi:10.1073/pnas.1525589113 (2016) (cit. on p. 149).
 145. Kostina, N. Y., Rahimi, K., Xiao, Q., Haraszti, T., Dedisch, S., Spatz, J. P., Schwaneberg, U., Klein, M. L., Percec, V., Möller, M. & Rodriguez-Emmenegger, C. Membrane-Mimetic Dendrimerosomes Engulf Living Bacteria via Endocytosis. *Nano Letters* **19**, 5732–5738. doi:10.1021/acs.nanolett.9b02349 (2019) (cit. on p. 149).
 146. Franquelim, H. G., Khmelinskaia, A., Sobczak, J. P., Dietz, H. & Schwille, P. Membrane sculpting by curved DNA origami scaffolds. *Nature Communications* **9**, 1–10. doi:10.1038/s41467-018-03198-9 (2018) (cit. on p. 149).
 147. Dreher, Y., Jahnke, K., Bobkova, E., Spatz, J. P. & Göpfrich, K. Division and Regrowth of Phase-Separated Giant Unilamellar Vesicles. *Angewandte Chemie International Edition* **60**, 10661–10669. doi:10.1002/anie.202014174 (May 2021) (cit. on p. 149).
 148. Steinkühler, J., Knorr, R. L., Zhao, Z., Bhatia, T., Bartelt, S. M., Wegner, S., Dimova, R. & Lipowsky, R. Controlled division of cell-sized vesicles by low densities of membrane-bound proteins. *Nature Communications* **11**, 1–11. doi:10.1038/s41467-020-14696-0 (2020) (cit. on p. 149).
 149. Fletcher, D. A. & Mullins, R. D. Cell mechanics and the cytoskeleton. *Nature* **463**, 485–492. doi:10.1038/nature08908 (2010) (cit. on p. 150).
 150. Pollard, T. D. & Borisy, G. G. Cellular Motility Driven by Assembly and Disassembly of Actin Filaments. *Cell* **112**, 453–465. doi:10.1016/S0092-8674(03)00120-X (Feb. 2003) (cit. on p. 150).

BIBLIOGRAPHY

Acknowledgements

A heartfelt thank you to everyone who has helped me along this - what feel to me now as a - long, long journey, but one that equally feels like it just passed me by. The people with whom I have had the pleasure to spend time together have both scientifically and personally shaped who I am today, and I will be eternally grateful.

First of all, I would like to thank my supervisor, Petra Schwille. Part of my journey was to realise just how lucky I have been to be part of this lab and to be given this opportunity to explore the science that I like. The freedom that I had to drive my research has developed me as a researcher and has trained me up as a person. So thank you for this fruitful time.

I would also like to thank all of my collaborators and co-authors, who have had a direct impact on my research. Hiroyuki Noji and Naoki Soga, for giving me a head-start with the CYTOP project, and the enjoyable time I spent at the University of Tokyo. Cesar Rodriguez-Emmenegger, Mariia Vorobii, Anna Wagner and Anton Joseph for developing the dendrimer project together and teaching me the dark arts of chemistry. Chase Broedersz and his team for his theoretical input. Ralf Jungmann and Kimberley Cramer for approaching me with microscopy projects and helping me to develop my expertise. Allen Liu, for your scientific insight and kind advice, and it was also a pleasure to share our multicultural views. Frank and Helge for your wonderful support in the cleanroom, as well as Sigi for your rich expertise in the membrane lab.

My thanks to all my past and present colleagues, who became my advisers but also my friends. Micha, at times for being an absolute mess but still managing to make many of the biggest impacts on my research so far. Henri, because you really can answer just about any question. Bea, for being insightful and supportive. Philipp G., for staying so positive and encouraging, also for the few times we had jam sessions together. Kristina, for being helpful when I needed a bit of advice. Special mentions to my old "noisy" office mates. Philipp B., for your kind-heartedness and your thoughtful approach to life. Sonal, for showing me your transformative way of life by starting work at noon. Jonas, for coming up with numerous innuendoes and then easily looking at the below-the-waist ring. Alena, you kind of got away with being a bad-ass. Another special mention to the kicker crew, with Diego, Sven, Katharina, Freddie, Benni, and a whole bunch of others. Quotes of "bam", "banana", "do the dance", "Lamer Platz" and "do a Roel" spring to mind, and getting "Hiroed" became a thing, which I am proud of. Johannes, Flo and Leon - I will treasure our memories from Klosters with our good old friend David. Tamara, for being reliably stressed but always helpful. Shunshi, for adding a spice of Japan to lab life. Christian, ever the philosopher. Adrian, for the fun breaks in between experiments. Also my students Po-Chun and Milena, as well as Maria, who helped me to think about my projects deeply and to grow as a teacher and an adviser. And to all those others who helped make the Schwille Lab a comfortable and enjoyable place to be.

I thank all of my friends and family, who have supported me throughout my life, who have looked after me from a distance even as I go moving around in the world.

ACKNOWLEDGEMENTS

Also Samba, our dog, who is always hungry but is also always happy, whatever happens. And last but not least, my special person, Marion. I could not have wished for a more kind, intelligent and understanding person to have by my side. You supported me in more ways than you care to realise, so thank you - it has been a joy to go through this journey with you.